

**SYNTHESIS OF ACTIVATED CARBON FROM
BIOMASS WASTE AND STUDY OF ITS SUITABILITY
FOR APPLICATIONS IN ELECTROCHEMICAL
SYSTEMS**

Thesis submitted to

University of Calicut, Kerala
*in partial fulfilment of the requirements
for the award of the degree of*

DOCTOR OF PHILOSOPHY IN PHYSICS

Under the Faculty of Science

By

Merin Pulikkottil

Under the guidance of

Dr. A Seema (Supervisor)

Scientist E, C-MET, Thrissur

Dr. Veena Gopalan E (Co-supervisor)

Assistant professor, Vimala College, Thrissur



CENTRE FOR MATERIALS FOR ELECTRONICS TECHNOLOGY (C-MET)
Scientific Society, Ministry of Electronics and Information Technology, Government of
India, Shornur Road, Mulangunnathukavu P.O, Athani, Thrissur- 680581, Kerala, India

May 2025

Synthesis of activated carbon from biomass waste and study of its suitability for applications in electrochemical systems

PhD Thesis

Submitted by

Merin Pulikkottil

Kollannoor house,
Near M.D College,
Aruvai, Pazhanji (P.O),
Thrissur-680542
Kerala,India
Email: merinpulikkottil@gmail.com

Research Supervisor

Dr. A Seema

Scientist E
Centre for Materials for Electronics Technology (C-MET), Thrissur
Email: seema@cmet.gov.in

Research Co-supervisor

Dr. Veena Gopalan E

Assistant Professor, Department of Physics, Vimala College, Thrissur
Email: veenasreejith@gmail.com

May 2025



सेन्टर फॉर मेटिरियल्स फॉर इलेक्ट्रॉनिक्स टेक्नोलॉजी (सी-मेट)

(वैज्ञानिक संस्था, इलेक्ट्रॉनिक्स और सूचना प्रौद्योगिकी मंत्रालय, भारत सरकार)

षोरनूर रोड, मुलंगुन्नतुकावु पोस्ट, अत्तानि, त्रिश्शूर - 680 581, केरला, भारत



CENTRE FOR MATERIALS FOR ELECTRONICS TECHNOLOGY

(Scientific Society, Ministry of Electronics and Information Technology, Government of India)

Shoranur Road, P.O. Mulangunnathukavu, Athani, Thrissur - 680 581, Kerala, India

Tel : EPABX : 91-487-2201156-59 (4 LINES). Fax : 91-487-2201347

E-mail : cmett@cmet.gov.in URL : www.cmet.gov.in



Date: 28.04.2025

CERTIFICATE

This is to certify that the thesis entitled “**SYNTHESIS OF ACTIVATED CARBON FROM BIOMASS WASTE AND STUDY OF ITS SUITABILITY FOR APPLICATIONS IN ELECTROCHEMICAL SYSTEMS**” submitted to University of Calicut in partial fulfilment of the requirements for the award of the degree of **Doctor of Philosophy in Physics** under the Faculty of Science, is a record of the authentic work carried out by Mrs. Merin Pulikkottil, at Centre for Materials for Electronics Technology (C-MET), Thrissur, under my guidance. The work presented in this thesis has not been submitted for any other degree or diploma of this or any other University and has been found to have no plagiarism using the software approved by the UGC/University.

Thrissur

Seema A

Dr. A. Seema

Supervising Guide

VIMALA COLLEGE

(Autonomous)

THRISSUR - 680 009, KERALA, INDIA

PH: +91 0487 - 2332080, 2328232

Visit us : www.vimalacollege.edu.in

E-mail: mail@vimalacollege.edu.in

(Affiliated to the University of Calicut & Nationally Re-accredited with A+ Grade - 4th Cycle)



Date: 28.04.2025

CERTIFICATE

This is to certify that the thesis entitled “SYNTHESIS OF ACTIVATED CARBON FROM BIOMASS WASTE AND STUDY OF ITS SUITABILITY FOR APPLICATIONS IN ELECTROCHEMICAL SYSTEMS” submitted to University of Calicut in partial fulfilment of the requirements for the award of the degree of **Doctor of Philosophy in Physics** under the Faculty of Science, is a record of the authentic work carried out by Mrs. Merin Pulikkottil, at Centre for Materials for Electronics Technology (C-MET), Thrissur, under my Co-supervision. The work presented in this thesis has not been submitted for any other degree or diploma of this or any other University and has been found to have no plagiarism using the software approved by the UGC/University.

Thrissur

A handwritten signature in blue ink, appearing to read 'V. Gopalan E', written over a horizontal line.

Dr. Veena Gopalan E

Co-supervisor

Declaration

I hereby declare that the work presented in the thesis entitled “SYNTHESIS OF ACTIVATED CARBON FROM BIOMASS WASTE AND STUDY OF ITS SUITABILITY FOR APPLICATIONS IN ELECTROCHEMICAL SYSTEMS” is based on the original work done by me under the supervision and guidance of Dr. A Seema, Scientist E, Centre for Materials for Electronics Technology (C-MET), Thrissur and Dr. Veena Gopalan E, Assistant Professor, Vimala College, Thrissur and has not been included in any other thesis submitted previously for the award of any degree. The contents of the thesis are undergone plagiarism check using Ithenticate software at C.H.M.K. Library, University of Calicut, and the similarity index found within the permissible limit. I also declare that the thesis is free from AI generated contents.

Thrissur



Merin Pulikkottil.

Dedicated to my family

.....— Acknowledgement

This research work was possible due to the help, support, inspiration, and love of many influential individuals throughout my life. First and foremost, I sincerely thank God Almighty and nature for enabling me to complete this work.

I have great pleasure to express my heartfelt gratitude to my research supervisor, Dr. A. Seema, Scientist E at the Centre for Materials for Electronics Technology (C-MET) in Thrissur. Her unwavering support and constant encouragement have been invaluable throughout my research journey. Dr. Seema's insightful suggestions and advice have always guided me to make the right decisions at crucial moments. Her honest feedback and engaging discussions have deepened my understanding and knowledge in the field of science. I am truly thankful to Dr. Seema for the opportunity to engage in such interesting research work.

I would like to express my sincere gratitude to my co-supervisor, Dr. Veena Gopalan, Assistant Professor in the Department of Physics at Vimala College, Thrissur, for her continuous support and valuable suggestions during my research.

I would like to sincerely thank Dr. S. Rajesh Kumar, Director of C-MET, Thrissur, Dr. B.B. Kale, Former Director General of C-MET, and Dr. N. Raghu, Former Director of C-MET, Thrissur, for providing me with the opportunity to pursue my research work at C-MET.

I would like to express my heartfelt gratitude to Dr. M. N. Muralidharan, Scientist-C at C-MET Thrissur, for his support and encouragement throughout my tenure. Additionally, I would like to thank Dr. Digambar Y. Nadargi, Scientist D; Dr. Abhisek Choudhary, Scientist-C; and Dr. Bhagyashri Bhangare Kisan, Scientist B, all from C-MET Thrissur, for their support.

I express my sincere gratitude to Dr. Malini K.A. and Dr. Mini Krishna K., Assistant Professors in the Department of Physics at Vimala College, Thrissur, for their valuable suggestions and encouragement. I also want to acknowledge all the faculty members of the Department of Physics at Vimala College for laying the foundation of my research journey.

I wish to thank all the scientists from C-MET, Thrissur, for their suggestions and encouragement. I also want to thank Mr. Anilkumar, the Administrative Officer, and Mr. T. Paramasivan, the Finance Officer, for their ongoing support. Additionally, I extend my appreciation to all the administrative and finance staff at C-MET, Thrissur.

I also express my thanks to Mr. Sreedhar Krishna, Mr. Muhammad Shafi, Mr. Arun, Mr. Pakia Selvam and all other technical staff of C-MET Thrissur for their assistance in various situations.

My special thanks to my colleagues Dr. Arathy K, Mrs. Nimmi Sudarsan, Mrs. Linta Antony, Mr. Deepak K, Mr. Jimmy Joy, Mr Alastin, Dr. Lakshmi Varrier, Mr. Hennock, Mrs. Silpa, Mr. Jithu C.J, Mr. Raashid, Mr. Amal, Mr. Haris, Mr. Febin, Mr. Anand, Ms. Ashna, Mr. Vishnu, Mr. Jo, Mrs. Deepa, Mr. Annleo, Mr. Sreekumar E.B, Mr. Sreekumar M.G, Ms. Anitta Thomas, Mr. Kalesh, Mr. Abhijith, Mr. Ambareesh, Mr. Midhun, Mr. Amal, Mr. Ansaf, Mr. Arun, Mr. Praveen, Dr. Manuraj Mohan, Ms. Maria, Dr. Geevarghese, Dr. Ramesh, Dr. Partha, Dr. Jitha, Dr. Thomas, Dr. Athira, Mr. Rahul, Mr. Sunil, Mrs. Athira K, Mr. Joel, Mr. Jepsin, Mr. Shebin, Mr Vishnu, Mr. Shemilal, Ms. Aiswarya, Mr. Vishnu Prasad, Ms. Ashmi, Ms. Ummimaya, Mr. Rijo, Dr. Aswathy, Ms. Amrutha, Mrs Adhya, Mr. Jestin, Ms. Athira C. M, Mr. Nikhil, Mr. Jomon, Mr. Amaljith, Mr. Sreejith, Mr. Noufal, Ms. Sandra, Mrs. Theertha, Mr. Nandhakishor and all other lab mates for their beautiful friendship. I would like to thank Dr. Soumya, Mrs. Liya Tony, Mrs. Jumana, Mrs. Anagha, Mr. Athul, Mrs. Nimisha, Mr. Nidhin, Mr. Daniel, Mr. Binto, and Mrs. Swetha for their support and friendship.

I have no words to express my heartfelt gratitude to my family for their unwavering support in helping me achieve my goals. I extend my sincere thanks to my husband (Prajish), my mother-in-law (Prasanna), my father (Anil), my mother (Sunitha), and my brother (Cherin) for their endless care and affection. I am also grateful to my daughters, Jewel, Angel, and Estel, for allowing me to focus on my work without any interruptions. I would like to thank my entire family and everyone who embraced my research as their own dreams.

I sincerely thank the Council of Scientific & Industrial Research (CSIR), Government of India, for providing me with the research fellowship throughout the tenure period. I am also grateful to the University of Calicut for the PhD registration. Lastly, I would like to thank all those who contributed to the successful completion of my research work.

Merin Pulikkottil

Preface

The global challenges, such as climate change, fossil fuel depletion, and environmental degradation, have garnered significant research interest across various fields, all focusing on sustainability. This significant transformation primarily relies on energy storage, conversion, and environmental monitoring. In this endeavour, electrochemical energy storage systems and electrochemical sensors play a pivotal role. Among the various energy storage systems, supercapacitors and lithium-ion batteries (LIBs) have emerged as leading candidates due to their high energy and power densities, long cycle lives, and wide range of applications from portable electronics to electric vehicles. Concurrently, non-enzymatic sensors offer advantages such as stability, cost-effectiveness, and ease of fabrication.

The performance of electrochemical systems is significantly influenced by the choice of electrode material. Traditional carbon-based materials are commonly used due to their excellent electrical conductivity and structural stability. However, their high production costs, dependence on non-renewable resources, and energy-intensive manufacturing processes pose challenges to their sustainability and scalability. In contrast, biomass-derived activated carbon (BDAC) is a promising alternative, offering a combination of high surface area, tunable porosity, excellent electrochemical properties, and environmental sustainability. The conversion of biomass waste into high-performance carbon materials not only addresses waste management challenges but also enables optimal resource utilisation and supports a circular economy. Using low-cost, abundant biomass precursors helps to reduce the carbon footprint associated with traditional activated carbon production methods. This approach aligns with global sustainability goals and provides a viable pathway for the development of next-generation energy storage and sensing materials.

The high porosity and large surface area of BDAC provide numerous sites for the adsorption and desorption of ions, enabling efficient charge storage in supercapacitors. Additionally, the presence of micropores and mesopores enhances the rapid diffusion of ions, leading to high capacitance and improved energy storage performance.

BDAC-based anode materials in LIBs have attracted considerable attention due to their cost-effectiveness, high availability, thermal stability, minimal environmental impact, high electrical conductivity, and stability in adverse chemical conditions. Moreover, BDAC facilitates the reversible intercalation and deintercalation of lithium ions during charge and discharge cycles, thereby enhancing the overall energy storage capacity of LIBs.

Additionally, the effectiveness of electrochemical sensors is often limited by the restricted accessible surface area of their electrode materials. Increasing this surface area by incorporating BDAC can significantly enhance the performance of the sensors, as it provides a conductive surface that facilitates the detection of target analytes through redox reactions or adsorption processes. Its high surface area allows a greater number of analyte molecules to interact with the electrode, thereby improving the sensitivity and overall performance of the sensor.

This thesis highlights the systematic investigation of the synthesis, characterisation, and electrochemical performance of BDAC. Furthermore, this work aims to bridge the gap between sustainable material development and practical applications in energy storage and sensing technologies.

This dissertation work discusses the overall research in the following eight chapters.

Chapter 1: Introduction

This chapter describes the role and importance of AC in different sectors. It highlights the unique properties of AC, which include its high surface area, porosity, and conductivity, making it a versatile material for various applications across different fields. This chapter focuses on the relevance of AC derived from biomass waste in various electrochemical systems. Additionally, the chapter provides an extensive literature survey on the electrochemical performance of various BDAC electrode materials used in electrochemical systems to date.

Chapter 2: Experimental Techniques

This chapter provides a comprehensive overview of the synthesis methods and materials used in this study. We employed a simple and cost-effective chemical

activation process using KOH for the preparation of BDAC. Furthermore, the chapter examines the benefits of specific biomass precursors utilised for producing BDAC samples in this study. It also details various analytical techniques used to investigate the structural and material properties of the synthesised BDAC. Furthermore, the electrochemical performance of BDAC is crucial for evaluating its suitability for various applications. This chapter also includes information on electrode preparation, device fabrication methods, and electrochemical analysis techniques such as cyclic voltammetry (CV), galvanostatic charge-discharge (GCD), electrochemical impedance spectroscopy (EIS), and scanning electrochemical microscopy (SECM).

Chapter 3: Cashew Nutshell-Derived Activated Carbon for Effective Supercapacitor Applications

This chapter illustrates the preparation of BDAC from cashew nutshell waste. As a leading exporter of cashew nuts, India faces an environmental challenge due to the accumulation of large amounts of cashew nutshell waste each year. This study employs a simple and cost-effective strategy using KOH activation to produce AC derived from cashew nutshells (CNSAC). The research identifies optimised conditions for preparing CNSAC, which exhibits excellent structural and electrochemical properties. The chapter discusses how the activation ratio and carbonisation temperature affect both the electrochemical properties and the morphology of the prepared AC. The potential of CNSAC for use in supercapacitor applications is validated by the fabrication of symmetric supercapacitors utilising salt-in-water (SIW) aqueous electrolytes and water-in-salt (WIS) electrolytes.

Chapter 4: Efficient Solid-state Supercapacitor with Mahogany Fruit Shell-Based Porous Electrode Material

Solid-state supercapacitors represent the next generation of conventional supercapacitor systems. This chapter uses non-economic mahogany fruit shell waste to prepare BDAC. The suitability of mahogany fruit shell-derived AC (MSAC) was confirmed through various material characterisation techniques, like XRD, Raman spectroscopy, surface area analysis, and SEM imaging. The well-developed porous structure of MSAC is advantageous for practical supercapacitor applications. This chapter also discusses the electrochemical efficiency of MSAC in both three-electrode

and two-electrode configurations. Furthermore, it highlights the impressive performance of MSAC in developing flexible supercapacitors.

Chapter 5: Suitability of Nutmeg Shell-derived Activated Carbon for Applications in Li-ion Batteries and Supercapacitors

This chapter introduces a highly efficient electrode material for electrochemical energy storage applications. It explains the detailed procedure for preparing the electrode material from nutmeg shell waste. The chapter also covers the preparation and fabrication of supercapacitors and LIBs. The suitability of the material for these applications is validated through various material and structural analyses. Additionally, the chapter presents a detailed discussion of the material's electrochemical performance in these systems. The SEI is crucial for anode performance in LIBs. This chapter also offers insights into the formation and stability of the solid electrolyte interface.

Chapter 6: High-performance Non-enzymatic Urea Sensor with AC/NiO Composite Material

This chapter focuses on the preparation of a more versatile composite material, AC/NiO. It outlines a complete and cost-efficient procedure for producing this material. Various physicochemical properties of the prepared composite materials are also highlighted. Additionally, the chapter discusses the suitability of these materials for applications in supercapacitors and electrochemical sensors. The electrochemical studies related to sensing applications, specifically for identifying traces of urea, are explained in detail in this chapter. The chapter provides insights into the sensitivity, selectivity, repeatability, and reproducibility of sensors. It also discusses the viability of electrode materials for practical applications involving real-world samples.

Chapter 7: Conclusion

This chapter provides an overview of the results obtained throughout this research. The findings indicate a wide range of applications for prepared BDACs. The study not only emphasises the potential of BDAC in electrochemical systems but also offers a sustainable solution for waste management across multiple sectors. It successfully demonstrates the feasibility of the prepared BDAC for use in LIBs,

supercapacitors, and electrochemical sensors. Additionally, the stability and cycle life of these systems are impressive. The outstanding performance across these applications is due to their unique structural characteristics, including a large surface area and a well-developed pore distribution of the electrode materials.

Chapter 8: Recommendations

This chapter provides recommendations for future research related to the prepared materials. These materials demonstrated exceptional structural and electrochemical properties, making them suitable for various electrochemical systems. The current study on prepared BDAC can be expanded to other electrochemical applications in the future. Additionally, the successful fabrication of devices like full-cell LIBs, portable urea sensors, etc., using these materials is also achievable.

Abstract

The increasing demand for sustainable electrode materials across various fields has led to significant interest in biomass-derived activated carbon (BDAC) as a renewable, low-cost, and high-performance alternative to conventional carbon materials. This study investigates the preparation methods, material properties, and electrochemical performance of BDAC, providing insights into its suitability for electrochemical applications such as supercapacitors, lithium-ion batteries (LIBs), and non-enzymatic electrochemical sensors. Different biomass waste materials were used as precursors to create BDAC with desirable characteristics. The physicochemical characterisation of the synthesised BDAC materials reveals unique structural features, including a large surface area and well-defined pore size distribution. BDAC electrodes used in supercapacitors demonstrate excellent electrochemical performance, exhibiting a high specific capacitance and impressive cycling stability. Furthermore, these materials show superior energy and power densities compared to commercial activated carbons. BDAC-based anodes demonstrate promising lithium storage capabilities, achieving high reversible capacity and exhibiting good cycling stability over 200 cycles. The performance of LIBs is further analysed, focusing on the formation of a solid electrolyte interface and its influence on the irreversible capacity fading associated with it. The rate performance and long-term cycling behaviour of these anodes are compared to previously reported BDAC materials. Additionally, a BDAC-nickel oxide composite material is utilised for the detection of urea through a non-enzymatic electrochemical sensing approach. These sensors show a high sensitivity, low detection limits, and excellent selectivity in the presence of interfering substances. The electrocatalytic activity is attributed to the synergistic effects arising from a high surface area and abundant active sites. The study also investigates the potential of this material for urea sensing applications in real-world samples. These findings underscore the versatility and potential of BDAC as a sustainable electrode material for energy storage and sensing applications. Furthermore, the research offers a green and scalable solution for future energy and sensing technologies.

List of Publications

International Journals

1. **Merin, P.**, Jimmy Joy, P., Muralidharan, M. N., Veena Gopalan, E., & Seema, A. Biomass-Derived Activated Carbon for High-Performance Supercapacitor Electrode Applications. *Chemical Engineering & Technology*, (2021) 44(5), 844-851.
2. **Merin, P.**, Henock Antony, Muralidharan, M. N., Veena Gopalan, E., & Seema, A. Cashew Nut Shell Derived Porous Activated Carbon Electrodes for “Water-in-Salt” Electrolyte Based Symmetric Supercapacitor. *Chemistryselect*, (2022) 7(23), e202200984.
3. **P. Merin**, T. Anitta, E. G. Veena, M. N. Muralidharan, A. Seema, Highly Efficient Solid-state Supercapacitor with Porous Electrode Material, *Energy Technology*, (2023), 11 (9), 2300398.
4. **M. Pulikkottil**, R.R. Baby, A. Seema, Impact of the Stable Solid–Electrolyte Interphase in Sustainable and High-Performance Lithium-Ion Battery Anodes, *Batteries & Supercaps*, (2025), 2500228.
5. **P. Merin**, M. N. Muralidharan, A. Seema, High-Performance Nonenzymatic Urea Sensors with Cost-Effective Electrode Material, *Chemical Papers* (Manuscript Submitted).

Conference Proceedings

1. “Effect of redox-active additives to aqueous electrolytes on activated carbon-based supercapacitors”; **Merin Pulikkottil**, A Seema in the National seminar on Recent trends in material science & technology, NCMST 2022, Organized by Dept. of Chemistry, IIST during 28-30 December 2022.

2. “Biomass-derived activated carbon and its suitability for high-performance supercapacitor electrode applications”; **Merin Pulikkottil**, Jimmy Joy P, M N Muralidharan, A Seema in the International Conference on green energy for environmental sustainability (ICGEES-2020), Organized by the Department of Chemical Engineering, NIT Calicut on 5th and 6th August 2020.
3. “Production and Characterization of Supercapacitor Grade Activated Carbon from Cashew Nutshell Waste”; **Merin Pulikkottil**, Jimmy Joy P, M N Muralidharan, A Seema in the National seminar on FCS-2020, Organized by Dept. of Chemistry, University of Calicut during 29-31 January 2020.

Contents

List of Figures

List of Tables

Abbreviations

<i>Chapter No.</i>	<i>Title</i>	<i>Page No.</i>
1	Introduction	1- 48
1.1	Activated carbon (AC)	2
1.1.1	Structure of AC	3
1.1.2	Potential Properties of AC	4
1.1.3	Preparation Methods	6
1.1.3.1	Physical Activation	6
1.1.3.2	Chemical Activation.....	6
1.1.3.3	Combination Methods.....	6
1.1.3.4	Advantages of chemical activation over physical activation.....	7
1.1.4	Sources of AC	7
1.1.5	Biomass Derived AC (BDAC): A Sustainable Alternative for Conventional AC	8
1.1.6	Applications	10
1.2	Electrochemical Systems: An Overview	12
1.2.1	Supercapacitors (SCs).....	12
1.2.1.1	Electrochemical Double-Layer Capacitors (EDLCs).....	13
1.2.1.2	Pseudocapacitors (PCs).....	13
1.2.1.3	Hybrid Capacitors	14
1.2.1.4	Major Components of a SC.....	14
1.2.2	Li-ion Batteries (LIBs).....	16
1.2.2.1	Charging and Discharging Mechanism in LIBs.....	16
1.2.2.2	Major Components of a LIB	17
1.2.3	Electrochemical Sensors	18
1.2.3.1	Enzymatic Electrochemical Sensors	19

	1.2.3.2 Non-enzymatic Electrochemical Sensors	19
	1.2.3.3 Major Components of a Non-enzymatic Electrochemical Sensor.....	20
1.3	Application of AC in different electrochemical systems	21
	1.3.1 Role of BDAC in EDLCs	22
	1.3.2 Role of BDAC in LIBs	25
	1.3.3 Role of BDAC in Electrochemical Sensors	28
1.4	Motivation and objectives of the work.....	29
1.5	Scope of the work	31
	References	32
2	Experimental Techniques.....	45-84
2.1	Materials.....	46
	2.1.1 Selection of precursors for AC synthesis	46
	2.1.1.1 Anacardium occidentale (Seed shell waste)	46
	2.1.1.2 Swietenia mahagoni (Fruit shell waste)	47
	2.1.1.3 Myristica fragrans Houtt. (Seed shell waste)	49
	2.1.2 Chemicals used in for preparation of AC and other applications	50
2.2	Preparation of AC from biomass precursor	51
2.3	Synthesis of AC/NiO composite	53
2.4	Physicochemical characterization of materials	54
	2.4.1 X-ray diffraction (XRD)	54
	2.4.2 Scanning electron microscopy (SEM)	56
	2.4.3 Raman spectroscopy	57
	2.4.4 Surface area analysis	58
	2.4.4.1 Nitrogen adsorption-desorption isotherm	58
	2.4.4.2 Brunauer, Emmett, and Teller (BET) surface area analysis	61
	2.4.4.3 Barrett-Joyner-Halenda (BJH) method	62
	2.4.4.4 The t-plot method	62
	2.4.5 Fourier Transform Infrared Spectroscopy (FTIR)	63
	2.4.6 Thermogravimetry and Differential Thermal Analyses (TG/DTA)	64

2.4.7	X-ray photoelectron spectroscopy (XPS)	65
2.4.8	Transmission electron microscopy (TEM)	67
2.5	Electrode preparation	68
2.5.1	Modified working electrode (WE) in three-electrode system	68
2.5.2	Supercapacitor electrode	68
2.5.3	Anode in Li-ion Batteries	69
2.5.4	Electrode for electrochemical sensors	69
2.6	Fabrication of Various Electrochemical Systems	69
2.6.1	Fabrication of symmetric supercapacitor (SSC)	69
2.6.2	Assembling of flexible supercapacitor (FSC)	70
2.6.3	LIB half-cell fabrication	71
2.6.4	Electrochemical sensor for urea detection	72
2.7	Electrochemical Characterisations	72
2.7.1	Cyclic voltammetry (CV)	72
2.7.2	Galvanostatic charge-discharge (GCD)	74
2.7.3	Electrochemical impedance spectroscopy (EIS)	75
2.7.4	Scanning Electrochemical Microscopy (SECM)	78
	References.....	79
3	Cashew nutshell-derived activated carbon for effective supercapacitor applications	85-118
3.1	Introduction.....	86
3.2	Experimental details	86
3.2.1	Preparation of Cashew Nutshell-derived Activated Carbon	86
3.2.2	Preparation of Electrode.....	87
3.2.3	Fabrication of Symmetric Supercapacitors (SSCs).....	88
3.3	Results and discussions.....	88
3.3.1	Material characterisation.....	88
3.3.1.1	XRD analysis	88
3.3.1.2	FTIR analysis	90
3.3.1.3	SEM analysis	91
3.3.1.4	Raman Spectroscopy.....	93

	3.3.1.5	Surface area analysis.....	94
	3.3.2	Electrochemical characterisations.....	96
	3.3.2.1	Cyclic voltammetry (CV)	97
	3.3.2.2	Galvanostatic charge-discharge (GCD)	98
	3.3.2.3	Electrochemical impedance spectroscopy (EIS)	103
	3.3.3	The electrochemical characterisations of symmetric supercapacitors (SSC-Na ₂ SO ₄ , SSC-NaNO ₃)	105
	3.4	Conclusion	114
		References.....	114
4		Efficient solid-state supercapacitor with mahogany fruit shell-based porous electrode	119-150
	4.1	Introduction.....	120
	4.2	Experimental details	121
	4.2.1	Preparation of Mahogany Fruit Shell-derived Activated Carbon	121
	4.2.2	Conductivity studies of PVA Na ₂ SO ₄ GPEs	121
	4.2.3	Preparation of flexible solid-state supercapacitors (FSCs)	122
	4.3	Results and Discussions.....	122
	4.3.1	Material characterisation.....	123
	4.3.1.1	XRD analysis	123
	4.3.1.2	Raman Spectroscopy	124
	4.3.1.3	TGA analysis	125
	4.3.1.4	SEM analysis	126
	4.3.1.5	Surface area analysis.....	128
	4.3.1.6	FTIR analysis	130
	4.3.1.7	TEM analysis	131
	4.3.2	Electrochemical characterisations.....	132
	4.3.2.1	Cyclic voltammetry (CV)	133
	4.3.2.2	Galvanostatic charge-discharge (GCD)	134
	4.3.2.3	Electrochemical impedance spectroscopy (EIS)	139

4.3.3	Electrochemical analysis of gel polymer-based flexible solid-state supercapacitors (FSCs)	141
4.4	Conclusion	146
	References	147
5	Suitability of nutmeg shell-derived activated carbon for applications in Li-ion batteries and supercapacitors	151-190
5.1	Introduction.....	152
5.2	Experimental details	153
5.2.1	Preparation of Nutmeg Shell-derived Activated Carbon	153
5.2.2	Preparation of ACNM-based electrode material	154
5.2.3	Half-cell preparation and performance testing.....	154
5.3	Results and Discussions.....	154
5.3.1	Material characterisation.....	155
5.3.1.1	XRD analysis	155
5.3.1.2	Raman Spectroscopy	156
5.3.1.3	TGA analysis	157
5.3.1.4	SEM analysis	158
5.3.1.5	Surface area analysis.....	160
5.3.1.6	FTIR analysis	162
5.3.1.7	XPS analysis	163
5.3.1.8	TEM analysis	165
5.3.2	Electrochemical characterisations of ACNM-X-Ys.....	166
5.3.2.1	Cyclic voltammetry (CV)	166
5.3.2.2	Galvanostatic charge-discharge (GCD).....	168
5.3.2.3	Electrochemical impedance spectroscopy (EIS)	173
5.3.3	Study of the suitability of ACNMs as LIB anode material	174
5.3.4	Mapping of SEI layer on the surface of anode with SECM	182
5.4	Conclusion	184
	References	185

6	High-performance non-enzymatic urea sensor with AC/NiO composite material	191-216
6.1	Introduction.....	192
6.2	Experimental details	193
6.2.1	Synthesis of AC/NiO composites	193
6.2.2	Analysis of the electrochemical performance of AC/NiO for sensing applications.....	194
6.3	Results and Discussions.....	195
6.3.1	Material characterisation.....	195
6.3.1.1	TGA analysis	195
6.3.1.2	XRD analysis	196
6.3.1.3	Raman Spectroscopy	197
6.3.1.4	SEM analysis	198
6.3.1.5	Surface area analysis.....	199
6.3.1.6	XPS analysis	201
6.3.1.7	TEM analysis	202
6.3.2	Electrochemical investigation of urea with AC-NiO-based sensors.....	203
6.4	Conclusion	214
	References	214
7	Conclusions	219-222
8	Recommendations	223-226
8.1	Future works	224

Certificate of Plagiarism Check

List of Figures

<i>Figure No.</i>	<i>Figure Caption</i>	<i>Page No.</i>
1.1	Schematic representation of the porous structure of AC.....	3
1.2	Schematic representation of pores in AC	4
1.3	Essential features of AC sources	8
1.4	Lignocellulos biomass	9
1.5	Applications of BDAC	11
1.6	Schematic representation of (a) EDLC, (b) PC, and (c) Hybrid capacitors..	12
1.7	Classification of electrolytes for SC systems	15
1.8	Charging and discharging mechanism in LIBs	16
1.9	Experimental set up for non-enzymatic electrochemical sensor	20
2.1	Cashew apple and cashew nut shell	47
2.2	Mahogany fruit and fruit shell (husk)	48
2.3	Nutmeg fruit and seed	50
2.4	Preparation of AC from biomass waste	51
2.5	Schematic of synthesis of AC-NiO composite materials	53
2.6	XRD instrumentation setup	55
2.7	Schematic diagram of Scanning Electron Microscope	56
2.8	Raman spectrophotometer setup	57
2.9	The IUPAC classification of adsorption isotherms	59
2.10	The four types of hysteresis loops classified by IUPAC	60
2.11	Instrumentation of FTIR	63
2.12	Schematic diagram of a typical TG/DTA equipment	64
2.13	Typical TG/DTA curve for biomass	65
2.14	Schematic diagram of an X-ray photoelectron spectroscope	66
2.15	Schematic diagram of transmission electron microscope	67
2.16	Three-electrode setup for the electrochemical analysis	68
2.17	Schematic representation of SSC	70
2.18	Schematic representation of FSC	70
2.19	Schematic representation of LIB half-cell	71
2.20	Equivalent circuits and their corresponding Nyquist plots	76
2.21	Randles circuit and corresponding Nyquist plot	77
2.22	Schematic illustration of the SECM imaging apparatus	78

3.1	Schematic representation of methodology.....	87
3.2	Comparison of XRD patterns of CNSAC-X-Ys.....	89
3.3	FTIR spectra of CNSAC-X-Ys.....	90
3.4	SEM images of (a, b) CNSAC-1-700, (c, d) CNSAC-2-700, (e, f) CNSAC-3-700, (g, h) CNSAC-2-600 and (i, j) CNSAC-2-800 at a magnification of 15000 and 20000 X, respectively.	92
3.5	Raman spectra of CNSAC-X-Ys	94
3.6	N ₂ adsorption-desorption isotherm of CNSAC-X-Ys	95
3.7	Cyclic voltammogram of CNSAC-X-Ys.....	97
3.8	Cyclic voltammogram of CNSAC-2-700 at different scan rates.....	98
3.9	Galvanostatic charge-discharge curves of CNSAC-X-Ys.	99
3.10	GCD curves of CNSAC-2-700 at different current rates.....	100
3.11	Dependence of specific capacitance on current densities.	101
3.12	Cycle life test of CNSAC-2-700 at a current density of 10 Ag ⁻¹	101
3.13	Nyquist plot for a frequency range 10 ⁵ Hz to 10 ⁻³ Hz (the enlarged curves at a high frequency range are given as an inset)	103
3.14	Equivalent circuit diagram of CNSAC-X-Ys	104
3.15	CV curves of SSC-Na ₂ SO ₄ at different scan rates (1 to 100 mVs ⁻¹)	105
3.16	GCD curves of SSC-Na ₂ SO ₄ at current densities from 1 to 5 Ag ⁻¹	106
3.17	LSV curves with different concentrations of SSC-NaNO ₃	106
3.18	CV curves at different ESWs.....	107
3.19	CV curves of SSC-NaNO ₃ at different scan rates (1 to 100 mVs ⁻¹).....	108
3.20	GCD curves of SSC-NaNO ₃ at current densities from 1 to 5 Ag ⁻¹	108
3.21	CV curves of SSCs at a scan rate of 50 mVs ⁻¹	109
3.22	GCD curves of SSCs at the current density of 2 Ag ⁻¹	110
3.23	Variation in the value of specific capacitance with current density	111
3.24	Cycle test of SSCs at a current density of 10 Ag ⁻¹ for 10000 cycles.....	111
3.25	Nyquist plots of SSC-Na ₂ SO ₄ and SSC-NaNO ₃ (the inset shows the enlarged curves in a high frequency range and the equivalent circuit diagram)	112
4.1	Schematic representation of methodology.....	121
4.2	XRD patterns of MSAC-X-Ys.....	123
4.3	Raman spectra of MSAC-X-Ys	124
4.4	TGA curve of pristine mahogany fruit shell	125

4.5	SEM images of pristine mahogany fruit shell at 5000 and 10000 X magnification, respectively.....	126
4.6	SEM images of (a, b) MSAC-1-700, (c, d) MSAC-2-700, (e, f) MSAC-3-700, (g, h) MSAC-2-500, (i, j) MSAC-2-600, and (k, l) MSAC-2-800 at a magnification of 10000 and 20000 X, respectively.....	127
4.7	N ₂ adsorption–desorption isotherms of MSACs.....	128
4.8	Pore size distributions of MSACs (the inset shows the enlarged curves at smaller pore diameters)	130
4.9	FTIR spectra of MSAC-X-Ys.....	131
4.10	TEM images of the MSAC-2-700 at various magnifications showing porous structures with micro, meso, and macropores.....	132
4.11	CV curves of MSAC-X-Ys at a scan rate of 1 mV s ⁻¹	133
4.12	CV curves of MSAC-2-700 at different scan rates.....	134
4.13	GCD curves of MSAC-X-Ys at a current density of 1 A g ⁻¹	135
4.14	GCD curves of MSAC-2-700 at various current densities	136
4.15	Dependence of specific capacitance and IR drop on the current density for MSAC-2-700	137
4.16	Cycle life of MSAC-2-700 at a current density of 20 A g ⁻¹ for 10,000 cycles with the first and last five charge–discharge cycles in the inset.....	138
4.17	Ragone plot of MSAC-2-700 compared with various biomass-derived AC electrode materials	138
4.18	Nyquist plot of the electrode materials (the enlarged curves at the high-frequency range and equivalent circuit diagram are shown in the insets)	140
4.19	CV curves of the FSC at different scan rates from 1 to 100 mV s ⁻¹	141
4.20	GCD curves of the FSC at current densities from 1 to 5 A g ⁻¹	142
4.21	Dependence of specific capacitance and IR drop on the current density of FSC	143
4.22	Cycle life of the FSC at a current density of 20 A g ⁻¹ for 2,000 cycles with the first and last five charge–discharge cycles in the inset.....	143
4.23	Ragone plot of the FSC in comparison with previously reported values	144
4.24	Nyquist plot of the FSC (the equivalent circuit diagram is shown as an inset)	145

4.25	CV curves of FSC subjected to bending at various angles; scan rate: 20 mV s ⁻¹ (inset displays the bending angle)	146
5.1	Methodology for preparing ACNM-based sustainable electrodes	153
5.2	XRD patterns of ACNM-X-Ys	155
5.3	Raman spectra of ACNM-X-Ys	156
5.4	TGA curve of pristine nutmeg shell	158
5.5	SEM images of (a) ACNM-1-700, (b) ACNM-2-700, (c) ACNM-3-700, (d) ACNM-2-500, (e) ACNM-2-600, and (f) ACNM-2-800 at 20,000 X magnification.	159
5.6	N ₂ adsorption–desorption isotherms of ACNMs	160
5.7	Pore size distributions of ACNMs (the inset shows the enlarged curves at smaller pore diameters)	161
5.8	FTIR spectra of ACNM-X-Ys	163
5.9	(a) XPS Survey spectrum, (b) C 1s spectrum, and (c) O 1s spectrum of ACNM.	164
5.10	TEM images of the ACNM-2-700 at various magnifications showing porous structures with micro, meso, and macropores.....	165
5.11	CV curves of ACNM-X-Ys at a scan rate of 1 mV s ⁻¹	166
5.12	CV curves of ACNM-2-700 at different scan rates	167
5.13	GCD curves of ACNM-X-Ys at a current density of 1 A g ⁻¹	168
5.14	GCD curves of ACNM-2-700 at various current densities.....	169
5.15	Dependence of specific capacitance on the current density	170
5.16	Cycle life of ACNM-2-700 at a current density of 20 A g ⁻¹ for 10,000 cycles with the first and last ten charge–discharge cycles in the inset	171
5.17	Ragone plot of ACNM-2-700 compared with various BD AC electrode materials.....	171
5.18	Nyquist plot of the electrode materials (the enlarged curves at the high- frequency range and equivalent circuit diagram are shown in the insets)	173
5.19	Cyclic voltammogram of anode half-cell at a scan rate of 0.1 mVs ⁻¹	175
5.20	The charge-discharge profile of the half-cell at a current rate of 0.1C....	176
5.21	GCD profile of the half-cell at various current rates	177
5.22	Variation in capacity during rate capability test	179

5.23	Cycling performance of the anode half-cell at a current rate of 2C for 200 cycles	180
5.24	Nyquist plot of ACNM-2-700 based anode half cells before and after cycling with higher frequency region and equivalent circuit as inset	181
5.25	(a) Schematic illustration of SECM experimental setup, SECM area scan measurement of (b) pristine anode, (c) after the first cycle, and (d) after 200 cycles of charging and discharging.....	183
6.1	Schematic representation of the preparation of the AC/NiO composite..	194
6.2	TGA curve of AC/NiO	195
6.3	XRDs of AC/NiO composite materials	196
6.4	Raman spectra of AC/NiO composite materials.....	197
6.5	SEM images of (a) AC, (b) ACNiO_9:1_400, (c) ACNiO_8:2_400, (d) ACNiO_7:3_400, (e) ACNiO_8:2_300, and (f) ACNiO_8:2_500 at 15,000 X magnification.	198
6.6	N ₂ adsorption-desorption isotherms of AC/NiO composite materials	200
6.7	XPS spectra of ACNiO_8:2_400: (a) Survey spectrum, (b) Ni 2p, (c) O 1s (d) C 1s.	201
6.8	TEM images of the AC/NiO composites at various magnifications	202
6.9	CV curves of AC/NiO composite materials at a scan rate of 20 mV s ⁻¹ .	203
6.10	Nyquist plots of AC/NiO electrode materials	204
6.11	CV curves at various pH values of the supporting electrolyte	206
6.12	CV curves of ACNiO_8:2_400 at different scan rates with enlarged anodic peak as an inset.	206
6.13	Variation of anodic peak current with scan rate	207
6.14	CV curve with varying urea concentrations.....	207
6.15	Calibration curve of anodic peak current against the concentration	208
6.16	DPV curves for different concentrations of urea (10–80 μM).....	209
6.17	Variation in the reduction peak current against concentration	210
6.18	(a) CV curves obtained with a 0.1 mM urea in the presence of 0.1 M KOH for 25 repetitive cycles at a scan rate of 20 mVs ⁻¹	211
6.19	The variation in the anodic peak current for different electrodes	211
6.20	CV curves obtained for urea with different interfering species.....	212
6.21	Relative response of interferents.....	212

List of Tables

<i>Table No.</i>	<i>Table Title</i>	<i>Page No.</i>
2.1	List of chemicals used in this study.....	50
3.1	Elemental analysis of CNSAC-X-Ys	93
3.2	Pore structure parameters of CNSAC-X-Ys.....	96
3.3	Specific capacitance values of CNSAC-X-Ys	100
3.4	Comparison of electrochemical properties of different AC materials...	102
3.5	The values of elements in the equivalent circuit of CNSACs	104
3.6	The values of elements in the equivalent circuit of two SSCs	113
3.7	Comparison of electrochemical properties of activated carbon electrode materials in various WIS-based SSC systems.	113
4.1	Elemental analysis of MSAC-X-Ys	128
4.2	Pore structure parameters of MSAC-X-Ys.....	129
4.3	Specific capacitance values of MSAC-X-Ys.	135
4.4	Comparison of specific capacitance of different biomass-derived AC materials.	139
4.5	Fitted values of components in equivalent circuit derived from the EIS curves for MSAC-X-Ys.....	141
5.1	Elemental analysis of ACNM-X-Ys.....	159
5.2	Pore structure parameters of ACNM-X-Ys.....	162
5.3	Comparison of specific capacitance of different BDAC materials	172
5.4	Fitted values of R_s , R_{ct} , C_{dl} , and Z_w derived from the EIS curves for ACNM-X-Ys.	174
5.5	Values of specific capacity of ACNMs.....	177
5.6	Specific capacity values of sustainable AC anode materials.....	178
5.7	Components in the equivalent circuits of the anode half-cell	182
6.1	Elemental analysis of AC/NiO composites	199
6.2	Pore structure parameters of AC/NiO composites	200
6.3	Fitted values of R_s , R_{ct} , C_{dl} , and Z_w derived from the EIS curves.....	205
6.4	Comparison of various electrodes used for urea sensing	210
6.4	The influence of other interfering species on the detection of urea.	213
6.5	Real sample analysis of urea.	213

Abbreviations

SC	:	Supercapacitor
LIB	:	Lithium-ion battery
AC	:	Activated carbon
IUPAC	:	International Union of Pure and Applied Chemistry
BDAC	:	Biomass Derived AC
EDLC	:	Electrical double-layer capacitors
PC	:	Pseudocapacitors
WIS	:	Water-in-salt
PP	:	Polypropylene
PE	:	Polyethylene
SEI	:	Solid electrolyte interphase
2D	:	Two dimensional
LOD	:	Limit of detection
CNS	:	Cashew nutshell
MFS	:	Mahogany fruit shells
NMS	:	Nutmeg shells
XRD	:	X-ray diffraction
SEM	:	Scanning electron microscopy
BET	:	Brunauer-Emmett-Teller
BJH	:	Barrett-Joyner-Halenda
FTIR	:	Fourier transform infrared spectroscopy

TG/DTA	:	Thermogravimetry/differential thermal analyses
XPS	:	X-ray photoelectron spectroscopy
TEM	:	Transmission electron microscopy
EDAX	:	Energy-dispersive X-ray Spectroscopy
WE	:	Working electrode
MGCE	:	Modified glassy carbon electrode
SSC	:	Symmetric supercapacitor
FSC	:	Flexible supercapacitors
GPE	:	Gel polymer electrolyte
CNSAC	:	Activated carbon derived from cashew nut shells
MSAC	:	Mahogany fruit shell-derived AC
ACNM	:	Nutmeg-derived AC
CV	:	Cyclic voltammetry
GCD	:	Galvanostatic charge-discharge
EIS	:	Electrochemical impedance spectroscopy
SECM	:	Scanning electrochemical microscopy
LOQ	:	Limit of quantification
CPE	:	Constant phase element
UME	:	Ultramicroelectrode
TG	:	Tip generation
SC	:	Substrate collection
LSV	:	Linear sweep voltammetry

ESR	:	Equivalent series resistance
ESW	:	Electrochemical stability window
EC	:	Ethylene carbonate
DMC	:	Dimethyl carbonate
DPV	:	Differential pulse voltammetry

Chapter **1**

INTRODUCTION

1. Introduction

Sustainability has become a fundamental focus of recent research across various fields to address urgent global challenges like climate change, fossil fuel depletion, and environmental degradation. Electrochemical systems, such as supercapacitors (SCs), Li-ion batteries (LIBs), and electrochemical sensors, play a pivotal role in this endeavour by enabling efficient energy storage, conversion, and monitoring. However, the performance and sustainability of these systems highly depend on the materials used in their construction. Thus, there is increasing recognition of developing eco-friendly and renewable materials, minimising waste, and optimising resource utilisation.

Activated carbon (AC), known for its exceptional adsorption capabilities due to its high surface area and porous structure, has emerged as a versatile and cost-effective candidate in this context. The wide range of applications of AC in environmental protection, resource conservation, and pollution control are vital to sustainable development initiatives. AC is traditionally derived from fossil fuel-based precursors, such as coal and petroleum, which are neither sustainable nor environmentally friendly. In contrast, the production of AC from renewable and waste biomass sources further enhances its sustainability profile by promoting resource efficiency and reducing dependence on non-renewable materials. Overall, AC is a crucial component of sustainable practices, helping to achieve the balance between environmental stewardship, economic progress, and social well-being. This work explores the preparation of AC from different biomass waste and its applications in electrochemical systems, with a focus on SCs, LIBs, and electrochemical sensors.

1.1 Activated carbon (AC)

AC is a highly porous form of carbon with a large surface area. It has a significant role in shaping various facets of human development and facilitating technological progress from prehistoric times to modern times. In ancient times, people were only aware of the adsorptive properties of AC which was widely used for filtration purposes.(1) From the beginning of the 18th century, the application of AC extended to more fields such as decolorising liquids, sugar refining, and purifying air. Over the

years, the porous nature of AC gained more prominence and was used in various industrial applications.(2)

In recent decades, the production methods and raw materials for the preparation of AC were improved tremendously to achieve its specific properties, including surface chemistry, pore structure, and adsorption capacity.(3) Today, AC is widely used in numerous fields, from drinking water treatment to pharmaceutical applications. Ongoing research continues to explore ways to enhance the properties and performance of AC and develop new applications using this versatile material.(4,5)

1.1.1 Structure of AC

AC is a specialised form of carbon, where carbon atoms are arranged in a disordered structure. Within this amorphous structure, there are small, random regions where the carbon atoms are arranged in hexagonal layers, similar to graphite. However, these graphitic structures are not continuous, and this lack of regularity results in numerous tiny pores.(6,7) Figure 1.1 displays a schematic representation of the porous, disordered structure present in AC.

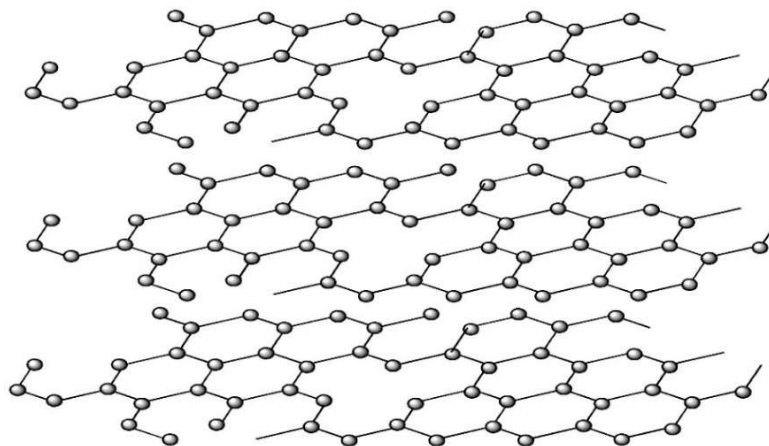


Figure 1.1. Schematic representation of the porous structure of AC

The pores present in AC have diameters ranging from several angstroms to several thousand nanometres. These pores are classified based on size and shape by the International Union of Pure and Applied Chemistry (IUPAC). According to the IUPAC classification, pores are grouped into three main types: micropores, mesopores, and macropores.(5) Micropores of a diameter less than 2 nm can create narrow channels or

cages which in turn are beneficial for improving the adsorption capacity, pore volume, and surface area of AC. Mesopores are larger than micropores but smaller than macropores with diameters ranging from 2 to 50 nm. The larger pores of diameters greater than 50 nm are called macropores, which offer less resistance to diffusion compared to smaller pores. (8,9)

Figure 1.2 shows a schematic representation of various pores present in the AC matrix. The interconnected porous network allows AC to trap and hold a wide range of molecules. Micro and mesopores are crucial for kinetics as they facilitate adsorption into the carbon particle.(10) The internal surface area of the AC surface is majorly contributed by micropores. The combination of micropores, mesopores, and macropores contributes an exceptionally high surface area, typically ranging from 500 to 1500 m²g⁻¹. The porous nature of AC along with its larger surface area is critical for diverse applications from water purification to gas adsorption.(11,12)

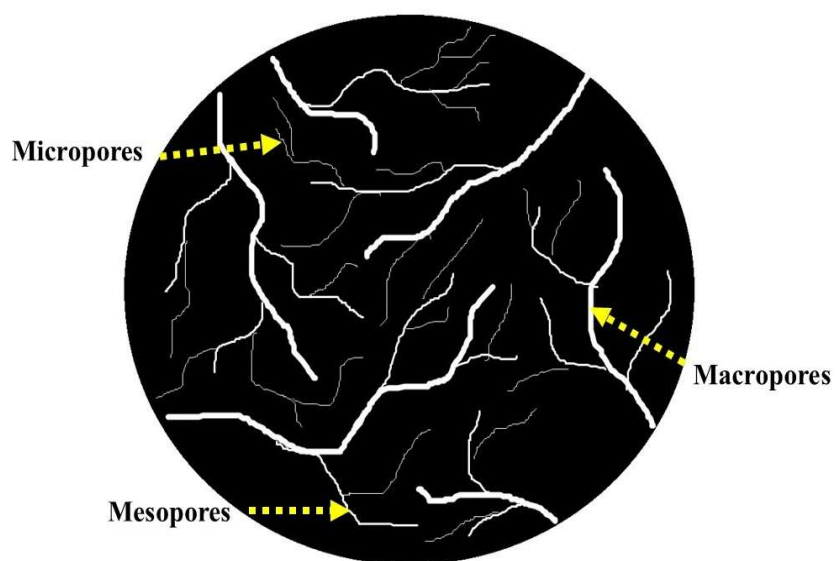


Figure 1.2. Schematic representation of pores in AC

1.1.2 Potential Properties of AC

AC exhibits various unique properties contributing to its versatility and effectiveness across numerous applications. These properties enable it to address multiple environmental, industrial, and medical needs. AC is well-known for its

remarkably high surface area and well-developed porous structure. The surface area is mainly contributed by micropores present in the structure.(13) Whereas, the contribution of mesopores and macropores to the total surface area does not exceed 10% of the total value. The porous nature of AC can be tuned by the proper choice of synthesis method, precursor material, and preparation conditions. The surface area of AC usually ranges from several hundred to over 1500 m²g⁻¹.(14,15)

The high surface area and porous structure of AC are critical for its widespread applications, such as water filtration, air purification, gas adsorption, solvent recovery, energy storage, and various industrial processes.(2,16) Moreover, the porosity of AC has a strong influence on other properties, such as its mechanical strength and density characteristics. Therefore, understanding and controlling the porosity of AC is essential for optimising its performance in various industrial and environmental applications.(17,18)

The greater surface area and well-developed pore distribution of AC enhance the adsorption capacity of the material by creating a vast number of adsorption sites for molecules to interact with and facilitating the diffusion of molecules into the carbon matrix. It can effectively adsorb a wide range of substances, such as organic compounds, gases, liquids, and dissolved species.(19) Micropores, in particular, enhance the adsorption of small molecules and gases. The choice of various synthesis conditions is crucial for achieving the desired adsorption capacity of AC for a given application. The surface chemistry, pore size distribution, and availability of functional groups have a remarkable influence on the selective adsorption by AC.(14,20)

Moreover, AC is chemically stable as it does not undergo significant chemical reactions in most of the chemical environments and can withstand elevated temperatures without significant degradation. These properties ensure the long-term stability and durability of AC in various applications, as it can be regenerated through chemical or thermal processes depending on the adsorbed substances.(21) Low density and less weight of AC are beneficial in applications where weight is a concern, such as in portable filtration devices, spacecraft, and other weight-sensitive environments. Additionally, the remarkable electrical conductivity of AC is suitable for electrode applications in various energy storage devices and sensors.(22–24)

Various factors influence the potential properties of AC during its production and post-treatment. These include the choice of raw materials, the activation process, carbonisation conditions, pore structure, and surface chemistry.

1.1.3 Preparation Methods

AC is typically prepared through a process called activation, which involves the physical or chemical treatment of carbonaceous materials. The major methods for the preparation of AC are physical activation and chemical activation.

1.1.3.1 Physical Activation

In this method, carbonaceous materials are physically activated with steam or active gases. Carbon dioxide (CO_2) and air are widely used active gases. The physical activation process is usually carried out at high temperatures ranging from 800 to 1000°C .⁽²⁵⁾ During physical activation, carbon undergoes pyrolysis and creates a highly porous structure with a remarkable surface area.⁽²⁶⁾ Steam activation of carbonaceous material results in AC with high surface area and porosity. However, gas activation is more popular as it requires lower temperatures compared to steam activation.^(2,16)

1.1.3.2 Chemical Activation

The chemical activation involves the impregnation of the carbonaceous material with a chemical activating agent. Phosphoric acid (H_3PO_4), zinc chloride (ZnCl_2), potassium hydroxide (KOH), sulfuric acid (H_2SO_4), and sodium hydroxide (NaOH) are the typical activating agents.⁽²⁷⁾ The impregnated material is then carbonised at relatively lower temperatures from 400 to 800°C .^(28,29) AC prepared through chemical activation exhibits well-developed pores and improved surface area.

1.1.3.3 Combination Methods

The activation process can be enhanced by using both physical and chemical methods. In combination methods, a chemically impregnated carbonaceous material is then subjected to carbonisation in the presence of steam. Such an approach helps prepare AC with specific characteristics.^(30,31)

1.1.3.4 Advantages of Chemical Activation Over Physical Activation

Chemical activation offers several advantages over physical activation, including lower energy consumption. Unlike physical activation, which typically requires higher temperatures generally between 800-1200°C, chemical activation is usually performed at a lower temperature range from 400-800°C. This slower heating process facilitates the formation of a more ordered carbon structure. Additionally, the use of inert gases such as nitrogen or argon during chemical activation helps prevent combustion throughout the preparation process. Although physical activation often results in AC with higher carbon content and mechanical strength, it can also lead to a reduction in surface area. In contrast, chemical activation not only accelerates the development of pores but also enhances the surface area of the resulting AC.(29,32)

Moreover, the pore structure and morphology of the AC can be precisely controlled during the chemical activation process. Depending on the intended applications, specific properties such as pore size distribution, pore volume, and surface area can be tailored by selecting the appropriate type and concentration of the chemical agent used. Overall, chemical activation of the precursor material often results in AC with a higher surface area compared to that prepared through physical activation.(15,33)

1.1.4 Sources of AC

Typical AC sources are organic substances that contain high carbon content. Additionally, these sources should have some essential features. These factors are illustrated in Figure 1.3.

The conventional sources of AC are coal (bituminous and lignite), petroleum pitch, peat, and other non-renewable biomass. However, harvesting these materials is lengthy, expensive, and unsustainable. For example, the high-temperature activation processes involved in coal mining cause habitat destruction and water pollution.(34) Similarly, the extraction and refining of petroleum create oil spills and air pollution.(35) Whereas, peat harvesting destroys peatlands and significantly contributes to climate change. The dependence on these conventional sources also accelerates deforestation, leading to soil erosion and environmental degradation.(36)

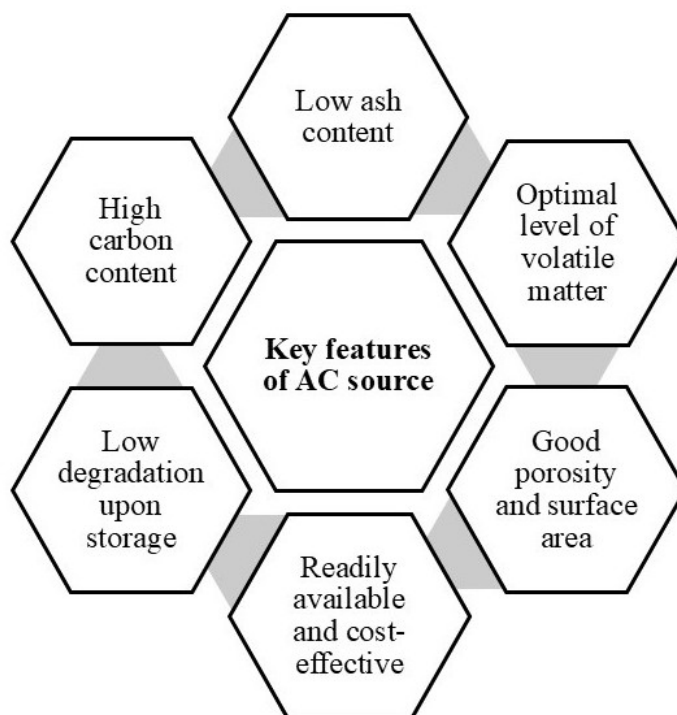


Figure 1.3. Essential features of AC sources

The depletion of fossil fuel resources and growing environmental concerns have made it essential to search for renewable and sustainable sources to prepare AC. In this context, biomass waste presents an eco-friendly solution due to its abundant availability, low cost, and excellent physicochemical properties.

1.1.5 Biomass-derived AC (BDAC): A Sustainable Alternative for Conventional AC

As mentioned above, traditional sources for AC production are environmentally hazardous, leading to an increasing research interest in sustainable and renewable alternatives. Biomass waste-derived AC (BDAC) plays a significant role in this endeavour as it effectively repurposes organic waste materials that would otherwise contribute to landfills or incineration.(4,37) The biomass used for BDAC production includes organic materials such as agricultural waste, forestry residues, and algae. The production and utilisation of BDAC are eco-friendly initiatives that ensure minimal waste. Moreover, the effective use of BDAC ensures that the resources are used to their fullest potential. BDAC is also beneficial as it reduces the carbon footprint related to

traditional AC production methods.(19,38) Additionally, renewability, inherent carbon content, ease of handling, high porosity, wide availability, and low cost of biomass waste are desirable for AC production and make it a cost-effective alternative to conventional precursors.(39)

BDAC demonstrates superior porosity compared to AC derived from other sources, which can be attributed to the lignocellulosic nature of biomass waste.(40) Most plant-based materials, including agricultural residues (such as straw, husks, and corn stover), forestry waste (like sawdust and bark), and dedicated energy crops (including switchgrass and miscanthus), are lignocellulosic. As a sustainable alternative to fossil fuels and synthetic polymers, lignocellulosic biomass has gained significant interest in advanced material synthesis.(32) The lignocellulosic biomass is schematically displayed in Figure 1.4.

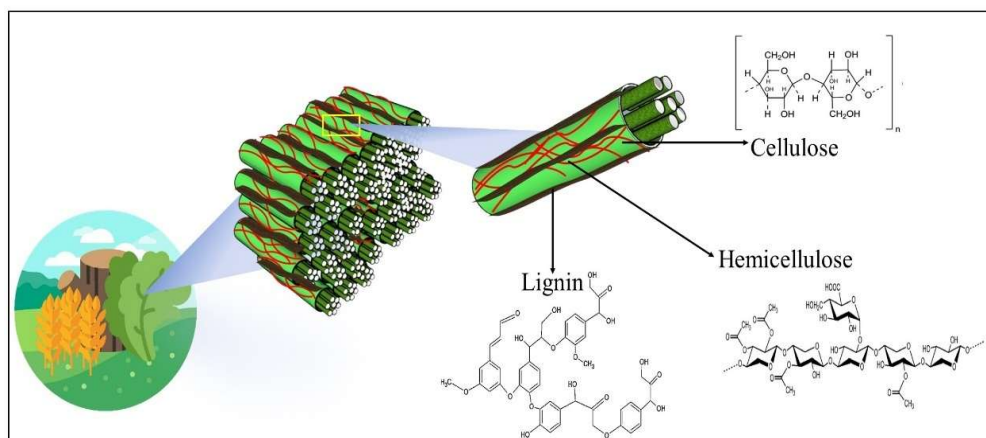


Figure 1.4. Lignocellulos biomass

The complex structure of biomass is mainly made up of biopolymers such as cellulose, hemicellulose, and lignin, which significantly affect its physicochemical properties and conversion efficiency. These components contribute to the structural integrity of plant cell walls. The proportions of each constituent vary based on the plant species, environmental conditions, and methods used for processing the biomass.

Cellulose is the most abundant polysaccharide in lignocellulosic biomass, constituting approximately 35–50% of its dry weight. It consists of linear chains of $\beta(1\rightarrow4)$ -linked D-glucose units that aggregate into microfibrils through extensive hydrogen bonding. These microfibrils provide mechanical strength and rigidity to plant

cell walls, as this crystalline structure is relatively resistant to enzymatic degradation.
(17)

In lignocellulosic biomass, about 20–35% of the total dry weight is contributed by hemicellulose. Unlike cellulose, hemicellulose has a heterogeneous and branched structure comprising various sugar monomers, including xylose, mannose, arabinose, and galactose. In contrast to cellulose, hemicellulose has an amorphous structure, making it more susceptible to hydrolysis. It is a matrix between cellulose and lignin in plant cell walls, contributing to flexibility and structural stability.(41)

Lignin is a complex aromatic polymer that constitutes 10–25% of lignocellulosic biomass. It is composed of phenylpropanoid units, primarily coniferyl, sinapyl, and p-coumaryl alcohols. Lignin provides structural rigidity, hydrophobic properties, and resistance to microbial degradation, acting as a protective barrier in plant cell walls. However, its recalcitrant nature poses challenges for biomass processing and enzymatic hydrolysis.(42)

These compounds play a significant role in forming a highly intricate pore structure during AC preparation. This hierarchical pore structure, comprising micropores, mesopores, and macropores, significantly enhances the surface area, pore volume, and adsorption capacity of the AC material and makes it suitable for various applications.(17,43) BDAC is highly versatile in multiple fields as a more environmentally friendly alternative. Furthermore, using renewable biomass sources along with energy-efficient methods will lead to a more sustainable and eco-friendly industry.(30,42) In this way, BDAC is highly beneficial over environmentally hazardous traditional AC production.

1.1.6 Applications

The well-developed pore distribution and large surface area of AC make it suitable for a variety of applications. Numerous BDACs have been developed from various sources, including plant waste, food waste, bio-waste, and fruit waste.(44–47) Figure 1.5 illustrates common uses of AC.(39) Several studies have explored the diverse applications of BDAC in purification and filtration applications, ranging from portable water purifiers to large-scale municipal water treatment systems.(10,48)

Additionally, BDAC materials are highly effective in removing metals, chlorine, synthetic dyes, and other impurities. (49–51)



Figure 1.5. Applications of BDAC

BDAC is utilised in air filtration systems to eliminate organic volatile compounds, harmful gases, and odours.(36,52) This includes applications in gas masks, solvent recovery, and general air purification.(53,54) Recent studies by Wang Shuang et al. and Sarwar Azeem et al. have demonstrated the effectiveness of BDAC in CO₂ adsorption, highlighting the regeneration and reusability of AC used in these studies. (33,55) Additionally, there are reports on the production of biodiesel using BDAC.(9)

BDAC plays a significant role in environmental remediation, effectively removing pollutants such as pesticides, hydrocarbons, and heavy metals from groundwater and soil systems.(12,18) The pharmaceutical and chemical industries also employ AC for processes like purification and separation.(15,56) For example, Dada Adewumi et al. reported the use of plantain peel-derived AC for the adsorption of chloroquine, a synthetic pharmaceutical used in COVID-19 treatment.(57)

Beyond these applications, AC has potential uses in the food industry, gold recovery, energy storage, and as a catalyst support.(58,59) However, even though BDAC has been extensively studied for various applications, including water purification, air filtration, and medical treatments, there remains a lack of research focused on its applications in various electrochemical systems.

1.2 Electrochemical Systems: An Overview

Electrochemical systems are crucial in modern energy storage, conversion, and environmental technologies. These systems include devices and processes that convert chemical energy into electrical energy or vice versa through redox (reduction-oxidation) reactions. This capability enables a wide range of applications in this field.

1.2.1 Supercapacitors (SCs)

SCs, also known as ultracapacitors or electrochemical capacitors, are energy storage devices that serve as a bridge between traditional capacitors and rechargeable batteries. They provide high power density and rapid charging and discharging, along with long cycle life.(60) While their energy density is lower than that of batteries, it is significantly higher than that of conventional capacitors.(61)

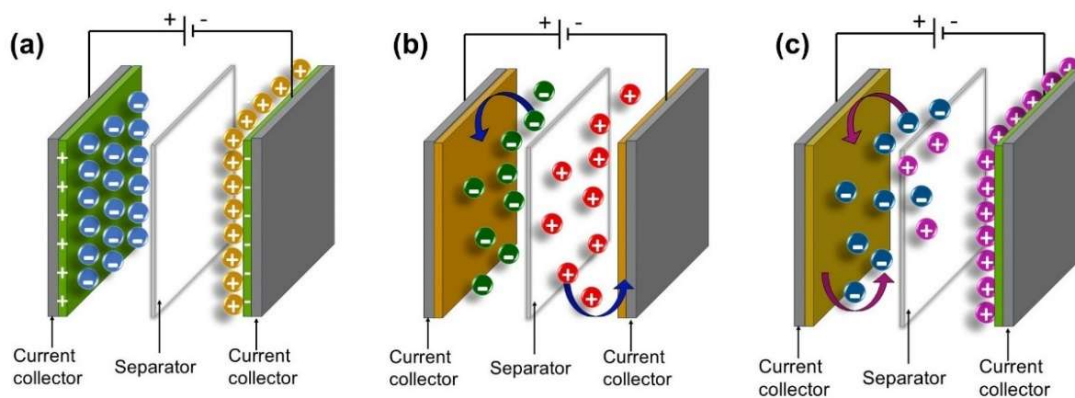


Figure 1.6. Schematic representation of (a) EDLC, (b) PC, and (c) Hybrid capacitors

The charge storage mechanism of SCs contributes to their high power density. SCs store energy either through electrostatic or electrochemical processes. Based on

these energy storage mechanisms, SCs can be classified into three categories: electrical double-layer capacitors (EDLC), pseudocapacitors (PC), and hybrid capacitors.(62) The schematic representation of these SCs is illustrated in Figure 1.6.

1.2.1.1 Electrochemical Double-Layer Capacitors (EDLC)

Electric double-layer capacitors (EDLCs) store energy by creating an electric double layer at the interface between the electrode material and the electrolyte. The reversible adsorption and desorption of electrolytic ions at the electrode-electrolyte interfaces lead to the electrostatic charge accumulation in EDLC.(63) Unlike conventional capacitors, EDLCs achieve significantly higher capacitance by utilising electrodes with high surface area and leveraging the unique electrochemical properties of the electric double layer.(64,65)

Electrode materials used in EDLCs must exhibit desirable properties such as large specific surface area, high porosity, excellent electrical conductivity, and good wettability. Because of their superior physicochemical properties, natural abundance, and excellent stability, carbon-based porous materials, including AC, graphene, carbon nanotubes, etc., are widely used in these applications.(66,67)

1.2.1.2 Pseudocapacitors (PC)

Pseudocapacitors (PCs) are a class of electrochemical capacitors that store energy through fast, reversible redox reactions, intercalation processes, or ion adsorption occurring on the surface or within the bulk of the electrode material. They utilise electrostatic means involving faradaic (electrochemical) processes to store energy.(68) Compared to EDLCs, PCs offer greater energy density and capacitance, although they typically exhibit slightly lower power densities. Additionally, PCs generally have a shorter cycle life than EDLCs due to the involvement of chemical reactions. The electrode materials, like metal oxides in PCs, can increase the overall expense.(69–71)

1.2.1.3 Hybrid Capacitors

Hybrid capacitors combine the advantages of both EDLCs and PCs. In these SCs, energy storage occurs through both electrostatic and electrochemical processes.(72) Hybrid capacitors provide high energy and power density, although they typically have a relatively short lifespan. Their popularity is limited by the challenges in finding the optimal combination of electrodes to enhance specific capacitance, potential window, energy density, and power density.(71,73)

1.2.1.4 Major Components of a SC

The efficiency of SCs is largely determined by the key components used in their fabrication. Proper selection of these components is essential for achieving excellent electrochemical performance. The main components of a SC are the electrode, electrolyte, and separator.

The electrodes play a crucial role in the accumulation of electric charges and energy. The performance of the electrodes depends on several properties, including surface area, electrical conductivity, electrochemical stability, mechanical integrity, and compatibility with electrolytes.(73) Electrode materials with a high surface area enhance contact between the electrode and electrolyte. Their porous structures also promote rapid ion transport, leading to improved capacity.(74) The electrochemical stability of the electrodes is vital for ensuring a long cycle life without significant degradation. Choosing the right electrodes is important, as they provide a stable framework for ionic movement and charge accumulation. Popular electrode materials include AC, carbon nanotubes, graphene, metal oxides (e.g., RuO₂, MnO₂), and conductive polymers (e.g., polyaniline, polypyrrole).(47,75)

In addition to electrode materials, the electrolyte in the SC significantly influences its performance by supplying the ions necessary for charge storage and transfer.(76) The physical and chemical properties of electrolytes significantly influence the performance of SCs, including their operating voltage range, capacity, energy density, rate performance, cyclability and safety. The electrolyte not only provides the ions involved in charge storage but also plays a crucial role in transferring and balancing charges between the two electrodes.(77)

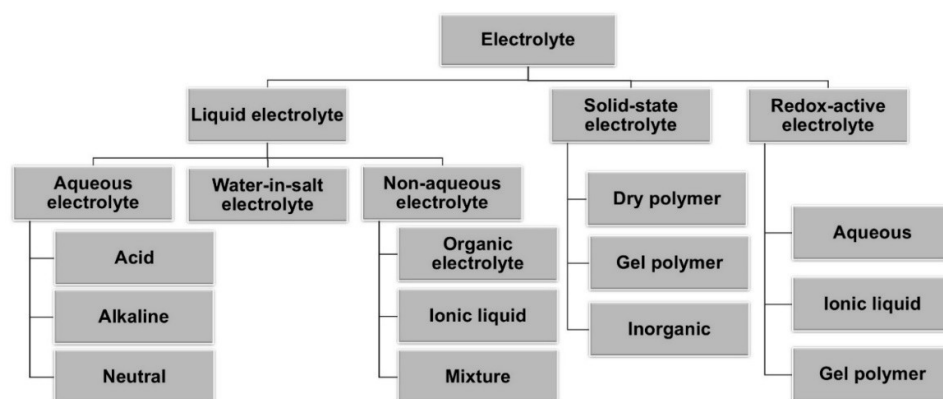


Figure 1.7. Classification of electrolytes for SC systems

The electrolytes for SC applications are classified into various categories, which is displayed in Figure 1.7. Among these, aqueous electrolytes have high conductivity and capacitance but generally exhibit low energy density, poor cycling stability, and leakage issues. While organic electrolytes and ionic liquids can operate at higher voltages, they tend to have much lower ionic conductivity. Solid-state electrolytes can mitigate the potential leakage problems associated with liquid electrolytes; however, they also suffer from low ionic conductivity.⁽⁷⁸⁾ Highly concentrated “water-in-salt” (WIS) electrolytes are promising for energy storage devices due to their non-flammable nature, wide electrochemical stability windows, and moisture tolerance. However, high viscosity, low conductivity, and salt precipitation at low temperatures of WIS electrolytes can impact their performance.⁽⁷⁹⁾ Moreover, the interaction between the electrolyte and the electrodes significantly impacts the electrode-electrolyte interface and the internal structure of the active materials. Therefore, the choice of electrolyte is key to creating safe and high-performance SC devices.⁽⁸⁰⁾

The separator and current collector play vital roles in the overall performance of SCs. The separator is a thin, porous membrane placed between the electrodes to electrically insulate them from each other while permitting the ionic movement essential for the electrochemical functionality of the device. These separators are typically made from polymers such as polypropylene (PP) or polyethylene (PE).⁽⁷¹⁾ Current collectors in SCs facilitate effective energy storage and transfer. They serve as

the interface between the active material and the external circuit, enhancing electron transport and providing structural support.(69)

1.2.2 Li-ion Batteries (LIBs)

Rechargeable battery technology has gained significant research attention over the past few decades. LIBs are among the most widely used rechargeable energy storage systems due to their high energy density, high operating potential window, lightweight design, and long cycle life. Additionally, they offer low self-discharge and fast charging capability.(81) They have a broad range of applications from consumer electronics to electric vehicles and grid storage.

1.2.2.1 Charging and Discharging Mechanism in LIBs

In LIBs, charge storage primarily relies on the reversible intercalation and deintercalation of lithium ions between the cathode and anode electrodes, which are separated by an electrolyte.(82) Figure 1.8 schematically represents the charge-storage mechanism in LIBs. During the charging process, lithium ions move from the cathode to the anode through the separator, aided by a conductive electrolyte. This transfer occurs as lithium ions migrate from the lithium metal oxide cathode to the carbon-based anode.(83)

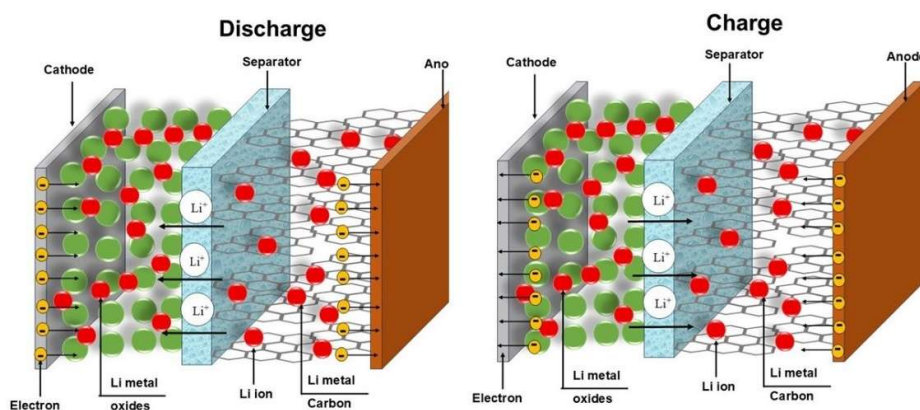


Figure 1.8. Charging and discharging mechanism in LIBs

During discharging, lithium atoms that have intercalated in the anode lose electrons, and lithium ions move from the anode to the cathode through the electrolyte. Electrons flow through an external circuit to power the connected device.(84) The composition and structure of both the cathode and anode are crucial factors that influence battery performance. Additionally, the movement of lithium ions is facilitated by an electrolyte, which typically contains a highly flammable and volatile solvent. Therefore, safety is a significant concern for LIBs due to issues like thermal instability, the risk of leakage, internal short circuits, and the flammability of electrolytes.(85)

1.2.2.2 Major Components of a LIB

Anode materials function as the hosts for lithium ions during the charging process. They provide sufficient sites to store these lithium ions while charging, and their subsequent release during discharge generates electrical energy.(86–88) Features such as a large surface area and a hierarchical pore distribution are desirable for efficient anode materials. Common materials used for anode applications in LIB include AC, graphite, silicon-based materials, and lithium titanate. The specific capacity and operating voltage of the anode material significantly influence the overall energy density of the battery.(89–91)

Solid electrolyte interphases (SEIs) in LIBs are insulating layers that form on the interfaces between electrodes and electrolytes during the first cycle of a battery. This formation occurs near anodes due to the decomposition of electrolytes. While SEIs help prevent further decomposition of electrolytes, their creation can lead to the consumption of active lithium and electrolytes.(92) Controlling the structures and properties of SEIs is crucial for achieving cycle stability and minimising capacity loss in LIBs. The formation of SEIs is significantly influenced by the chemical composition and surface characteristics of the anode materials used in these systems. (93)

The performance of LIBs is significantly influenced by their cathode materials, which serve as effective sources of lithium ions. During the discharging process, lithium ions are stored in these electrodes.(82) The materials used as cathode in LIBs are lithium-based compounds including lithium cobalt oxide (LiCoO_2), Lithium Iron Phosphate (LiFePO_4), Lithium Manganese Oxide (LiMn_2O_4), Lithium Nickel

Manganese Cobalt Oxide (NMC), and Lithium Nickel Cobalt Aluminum Oxide (NCA). These materials offer high energy density to LIBs.(94–98)

The electrolyte in LIBs is a crucial component that facilitates the movement of lithium ions between the anode and cathode during charging and discharging. Its composition and stability directly influence the battery's safety and overall performance.(99) Electrolytes provide a desirable medium for charge transfer between the cathode and anode. Common electrolytes include lithium salts dissolved in organic solvents like ethylene carbonate and dimethyl carbonate.(97) Conversely, electrolytes can play a vital role in the formation of SEI during lithiation/delithiation of lithium ions between anode layers, which further improves the battery life stability.

The separator is a porous membrane that prevents physical contact between the electrodes while allowing the flow of ions. This separator absorbs and retains the liquid electrolyte within its porous structure, ensuring consistent ionic pathways for stable battery operation during charge and discharge cycles. Common materials used for separators include PE and PP.(100,101) Current collector components facilitate the efficient transport of electrical energy within the battery. They serve as a medium to collect and transfer electrons between the external circuit and the electrodes. In LIBs, aluminium is used as the current collector for the cathode material, while copper is used for the anode material. (102,103) They also have a significant impact on the capacity, discharge rate, and long-term stability of LIBs.(104)

1.2.3 Electrochemical Sensors

Electrochemical sensors are analytical devices designed to detect and quantify specific chemical substances by converting a chemical reaction, typically involving oxidation or reduction, into an electrical signal.(105) These sensors leverage principles of electrochemistry, such as current, potential, or conductivity, to provide quantitative or qualitative information about the target analyte in a sample.(106) They are widely used in various fields, including environmental monitoring, medical diagnostics, food safety, and industrial applications. Compared to conventional sensing techniques, electrochemical sensors offer high sensitivity, specificity, rapid response times, portability, and cost-effectiveness.(107,108)

1.2.3.1 Enzymatic Electrochemical Sensors

Enzymatic electrochemical sensors utilise specific enzymes as biorecognition elements to detect target analytes. These sensors depend on the catalytic activity of enzymes to produce an electrochemically detectable signal, which is typically represented as current, voltage, or charge. During operation, the enzyme binds to the target analyte and catalyses its conversion into products.(109) The electron transfer that occurs during this reaction is either directly captured by the electrode or mediated by an electron carrier. The resulting electrical signal is proportional to the concentration of the analyte. These sensors offer several advantages, including high specificity, high sensitivity, rapid response times, and versatility.(110) However, their practical applications are limited by the instability of enzymes under varying temperatures, pH levels, and storage conditions. They may also be affected by interference from certain electroactive species in the sample during testing, along with issues related to cost and a restricted operational range.(111,112)

1.2.3.2 Non-enzymatic Electrochemical Sensors

These sensors detect analytes through direct electrochemical reactions occurring at the electrode surface. They utilise the intrinsic catalytic properties of the electrode materials to facilitate redox reactions with the target analytes. A range of chemically stable, conductive, and catalytically active materials, such as metals and metal oxides, are commonly used.(113) Additionally, carbon-based materials, like AC and graphene, are often employed to enhance the electrode surface, improving sensitivity and selectivity for specific analytes.(114,115)

During the analysis with these sensors, the target analyte directly undergoes a redox reaction at the electrode surface, facilitated by the catalytically active electrode material. This process allows for electron transfer between the analyte and the electrode, generating an electrochemical signal that is proportional to the analyte concentration.(24) The benefits of these sensors include enhanced stability, cost-effectiveness, a wider operational range, high sensitivity, and ease of fabrication. Due to these attractive features, they are more widely used than enzymatic electrochemical sensors.(116,117)

1.2.3.3 Major Components in a Non-enzymatic Electrochemical Sensor

The working electrode serves as the platform where the analyte undergoes direct electrochemical reactions, such as oxidation or reduction. These electrodes facilitate electron transfer during the redox process. Commonly used metal working electrodes include gold (Au), platinum (Pt), nickel (Ni), copper (Cu), and cobalt (Co).^(118,119) In addition, metal oxides like nickel oxide (NiO), cobalt oxide (Co₃O₄), and copper oxide (CuO), as well as carbon-based materials like AC, graphene, carbon nanotubes, and carbon black, are also employed.^(120,121) Recently, electrodes made from composites of metals, oxides, and carbon have been utilised to enhance performance. These composite electrodes provide a higher surface area, which increases sensitivity, and offer more catalytically active sites that improve reaction rates.^(111,122–124)

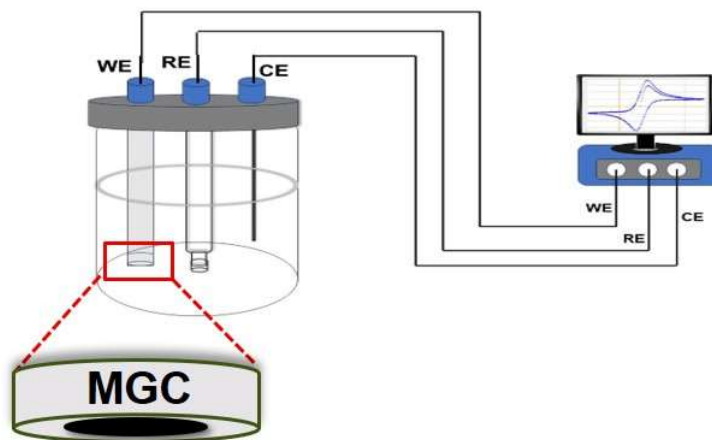


Figure 1.9. Experimental set up for non-enzymatic electrochemical sensor

Counter electrodes and reference electrodes play a crucial role in the function of these sensors. The counter electrodes are usually made of inert materials like platinum or carbon. They provide a pathway for electron flow during analysis.⁽¹²⁵⁾ The stable potential for accurate measurements is provided by a reference electrode, which ensures a consistent reference potential for the working electrode. Common examples include silver/silver chloride (Ag/AgCl) and saturated calomel electrodes

(SCE).(126) Figure 1.9 represents schematic of experimental set up for a non-enzymatic electrochemical sensor.

The electrolyte facilitates ion transport between the working and counter electrodes. It maintains electrical conductivity and supports the redox reaction of the analyte. Various liquid electrolytes, such as aqueous solutions (e.g., KOH, H₂SO₄) or organic solvents, as well as gel or solid-state electrolytes, are utilised in portable sensor systems.(120,127) The transducer is responsible for converting and processing the electrical signal for analysis.(128)

1.3 Application of AC in different electrochemical systems

The AC-based electrodes are widely used in various electrochemical systems owing to their superior features, including large surface area, well-developed pore distribution, good electrical conductivity, better pore parameters, tunable surface chemistry, and good physicochemical stability. These unique properties have a significant role in determining the efficiency of the respective systems. The viability of AC electrodes primarily depends on their ability to adsorb, interact with, or store various guest elements on the pore walls and in the bulk material. The activity of these materials can be further improved or modified by tuning their structural properties to suit specific applications such as SCs, LIBs, electrochemical sensors, etc.

The presence of aromatic structures and short-range, localised carbon layers creates numerous slits and pores throughout the AC structure. These interconnected pores, which exhibit fractal geometry, are advantageous in increasing the number of reactive sites that improves the working of these systems. The performance of AC is significantly influenced by their porous texture, degree of graphitisation, heteroatom doping, and the presence of surface functional groups. These characteristics affect the surface area, porosity, wettability, and electrical conductivity of AC, all of which play critical roles in promoting various electrochemical processes within the respective systems.

The large surface area is essential for electrochemical applications involving physical or chemical adsorption, storage, or interactions at the surface of AC. The surface area is hypothetically considered proportional to the number of available active

sites. In contrast, the number of active sites is highly related to the pore distribution, electrolyte ions and other guest species present in the system.

1.3.1 Role of BDAC in EDLCs

EDLCs are a highly explored area due to their widespread applications in next-generation technologies such as electric vehicles and portable devices. EDLCs have gained popularity over other SCs due to their unique characteristics, such as excellent power density, long cycle life, and high specific capacitance.(129,130) However, the energy density of a SC is relatively low compared to other energy storage devices. The efficiency of EDLCs is mainly influenced by the structural and electrochemical properties of the electrode material. Therefore, it is crucial to prepare electrode materials with innovative morphologies and strong electrochemical performance to develop SCs with higher energy density.(131,132) AC has attracted significant research interest due to its unique properties, including a large surface area and a well-developed porous structure. These characteristics provide an extensive network of active sites for electrochemical reactions, making AC an ideal material for energy storage and conversion devices, allowing efficient charge storage in EDLCs. (133–135)

A large surface area and sufficient active sites are crucial for the effective adsorption of electrolyte in EDLC systems. These active sites are essential for forming ideal electrochemical double layers on the pore walls, ensuring good contact with the electrolytes. In EDLCs, charge storage occurs when the electrolyte ions form electric double layers at the electrode surface, which is directly related to the available surface area of the electrode materials. The value of specific capacitance is also proportional to this accessible surface area. Therefore, in addition to maximising surface area, it is important to control factors such as pore size distribution, pore shape, and electrical conductivity to enhance accessible surface area and consequently, improves the capacitive properties of EDLCs.

According to the theory proposed by Helmholtz, a rigid layer of adsorbed counter ions was considered at the electrode surface. The capacitance of the electric double layer on a flat surface is given by

$$\frac{C}{A} = \frac{\epsilon_0 \epsilon_r}{d} \quad (1.1)$$

Here, C represents normalised capacitance by the accessible surface area (A) with vacuum permittivity (ϵ_0) and the relative permittivity (ϵ_r) of the electrolyte and d stands for the thickness of the double-layer.

Later, a conflict arose regarding the contribution of partially or fully desolvated electrolyte ions to the total capacitance value associated with the electric double layer. In this context, the Helmholtz model, which is applicable only for perfectly ordered slit pores, could not effectively explain the mechanisms associated with different pore geometries. This led to the development of new models that describe the formation of electric double layers in electrodes, particularly in AC-like porous electrode materials. The variation in preparation methods is responsible for the formation of various pore geometries including slit, cylindrical and spherical types. Huang et al. introduced the concept of cylindrical mesopores and micropores, which illustrates the formation of electric double-cylinder capacitors. This model proposed the surface area-normalised double cylinder capacitance in the mesopore regime, described by the following formula:

$$\frac{C}{A} = \frac{\epsilon_0 \epsilon_r}{b \ln \left[\frac{b}{b-d} \right]} \quad (1.2)$$

Here, b is the radius of the cylinder pore, and d is the thickness of the double-layer.

thickness. Whereas, in the micropore regime, desolvated ions form a type of electric wire-in-cylinder capacitor, with capacitance expressed as

$$\frac{C}{A} = \frac{\epsilon_0 \epsilon_r}{b \ln \left[\frac{b}{a_0} \right]} \quad (1.3)$$

Here a_0 gives the effective size of the electrolyte ion.

These models can be effectively applied to various EDLC porous electrode material systems that contain micropores, mesopores, and macropores. However, for the pore distribution involving spherical pores, Wang et.al proposed new equation as follows:

$$\frac{C}{A} = \frac{\epsilon_0 \epsilon_r}{d} \left[\frac{b-d}{b} \right] \quad (1.4)$$

Subsequently, Feng et al. proposed slit-shaped micropores and introduced a sandwich-type capacitor model. The capacitance value in this model is described as

$$\frac{C}{A} = \frac{\epsilon_0 \epsilon_r}{b-a_0} \quad (1.5)$$

The model further introduced the effective double-layer thickness (d_{eff}), which is the distance between the pore wall and the outer electron shell of the electrolyte ion. This parameter helps explain the observed increase in capacitance for sub-nanopores. Although earlier theories suggested that micropores contributed minimally to the capacitive behaviour of EDLC systems, later studies have demonstrated an unexpected increase in specific capacitance in systems with pores less than 1 nm in diameter. Subsequently, various studies have utilized these theories both individually and in combination to elucidate the formation and functioning of the electric double layer in porous electrode materials.

Additionally, the mass transfer in EDLC systems is significantly influenced by the distribution of pores. Larger pores facilitate faster mass transfer, while smaller pores promote slow self-discharge in EDLCs. The micropores maximise ion adsorption, while mesopores enhance ion transport in the system. Additionally, macropores in the electrode material serve as ion reservoirs and help reduce diffusion resistance. So, a well-balanced porous structure is essential for achieving high capacitance and improved energy storage performance in EDLCs.

Although there are various carbonaceous precursors available for synthesising AC, natural and sustainable biomass has replaced conventional precursors. Several research initiatives have reported on the application of various BDAC in the fabrication of EDLCs.(136,137) These studies are crucial because the electrochemical properties of BDAC prepared from different precursors vary significantly. In their review article, Luo Lu and his colleagues summarise the current state of research on BDAC in the field of SCs. They also provide insights into future development prospects and challenges in this area.(138) Boujibar O and his group prepared AC from waste biomass with an exceptionally high surface area and tailored nanoporosity, and they studied its suitability for SC applications.(139) Numerous initiatives have been reported to enhance the physical and electrochemical properties of BDAC through

various strategies.(140–143) For instance, Rajasekaran et al. synthesised AC from palmyra palm flowers, achieving a significant energy density of 15.1 Wh kg^{-1} and an impressive power density of 100.6 W k g^{-1} .(129) Similarly, Zaman Fakhar and his co-workers adopted a facile two-step green approach to convert Himalayan horse chestnuts into AC materials. They explored the suitability of these materials as SC electrodes, which demonstrated high specific capacitance and long cycle life.(141) Additionally, Liao Yuyi et al. prepared N-doped carbon material with a large surface area and high pore volume by directly pyrolysing reed straw and melamine. This material exhibited a capacitance of 202.8 Fg^{-1} at a current density of 1 Ag^{-1} , showing significant capacitance retention.(144)

As previously discussed, the porous structure significantly influences the efficient performance of BDAC-based electrodes.(145–147) Recently, Sayed Mostafa and his research team highlighted the role of the pore structure of biomass-derived porous carbon in charge storage mechanisms for SCs.(131) The fabrication strategies for SC systems are undergoing significant changes, shifting from traditional aqueous electrolyte-based SCs to widely accepted flexible all-solid-state SCs.(148,149) Recent research focuses on discovering efficient electrode materials that offer both economic advantages and environmental benefits.

1.3.2 Role of BDAC in LIBs

LIBs have garnered significant research interest due to their potential in designing next-generation applications. The role of anode materials that offer improved capacity at a low cost is crucial for the future of electric and hybrid vehicles. Furthermore, the choice of raw materials and methods for fabricating anodes must be more sustainable than conventional anodes. Furthermore, the anode materials must meet several key requirements to ensure optimal performance, which include having a high degree of interconnected porosity, short diffusion pathways, minimal volume change, low internal resistance, cost-effectiveness, and environmental friendliness. These characteristics contribute to improved rate capability, cycling stability, and charging performance of LIBs.

In this regard, BDAC has gained considerable attention as a promising, sustainable alternative to traditional anode materials because of its large surface area

and unique pore distribution.(150) These surface characteristics of BDAC enhance the storage of lithium ions and improve electron transport and diffusion of the electrolyte, resulting in higher energy density and better charging rates. The available pores in BDAC can accommodate large volume changes during charging and discharging cycles, leading to the stability and lifespan of LIBs. The availability of a large interfacial area of BDAC improves the electrochemical behaviour and enhances ion diffusion and electron transfer, leading to higher energy density and faster charging rates. Subsequently, BDAC can achieve high capacity because of its effective high surface area and well-distributed pores.(151) Furthermore, the utilisation of BDAC for LIB anode applications has several additional benefits including high availability, minimal environmental impact, the presence of surface functional groups, better thermal stability, high electrical conductivity, and good chemical stability. Additionally, BDAC enables the reversible intercalation and deintercalation of lithium ions during the charging and discharging cycles, which enhances the overall energy storage capacity of LIBs.(150–152)

The pore distribution has a remarkable role in determining the performance of LIBs. A combination of micropores, mesopores, and interconnected macropores is ideal for effective anode applications. This arrangement not only enhances the surface area but also provides improved pathways for the mass transfer of lithium ions. The anode materials with high surface area and a majority of mesopores generally exhibit better performance as LIB anode material. The enhanced performance of these materials is often related to fast ion diffusion through anode, availability of more active sites, effective intercalation of lithium ions, minimum volume change during cycling etc. These improvements enable higher rate capability and better cycle life for the LIB systems. Therefore, optimising factors such as surface area, porosity, and pore size distribution is essential for creating efficient anode materials.

In addition to these factors, the formation of a stable SEI is also crucial for the better performance of LIBs. The SEI is important as it acts as both an electronic insulator and a lithium-ion conductor. A stable SEI is beneficial as it prevents excessive electrolyte decomposition that may lead to a short life of the entire LIB system. The kinetic stability of SEI is vital during lithiation and delithiation processes. However, the presence of micropores can lead to excessive SEI layer formation, causing

significant capacity fading in LIBs. Anodes that incorporate mesopores can better control SEI formation.

Overall, controlling features such as surface area and pore distribution is highly recommended for effective anode materials. In this context, the tunability of BDAC makes it a promising candidate for electrode applications in LIBs.(153–156) For example, Ahmed Faheem et al. synthesised rice husk-derived AC using a simple chemical method. This material served as an anode for LIBs, achieving a discharge capacity of 321 mAhg^{-1} at a current density of $100 \text{ mA} \text{g}^{-1}$ for the first cycle, and maintaining a capacity of 253 mAhg^{-1} for 400 cycles.(157) Porous carbon obtained from banana peel waste exhibited a specific capacity of 272 mAhg^{-1} , demonstrating remarkable retention and good cycling performance even at high current densities, as noted by Luna-Lama et al.(158) Recently, Sun Yu and his colleagues discussed effective strategies for designing BDAC materials in battery development in their review article.(159)

Tian et al. later demonstrated the preparation of hard carbon from coconut shells, which was used as an anode and exhibited an exceptionally high reversible capacity along with improved coulombic efficiency.(160) Similarly, Yudha Cornelius Satria et al. reported an efficient conversion of Nypa fiber waste into AC for LIB anodes, achieving a specific capacity of 189 mAhg^{-1} .(161) Furthermore, Yarramsetti Saisrinu and his research group introduced low-cost and sustainable electrode materials for LIBs, synthesised from whole black gram skins. This material showed a capacity of 750 mAhg^{-1} at 0.1 Ag^{-1} with a reversible capacity of 687 mAhg^{-1} after 100 cycles.(35)

Recently, palm oil fruit bunches were converted into efficient BDAC using a single-step K_2FeO_4 -KOH impregnation-activation method developed by Nuriskasari Isnanda and co-workers that has a capacity of 330.3 mAhg^{-1} at 0.1 C , with an excellent rate capability.(162) Subsequently, P.U. Nzereogu et al. have demonstrated that the formation of SEI leads to the depletion of several lithium ions from the system and contributes to irreversible capacity loss in LIBs. This study highlights the importance of optimising the structure of anode materials.(90)

1.3.3 Role of BDAC in Electrochemical Sensors

The effectiveness of electrochemical sensors is often limited by the restricted accessible surface area of their electrode materials. Increasing this surface area can significantly enhance their applications and effectiveness. Furthermore, electrochemical sensors that incorporate electrode materials with a substantial surface area and well-developed porous structures exhibit fast charge transfer kinetics. This results in higher peak currents associated with the redox reactions being studied. AC is commonly used to improve the performance of electrochemical sensors, as it provides a conductive surface that facilitates the detection of target analytes through redox reactions or adsorption processes.(163,164)

The high surface area of AC offers more active sites for analyte adsorption, allowing a greater number of analyte molecules to interact with the electrode. This interaction improves the sensitivity and overall performance of the sensor. Additionally, the pore distribution of AC is also very effective in enhancing mass transport, leading to rapid response times and a reduced limit of detection (LOD). Furthermore, the carbon network and pore characteristics such as pore volume and pore size, significantly influence the performance of these sensors. Accordingly, the factors such as porosity, surface chemistry, presence of defects in electrode material, chemical activity of the electroactive species and characteristics of analyte contribute remarkably to the performance of the sensor as they influence sensitivity, LOD and detection limits.

Recent research has focused on utilising biomass waste as a cost-effective and sustainable source for AC, specifically through the development of BDAC for these sensing applications.(165–167) For instance, Terbouche et al. prepared AC derived from the pits of Algerian date palms, which was used to detect gallic acid with a lowest LOD of 3.64 μM .(168) Additionally, a review article by Onfray Christian and Thiam Abdoulaye summarises various treatments and synthesis methods for BDAC materials obtained from diverse sources, including herbaceous plants, wood, animal, and human waste, as well as aquatic and industrial waste. This review highlights the significant potential of these materials for use in practical electrochemical sensing devices. (163)

Nikhil et al. used meso/microporous 2D-AC, synthesised from a natural biomass *desmostachya bipinnata*, for electrochemical detection of roxarsone. The study

also introduces disposable screen-printed carbon electrodes for the clinical diagnosis of roxarsone and other similar drugs through electrochemical sensing.(127) Recently, Selvi Gopal and her team employed an MXene-embedded porous carbon-based Cu_2O nanocomposite for the electrochemical sensing of glucose, which exhibited an LOD of $1.96 \mu\text{M}$ and a sensitivity of $240.5 \mu\text{AmM}^{-1}\text{cm}^{-2}$.(119) Additionally, Shweta J Malode et al. reported the synthesis of BDAC material for the nanomolar detection of glucose in biological samples.(169)

Urea is prevalent as a byproduct of various processes, making its detection essential in many fields. Numerous researchers have reported on urea detection using various sensing applications.(170–172) Recently, G. Padmalaya utilised a copper oxide/multiwall carbon nanotube nanocomposite for real-time electrochemical sensing of urea in rice water samples, achieving an LOD of 0.26mML^{-1} .(105) While BDAC demonstrates an effective pore structure and provides more active sites suitable for urea sensing applications, there appears to be a lack of research focus on BDAC-based urea sensors.(105,173)

1.4 Motivation and objectives of the work

AC is a common but multifaceted material. However, the conventional methods for producing AC are costly and pose significant environmental risks. These unsustainable practices hinder the effective utilisation of AC in various applications, including energy storage and sensors. To overcome this limitation, there is a growing research interest in producing AC from biomass precursors. From biomass waste, AC can be produced in a more sustainable, eco-friendly, and economical manner. The benefits of production and utilisation of BDAC include:

- 1) cost-effectiveness
- 2) abundance of precursor
- 3) environmental friendliness
- 4) easiness to prepare BDAC
- 5) excellent pore distribution

- 6) high surface area
- 7) better pore volume
- 8) high stability
- 9) good adsorption capacity
- 10) low density

The present work aims to prepare efficient BDAC materials through a more sustainable, cost-efficient, and environmentally friendly method for electrode applications in various electrochemical systems. The work further discusses the suitability of prepared BDAC for different SC systems, LIBs, and electrochemical sensors. The performance of prepared BDAC materials was evaluated and their viability for electrode applications in various SC systems such as symmetric SCs, WIS SCs, and flexible SCs was validated. Furthermore, prepared BDAC with remarkable structural properties was used for anode application in LIBs. Based on various electrochemical analyses, their significance for anode applications was confirmed. Additionally, the BDAC was used for the preparation of AC/NiO composite, and its electrochemical and urea sensing performance were studied systematically. The suitability of prepared BDAC material for three major domains indicates they can be significant candidates for next-generation electrochemical applications.

This study highlights the advantage of BDAC beyond its electrochemical performance. As a sustainable option, BDAC utilises biomass waste and transform it into a value-added product. This action benefits in reducing the carbon footprint and significantly lowers the costs associated with various electrochemical devices. Additionally, the hierarchical features of BDAC can be customised through careful selection of biomass precursors, preparation methods, and post-treatment processes. Overall, BDAC is a transformative material that has the potential to make a significant impact in the field of electrochemical systems. Its high surface area and remarkable porous structure can lead to the development of high-performance, cost-effective and sustainable solutions in the field of energy storage and environmental monitoring.

1.5 Scope of the work

In this research, we are interested in synthesising BDAC-based electrodes for different electrochemical systems in an economical and environmentally friendly method. BDAC exhibits unique properties, including high surface area, excellent adsorption capacity, good electrical conductivity, and significant porosity. These characteristics significantly enhance the efficiency of these systems. Additionally, using biomass waste allows for the optimal utilisation of resources and reduces the carbon footprint associated with conventional AC production methods.

This study evaluates the effectiveness of BDAC-based electrodes in several electrochemical systems, including EDLCs, LIBs, and electrochemical sensors. The high porosity and large surface area of BDAC provide numerous sites for the adsorption and desorption of ions, enabling efficient charge storage in EDLCs. Additionally, the presence of micropores and mesopores enhances the rapid diffusion of ions, leading to high capacitance and improved energy storage performance.

BDAC-based anode materials in LIBs have garnered considerable attention due to their cost effectiveness, high availability, thermal stability, minimal environmental impact, high electrical conductivity, and stability in adverse chemical conditions. The effect of these anode materials on the formation of a stable SEI was also evaluated successfully. Moreover, BDAC facilitates the reversible intercalation and deintercalation of lithium ions during charge and discharge cycles, thereby enhancing the overall energy storage capacity of LIBs.

Additionally, the effectiveness of electrochemical sensors is often limited by the restricted accessible surface area of their electrode materials. Increasing this surface area by incorporating BDAC can significantly enhance the performance of the sensors, as it provides a conductive surface that facilitates the detection of target analytes through redox reactions or adsorption processes. Its high surface area allows a greater number of analyte molecules to interact with the electrode, thereby improving the sensitivity and overall performance of the sensor.

This study highlights the potential of BDAC in different electrochemical systems and provides a sustainable solution for waste management in various sectors.

It demonstrates the feasibility of using the prepared BDAC in LIBs, EDLCs, and electrochemical sensors. Furthermore, the stability and cycle life of these systems are remarkable. The outstanding performance in these applications is attributed to their unique structural characteristics, including a large surface area and well-developed pore distribution.

References

1. Nguyen TN, Le PA, Phung VBT. Facile green synthesis of carbon quantum dots and biomass-derived activated carbon from banana peels: synthesis and investigation. *Biomass Convers Biorefin.* 2022 Jul 1;12(7):2407–16.
2. Gayathiri M, Pulingam T, Lee KT, Sudesh K. Activated carbon from biomass waste precursors: Factors affecting production and adsorption mechanism. *Chemosphere.* 2022 May 1;294:133764.
3. Zhou Y, He J, Chen R, Li X. Recent advances in biomass-derived graphene and carbon nanotubes. *Materials Today Sustainability.* 2022 Jun 1;18:100138.
4. Kabir Ahmad R, Anwar Sulaiman S, Yusup S, Sham Dol S, Inayat M, Aminu Umar H. Exploring the potential of coconut shell biomass for charcoal production. *Ain Shams Engineering Journal.* 2022 Jan 1;13(1).
5. Mbarki F, Selmi T, Kesraoui A, Seffen M. Low-cost activated carbon preparation from Corn stigmata fibers chemically activated using H₃PO₄, ZnCl₂ and KOH: Study of methylene blue adsorption, stochastic isotherm and fractal kinetic. *Industrial Crops and Products.* 2022 Apr 1;178:114546.
6. Yan B, Zheng J, Feng L, Du C, Jian S, Yang W, et al. Wood-derived biochar as thick electrodes for high-rate performance supercapacitors. *Biochar.* 2022 Dec 1;4(1).
7. Palmer JC, Brennan JK, Hurley MM, Balboa A, Gubbins KE. Detailed structural models for activated carbons from molecular simulation. *Carbon N Y.* 2009 Oct;47(12):2904–13.
8. Yan B, Zheng J, Feng L, Zhang Q, Zhang C, Ding Y, Han J, Jiang S, He S. Pore engineering: Structure-capacitance correlations for biomass-derived porous carbon materials. *Materials & Design.* 2023 May 1;229:111904.
9. Naji SZ, Tye CT. A review of the synthesis of activated carbon for biodiesel production: Precursor, preparation, and modification. *Energy Conversion and Management: X.* 2022 Jan 1;13.
10. Sujiono EH, Zabrian D, Zurnansyah, Mulyati, Zharvan V, Samnur, et al. Fabrication and characterization of coconut shell activated carbon using variation chemical activation for wastewater treatment application. *Results Chem.* 2022 Jan 1;4.
11. Neme I, Gonfa G, Masi C. Preparation and characterization of activated carbon from castor seed hull by chemical activation with H₃PO₄. *Results in Materials.* 2022 Sep 1;15.
12. Karimi-Maleh H, Karaman C, Karaman O, Karimi F, Vasseghian Y, Fu L, et al. Nanochemistry approach for the fabrication of Fe and N co-decorated biomass-derived

- activated carbon frameworks: a promising oxygen reduction reaction electrocatalyst in neutral media. *J Nanostructure Chem.* 2022 Jun 1;12(3):429–39.
13. Saka T, San-Pedro L, Abubakar A, Sylvain T, Budianto A, Rabet S. Evaluation of the physical properties of various biomass materials for the production of activated carbon. *J. Chem. Environ.* 2023;1(2):30-9.
 14. Neolaka YAB, Riwu AAP, Aigbe UO, Ukhurebor KE, Onyancha RB, Darmokoesoemo H, et al. Potential of activated carbon from various sources as a low-cost adsorbent to remove heavy metals and synthetic dyes. *Results Chem.* 2023 Jan 1;5.
 15. Razali NS, Abdulhameed AS, Jawad AH, ALOthman ZA, Yousef TA, Al-Duaij OK, et al. High-Surface-Area-Activated Carbon Derived from Mango Peels and Seeds Wastes via Microwave-Induced ZnCl₂ Activation for Adsorption of Methylene Blue Dye Molecules: Statistical Optimization and Mechanism. *Molecules.* 2022 Oct 1;27(20).
 16. Gopalan J, Buthiyappan A, Raman AA. Insight into metal-impregnated biomass based activated carbon for enhanced carbon dioxide adsorption: A review. *Journal of Industrial and Engineering Chemistry.* 2022 Sep 25;113:72-95.
 17. Sellaoui L, Gómez-Avilés A, Dhaouadi F, Bedia J, Bonilla-Petriciolet A, Rtimi S, Belder C. Adsorption of emerging pollutants on lignin-based activated carbon: Analysis of adsorption mechanism via characterization, kinetics and equilibrium studies. *Chemical Engineering Journal.* 2023 Jan 15;452:139399.
 18. Bayuo J, Rwiza MJ, Mtei KM. Modeling and optimization of trivalent arsenic removal from wastewater using activated carbon produced from maize plant biomass: a multivariate experimental design approach. *Biomass Conversion and Biorefinery.* 2024 Oct;14(19):24809-32.
 19. AlSalem HS, Katubi KMS, Binkadem MS, Al-Goul ST, Wahba AM. Fabrication of Asymmetric Supercapacitors (AC@GQDs//AC) with High Electrochemical Performance Utilizing Activated Carbon and Graphene Quantum Dots. *ACS Omega.* 2023 Oct 31;8(43):40808–16.
 20. Wang B, Lan J, Bo C, Gong B, Ou J. Preparation of Ganoderma Lucidum Bran-Based Biological Activated Carbon for Dual-Functional Adsorption and Detection of Copper Ions. *Materials.* 2023 Jan 1;16(2).
 21. He H, Zhang R, Zhang P, Wang P, Chen N, Qian B, Zhang L, Yu J, Dai B. Functional carbon from nature: biomass-derived carbon materials and the recent progress of their applications. *Advanced science.* 2023 Jun;10(16):2205557.
 22. Ahmed F, Almutairi G, Hasan PM, Rehman S, Kumar S, Shaalan NM, Aljaafari A, Alshoaibi A, Alotaibi B, Khan K. Fabrication of a biomass-derived activated carbon-based anode for high-performance li-ion batteries. *Micromachines.* 2023 Jan 12;14(1):192.
 23. Pulikkottil M, Thomas A, Malamal Neelanchery M, Gopalan Elavumkal V, Ansari S. Highly Efficient Solid-State Supercapacitor with Porous Electrode Material. *Energy Technology.* 2023 Sep 1;11(9).
 24. Botewad SN, Gaikwad DK, Girhe NB, Thorat HN, Pawar PP. Urea biosensors: A comprehensive review. *Biotechnology and Applied Biochemistry.* 2023 Apr;70(2):485-501.

25. Zhang S, Yu Y, Xie M, Du C, Chen J, Wan L, Zhang Y. Clean production of N, O-doped activated carbon by water vapor carbonization/activation of expired coffee for high-volumetric supercapacitor. *Applied Surface Science*. 2022 Jul 1;589:153011.
26. Khuong DA, Nguyen HN, Tsubota T. Activated carbon produced from bamboo and solid residue by CO₂ activation utilized as CO₂ adsorbents. *Biomass and Bioenergy*. 2021 May 1;148:106039.
27. Wang B, Lan J, Bo C, Gong B, Ou J. Adsorption of heavy metal onto biomass-derived activated carbon. *RSC advances*. 2023;13(7):4275-302.
28. Jawad AH, Abdulhameed AS, Bahrudin NN, Hum NNMF, Surip SN, Syed-Hassan SSA, et al. Microporous activated carbon developed from KOH activated biomass waste: surface mechanistic study of methylene blue dye adsorption. *Water Science and Technology*. 2021 Oct 15;84(8):1858–72.
29. Kanjana K, Harding P, Kwamman T, Kingkam W, Chutimasakul T. Biomass-derived activated carbons with extremely narrow pore size distribution via eco-friendly synthesis for supercapacitor application. *Biomass Bioenergy*. 2021 Oct 1;153.
30. Neolaka YAB, Lawa Y, Naat J, Riwu AAP, Darmokoesoemo H, Widyaningrum BA, et al. Indonesian Kesambi wood (*Schleichera oleosa*) activated with pyrolysis and H₂SO₄ combination methods to produce mesoporous activated carbon for Pb(II) adsorption from aqueous solution. *Environ Technol Innov*. 2021 Nov 1;24.
31. Keppetipola NM, Dissanayake M, Dissanayake P, Karunarathne B, Dourges MA, Talaga D, et al. Graphite-type activated carbon from coconut shell: a natural source for eco-friendly non-volatile storage devices. *RSC Adv*. 2021 Jan 13;11(5):2854–65.
32. El-Bery HM, Saleh M, El-Gendy RA, Saleh MR, Thabet SM. High adsorption capacity of phenol and methylene blue using activated carbon derived from lignocellulosic agriculture wastes. *Sci Rep*. 2022 Dec 1;12(1).
33. Wang S, Lee YR, Won Y, Kim H, Jeong SE, Hwang BW, Cho AR, Kim JY, Park YC, Nam H, Lee DH. Development of high-performance adsorbent using KOH-impregnated rice husk-based activated carbon for indoor CO₂ adsorption. *Chemical Engineering Journal*. 2022 Jun 1;437:135378.
34. Kim IT, Sinha TK, Lee J, Lee Y, Oh JS. Ultrasonic treatment: An acid-free green approach toward preparing high-performance activated carbon from lignin. *Ind Eng Chem Res*. 2021 Feb 17;60(6):2439–46.
35. Yarramsetti S, Girirajan M, Kalluri S, Sangaraju S, Maram PS. Multifunctional activated carbon derived from novel biomass for high-performance energy storage applications: A sustainable alternative to fossil-fuel-derived carbon. *Mater Chem Phys*. 2024 Jul 1;320.
36. Serafin J, Dziejarski B. Activated carbons—preparation, characterization and their application in CO₂ capture: A review. *Environmental Science and Pollution Research*. 2024 Jun 1;31(28):40008–62.
37. Sun Y, Shi XL, Yang YL, Suo G, Zhang L, Lu S, Chen ZG. Biomass-derived carbon for high-performance batteries: from structure to properties. *Advanced Functional Materials*. 2022 Jun;32(24):2201584.

38. Heeley K, Orozco RL, Macaskie LE, Love J, Al-Duri B. Supercritical water gasification of microalgal biomass for hydrogen production-A review. *international journal of hydrogen energy*. 2024 Jan 2;49:310-36.
39. Gan YX. Activated carbon from biomass sustainable sources. *C*. 2021 Apr 27;7(2):39.
40. Vinayagam M, Suresh Babu R, Sivasamy A, de Barros ALF. Biomass-derived porous activated carbon nanofibers from *Sapindus trifoliatus* nut shells for high-performance symmetric supercapacitor applications. *Carbon Letters*. 2021 Dec 1;31(6):1133–43.
41. Li Y, Zhang D, Zhang Y, He J, Wang Y, Wang K, et al. Biomass-derived microporous carbon with large micropore size for high-performance supercapacitors. *J Power Sources*. 2020 Feb 1;448.
42. Gan YX. Activated carbon from biomass sustainable sources. *C*. 2021 Apr 27;7(2):39.
43. Wang H, Pu Y, Ragauskas A, Yang B. From lignin to valuable products—strategies, challenges, and prospects. *Bioresource technology*. 2019 Jan 1;271:449-61.
44. Zhou J, Zhang S, Zhou YN, Tang W, Yang J, Peng C, Guo Z. Biomass-derived carbon materials for high-performance supercapacitors: current status and perspective. *Electrochemical Energy Reviews*. 2021 Jun;4:219-48.
45. Zhou Y, Li J, Hu S, Qian G, Shi J, Zhao S, et al. Sawdust-Derived Activated Carbon with Hierarchical Pores for High-Performance Symmetric Supercapacitors. *Nanomaterials*. 2022 Feb 28;12(5):810.
46. Thota SP, Bag PP, Vadlani PV, Belliraj SK. Plant Biomass Derived Multidimensional Nanostructured Materials: A Green Alternative for Energy Storage. *Engineered Science*. 2022;18:31–58.
47. Palanisamy R, Karuppiyah D, Rengapillai S, Abdollahifar M, Ramasamy G, Wang FM, et al. A reign of bio-mass derived carbon with the synergy of energy storage and biomedical applications. *J Energy Storage*. 2022 Jul 1;51.
48. Jjagwe J, Olupot PW, Menya E, Kalibbala HM. Synthesis and application of granular activated carbon from biomass waste materials for water treatment: a review. *Journal of Bioresources and Bioproducts*. 2021 Nov 1;6(4):292-322.
49. Abou-Hadid AF, El-Beairy UA, Elmalih MM, Amdeha E, Naggar AMAE, Taha MH, et al. Conversion of corn shell as biomass solid waste into carbon species for efficient decontamination of wastewater via heavy metals adsorption. *Biomass Convers Biorefin*. 2024 Jul 1;14(14):16435–49.
50. Baloo L, Isa MH, Sapari N Bin, Jagaba AH, Wei LJ, Yavari S, et al. Adsorptive removal of methylene blue and acid orange 10 dyes from aqueous solutions using oil palm wastes-derived activated carbons. *Alexandria Engineering Journal*. 2021 Dec 1;60(6):5611–29.
51. Argumedo-Delira R, Gómez-Martínez MJ, Uribe-Kaffure R. *Trichoderma* biomass as an alternative for removal of congo red and malachite green industrial dyes. *Applied Sciences*. 2021 Jan 5;11(1):448.
52. Zahoor M, Wahab M, Salman SM, Sohail A, Ali EA, Ullah R. Removal of Doxycycline from Water using *Dalbergia sissoo* Waste Biomass Based Activated Carbon and Magnetic Oxide/Activated Bioinorganic Nanocomposite in Batch Adsorption and Adsorption/Membrane Hybrid Processes. *Bioinorg Chem Appl*. 2022;2022.

53. Ouardi Y El, Aissouq A El, Chennah A, Ouammou A, Laatikainen K. Synthesis, characterization, and DFT investigation of rhodamine B dye removal by activated carbon produced from argan nutshell. *Biomass Convers Biorefin.* 2024 Jul 1;14(13):15107–18.
54. Akpomie KG, Adegoke KA, Oyedotun KO, Ighalo JO, Amaku JF, Olisah C, Adeola AO, Iwuzor KO, Conradie J. Removal of bromophenol blue dye from water onto biomass, activated carbon, biochar, polymer, nanoparticle, and composite adsorbents. *Biomass Conversion and Biorefinery.* 2024 Jul;14(13):13629-57.
55. Sarwar A, Ali M, Khoja AH, Nawar A, Waqas A, Liaquat R, Naqvi SR, Asjid M. Synthesis and characterization of biomass-derived surface-modified activated carbon for enhanced CO₂ adsorption. *Journal of CO₂ Utilization.* 2021 Apr 1;46:101476.
56. Saleh TS, Badawi AK, Salama RS, Mostafa MMM. Design and Development of Novel Composites Containing Nickel Ferrites Supported on Activated Carbon Derived from Agricultural Wastes and Its Application in Water Remediation. *Materials.* 2023 Mar 1;16(6).
57. Dada AO, Inyinbor AA, Bello OS, Tokula BE. Novel plantain peel activated carbon-supported zinc oxide nanocomposites (PPAC-ZnO-NC) for adsorption of chloroquine synthetic pharmaceutical used for COVID-19 treatment. *Biomass Convers Biorefin.* 2023 Jul 1;13(10):9181–93.
58. Hassan MF, Sabri MA, Fazal H, Hafeez A, Shezad N, Hussain M. Recent trends in activated carbon fibers production from various precursors and applications—A comparative review. *Journal of Analytical and Applied Pyrolysis.* 2020 Jan 1;145:104715.
59. Zhao W, Yan B, Chen D, Chen J, Zhang Q, Jiang L, Lan T, Zhang C, Yang W, He S. Free-standing carbon network with enhanced capacitive performance synthesized via green H₂O₂ activation. *Colloids and Surfaces A: Physicochemical and Engineering Aspects.* 2023 Jul 5;668:131425..
60. Huo S, Zhang X, Liang B, Zhao Y, Li K. Synthesis of interconnected hierarchically porous carbon networks with excellent diffusion ability based on NaNO₃ crystal-assisted strategy for high performance supercapacitors. *Journal of Power Sources.* 2020 Feb 29;450:227612.
61. Freitas B, Nunes WG, Soares DM, Rufino FC, Moreira CM, Da Silva LM, et al. Robust, flexible, freestanding and high surface area activated carbon and multi-walled carbon nanotubes composite material with outstanding electrode properties for aqueous-based supercapacitors. *Mater Adv.* 2021 Jul 7;2(13):4264–76.
62. Boulanger N, Talyzin A V., Xiong S, Hultberg M, Grimm A. High surface area activated carbon prepared from wood-based spent mushroom substrate for supercapacitors and water treatment. *Colloids Surf A Physicochem Eng Asp.* 2024 Jan 5;680.
63. Hiremath V, Lim AC, Seo JG. Highly porous honeycomb-like activated carbon derived using cellulose pulp for symmetric supercapacitors. *Int J Energy Res.* 2021 Mar 10;45(3):4385–95.
64. Zhang M, Zhang J, Ran S, Sun W, Zhu Z. Biomass-Derived sustainable carbon materials in energy conversion and storage applications: Status and opportunities. A mini review. *Electrochemistry Communications.* 2022 May 1;138:107283.

65. Zhang M, Peng L. Research progress of biomass-derived carbon for the supercapacitors. *Materials Research Express*. 2024 Jan 23;11(1):012004.
66. Taslim R, Apriwandi A, Taer E. Novel Moringa oleifera Leaves 3D Porous Carbon-Based Electrode Material as a High-Performance EDLC Supercapacitor. *ACS Omega*. 2022 Oct 18;7(41):36489–502.
67. Sharma P, Singh D, Minakshi M, Quadsia S, Ahuja R. Activation-Induced Surface Modulation of Biowaste-Derived Hierarchical Porous Carbon for Supercapacitors. *Chempluschem*. 2022 Jun 1;87(6).
68. Tu J, Qiao Z, Wang Y, Li G, Zhang X, Li G. American ginseng biowaste-derived activated carbon for high-performance supercapacitors. *Int J Electrochem Sci*. 2023;18(2):16–24.
69. Mandal S, Hu J, Shi SQ. A comprehensive review of hybrid supercapacitor from transition metal and industrial crop based activated carbon for energy storage applications. *Materials Today Communications*. 2023 Mar 1;34:105207.
70. Hamouda HA, Cui S, Dai X, Xie X, Peng H, Ma G, et al. High-performance asymmetric supercapacitor based on urchin-like cobalt manganese oxide nanoneedles and biomass-derived carbon nanosheet electrode materials. *J Energy Storage*. 2022 Mar 1;47.
71. George NS, Singh G, Bahadur R, Kumar P, Ramadass K, Sathish CI, Benzigar M, Sajan D, Aravind A, Vinu A. Recent Advances in Functionalized Biomass-Derived Porous Carbons and their Composites for Hybrid Ion Capacitors. *Advanced Science*. 2024 Sep;11(35):2406235.
72. Lv H, Xiao Z, Zhai S, Wang X, Hao J, Tong Y, An Q. Ni₃S₂ nanoparticles encapsulated in S-doped biomass-derived hierarchically porous carbon as an advanced electrode for excellent hybrid supercapacitors performance. *Industrial Crops and Products*. 2023 Apr 1;194:116320.
73. Selvaraj AR, Chinnadurai D, Cho I, Bak JS, Prabakar K. Bio-waste wood-derived porous activated carbon with tuned microporosity for high performance supercapacitors. *Journal of Energy Storage*. 2022 Aug 15;52:104928.
74. Huang W, Khalafallah D, Ouyang C, Zhi M, Hong Z. Strategic N/P self-doped biomass-derived hierarchical porous carbon for regulating the supercapacitive performances. *Renew Energy*. 2023 Jan 1;202:1259–72.
75. Zhang H, Zhang Y, Bai L, Zhang Y, Sun L. Effect of physiochemical properties in biomass-derived materials caused by different synthesis methods and their electrochemical properties in supercapacitors. *Journal of Materials Chemistry A*. 2021;9(21):12521-52.
76. Khan IA, Wang YL, Shah FU. Effect of structural variation in biomass-derived nonfluorinated ionic liquids electrolytes on the performance of supercapacitors. *Journal of Energy Chemistry*. 2022 Jun 1;69:174–84.
77. Ramachandran R, Wang F. Electrochemical capacitor performance: influence of aqueous electrolytes. *Supercapacitors-theoretical and practical solutions*. 2018 Jun 27:51-68.
78. Pal B, Yang S, Ramesh S, Thangadurai V, Jose R. Electrolyte selection for supercapacitive devices: A critical review. *Nanoscale Adv*. 2019;1(10):3807–35.

79. Rai S, Bhujel R, Biswas J, Swain BP. Effect of electrolyte on the supercapacitive behaviour of copper oxide/reduced graphene oxide nanocomposite. *Ceram Int*. 2019 Aug 1;45(11):14136–45.
80. Rajasekaran SJ, Grace AN, Jacob G, Alodhayb A, Pandiaraj S, Raghavan V. Investigation of Different Aqueous Electrolytes for Biomass-Derived Activated Carbon-Based Supercapacitors. *Catalysts*. 2023 Feb 1;13(2).
81. Nzereogu PU, Omah AD, Ezema FI, Iwuoha EI, Nwanya AC. Anode materials for lithium-ion batteries: A review. *Applied Surface Science Advances*. 2022 Jun 1;9:100233.
82. Zhang Y, Liu L, Zhao L, Hou C, Huang M, Algadi H, Li D, Xia Q, Wang J, Zhou Z, Han X. Sandwich-like CoMoP₂/MoP heterostructures coupling N, P co-doped carbon nanosheets as advanced anodes for high-performance lithium-ion batteries. *Advanced Composites and Hybrid Materials*. 2022 Sep;5(3):2601-10.
83. Xing B, Shi F, Jin Z, Zeng H, Qu X, Huang G, Zhang C, Xu Y, Chen Z, Lu J. A facile ice-templating-induced puzzle coupled with carbonization strategy for kilogram-level production of porous carbon nanosheets as high-capacity anode for lithium-ion batteries. *Carbon Energy*. 2024 Dec;6(12):e633.
84. Ray A, Saruhan B. Application of ionic liquids for batteries and supercapacitors. *Materials*. 2021 May 29;14(11):2942.
85. Astuti Y, Insani RR, Ekaningsih AZ, Nurhasanah I, Lestariningsih T, Suseno A. Synthesis, characterization and electrochemical performance of Bi₂S₃/rice husk-based activated carbon composites as lithium ion battery anodes. *Results in Engineering*. 2024 Dec 1;24:103211.
86. Mei S, Guo S, Xiang B, Deng J, Fu J, Zhang X, et al. Enhanced ion conductivity and electrode–electrolyte interphase stability of porous Si anodes enabled by silicon nitride nanocoating for high-performance Li-ion batteries. *Journal of Energy Chemistry*. 2022 Jun 1;69:616–25.
87. Sui D, Yao M, Si L, Yan K, Shi J, Wang J, Xu CC, Zhang Y. Biomass-derived carbon coated SiO₂ nanotubes as superior anode for lithium-ion batteries. *Carbon*. 2023 Mar 5;205:510-8.
88. Ehi-Eromosele CO, Onwucha CN, Ajayi SO, Melinte G, Hansen AL, Indris S, et al. Ionothermal synthesis of activated carbon from waste PET bottles as anode materials for lithium-ion batteries. *RSC Adv*. 2022 Dec 2;12(53):34670–84.
89. Soltani N, Bahrami A, Giebeler L, Gemming T, Mikhailova D. Progress and challenges in using sustainable carbon anodes in rechargeable metal-ion batteries. *Progress in Energy and Combustion Science*. 2021 Nov 1;87:100929.
90. Nzereogu PU, Omah AD, Ezema FI, Iwuoha EI, Nwanya AC. Anode materials for lithium-ion batteries: A review. *Applied Surface Science Advances*. 2022 Jun 1;9:100233.
91. Culebras M, Collins GA, Beaucamp A, Geaney H, Collins MN. Lignin/Si Hybrid Carbon Nanofibers towards Highly Efficient Sustainable Li-ion Anode Materials. *Engineered Science*. 2022;17:195–203.
92. Mozhzhukhina N, Flores E, Lundström R, Nyström V, Kitz PG, Edström K, et al. Direct Operando Observation of Double Layer Charging and Early Solid Electrolyte

- Interphase Formation in Li-Ion Battery Electrolytes. *Journal of Physical Chemistry Letters*. 2020 May 21;11(10):4119–23.
93. Chu Y, Shen Y, Guo F, Zhao X, Dong Q, Zhang Q, Li W, Chen H, Luo Z, Chen L. Advanced characterizations of solid electrolyte interphases in lithium-ion batteries. *Electrochemical energy reviews*. 2020 Mar;3:187-219..
 94. Zhao Y, Wu M, Chen H, Zhu J, Liu J, Ye Z, et al. Balance cathode-active and anode-active groups in one conjugated polymer towards high-performance all-organic lithium-ion batteries. *Nano Energy*. 2021 Aug 1;86.
 95. Ling J, Karupiah C, Krishnan SG, Reddy MV, Misnon II, Ab Rahim MH, Yang CC, Jose R. Phosphate polyanion materials as high-voltage lithium-ion battery cathode: a review. *Energy & Fuels*. 2021 Jun 12;35(13):10428-50.
 96. Ramasubramanian B, Sundarrajan S, Chellappan V, Reddy MV, Ramakrishna S, Zaghbi K. Recent development in carbon-LiFePO₄ cathodes for lithium-ion batteries: a mini review. *Batteries*. 2022 Sep 21;8(10):133.
 97. Tsao Y, Gong H, Chen S, Chen G, Liu Y, Gao TZ, et al. A Nickel-Decorated Carbon Flower/Sulfur Cathode for Lean-Electrolyte Lithium–Sulfur Batteries. *Adv Energy Mater*. 2021 Sep 1;11(36).
 98. Versaci D, Colombo R, Montinaro G, Buga M, Cortes Felix N, Evans G, et al. Tailoring cathode materials: A comprehensive study on LNMO/LFP blending for next generation lithium-ion batteries. *J Power Sources*. 2024 Sep 1;613.
 99. Liu Y, Elias Y, Meng J, Aurbach D, Zou R, Xia D, Pang Q. Electrolyte solutions design for lithium-sulfur batteries. *Joule*. 2021 Sep 15;5(9):2323-64.
 100. Liu Y, Elias Y, Meng J, Aurbach D, Zou R, Xia D, Pang Q. Electrolyte solutions design for lithium-sulfur batteries. *Joule*. 2021 Sep 15;5(9):2323-64.
 101. Xu J, Cai X, Cai S, Shao Y, Hu C, Lu S, Ding S. High-energy lithium-ion batteries: recent progress and a promising future in applications. *Energy & Environmental Materials*. 2023 Sep;6(5):e12450.
 102. Versaci D, Colombo R, Montinaro G, Buga M, Cortes Felix N, Evans G, et al. Tailoring cathode materials: A comprehensive study on LNMO/LFP blending for next generation lithium-ion batteries. *J Power Sources*. 2024 Sep 1;613.
 103. Zhang Y, Wang Y, Zhao W, Zuo P, Tong Y, Yin G, et al. Delocalized electronic engineering of TiNb₂O₇ enables low temperature capability for high-areal-capacity lithium-ion batteries. *Nat Commun*. 2024 Dec 1;15(1).
 104. Zhu P, Gastol D, Marshall J, Sommerville R, Goodship V, Kendrick E. A review of current collectors for lithium-ion batteries. *Journal of Power Sources*. 2021 Feb 15;485:229321.
 105. G P, Rathi BS, Kumar PS, Rangasamy G. Electrochemical sensor for urea determination using structural c-multiwall carbon nanotubes decorated CuO hybrid nanocomposite: Application in rice water samples. *Desalination Water Treat*. 2024 Oct 1;320.
 106. Lete C, López-iglesias D, García-guzmán JJ, Leau SA, Stanciu AE, Marin M, et al. A sensitive electrochemical sensor based on sonogel-carbon material enriched with gold nanoparticles for melatonin determination. *Sensors*. 2022 Jan 1;22(1).

107. Pitiphattharabun S, Auewattanapun K, Htet TL, Thu MM, Panomsuwan G, Techapiesancharoenkij R, et al. Reduced graphene oxide/zinc oxide composite as an electrochemical sensor for acetylcholine detection. *Sci Rep.* 2024 Dec 1;14(1).
108. Xu W, Walpen N, Keiluweit M, Kleber M, Sander M. Redox Properties of Pyrogenic Dissolved Organic Matter (pyDOM) from Biomass-Derived Chars. *Environ Sci Technol.* 2021 Aug 17;55(16):11434–44.
109. Arivazhagan M, Mohan B, Jakmunee J. Nanostructured metallic enzymes mimic for electrochemical biosensing of glucose. *Green Analytical Chemistry.* 2024 Sep 1;10:100127.
110. Liu D, Cao W, Li F, Hu Y, Ding Y. Controllable morphology engineering of Cu₂O nanoparticles for non-enzymatic glucose sensing. *Microchemical Journal.* 2023 Oct 1;193:108922.
111. Durai L, Gopalakrishnan A, Badhulika S. Silica embedded carbon nanosheets derived from biomass acorn cupule for non-enzymatic, label-free, and wide range detection of α 1-acid glycoprotein in biofluids. *Anal Chim Acta.* 2021 Jul 18;1169.
112. Madagalam M, Bartoli M, Tagliaferro A, Carrara S. Bismuth-Nanocomposites Modified SPCEs for Non-Enzymatic Electrochemical Sensors. *IEEE Sens J.* 2021 May 1;21(9):11155–62.
113. Magar HS, Hassan RYA, Abbas MN. Non-enzymatic disposable electrochemical sensors based on CuO/Co₃O₄@MWCNTs nanocomposite modified screen-printed electrode for the direct determination of urea. *Sci Rep.* 2023 Dec 1;13(1).
114. Chennah A, Khan MA, Zbair M, Ait Ahsaine H. NiO/AC Active Electrode for the Electrosorption of Rhodamine B: Structural Characterizations and Kinetic Study. *Catalysts.* 2023 Jun 1;13(6).
115. Chiu WT, Chang TF, Sone M, Hosoda H, Tixier-Mita A, Toshiyoshi H. Developments of the electroactive materials for non-enzymatic glucose sensing and their mechanisms. *Electrochem.* 2021 Jun 21;2(2):347-89.
116. Miya N, Machogo-Phao LF, Ntsendwana B. Exploring copper oxide and copper sulfide for non-enzymatic glucose sensors: Current progress and future directions. *Micromachines.* 2023 Sep 27;14(10):1849.
117. Phan TT, Nguyen TD, Nguyen MT, Lee JS. Facile synthesis of nickel-decorated multidimensional carbon nanofibers via oxygen plasma activation for non-enzymatic acetaminophen sensing. *Carbon.* 2023 Aug 1;212:118176.
118. Sharma KP, Shin M, Awasthi GP, Yu C. Single step hydrothermal synthesis of CuS/MnS composite for electrochemical non-enzymatic glucose sensor. *Solid State Sci.* 2023 Sep 1;143.
119. Selvi Gopal T, James JT, Gunaseelan B, Ramesh K, Raghavan V, Malathi A CJ, Amarnath K, Kumar VG, Rajasekaran SJ, Pandiaraj S, MR M. MXene-embedded porous carbon-based Cu₂O nanocomposites for non-enzymatic glucose sensors. *ACS omega.* 2024 Feb 12;9(7):8448-56.
120. Lawal AT. Recent developments in electrochemical sensors based on graphene for bioanalytical applications. *Sensing and Bio-Sensing Research.* 2023 Aug 1;41:100571.

121. Azeez MO, Ganiyu SA. Review of biomass derived-activated carbon for production of clean fuels by adsorptive desulfurization: Insights into processes, modifications, properties, and performances. *Arabian Journal of Chemistry*. 2023 Oct 1;16(10):105182.
122. Yuwen T, Zou H, Xu S, Wu C, Peng Q, Shu D, Yang X, Wang Y, Yu C, Fan J, Zhang Y. Effect of glucuronic acid on inducing self-assembly of Au nanoflowers@ glucuronic acid on carbon cloth for non-enzymatic glucose sensing. *Materials Today Chemistry*. 2023 Apr 1;29:101388.
123. Tao B, Li J, Miao F, Zang Y. Carbon Cloth Loaded NiCo₂O₄Nano-Arrays to Construct Co-MOF@GO Nanocubes: A High-Performance Electrochemical Sensor for Non-Enzymatic Glucose. *IEEE Sens J*. 2022 Jul 15;22(14):13898–907.
124. Waryani B, Tahira A, Akhtar S, Bibi A, Bhatti MA, Siddiqui A, Mahar IA, Parveen M, Dawi E, Shah AA, Tonezzer M. Non-enzymatic electrochemical detection of xanthine from edible oral arms of jellyfish *Catostylus Perezi* (Ranson 1945) using CuO nanostructures derived from sugar molasses.
125. Pinheiro T, Caetano J, Fortunato E, Sales MG, Almeida H, Martins R. One-Step Laser Synthesis of Copper Nanoparticles and Laser-Induced Graphene in a Paper Substrate for Non-Enzymatic Glucose Sensing. *Advanced Sensor Research*. 2024 Nov;3(11):240052.
126. Larasati LD, Ateş A, Oskay KO. Direct co-deposition of binder-free Cu-biochar-based nonenzymatic disposable sensing element for electrochemical glucose detection. *Surfaces and Interfaces*. 2023 Nov 1;42:103355.
127. Nikhil N, Srivastava SK, Srivastava A, Srivastava M, Prakash R. Electrochemical Sensing of Roxarsone on Natural Biomass-Derived Two-Dimensional Carbon Material as Promising Electrode Material. *ACS Omega*. 2022 Jan 25;7(3):2908–17.
128. Michenzi C, Espro C, Bressi V, Celesti C, Vetica F, Salvitti C, Chiarotto I. Electrochemical bottom-up synthesis of biomass-derived carbon dots for promoting Knoevenagel condensation. *Molecular Catalysis*. 2023 Jun 15;544:113182.
129. Rajasekaran SJ, Raghavan V. Palmyra palm flower biomass-derived activated porous carbon and its application as a supercapacitor electrode. *Journal of Electrochemical Science and Engineering*. 2022 Jun 13;12(3):545–56.
130. Pulikkottil M, Antony H, Muralidharan MN, Gopalan EV, Ansari S. Cashew Nut Shell Derived Porous Activated Carbon Electrodes for “Water-in-Salt” Electrolyte Based Symmetric Supercapacitor. *ChemistrySelect*. 2022 Jun 20;7(23).
131. Merin P, Jimmy Joy P, Muralidharan MN, Veena Gopalan E, Seema A. Biomass-derived activated carbon for high-performance supercapacitor electrode applications. *Chemical Engineering & Technology*. 2021 May;44(5):844-51.
132. Zhong X, Mao Q, Li Z, Wu Z, Xie Y, Li SH, et al. Biomass-derived O, N-codoped hierarchically porous carbon prepared by black fungus and *Hericium erinaceus* for high performance supercapacitor. *RSC Adv*. 2021 Aug 8;11(45):27860–7.
133. Adan-Mas A, Alcaraz L, Arévalo-Cid P, López-Gómez FA, Montemor F. Coffee-derived activated carbon from second biowaste for supercapacitor applications. *Waste Management*. 2021 Feb 1;120:280–9.

134. Kalu-Uka GM, Kumar S, Kalu-Uka AC, Vikram S, Ihekweme GO, Ranjan N, Anosike-Francis EN, Prajapati G, Nduba A, Onwualu AP, Kumar S. Production of activated carbon electrode for energy storage application in supercapacitors via KOH activation of waste termite biomass. *Waste and Biomass Valorization*. 2022 May 1:1-6.
135. Wang H, Li X, Peng J, Cai Y, Jiang J, Li Q. Control of the interface graphitized/amorphous carbon of biomass-derived carbon microspheres for symmetric supercapacitors. *Nanoscale Adv*. 2021 Aug 21;3(16):4858–65.
136. Wang Y, Wang J, Zhang X, Bhattacharyya D, Sabolsky EM. Quantifying environmental and economic impacts of highly porous activated carbon from lignocellulosic biomass for high-performance supercapacitors. *Energies*. 2022 Jan 4;15(1):351.
137. Hamouda HA, Cui S, Dai X, Xiao L, Xie X, Peng H, et al. Synthesis of porous carbon material based on biomass derived from hibiscus sabdariffa fruits as active electrodes for high-performance symmetric supercapacitors. *RSC Adv*. 2020 Dec 14;11(1):354–63.
138. Luo L, Lan Y, Zhang Q, Deng J, Luo L, Zeng Q, Gao H, Zhao W. A review on biomass-derived activated carbon as electrode materials for energy storage supercapacitors. *Journal of Energy Storage*. 2022 Nov 30;55:105839.
139. Boujibar O, Ghamouss F, Ghosh A, Achak O, Chafik T. Activated carbon with exceptionally high surface area and tailored nanoporosity obtained from natural anthracite and its use in supercapacitors. *Journal of power sources*. 2019 Oct 1;436:226882.
140. Wang Y, Xu T, Liu K, Zhang M, Cai XM, Si C. Biomass-based materials for advanced supercapacitor: principles, progress, and perspectives. *Aggregate*. 2024 Feb;5(1):e428.
141. Zaman F, Ishaq MW, Munawar A, Younas U, Ali Z. Aesculus indica-derived heteroatom-doped carbon as an electrode material for super-capacitor. *Carbon Letters*. 2023 Dec 1;33(7):1967–76.
142. Hamidah I, Ramdhani R, Wiyono A, Mulyanti B, Pawinanto RE, Hasanah L, et al. Biomass-Based Supercapacitors Electrodes for Electrical Energy Storage Systems Activated Using Chemical Activation Method: A Literature Review and Bibliometric Analysis. *Indonesian Journal of Science and Technology*. 2023 Dec 1;8(3):439–68.
143. Bejjanki D, Banothu P, Kumar VB, Kumar PS. Biomass-derived N-doped activated carbon from eucalyptus leaves as an efficient supercapacitor electrode material. *C*. 2023 Feb 17;9(1):24.
144. Liao Y, Shang Z, Ju G, Wang D, Yang Q, Wang Y, et al. Biomass Derived N-Doped Porous Carbon Made from Reed Straw for an Enhanced Supercapacitor. *Molecules*. 2023 Jun 1;28(12).
145. Andrew LJ, Gillman ER, Walters CM, Lizundia E, MacLachlan MJ. Multi-Responsive Supercapacitors from Chiral Nematic Cellulose Nanocrystal-Based Activated Carbon Aerogels. *Small*. 2023 Aug 23;19(34).
146. Yang C, Wu H, Cai M, Zhou Y, Guo C, Han Y, Zhang L. Valorization of biomass-derived polymers to functional biochar materials for supercapacitor applications via pyrolysis: Advances and perspectives. *Polymers*. 2023 Jun 19;15(12):2741.

147. Lesbayev B, Auyelkhankyzy M, Ustayeva G, Yeleuov M, Rakhymzhan N, Maral Y, Tolynbekov A. Modification of biomass-derived nanoporous carbon with nickel oxide nanoparticles for supercapacitor application. *Journal of Composites Science*. 2023 Jan 9;7(1):20.
148. Hu W, Xiang R, Lin J, Cheng Y, Lu C. Lignocellulosic biomass-derived carbon electrodes for flexible supercapacitors: An overview. *Materials*. 2021 Aug 14;14(16):4571.
149. Zhang X, Zhao M, Chen Z, Yan T, Li J, Ma Y, et al. The application of biomass-based carbon materials in flexible all-solid supercapacitors. *Journal of Materials Science: Materials in Electronics*. 2022 Jul 1;33(19):15422–32.
150. Rish SK, Tahmasebi A, Wang R, Dou J, Yu J. Novel composite nano-materials with 3D multilayer-graphene structures from biomass-based activated-carbon for ultrahigh Li-ion battery performance. *Electrochimica Acta*. 2021 Sep 10;390:138839.
151. Dou Y, Liu X, Wang X, Yu K, Liang C. Jute fiber based micro-mesoporous carbon: A biomass derived anode material with high-performance for lithium-ion batteries. *Materials Science and Engineering: B*. 2021 Mar 1;265:115015.
152. Hernández-Rentero C, Marangon V, Olivares-Marín M, Gómez-Serrano V, Caballero Á, Morales J, et al. Alternative lithium-ion battery using biomass-derived carbons as environmentally sustainable anode. *J Colloid Interface Sci*. 2020 Aug 1;573:396–408.
153. Lee SY, Choi Y, Kim JK, Lee SJ, Bae JS, Jeong ED. Biomass-garlic-peel-derived porous carbon framework as a sulfur host for lithium-sulfur batteries. *Journal of Industrial and Engineering Chemistry*. 2021 Feb 25;94:272–81.
154. Baskar AV, Singh G, Ruban AM, Davidraj JM, Bahadur R, Sooriyakumar P, Kumar P, Karakoti A, Yi J, Vinu A. Recent progress in synthesis and application of biomass-based hybrid electrodes for rechargeable batteries. *Advanced Functional Materials*. 2023 Jan;33(3):2208349.
155. Deng B, Huang Q, Zhang W, Liu J, Meng Q, Zhu Z, et al. Design high performance biomass-derived renewable carbon material for electric energy storage system. *J Clean Prod*. 2021 Aug 1;309.
156. Hernández-Rentero C, Marangon V, Olivares-Marín M, Gómez-Serrano V, Caballero Á, Morales J, Hassoun J. Alternative lithium-ion battery using biomass-derived carbons as environmentally sustainable anode. *Journal of colloid and interface science*. 2020 Aug 1;573:396-408.
157. Ahmed F, Almutairi G, Hasan PM, Rehman S, Kumar S, Shaalan NM, Aljaafari A, Alshoaibi A, AlOtaibi B, Khan K. Fabrication of a biomass-derived activated carbon-based anode for high-performance li-ion batteries. *Micromachines*. 2023 Jan 12;14(1):192.
158. Luna-Lama F, Morales J, Caballero A. Biomass porous carbons derived from banana peel waste as sustainable anodes for lithium-ion batteries. *Materials*. 2021 Oct 1;14(20).
159. Sun Y, Shi XL, Yang YL, Suo G, Zhang L, Lu S, Chen ZG. Biomass-derived carbon for high-performance batteries: from structure to properties. *Advanced Functional Materials*. 2022 Jun;32(24):2201584.

160. Molaiyan P, Dos Reis GS, Karuppiyah D, Subramaniyam CM, Garcia-Alvarado F, Lassi U. Recent progress in biomass-derived carbon materials for Li-ion and Na-ion batteries—A review. *Batteries*. 2023 Feb 7;9(2):116.
161. Yudha CS, Hutama AP, Gustiana HS, Suci WG, Al-Fuady MI. An Efficient Nypa Fiber Waste Conversion to Activated Carbon for Li-ion Battery Anode Material. 2024;11.
162. Nuriskasari I, Syahrial AZ, Ivandini TA, Sumboja A, Priyono B, Yan Q, Destyorini F, Priyono S. Synthesis of graphitic carbon from empty palm oil fruit bunches through single-step graphitization process using K₂FeO₄-KOH catalyst as lithium ion battery anode. *Results in Engineering*. 2024 Dec 1;24:103273.
163. Onfray C, Thiam A. Biomass-derived carbon-based electrodes for electrochemical sensing: a review. *Micromachines*. 2023 Aug 29;14(9):1688.
164. Moradian JM, Wang S, Ali A, Liu J, Mi J, Wang H. Biomass-derived carbon anode for high-performance microbial fuel cells. *Catalysts*. 2022 Aug 13;12(8):894.
165. Vinod A, Pulikkalparambil H, Jagadeesh P, Rangappa SM, Siengchin S. Recent advancements in lignocellulose biomass-based carbon fiber: Synthesis, properties, and applications. *Heliyon*. 2023 Mar 1;9(3).
166. Wang Q, Luo B, Wang Z, Hu Y, Du M. Pore Engineering in Biomass-Derived Carbon Materials for Enhanced Energy, Catalysis, and Environmental Applications. *Molecules*. 2024 Oct 31;29(21):5172.
167. Mehmandoust M, Li G, Erk N. Biomass-derived carbon materials as an emerging platform for advanced electrochemical sensors: recent advances and future perspectives. *Industrial & Engineering Chemistry Research*. 2022 Dec 27;62(11):4628-35.
168. Terbouche A, Boulahia S, Mecerli S, Ait-Ramdane-Terbouche C, Belkhalifa H, Guerniche D, Sehailia M, Bachari K, Mezaoui D, Hauchard D. A novel hybrid carbon materials-modified electrochemical sensor used for detection of gallic acid. *Measurement*. 2022 Jan 1;187:110369.
169. Malode SJ, Bilagi S, Shetti NP. Synthesis of biowaste-derived nanostructured material for the nanomolar detection of glucose: Biological sample analysis. *Journal of Pharmaceutical and Biomedical Analysis Open*. 2024 Jun 1;3:100026.
170. Xie A, Du J, Zhang J, Xiong Z, Shao F, Luo S. A High-Performance Nonenzymatic Urea Sensor Based on Graphene-NiO-Polyaniline. *J Electrochem Soc*. 2019;166(6):B456–63.
171. Kumar V, Kaur I, Arora S, Mehla R, Vellingiri K, Kim KH. Graphene nanoplatelet/graphitized nanodiamond-based nanocomposite for mediator-free electrochemical sensing of urea. *Food chemistry*. 2020 Jan 15;303:125375.
172. Babitha KB, Soorya PS, Peer Mohamed A, Rakhi RB, Ananthakumar S. Development of ZnO@rGO nanocomposites for the enzyme free electrochemical detection of urea and glucose. *Mater Adv*. 2020;1(6):1939–51.
173. Naik TS, Saravanan S, Saravana KS, Pratiush U, Ramamurthy PC. A non-enzymatic urea sensor based on the nickel sulfide/graphene oxide modified glassy carbon electrode. *Materials Chemistry and Physics*. 2020 Apr 15;245:122798.

Chapter **2**

EXPERIMENTAL TECHNIQUES

Experimental Techniques

This chapter describes the procedure for synthesising activated carbon (AC) derived from various biomass sources and the methods used for material characterisation and electrochemical analysis. Characterising and assessing the electrochemical performance of the prepared AC samples is essential for evaluating their suitability for use in different electrochemical systems. Typically, characterisation of the electrode materials includes (i) Physicochemical characterisations to identify surface and structural morphology and (ii) the electrochemical performance of electrode material for various applications using different electrochemical characterisation techniques. Additionally, this chapter provides a comprehensive overview of techniques used to fabricate various electrochemical systems.

2.1 Materials

2.1.1 Selection of precursors for AC synthesis

2.1.1.1 *Anacardium occidentale* (Seed shell waste)

Cashew (*Anacardium occidentale*) is one of India's most important and widely cultivated crops. As the leading producer and processor of cashews globally, India plays a crucial role in the international market. The cultivation and processing of cashews are essential for the country's agricultural economy, providing significant employment and economic benefits, especially in Kerala, where approximately 50% of India's cashew processing units are located. Most of these processing units operate as small-scale or cottage industries.(1)

When processed, cashew nuts yield about 35-40% kernel and 55-65% shell, these shells are often discarded as waste. However, the cashew nutshell (CNS) has a unique soft honeycomb matrix structure, giving it a porous nature. The high porosity and large specific surface area of CNS make it a suitable candidate for conversion into AC. Additionally, cashew nut shells contain natural polymers: cellulose (11.50%), hemicellulose (7.35%), and lignin (7.45%), which contribute to improving the surface area of the AC produced from them. Furthermore, utilising CNS waste to create AC

can significantly reduce the environmental impact associated with these cottage industries.(2)

This approach provides an effective means of managing and recycling waste, contributing to pollution reduction and sustainability. Converting CNS waste into AC represents a sustainable and economically beneficial solution for managing agricultural waste in India's cashew processing industry. It can help mitigate environmental pollution, create additional revenue streams, and promote the sustainable development of small-scale and cottage industries.(3) Figure 2.1 shows the cashew nut apple and the bisection of CNS.

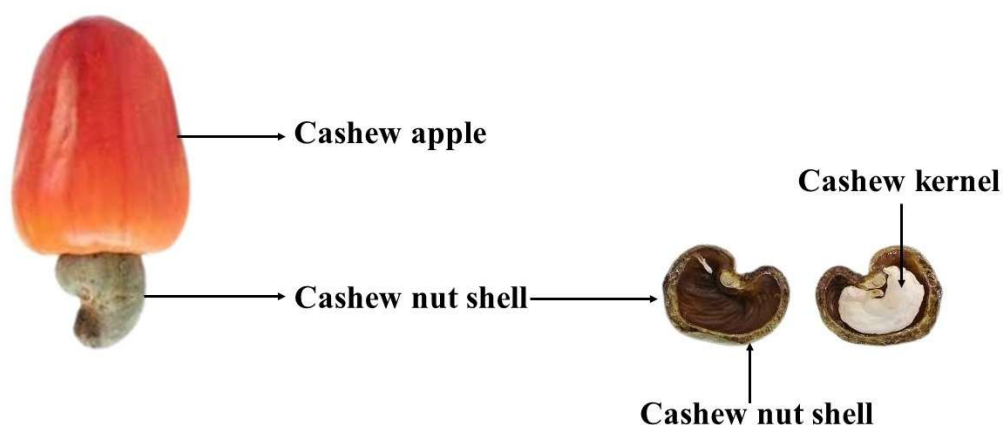


Figure 2.1 Cashew apple and cashew nut shell

CNS collected from local markets in Kerala, India was used as the precursor for the preparation of AC. The collected shell waste was washed thoroughly with distilled water to remove solid impurities and any residual organic materials. These shells were then dried and crushed into small pieces before initiating the synthesis of AC.

2.1.1.2 Swietenia mahagoni (Fruit shell waste)

Mahogany (*Swietenia mahagoni*) is a typical evergreen tree found in different regions of India. These trees offer numerous therapeutic benefits and economic advantages. Additionally, mahogany is renowned for its high-quality timber.(4) The fruit of the mahogany tree is a woody, grey-brown capsule that measures 5 to 10 cm in length and 3 to 6 cm in width. These capsules are filled with winged seeds and take

approximately 10 to 11 months to mature.(5) The structure of mahogany fruits and their components are illustrated in Figure 2.2.

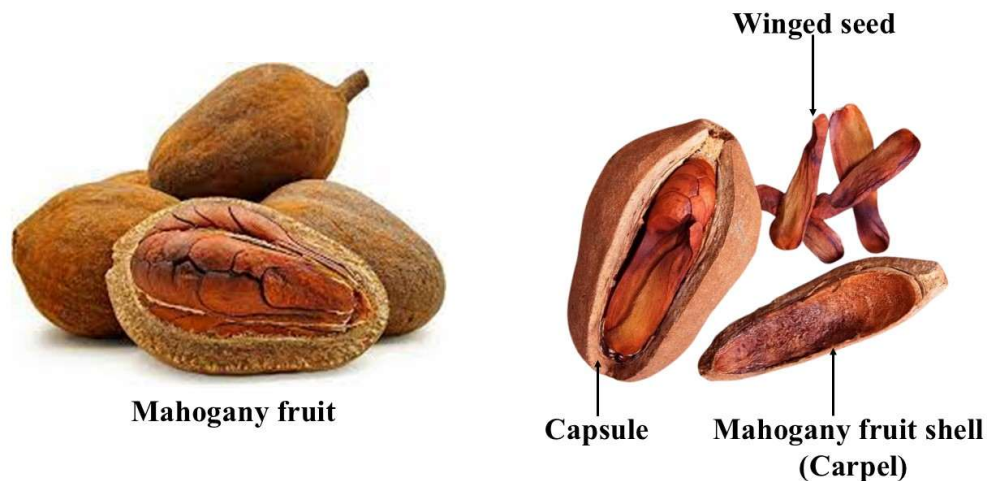


Figure 2.2 Mahogany fruit and fruit shell (husk)

As the ripe mahogany fruits explode, the carpels (fruit shells) drop off, releasing their seeds. These mahogany fruit shells (MFS) are often considered as waste and pose a significant environmental threat. Currently, there is no effective method for their disposal, and they are commonly burned, which contributes to air pollution. This degradation of MFS presents a considerable challenge for sustainable environmental practices.(6)

However, the lignocellulosic composition of MFS, which contains 75.61% holocellulose (including cellulose and hemicellulose) and 13.54% lignin, is advantageous for producing a well-developed porous AC. Additionally, the high cellulose content in MFS enhances pore distribution and surface area. Highly porous MFS-based AC has a wide range of applications, including serving as an effective adsorbent for water remediation and biodiesel production. The use of MFS as a precursor for preparing AC is a sustainable attempt to address the effective disposal of MFS waste.(7,8)

MFS is collected from the campus of the Centre for Materials for Electronics Technology (C-MET), Thrissur, Kerala, India. The collected MFS is thoroughly

washed with distilled water to remove any solid residues and is then properly dried. Afterward, it is crushed to a desired size of around 4-6 mm before initiating the preparation of AC.

2.1.1.3 *Myristica fragrans* Houtt. (Seed shell waste)

Nutmeg is a spice derived from the seed of the *Myristica fragrans* tree, which is native to several islands in Southeast Asia. This tree is a large, leafy evergreen plant. The fruit of nutmeg has a shape similar to an apricot, as the fruit matures, it splits into two parts. The nutmeg fruit contains both nutmeg and mace.(9) Nutmeg refers to the seed kernel inside the fruit, which is about the size of a plum, while mace is the reddish aril that surrounds the seed. Nutmeg is well known for its warm, sweet, and slightly nutty flavour. It has been used in culinary and medicinal applications for centuries. Whole nutmeg seeds have a hard, brown outer shell that needs to be grated or ground before use.(10)

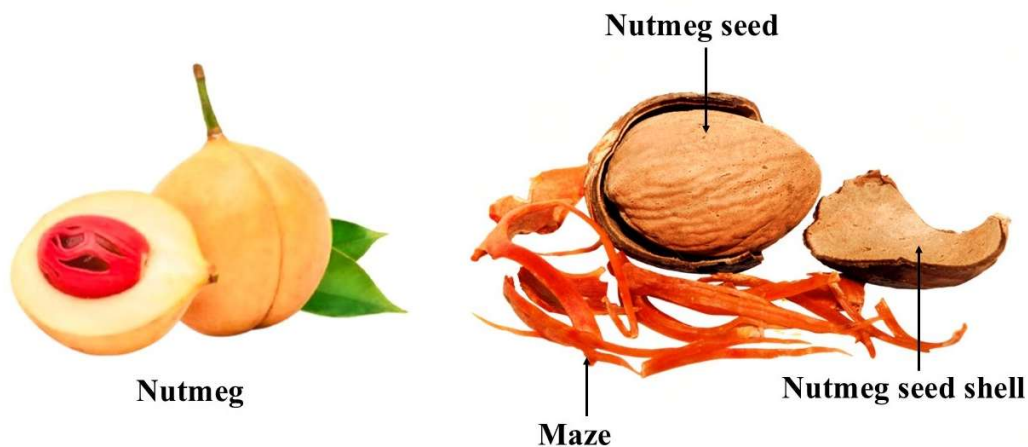


Figure 2.3 Nutmeg fruit and seed

India is a leading exporter of nutmeg, which holds significant economic value. Most of these exporting companies are located in Kerala. These industries primarily export nutmeg seeds and their mace, while the leftover shells from the shelling process are often regarded as waste. The disposal of these nutmeg shells (NMS) has become a significant challenge for these companies. Without an effective disposal strategy, the shells are often burned raising environmental concerns.(11) However, these shells contain a high lignin content, accounting for 50–59% of their total dry weight, along

with cellulose (11–28%) and hemicellulose (9–16%). This specific composition can lead to a well-developed pore distribution in AC produced from these shells. As a result, these waste shells can be utilised to produce highly porous AC with a large surface area, suitable for various applications.(12)

NMS waste is collected from exporting companies in Ernakulam, Kerala, after the kernels have been removed. The shells are thoroughly cleaned and washed to eliminate solid residues. After proper drying, these shells are crushed into a powdered form, which is then used for the preparation of AC.

2.1.2 Chemicals used in the preparation of AC and other applications

All chemicals used for the preparation of AC were pure and of analytical grade. The chemicals listed below were utilised in this study without any further purification.

Table 2.1 List of chemicals used in this study

Chemical Name	Manufacturer
Potassium hydroxide (KOH)	Merck Specialities Private Ltd., India
Hydrochloric acid (HCl)	Merck Specialities Private Ltd., India
Polyvinylidene fluoride (PVDF)	Sigma Aldrich Co, USA
Carbon black	Thermo Fisher Scientific Pvt. Ltd., India
N-methyl pyrrolidone (NMP)	Thermo Fisher Scientific Pvt. Ltd., India
Sodium sulphate (Na ₂ SO ₄)	Merck Life Science Private Ltd., India
Sodium nitrate (NaNO ₃)	Merck Specialities Private Ltd., India
Polyvinyl alcohol (PVA)	Hi Media Laboratories Private Ltd., India
Lithium hexafluorophosphate (LiPF ₆)	Matlabs, India
Nickel nitrate (Ni(NO ₃) ₂)	Sigma-Aldrich Co., USA.

Sodium hydroxide (NaOH)	Merck Specialties Private Ltd., India.
Urea (CH ₄ N ₂ O)	Merck Specialties Private Ltd., India.
Uric acid (C ₅ H ₄ N ₄ O ₃)	Nice Chemicals Private Ltd., India.
Ascorbic acid	Sigma-Aldrich Co., USA.
Glucose	Merck Specialties Private Ltd., India.

2.2 Preparation of AC from biomass precursor

The synthesis of biomass-derived AC (BDAC) using KOH as a chemical activating agent can be carried out in a single step. Figure 2.4 schematically represents the preparation method for the synthesis of BDAC. This process involves the impregnation of carbonaceous material in KOH, followed by carbonisation at relatively low temperatures. Selecting the appropriate carbon sources, such as nutshells, wood, or other biomass materials, is crucial for producing BDAC with desirable characteristics.(13)

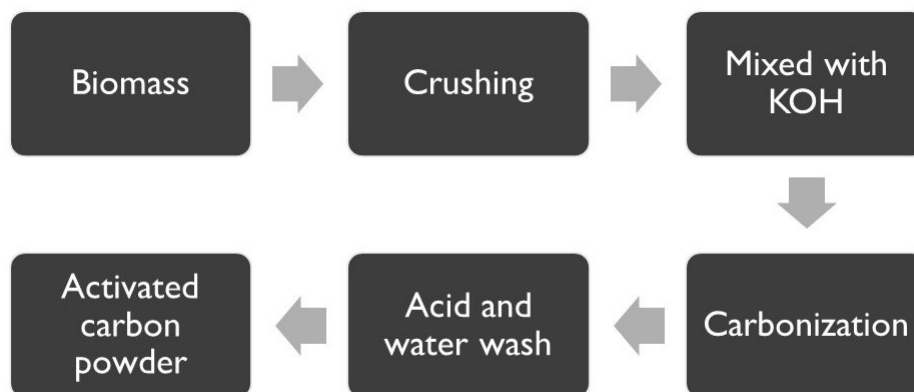


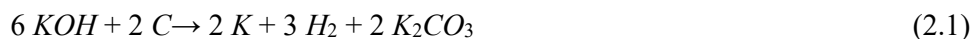
Figure 2.4 Preparation of AC from biomass waste

The carbonaceous material was first crushed to a suitable size and then mixed with a KOH impregnation solution, which was prepared by dissolving the required amount of KOH in distilled water. To ensure thorough impregnation, the mixture was continuously stirred, allowing the KOH solution to effectively penetrate the carbon

structure.(13,14) The impregnated material was then dried overnight at ambient temperature using an air oven and subjected to carbonisation at high temperatures ranging from 500°C to 800°C in an inert atmosphere. The use of inert gas such as nitrogen or argon is crucial during chemical activation, as it helps maintain the stability of activating agents, prevents the combustion of carbon material, improves yield, and ensures the development of a well-defined pore structure.(15)

The heating process induces chemical reactions between the carbon and KOH, leading to the formation of pores and the production of AC. After the activation process, the AC is washed to remove residual impurities and excess activating agents. This washing can be carried out using an acidic solution, followed by rinsing with distilled water. The filtered AC is then dried to remove moisture. The samples were then crushed, milled, or sieved to obtain the desired particle size suitable for specific applications.(16)

The overall mechanism involved in the KOH activation of biomass waste is described using Equations 2.1 to 2.4. The temperature during this preparation method significantly influences pore distribution present in the prepared BDAC. Initially, KOH begins to melt and creates a solid-liquid interface at a temperature of 360°C. This facilitates subsequent reactions, including the oxidation of carbon by KOH that produces metallic K, H₂, and K₂CO₃, as well as the reaction between C and K₂CO₃ at higher temperatures.(17)



The chemical etching by KOH and K₂CO₃ creates a porous structure in AC. Additionally, the release of gases such as H₂, CO₂, and CO contributes to the porous structures in BDAC. The physical intercalation of metallic K also enhances the number of micropores in BDAC and at elevated temperatures, the oxygen-containing functional

groups are removed. KOH activation significantly enhances the creation of a uniform and well-developed microporous structure.(18)

In the present study, the synthesis of BDAC was carried out using KOH chemical activation. The crushed precursor was washed and dried to remove solid impurities. The dried carbonaceous precursor was then impregnated with KOH at different activation ratios, specifically weight ratios of biomass waste to KOH of 1:1, 1:2, and 1:3. This impregnation was achieved through mechanical stirring for 2 hours. The activated samples were subsequently carbonised for 1 hour in a tubular furnace under a continuous supply of argon (99.99%) at a flow rate of 1 L/min. The carbonisation took place at various temperatures (500 °C, 600 °C, 700 °C, and 800 °C) at a heating rate of 5 °C/min. After carbonisation, the materials were washed with 0.1 M HCl and dried overnight at a temperature of 100 °C. The AC samples were then stored as fine powders which is further utilised for different characterisation studies and for application in various electrochemical systems. The activation ratio and carbonisation temperature were optimised based on the material and electrochemical characterisations discussed in the subsequent sections.(16,19)

2.3 Synthesis of AC/NiO composite

The AC/NiO composite is prepared using the co-precipitation method, as illustrated in Figure 2.5. For this study, AC derived from nutmeg shell waste was utilised.

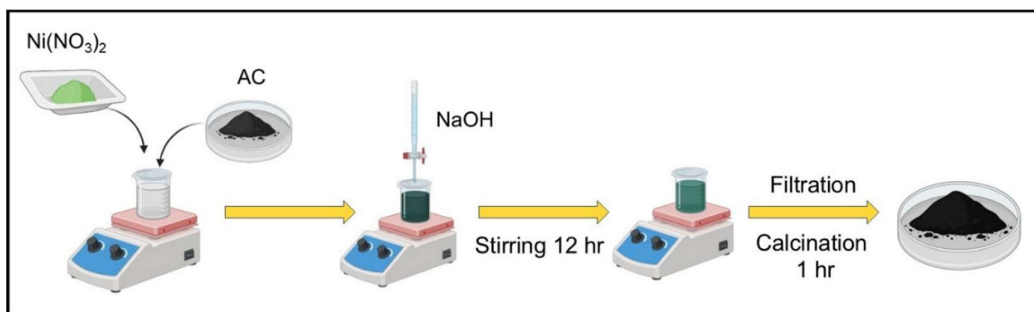


Figure 2.5 Schematic of synthesis of AC-NiO composite materials

This technique ensures a uniform distribution of NiO nanoparticles on the surface of AC. This enhances the surface characteristics, including the area and the number of active sites, which improves the reactivity and overall performance of the electrode

material. Furthermore, the process is scalable, cost-effective, and straightforward, making it suitable for large-scale applications.(20)

Initially, AC and $\text{Ni}(\text{NO}_3)_2$ (in water) were mixed in a beaker to form a homogeneous dispersion. NaOH is then added in a weight ratio of $\text{Ni}(\text{NO}_3)_2$ to NaOH of 1:2. This mixture is washed, filtered and dried in an air oven at 120 °C. Following this, the samples are subjected to calcination in a tubular furnace at 300 °C, 400 °C, and 500 °C for one hour with continuous argon (Ar, 99.99%) supply.(21) The as-prepared AC/NiO composites were then grounded into fine powder and used for further studies. Various AC/NiO composites were prepared with AC: NiO ratios of 70:30, 80:20, and 90:10.

2.4 Physicochemical characterisation of materials

The characterisation techniques used for structural and surface studies are X-ray diffraction (XRD) analysis, scanning electron microscopy (SEM) analysis, Raman spectroscopy, N_2 adsorption-desorption isotherm, Brunauer-Emmett-Teller (BET) surface area analysis, Barrett-Joyner-Halenda (BJH) method, t-plot method, Fourier transform infrared spectroscopy (FTIR), thermogravimetry/differential thermal analyses (TG/DTA), X-ray photoelectron spectroscopy (XPS) and transmission electron microscopy (TEM).

2.4.1 X-ray diffraction (XRD)

XRD is an essential analytical technique used to investigate the crystallographic structure of materials. This method depends on the interaction between X-rays and the crystal lattice, which results in constructive interference of the diffracted X-rays. XRD can also be employed to analyse non-crystalline or amorphous materials.(22) While these materials do not generate sharp diffraction peaks, XRD can still provide insights into short-range ordering and average atomic distances. The relationship between angles and intensities of diffracted X-rays provides insights into the structure, composition, and properties of the material under study.(23)

AC generally shows an amorphous structure, but it also contains regions that display graphitic characteristics. XRD can identify these graphitic structures by

detecting characteristic diffraction peaks corresponding to (002) diffraction plane of graphite around $2\theta \approx 26^\circ$. Additionally, the (100) graphitic plane is observed from peaks around 42° . The broadening of diffraction peaks is usually related to the disorder or amorphousness in AC.(17) Additionally, XRD can measure the interlayer spacing in graphitic regions, which affects the ion intercalation properties essential for the performance of electrochemical capacitors and batteries. XRD can identify and quantify the phases present in AC composites or doped materials. This information is vital for understanding how different components contribute to the electrochemical behaviour of AC.(18) Therefore, XRD provides comprehensive insights into the structural properties, including crystallinity, graphitic content, crystallite size, degree of disorder, and phase composition. These results are essential for optimising the material's performance in electrochemical applications.(24) Figure 2.6 illustrates the instrumentation setup of XRD.

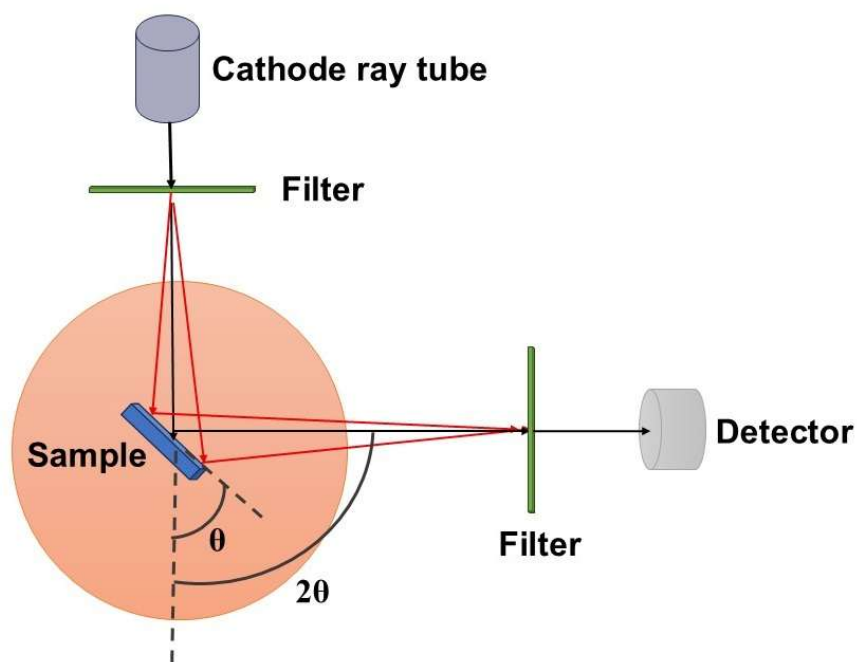


Figure 2.6 XRD instrumentation setup

In the present study, the prepared materials were subjected to XRD analysis using Rigaku Ultima IV (Rigaku Corp., Japan), which utilises $\text{CuK}\alpha$ radiation with a wavelength of 0.15418 nm. The X-ray generator was operating at 40kV and 30mA. The angle 2θ was measured over a range of 2° to 90° , with a scanning speed of 2° per minute.

2.4.2 Scanning electron microscopy (SEM)

SEM is a powerful technique that provides high-resolution images that reveal the detailed surface features of electrode materials, such as surface morphology, porosity, particle size, surface texture, elemental composition, and defects. These insights are essential for understanding how the material interacts with electrolytes, which is crucial for enhancing its electrochemical performance.⁽²⁵⁾ Figure 2.7 illustrates the schematic of a standard SEM analysis.

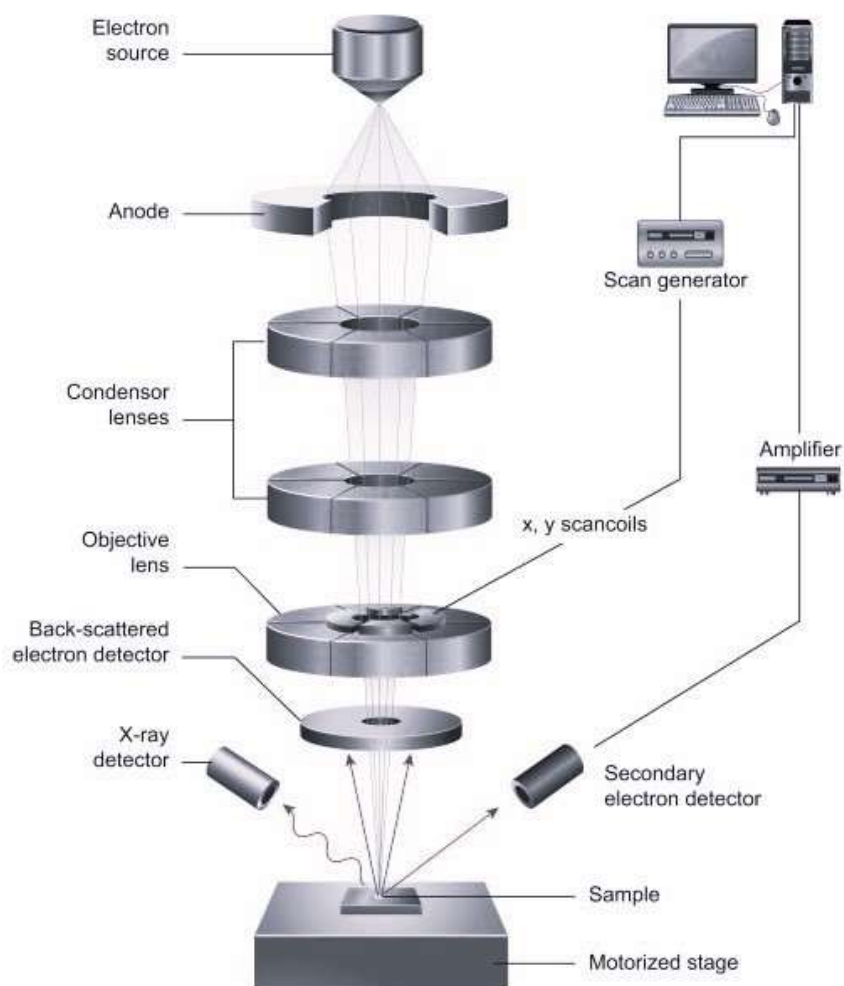


Figure 2.7 Schematic diagram of Scanning Electron Microscope

SEM can visualise pore distribution in the material surface that facilitates ion transport pathways, which are vital for charge storage and transfer processes. Energy-dispersive X-ray Spectroscopy (EDAX) along with SEM is useful in understanding the

elemental composition and spatial distribution of elements within the electrode material. This capability is particularly beneficial for identifying and quantifying dopants, binders, and other additives that may alter the electrochemical properties.(26)

The study utilises a Carl Zeiss EVO18 SEM (Carl Zeiss Microscopy Ltd., Germany) equipped with an energy-dispersive X-ray spectrometer attachment, model EDAX, to analyse the surface morphology and elemental composition of the prepared samples. Before analysis, the samples were coated with a gold-palladium alloy using a Quorum sputter coater (model SC7620). This coating process was conducted at a current of 10 mA and a vacuum of 10^{-2} mbar for 150 seconds.

2.4.3 Raman spectroscopy

Raman Spectroscopy is a powerful analytical technique used to study detailed information about the molecular composition, structure, and interactions of materials. The technique relies on the inelastic scattering of monochromatic light, typically from a laser. Various carbon structures in materials, such as graphitic and amorphous carbon can be identified using Raman spectroscopy. The Raman spectrum of carbon materials shows two prominent peaks: D band (around 1350 cm^{-1}) and the G band (around 1580 cm^{-1}). The D band is associated with disordered or defective carbon structures, while the G band corresponds to graphitic or ordered carbon structures.(27)

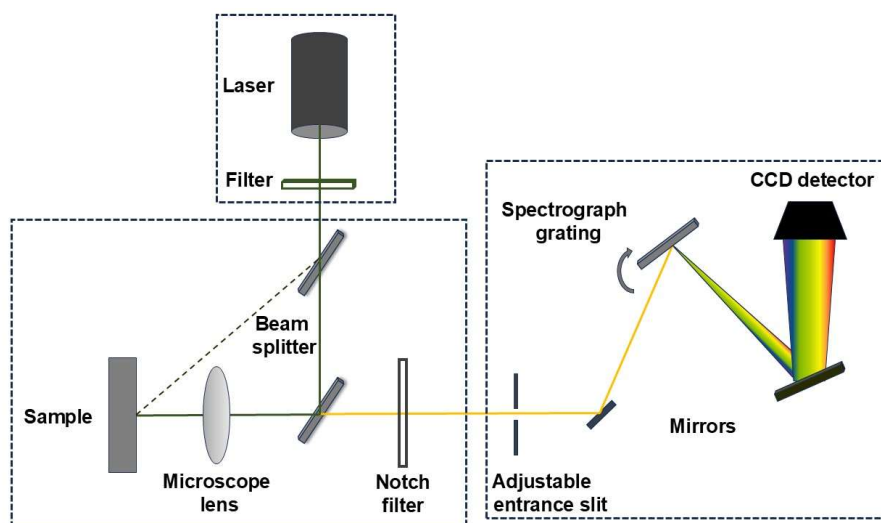


Figure 2.8 Raman spectrophotometer setup

The intensity ratio of these bands (I_D/I_G) is used to quantify the level of disorder and density of defects within the carbon structure. Additionally, Raman spectroscopy gives insights into the functional groups and chemical modifications present in the AC surface. Typically, smaller graphitic domains lead to broader and more intense D bands, while larger graphitic regions will exhibit more pronounced G bands. Raman spectroscopy can also reveal shifts in these bands, indicating mechanical stability of the electrode material under various electrochemical conditions. This information is essential for optimising the material's properties for specific electrochemical applications.(28) Figure 2.8 provides the instrumentation setup of a Raman spectrometer.

Raman spectroscopy for this study was conducted using a Renishaw InVia Reflex Raman spectrometer equipped with a 532 nm laser at room temperature. The Raman spectrometer identifies graphitic or disordered structures and helps determine the capabilities of AC-based electrode materials for applications in various electrochemical systems.

2.4.4 Surface area analysis

Surface area analysis is crucial in enhancing the adsorption capacity, catalytic activity, energy storage capabilities, and overall performance of electrode materials in various industrial and environmental applications. Understanding and controlling surface area ensures that AC meets the specific needs of efficient, diverse applications. Techniques such as nitrogen adsorption-desorption isotherm, BET method, BJH theory, and t-plot method are typically employed for identifying various pore structure parameters of AC.(29)

2.4.4.1 Nitrogen adsorption-desorption isotherm

Nitrogen adsorption-desorption isotherms are widely used in surface science to analyse pore structure and surface characteristics of various materials. The amount of nitrogen gas adsorbed onto the surface of a material at different relative pressures is measured to understand the surface area and pore distribution in the materials under study.(30)

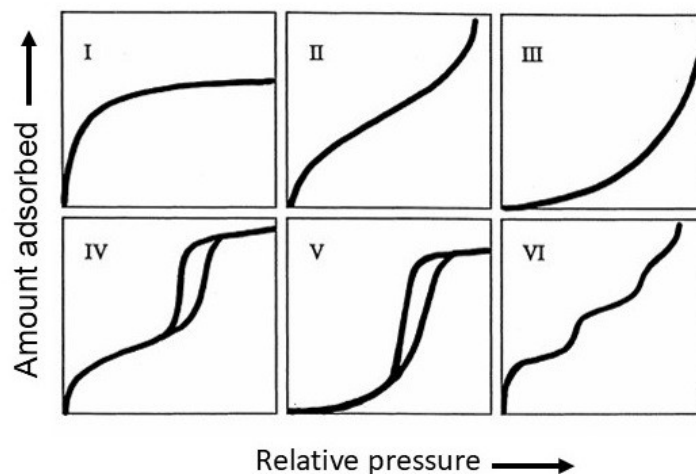


Figure 2.9 The IUPAC classification of adsorption isotherms

Nitrogen adsorption-desorption isotherms are obtained by exposing a sample to nitrogen gas at liquid nitrogen temperature (77 K) and measuring the amount of gas adsorbed as the pressure increases. After reaching a maximum pressure, the pressure is then decreased to measure desorption. The results are represented in the form of isotherm plots between the volume of nitrogen adsorbed (or desorbed) and the relative pressure (P/P_0), where P is the equilibrium pressure and P_0 is the saturation vapour pressure of nitrogen.(31)

According to IUPAC classifications, these isotherms (Figure 2.9) are classified into six, each associated with different pore structures. Type I or Langmuir Isotherm is a characteristic isotherm for microporous materials (pores < 2 nm). These isotherms show rapid initial adsorption at low P/P_0 followed by a plateau as the pores fill. In contrast, the type II isotherm shows a linear region at intermediate P/P_0 associated with the monolayer-multilayer adsorption corresponding to non-porous or macroporous materials. The type III isotherm with no distinct plateau, indicates continuous multilayer adsorption due to weak adsorbate-adsorbent interactions. The mesoporous materials usually exhibit a type IV isotherm with a hysteresis loop due to capillary condensation within the available mesopores (pores 2-50 nm). Type V isotherms are similar to type III but with a hysteresis loop, indicating weak adsorbate-adsorbent

interactions in mesoporous materials. Whereas, type VI isotherm is often seen in uniform non-porous surfaces suggesting stepwise multilayer adsorption.(30,32)

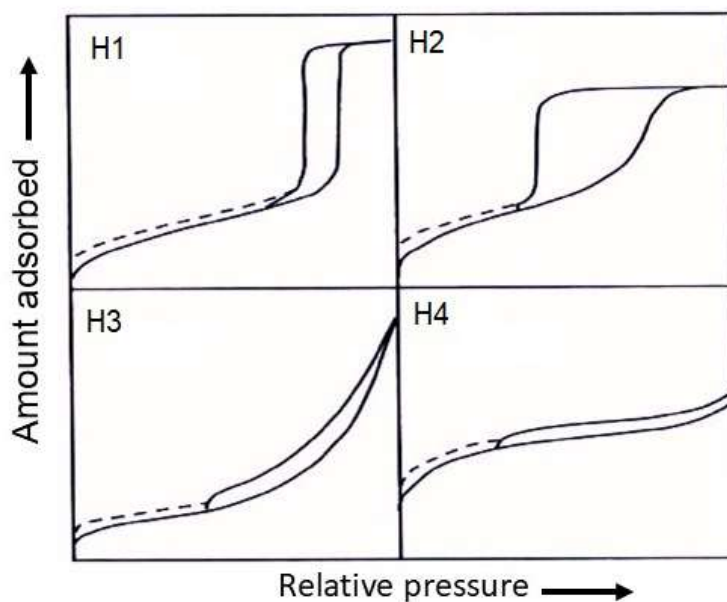


Figure 2.10 The four types of hysteresis loops classified by IUPAC

The hysteresis loop in isotherms indicates the presence of mesopores and provides information about the pore shape and connectivity of the material. These loops arise due to differences in adsorption and desorption pathways, generally, four types of hysteresis loops (H1, H2, H3, H4) are associated with different pore structures and adsorption mechanisms. Figure 2.10 displays the hysteresis loops classified by IUPAC. Type H1 hysteresis reflects a relatively narrow pore size distribution. They have sharp, nearly vertical adsorption and desorption branches usually associated with materials having uniform, cylindrical pores or well-defined mesopores.(33) A more complex loop with a steep adsorption branch and a more gradual desorption branch is ascribed to the type H2 hysteresis. These indicate complex pore systems, such as interconnected networks or pore-blocking mechanisms, are often found in materials with irregularly shaped pores or pore networks.(14) Additionally, type H3 has no distinct adsorption plateau and exhibits a nearly vertical desorption branch. These hysteresis loops are common for materials with non-rigid or layered structures representing slit-shaped pores or aggregates of plate-like particles. Similar to H3, the H4 type shows a more pronounced low-pressure hysteresis indicating narrow slit-like pores or microporous materials with limited mesoporosity.(13)

The N₂ adsorption-desorption isotherms provide information about the surface area, pore size distribution, and pore volume of the AC-based electrode materials, which are crucial for their performance in electrochemical systems. AC usually exhibits type I and type IV isotherms. These isotherms indicate the presence of micropores with a high surface area and mesoporous materials, respectively. AC often shows H4-type hysteresis loops in their isotherms, indicating the presence of slit-like pores or a combination of micropores and mesopores.(22)

2.4.4.2 Brunauer, Emmett, and Teller (BET) surface area analysis

The BET surface area analysis technique measures the specific surface area of porous materials by analysing the physical adsorption of gas molecules. It is extensively used as it offers detailed insights into surface properties. The BET theory describes monolayer adsorption, to multilayer adsorption. The theory assumes that gas molecules physically adsorb onto a solid in layers, with the first layer being adsorbed directly onto the solid surface and subsequent layers forming on top of it.(32) The BET equation derived from these assumptions is given by

$$\frac{1}{v \times \left(\frac{p_0}{p} - 1\right)} = \frac{c-1}{V_m c} \times \frac{p_0}{p} + \frac{1}{V_m c} \quad (2.5)$$

where v is the volume of adsorbed gas, p is the equilibrium pressure of the adsorbate, p_0 is the saturation pressure of the adsorbate, v_m is the volume of gas required to form a monolayer, and c is the BET constant, related to the energy of adsorption. The plot between $\frac{1}{v \times \left(\frac{p_0}{p} - 1\right)}$ and $\frac{p_0}{p}$ should yield a straight line, with slope S given by $S = \frac{c-1}{V_m c}$ and intercept I as $I = \frac{1}{V_m c}$. From these values, V_m and c can be determined. For greater accuracy, the BET equation is typically applied in the relative pressure range of 0.05 to 0.35.(23) The total surface area is calculated using the following equation:

$$A_{total} = V_m \times N_A \times s \quad (2.6)$$

Here N_A is Avogadro's number, s is the cross-sectional area of the adsorbate molecule (for nitrogen, it is typically 0.162 nm²), and V_m is the molar volume of the adsorbate gas at standard temperature and pressure.(14) For a sample of mass m , the specific surface area is given by the following equation,

$$A = \frac{A_{total}}{m} \quad (2.7)$$

2.4.4.3 Barrett-Joyner-Halenda (BJH) method

BJH method provides insights into the mesoporous structure by evaluating the volume of nitrogen adsorbed and desorbed at various relative pressures. The pore size distribution, pore volume, and surface area contributions of mesopores can be analysed using BJH theory. The BJH method is based on the Kelvin equation, which relates the pore radius to the pressure at which capillary condensation occurs. The calculation of pore size distribution is based on the desorption branch of the isotherm. As mesopores are very common in activated carbon, the BJH theory is frequently used for their study. The BJH method can also be applied to predict cumulative pore volume and average pore diameter.(13)

2.4.4.4 The t-plot method

The t-plot method is a classical technique used for distinguishing between micropore and mesopore volumes in porous materials. It also provides insights into the external surface area and total pore volume. The t-plot represents the volume of gas adsorbed (usually nitrogen) against the thickness of the adsorbed gas layer. The thickness is calculated using a reference isotherm, typically from a non-porous material, as a function of relative pressure. The slope and intercept of the linear portion of the t-plot provide information about the external surface area and micropore volume. The values of micropore volume, external surface area, and total pore volume can be estimated from the t-plot. Moreover, the linear region in the plot represents multilayer adsorption on the external surface and deviation from linearity indicates the filling of micropores. In this way, the t-plot method is a simple yet effective tool for analysing the microporous structure of materials like AC.(14)

In the present study, surface area analysis was carried out using a surface area analyser BELsorp MAX, BEL Japan Inc., Japan. The analysis gives insights into surface area, pore distribution, etc. During analysis, the materials are degassed to remove contaminants such as moisture and organic impurities that can affect adsorption measurements through heating the sample under a vacuum or in an inert gas flow. After degassing, the samples are exposed to a known quantity of adsorbate gas (usually

nitrogen) at liquid nitrogen temperature (77 K). The amount of gas adsorbed is measured at various relative pressures. These data are used for understanding the structure properties including pore distributions, surface area, and pore volume.

2.4.5 Fourier Transform Infrared Spectroscopy (FTIR)

FTIR is an essential technique for identifying various functional groups available in materials under study. This method relies on the differences in vibrational energy associated with the fundamental vibrational modes of different chemical bonds. The spectra are typically recorded within the fingerprint region, which ranges from 600 to 1900 cm^{-1} . Figure 2.11 illustrates a typical FTIR spectrometer with a beam splitter, a fixed mirror, and a moving mirror as key components. FTIR also highlights the dipole moment and force constants of various fundamental vibrational modes of the molecules.(34)

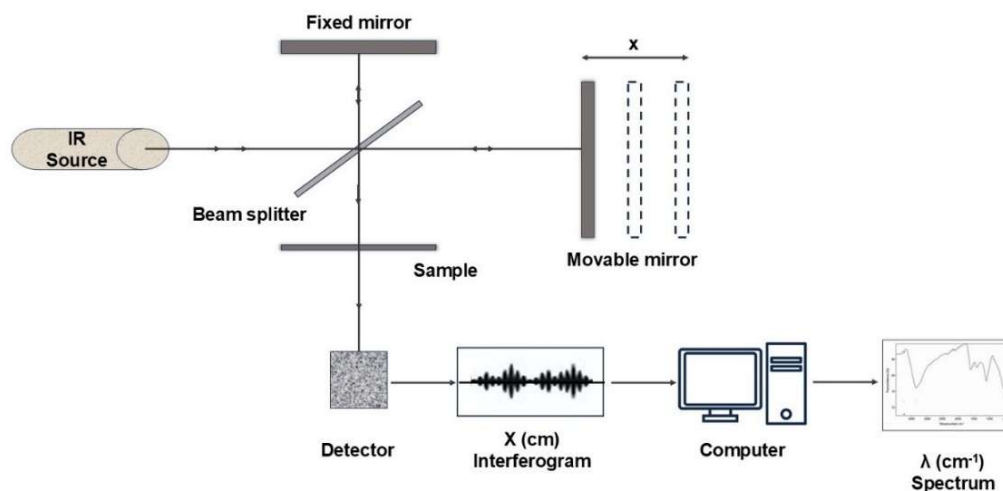


Figure 2.11 Instrumentation of FTIR

In the present study, all FTIR analyses of all samples were carried out using the KBr pellet technique with an FTIR spectrometer (IR Spirit-T, Shimadzu, US). The analysis was carried out by mixing materials and KBr in a 5:95 weight ratio. The FTIR spectra confirm the presence of diverse functional groups corresponding to characteristic vibrational frequencies.

2.4.6 Thermogravimetry and Differential Thermal Analyses (TG/DTA)

TG and DTA are crucial techniques for analysing the thermal behaviour of biomass precursors of AC. These methods provide valuable insights into the thermal stability, decomposition processes, and phase transitions in the precursors, which are essential for optimising the activation process and enhancing the properties of the resulting AC.(35)

TG measures the change in mass of a biomass sample as a function of temperature or time under a controlled atmosphere (e.g., inert, oxidative). This technique helps identify the temperatures at which different components in the biomass decompose, volatilise, or oxidise. DTA measures the temperature difference between a biomass sample and an inert reference material. It detects endothermic and exothermic events, providing insights into the thermal transitions and reactions occurring within the sample.(36) The typical TG/DTA equipment is displayed in Figure 2.12.

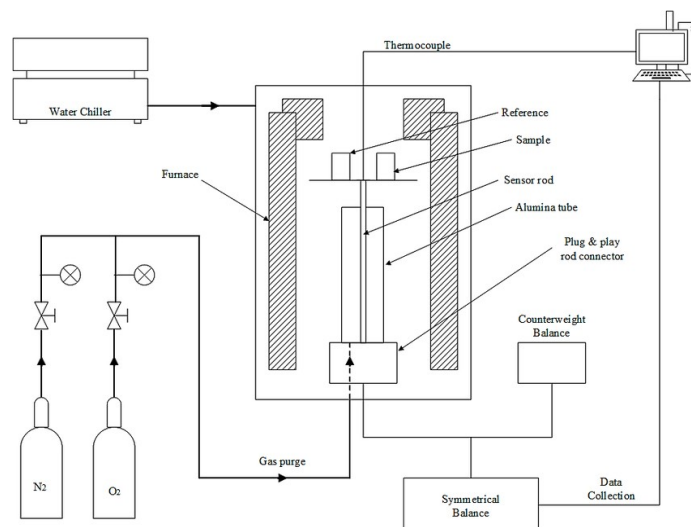


Figure 2.12 Schematic diagram of a typical TG/DTA equipment

The mass loss during the TG analysis suggests the decomposition temperatures of various biomass components such as hemicellulose, cellulose, and lignin. DTA complements TGA by indicating whether the decomposition processes are endothermic or exothermic. Figure 2.13 represents a typical TGA/DTA curve for biomass. The initial mass loss at lower temperatures (up to $\sim 150^{\circ}\text{C}$) is often attributed to the evaporation of moisture and low-boiling-point volatiles.(37) Quantifying this loss is

essential for understanding the drying requirements of the biomass before activation. Typically, hemicellulose decomposes between 200-300°C, cellulose between 300-400°C, and lignin over a broader range (200-500°C) due to its complex structure. In addition, the final mass remaining after high-temperature treatment (above 600°C) indicates the yield of char, which is the precursor for AC. This helps in evaluating the efficiency of carbonisation.(36)

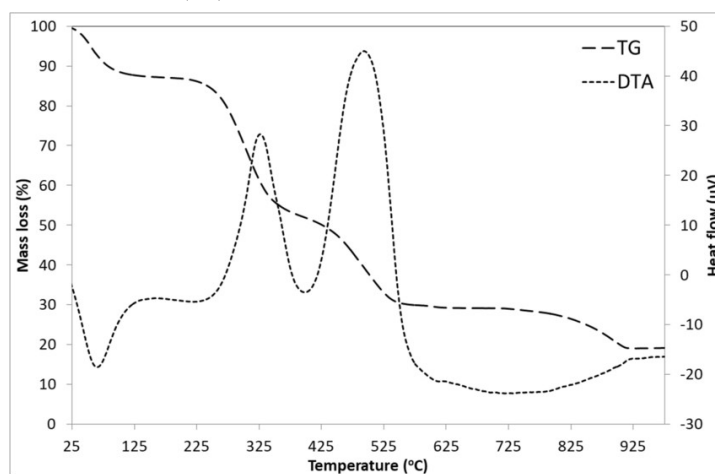


Figure 2.13 Typical TG/DTA curve for biomass (37)

In the current work, a thermogravimetric analyser, SDT Q600 (TA instruments, USA) was employed for TG/DTA analysis to understand the thermal degradation behaviour of pristine biomass precursors. The analysis was carried out under N₂ atmosphere for a temperature range of 30-1000 °C at a heating rate of 10 °C min⁻¹, and the sample loading was around 5-20 mg. The TG/DTA curves help to choose carbonisation temperatures appropriately.

2.4.7 X-ray photoelectron spectroscopy (XPS)

XPS is a powerful and surface-sensitive quantitative spectroscopic technique. It provides valuable information about the elemental composition, chemical states, empirical formulas, and electronic structures of materials. The technique operates by irradiating a material with X-rays, which causes the ejection of electrons. Figure 2.14 represents a schematic diagram of an X-ray photoelectron spectroscope. By measuring the energy of these emitted electrons, detailed information about the atoms from which they originated can be obtained. XPS is commonly used for analysing surface layers and thin film coatings of various materials.(38)

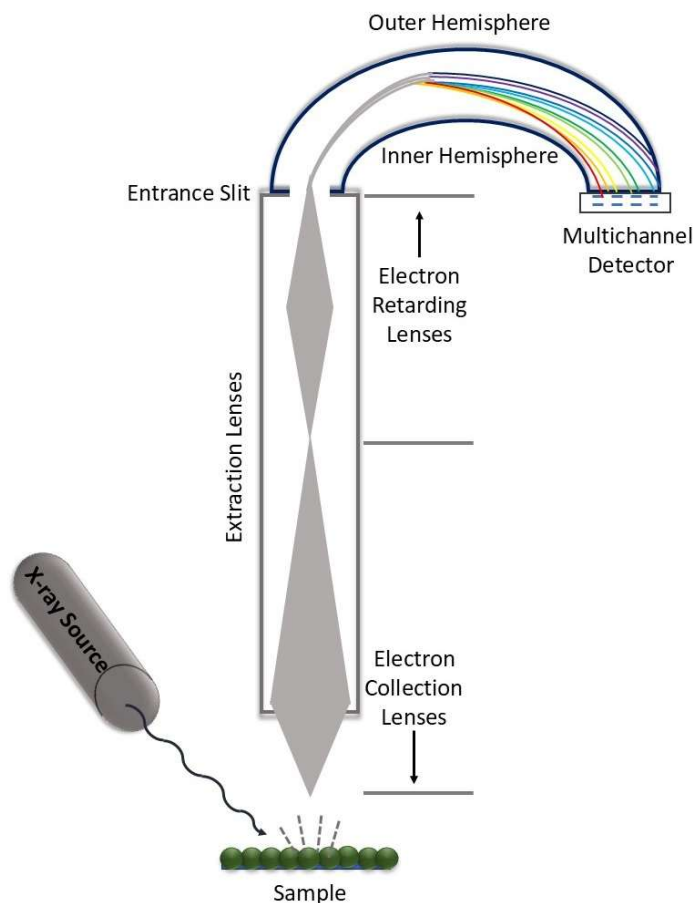


Figure 2.14 Schematic diagram of an X-ray photoelectron spectroscope

Each element has distinctive binding energy values and the changes in binding energy can reveal information about their oxidation states and chemical bonding. XPS usually analyses the top 5 to 10 nm of a material and determines the atomic concentration of elements by integrating the areas under the peaks. This technique enables elemental quantification with an accuracy of $\pm 10\%$.(39)

The C 1s and O 1s spectra of AC samples give valuable insights into the structural properties that improve their feasibility for various applications in electrochemical systems. The XPS analysis of the AC/NiO composite material provides information about the oxidation state of nickel in NiO (Ni^{2+} vs. Ni^{3+}). This analysis also confirms the presence of C–C, C–O, and C=O bonds and identifies surface changes after urea adsorption. In this study, the PHI Versaprobe III X-ray photoelectron spectrometer (ULVAC-PHI Inc., USA), which is equipped with a micro-focused (200

μm , 15 kV) monochromatic Al-K α X-ray source ($h\nu = 1486.6$ eV), was used to explore the surface elemental composition and chemical states of the prepared materials.

2.4.8 Transmission electron microscopy (TEM)

TEM is widely used to provide ultra-high-resolution imaging, structural analysis, and elemental characterisation at the nanoscale and atomic level. TEM is useful for understanding various characteristics of materials, including their shape, size, porosity, and defect structures, such as dislocations, grain boundaries, and stacking faults.⁽³⁷⁾ These images provide visual clarity related to the pore distribution in the materials under study. These observations can back up the predictions of surface area analysis to a great extent. TEM images of the samples in this research were obtained using HRTEM (Jeol/JEM 2100, USA) at an accelerating voltage of 200 kV.

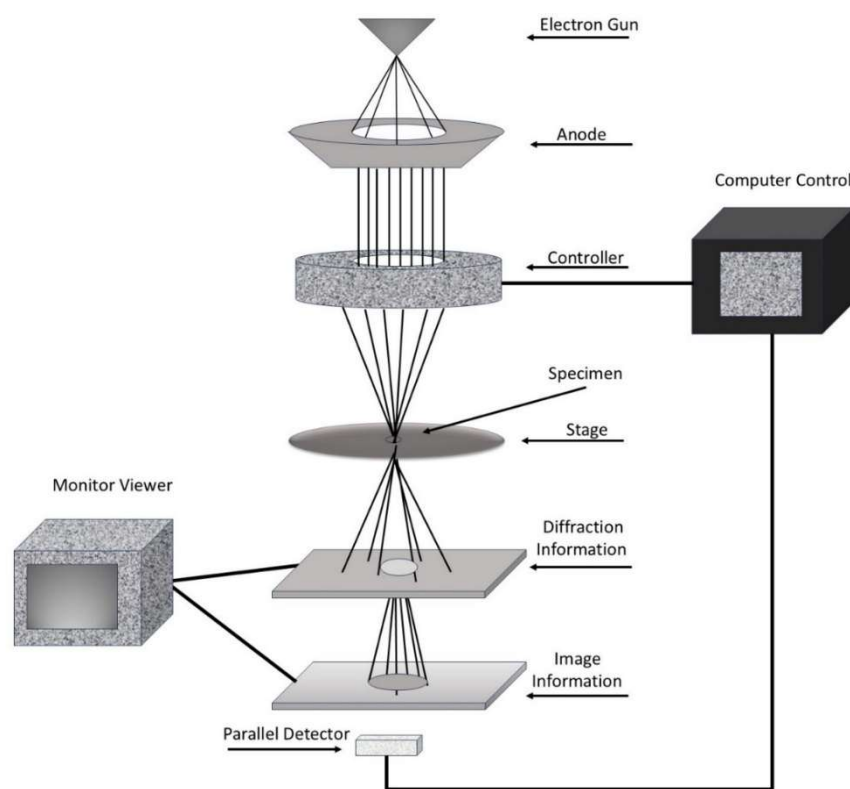


Figure 2.15 Schematic diagram of a transmission electron microscope

All prepared BDACs and composite materials were primarily examined using these characterisation techniques to gather information on their morphology, structure, pore distribution, particle size, crystallinity, etc.

2.5 Electrode preparation

2.5.1 Modified working electrode (WE) in a three-electrode system

Modified glassy carbon electrodes (MGCEs) were utilised for three electrode analyses of prepared BDAC materials. A uniform slurry was prepared using BDAC, PVDF as the binder, and carbon black as the conductive additive mixed in a weight ratio of 8:1:1 in the solvent NMP. Ultrasonic vibration was used to achieve a homogeneous mixture. For the electrochemical studies using a three-electrode configuration, 2 μL of the slurry was applied to the WE and dried for 5 minutes under an infrared lamp.

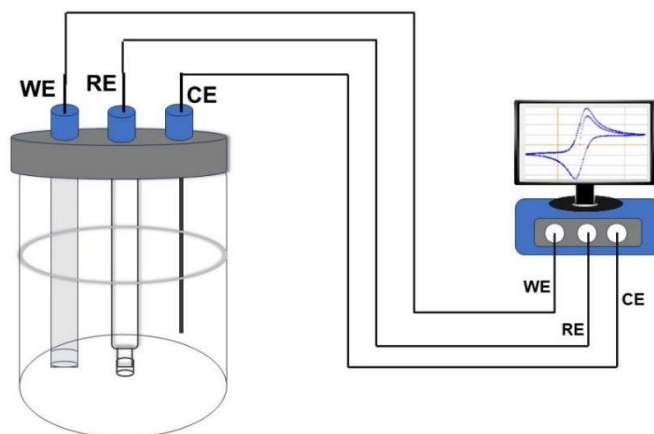


Figure 2.16 Three-electrode setup for the electrochemical analysis

The mass loading of the active electrode material was around 2-4 mg cm^{-2} .(19) Figure 2.16 displays the three-electrode configuration used for electrochemical analysis.

2.5.2 Supercapacitor electrode

A homogeneous slurry was prepared by mixing prepared BDAC material, carbon black, and PVDF at a weight ratio of 8:1:1 in the solvent NMP using a magnetic stirrer. This slurry was then coated onto an aluminium current collector with a thickness of 30 μm . The tape-casting method was employed to create uniformly coated electrodes, with the doctor blade gap optimised to 350 μm , resulting in casted electrodes with a thickness of 80 μm . After casting, the electrodes were dried in a

vacuum oven at 150 °C. The mass loading achieved was between 2 and 4 mg cm⁻². Finally, the prepared electrodes were slitted or punched into the desired dimensions and shapes.(16)

2.5.3 Anode in Li-ion Batteries

A homogeneous slurry consisting of ACNM, PVDF, and carbon black in an 80:10:10 weight ratio, using NMP as the solvent. For the fabrication of the anodes, a copper foil with a thickness of 40 μm was used as the current collector. The tape-casting method was employed to fabricate uniformly coated anodes. The casted electrodes were dried in a vacuum oven at 150 °C to remove excess solvents. The dried electrodes were punched into discs with a diameter of 20 mm. The mass loading of the active material was 2 mg cm⁻². These punched anodes were subsequently used for the assembly of anode half-cells.

2.5.4 Electrode for electrochemical sensors

An MGCE was used to evaluate the suitability of as-prepared AC-NiO composite electrochemical sensor applications. A homogenous slurry was prepared using a mixture of AC-NiO composite and PVDF in a 90:10 weight ratio. NMP served as the solvent, with a loading concentration of 20%. The active material was then applied to the glassy carbon electrode using a micropipette and dried under an infrared lamp. The mass loading of the active material on the MGCE was maintained between 5 and 10 mg cm⁻² to ensure optimal efficiency and performance. The MGCE was used as WE in a three-electrode configuration without further modifications.

2.6 Fabrication of Various Electrochemical Systems

2.6.1 Fabrication of Symmetric Supercapacitor (SSC)

The symmetric supercapacitor (SSC) was fabricated by assembling two CNSAC-700-based electrodes to serve as both the positive and negative electrodes, with a separator placed between them. Aluminium foil was used as the current collector, and a porous cellulose membrane functioned as the separator. Coin cells of type 2025 with dimensions 20×2.5 mm were used to fabricate SSC. The electrodes

were prepared using the tape-casting method as previously described. The SSC utilised 1M Na_2SO_4 and 10m NaNO_3 as electrolytes. The assembling was carried out inside a glove box. Figure 2.17 describes the arrangement. They were named SSC- Na_2SO_4 and SSC- NaNO_3 respectively.(15)

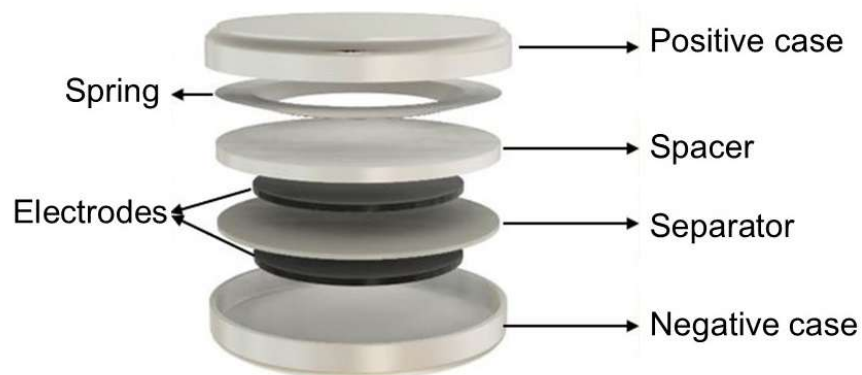


Figure 2.17 Schematic representation of SSC

2.6.2 Assembling of Flexible Supercapacitor (FSC)

The flexible supercapacitors (FSCs) were fabricated using MSAC-2-700 as the electrode material. The electrode was slitted into a dimension of 2×4 cm. PVA/ Na_2SO_4 -based gel polymer electrolyte was prepared with 10 wt% PVA and 0.1 M Na_2SO_4 . The obtained GPE film has a thickness of around $200 \mu\text{m}$. The GPE (2×4 cm) was then placed between the two electrodes to complete the fabrication.

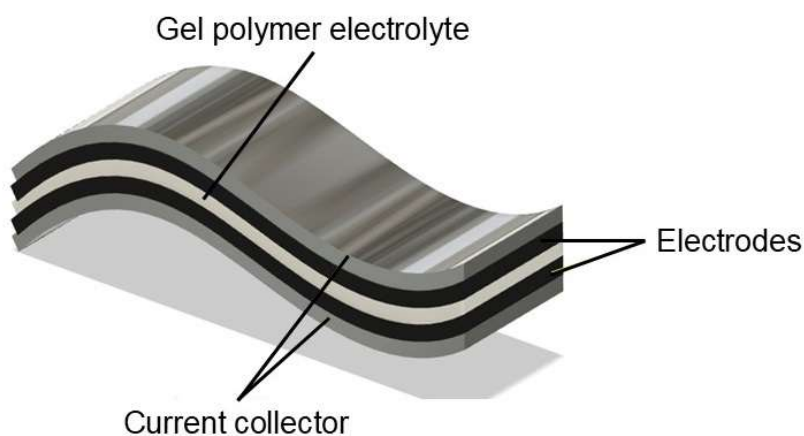


Figure 2.18 Schematic representation of FSC

No separator was used in this procedure; the GPE also served as the separator. The entire assembly was completed inside a glove box to ensure a controlled environment. These fabricated FSCs (Figure 2.18) were subjected to various electrochemical characterisation techniques to understand their electrochemical efficiency.(19)

2.6.3 LIB Half-cell Fabrication

The fabrication procedure for anodes is described in detail in subsection 2.5.3. The punched ACNM-based electrode and 45 μm -thick lithium disc were used as anode and cathode, respectively, for the assembled half-cell. Solupor[®], a microporous polyethylene (PE) membrane, is used as a separator in this study. The separator soaked in the LiPF_6 electrolyte is sandwiched between these electrodes.

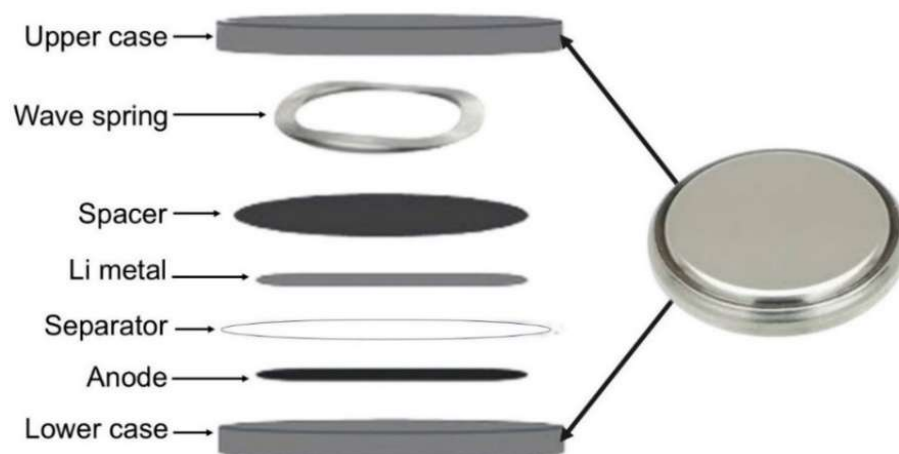


Figure 2.19 Schematic representation of LIB half-cell

This entire assembly was then inserted in the coin cell of type CR2025. The half-cell assembly process was conducted inside a glovebox filled with argon gas, ensuring that the anode half-cells were manufactured under controlled conditions. Figure 2.19 represents the schematic presentation of the fabricated anode half-cells. Subsequently, the half-cells were subjected to various electrochemical techniques.

2.6.4 Electrochemical Sensor for Urea Detection

The suitability of as-prepared AC/NiO for urea sensing applications was studied using a three-electrode configuration. In this study, MGCE was used as the WE, with an Ag/AgCl reference electrode and a platinum rod as the counter electrode. The electrochemical characterisations were performed with 0.1 M KOH as the supporting electrolyte for a potential window of 0-0.8 V.

2.7 Electrochemical Characterisations

Electrochemical analysis is based on the electrochemical reactions that occur within a medium and are related to structural changes, chemical composition, or concentration. The electrochemical characterisation techniques include qualitative and quantitative methods for effectively analysing the electrochemical system under study. Commonly used electrochemical characterisation techniques include cyclic voltammetry (CV), galvanostatic charge-discharge (GCD), and electrochemical impedance spectroscopy (EIS). Additionally, this study utilised scanning electrochemical microscopy (SECM) to investigate the surface current profile of the anode before and after cycling experiments.(40)

2.7.1 Cyclic voltammetry (CV)

CV is a widely used potential sweep method to study the redox reactions in an electrochemical system by analysing the current response at various potentials. The peaks observed in the CV curves reflect the redox behaviour of the material and its electrochemical activity within the system. An increase in current values indicates a higher charge transfer associated with the redox reactions occurring in the system. Conversely, a decrease in current values typically signifies a reduction in the mass transfer rate due to the depletion of reactant species at the electrode surface.(41)

CV analysis is typically conducted by applying a potential at a constant rate, starting from an initial potential (E_i) and moving to the first vertex potential (E_1). The process continues until it reaches the second vertex potential (E_2), after which it returns to the initial potential to complete the cycle. These CV loops illustrate the redox

reactions and their reversibility. The peak current values observed in a CV depend on the scan rate employed during the experiment.(42)

In an ideal EDLC system, the CV curve exhibits a quasi-rectangular shape. The CV curve without any redox peaks, even at low scan rates, indicates the formation of the electric double layer in the SC system. Furthermore, the reversibility of the curves indicates a fast electrochemical response in the systems. Since the current is proportional to both capacitance and scan rate in a supercapacitor system, the value of specific capacitance is calculated using the equation

$$C_{sp} = \frac{\int I \times dV}{2 \times v \times \Delta V \times m} \quad (2.8)$$

where $\int I \times dV$ represent the integral area under the CV curve, v is the scan rate, ΔV is potential window and m represents the weight of active material.(43)

The CV of batteries shows peaks related to the redox reactions in the system. The value of the specific capacity can be calculated using the equation

$$Q = \frac{\int_{V_2}^{V_1} i(V) dV}{2 \times 3.6 \times m \times v} \quad (2.9)$$

where Q is the specific capacity (mAhg^{-1}), $\int_{V_2}^{V_1} i(V) dV$ is the total charge storage, m is the mass of active material and v represents the scan rate.(44)

In these sensor systems, the peak current observed in CV associated with the redox reaction increases with increasing scan rate. Additionally, the peak current also rises linearly with increasing concentration of the analyte, which can be used to determine the unknown concentration of the analyte material through CV analysis. The lower limit of detection (LOD), limit of quantification (LOQ), and sensitivity are key metrics that quantitatively represent the efficiency of sensors. These parameters can be calculated from the equations

$$LOD = \frac{3 \times S}{m} \quad (2.10)$$

$$LOQ = \frac{10 \times S}{m} \quad (2.11)$$

and

$$\text{Sensitivity} = \frac{m}{A} \quad (2.12)$$

where S is the standard deviation of the response, m is the slope of the calibration plot and A is the surface area of MGCE.(45)

In the present research, CV analysis was conducted using an SP300 workstation from Biologic Science Instruments (France). The CV analysis of BDAC materials was performed at various scan rates within a fixed potential window. The anode half-cell was tested at a scan rate of 0.1 mVs⁻¹ over a voltage range from 0 to 3 V.

2.7.2 Galvanostatic charge-discharge (GCD)

GCD is a significant chronopotentiometric technique commonly employed to evaluate the performance of various electrochemical energy storage systems by providing insights into their capacity, capacitance, energy, power, efficiency, and cycling stability. During GCD analysis, a constant current is applied to WE in both forward and reverse directions.(13) The diffusion-controlled redox processes in the system typically exhibit plateaus at the potentials corresponding to the current peaks observed in CV curves. Ideal EDLCs show linear and triangular GCD curves, whereas battery systems exhibit nonlinear and asymmetrical GCD curves. The linear GCD curves in EDLCs suggest that charge is stored independently of electrochemical potential.(46)

The value of capacitance can be obtained from the discharge curve of GCD analysis. The values of specific capacitance (C_{sp}) can be calculated using the following equations:

For three-electrode systems,

$$C_{sp} = \frac{I \times \Delta t}{m \times \Delta v} \quad (2.13)$$

where I, m, Δt , Δv represent the current, active material's mass, discharge time, and potential range respectively.

For two-electrode systems,

$$C_{sp} = \frac{4 \times I \times \Delta t}{m \times \Delta v} \quad (2.14)$$

where ΔV , I , Δt , m represent the voltage difference between the beginning and end of discharge curves, current, time taken for complete discharge, and the total weight of two electrodes used respectively.(47)

The values of energy density and power density of an EDLC system can be calculated using the equations:

$$\text{Energy density, } E \text{ (Whkg}^{-1}\text{)} = \frac{0.5 \times C_{sp} \times V^2}{3.6} \quad (2.15)$$

$$\text{Power density, } P \text{ (Wkg}^{-1}\text{)} = \frac{3600 \times E}{t} \quad (2.16)$$

The value of capacity (mAh) is a crucial parameter for the performance of the battery material. This indicates the charges stored/delivered in the battery systems which can be calculated from the GCD curve by multiplying current and charge/discharge time.(48)

In this study, the capacitive properties of the prepared BDAC materials were analysed using GCD at various current densities, along with cycle tests for 10000 charging-discharging cycles at a current density of 20 Ag^{-1} . The potential of anode half-cells was also subjected to GCD analysis over a voltage range of 0-3 V at current rates of 0.1C, 1C, 2C, 3C, 4C and 5C. Additionally, a cycle stability test was conducted for 200 charging and discharging cycles at a current rate of 2C.

2.7.3 Electrochemical impedance spectroscopy (EIS)

EIS is an analytical technique used to study the variation in impedance with alternating voltage across different frequencies. It provides insights into the charge storage mechanisms within a system and the kinetics of charge transfer related to redox reactions and diffusion processes. The results of EIS are typically represented in two types of plots i) Nyquist plot: This plot displays the negative imaginary impedance ($-Z''$) values against the real component of impedance (Z'). In a Nyquist plot, data from lower frequencies appear on the right side, while higher frequencies are on the left. ii) Bode plot: This is a double-axis plot representing the frequency response for the

electrochemical system under study. The frequency values are plotted on a common x-axis, while the magnitude of impedance and phase angle are shown on the y-axis. Typically, the frequency and impedance magnitude are presented on a logarithmic scale, while the phase angle is represented on a linear scale.(49) The value of the impedance is generally represented as a complex function,

$$Z(\omega) = \frac{E_t}{I_t} = Z_0 e^{j\phi} = Z_0 (\cos \phi + j \sin \phi) \tag{2.17}$$

where the potential is $E_t = E_0 e^{j\omega t}$ and current is $I_t = I_0 e^{j(\omega t - \phi)}$

The value of overall impedance is obtained from Nyquist plots using the equation,

$$Z(\omega) = Z_{Re} - jZ_{Im} \tag{2.18}$$

Here, $Z(\omega)$, Z_{Re} , and Z_{Im} represent angular momentum-dependent impedance, the real and imaginary parts of $Z(\omega)$, respectively. The symbol j represents the imaginary unit ($\sqrt{-1}$). Figure 2.20 displays several equivalent circuits and their corresponding Nyquist plots. By analysing these plots, we can predict the behaviour of the system.(49)

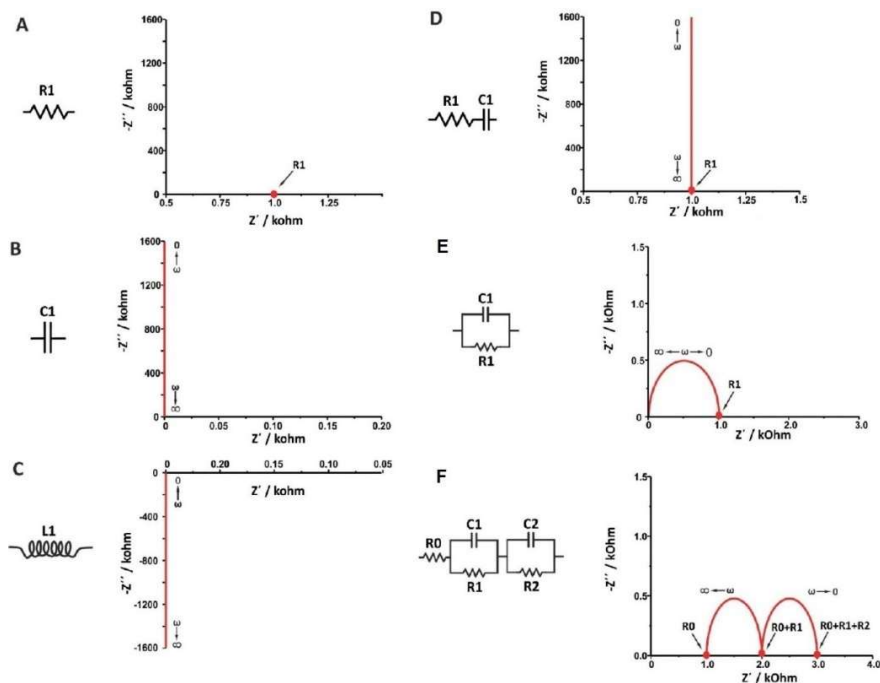


Figure 2.20 Equivalent circuits and their corresponding Nyquist plots (49)

The fundamental elements of electrical equivalent circuits for typical electrochemical systems include ohmic resistance (R), capacitance (C), constant phase element (CPE), and Warburg impedance (W). Here, R represents the transport of the charge carriers that occurs across interfaces or through thin layers. The value of R is independent of frequency and has no phase shift. C indicates the separation of charge carriers due to interfaces, exhibiting a phase shift of -90° between the current and the applied voltage. Its corresponding impedance is inversely related to frequency. On the other hand, the CPE is linked to non-ideal capacitive behaviour, which arises from the heterogeneity of the bulk material or its surface. CPE exhibits a phase shift that ranges from purely resistive (0°) to purely capacitive (-90°). W is associated with diffusion-controlled processes. The infinite Warburg element has a constant phase shift of -45° , while the finite Warburg element exhibits a phase shift between 0° and 45° .(50)

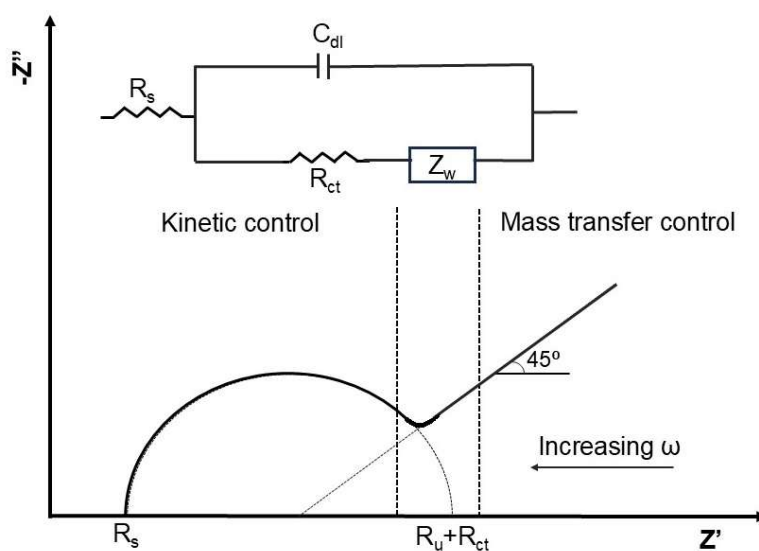


Figure 2.21 Randles circuit and corresponding Nyquist plot (51)

The Nyquist plot provides a detailed illustration of the charge transfer mechanism of the system being studied. For example, Figure 2.21 depicts the Randles circuit and the corresponding Nyquist plot. Here, R_u represents the solution resistance, C_{dl} is the capacitance value of EDLC, and Warburg impedance Z_w , arises from mass transfer. The charge-transfer resistance R_{ct} is in series with Z_w and represents the overall faradaic impedance (Z_f). In the Nyquist plot, the X-intercept indicates R_s , the diameter

of the semicircle refers to R_{ct} , and the linear line with about $\pi/4$ angle with the X axis indicates the Warburg element. Overall, the Nyquist plot provides direct insights into the system being analysed.(51)

In this study, EIS measurements of the electrode materials were conducted using an electrochemical workstation instrument SP300 available at the institution. Typically, the experiments are carried out with a perturbation potential of 10 mV in potentiostatic electrochemical impedance spectroscopy (PEIS) mode. For this study, we applied a sine wave with frequencies ranging from 100 kHz to 10 mHz during the experiments.

2.7.4 Scanning Electrochemical Microscopy (SECM)

SECM is an advanced analytical technique for investigating electrochemical systems at the microscale. It provides high-resolution images representing the surface reactivity of the system under study. SECM is widely used for applications including electrocatalysis, corrosion studies, biological systems, battery research, electrochemical sensors, etc.(52)

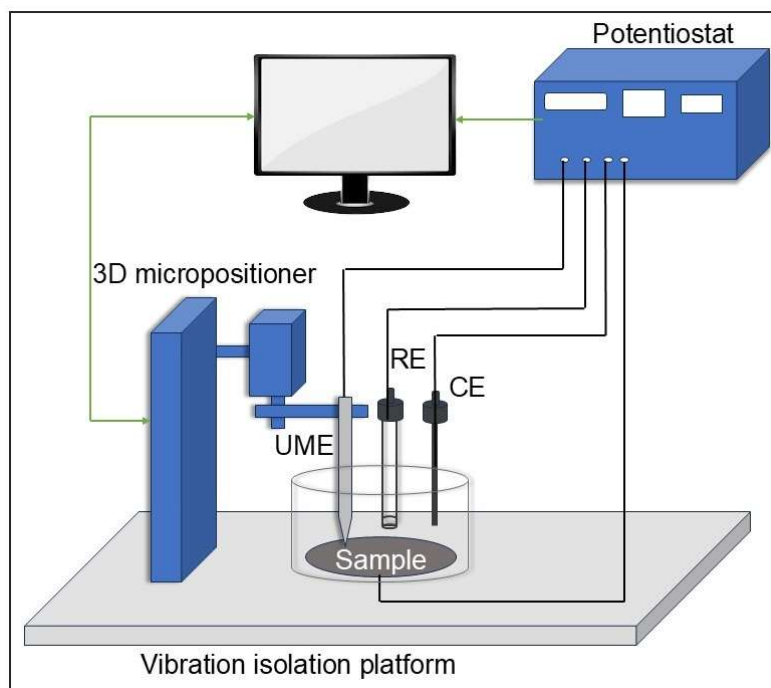


Figure 2.22 Schematic illustration of the SECM imaging apparatus

An ultramicroelectrode (UME) is effectively used in SECM. Figure 2.22 shows a schematic illustration of the SECM imaging apparatus. The mapping of local reactivity can be analysed by recording the feedback from the UME reflecting the electrochemical activity of the surface. The SECM analysis is usually carried out in five different modes including feedback mode, generation/collection mode, substrate generation/tip collection (SG/TC), tip generation/substrate collection (TG/SC) and surface interrogation mode.(53)

The properties of anodes of LIBs can be effectively studied using SECM analysis. The current profile of the anode surface usually represents the local topography of its surface. Before and after the cycling, of a LIB anode half-cell there will be a drastic change in this current profile ascribed to the solid electrolyte interface (SEI) formed on the surface of the anode. The significant reductions in the current profile after cycling are generally linked to a well-formed SEI. The data obtained from SECM can predict the formation of SEI in the battery system being investigated.(54)

In the current study, M470 (Biologic Science Instruments, France) was employed for SECM measurements of anode material before and after the cycling test. SECM analysis was carried out in a three-electrode configuration with a UME of diameter $\sim 15 \mu\text{m}$, Ag/AgCl and a platinum rod are used as the WE, reference electrode and counter electrode, respectively. The redox mediator used for this analysis is $\text{Fe}(\text{CN})_6^{3-}/\text{Fe}(\text{CN})_6^{4-}$. The approach curve was recorded with the UME approaching the anode at a constant voltage of 0.25 V before the surface scanning. The surface scan was carried out for $250 \mu\text{m} \times 250 \mu\text{m}$ at a step size of $5 \mu\text{m}$.

References

1. Aina EO, Adisa AF, Olayanju TMA, ismaila SO. Performance Evaluation of a Developed Cashew Nut Shell Liquid Expeller. *Agricultural Engineering*. 2018 Jul 1;22(2):5–19.
2. Bhoomika HR, Sudha Rani N. Problems and Prospects of Cashew Cultivation in India - An Overview. *Int J Curr Microbiol Appl Sci*. 2018 Oct 20;7(10):3687–94.
3. Anas M, Jahiding M, Ratna, Sudiana IN. Production and characterization of activated carbon from cashew nut shell using N₂ as activation agent. In: *IOP Conference Series: Materials Science and Engineering*. Institute of Physics Publishing; 2019.
4. Laino Gama R, Muellner-Riehl AN, Demarco D, Pirani JR. Evolution of reproductive traits in the mahogany family (Meliaceae). *J Syst Evol*. 2021 Jan 1;59(1):21–43.

5. Patil SA, Suryawanshi UP, Harale NS, Patil SK, Vadiyar MM, Luwang MN, Anuse MA, Kim JH, Kolekar SS. Adsorption of toxic Pb (II) on activated carbon derived from agriculture waste (Mahogany fruit shell): isotherm, kinetic and thermodynamic study. *International Journal of Environmental Analytical Chemistry*. 2022 Dec 30;102(19):8270-86.
6. Hossain M, Goni LKMO, Muntaha N, Jamal MS, Sujan SMA, Ahmed S, et al. Box–Behnken design-based optimization for biodiesel production from waste cooking oil using Mahogany (*Swietenia macrophylla*) fruit shell derived activated carbon as a heterogeneous base catalyst. *Reaction Kinetics, Mechanisms and Catalysis*. 2021 Jun 1;133(1):117–38.
7. Pranolo SH, Waluyo J, Paryanto, Susanti AD, Permana RB, Erwanda I, et al. Feasible tar cleaning method of producer gas from palm kernel shell and mahogany fruit shell gasification. *Mater Today Proc*. 2022 Jan 1;63:S237–43.
8. Jaroenta J, Siangsawad R, Onkate R, Jearjiratikul V, Thongpin C. Study of rubber composites between natural rubber and Mahogany Shell Powder (MHSP) and potential for pavement block. In: *IOP Conference Series: Materials Science and Engineering*. Institute of Physics Publishing; 2020.
9. Anooj ES, Suganthi V, Praseetha PK. Synthesis and characterization of graphene quantum dots from turmeric powder (*Berberis aristata*) and its biomedical applications. *Scopus Ijphrd Citation Score*. 2019 Jul;10(7):1239.
10. Ibrahim MA, Cantrell CL, Jeliakova EA, Astatkie T, Zheljazkov VD. Utilization of nutmeg (*Myristica fragrans* Houtt.) seed hydrodistillation time to produce essential oil fractions with varied compositions and pharmacological effects. *Molecules*. 2020 Jan 28;25(3).
11. Sipahelut SG, Patty JA, Patty Z, Kastanja AY, Lekahena VN. The antibacterial and antifungal activity of essential oil derived from the flesh of nutmeg fruit. *EurAsian Journal of BioSciences*. 2019;13(1):93-8.
12. Periasamy G, Karim A, Gibrelibanos M, Gebremedhin G, Gilani AU. Nutmeg (*Myristica fragrans* Houtt.) oils. In: *Essential oils in food preservation, flavor and safety 2016* Jan 1 (pp. 607-616). Academic Press.
13. Feng L, Yan B, Zheng J, Zhang Q, Wei R, Zhang C, et al. Chemical foaming-assisted synthesis of N, O co-doped hierarchical porous carbon from soybean protein for high rate performance supercapacitors. *Diam Relat Mater*. 2023 Mar;133:109767.
14. Zhao W, Yan B, Chen D, Chen J, Zhang Q, Jiang L, et al. Free-standing carbon network with enhanced capacitive performance synthesized via green H₂O₂ activation. *Colloids Surf A Physicochem Eng Asp*. 2023 Jul;668:131425.
15. Pulikkottil M, Antony H, Muralidharan MN, Gopalan EV, Ansari S. Cashew Nut Shell Derived Porous Activated Carbon Electrodes for “Water-in-Salt” Electrolyte Based Symmetric Supercapacitor. *ChemistrySelect*. 2022 Jun 20;7(23).
16. Merin P, Jimmy Joy P, Muralidharan MN, Veena Gopalan E, Seema A. Biomass-derived activated carbon for high-performance supercapacitor electrode applications. *Chemical Engineering & Technology*. 2021 May;44(5):844-51.

17. García JR, Sedran U, Zaini MAA, Zakaria ZA. Preparation, characterization, and dye removal study of activated carbon prepared from palm kernel shell. *Environmental Science and Pollution Research*. 2018 Feb 1;25(6):5076–85.
18. Wong S, Yac'cob NAN, Ngadi N, Hassan O, Inuwa IM. From pollutant to solution of wastewater pollution: Synthesis of activated carbon from textile sludge for dye adsorption. *Chin J Chem Eng*. 2018 Apr 1;26(4):870–8.
19. Pulikkottil M, Thomas A, Malamal Neelanchery M, Gopalan Elavumkal V, Ansari S. Highly Efficient Solid-State Supercapacitor with Porous Electrode Material. *Energy Technology*. 2023 Sep 1;11(9).
20. Chennah A, Khan MA, Zbair M, Ait Ahsaine H. NiO/AC Active Electrode for the Electrosorption of Rhodamine B: Structural Characterizations and Kinetic Study. *Catalysts*. 2023 Jun 1;13(6).
21. Mansurov ZA, Smagulova GT, Imash AA, Taurbekov AT, Elouadi B, Kaidar BB. Carbon/NiO Compositional Fibers. *Eurasian Chemico-Technological Journal*. 2022;24(2):59–67.
22. Yan B, Zheng J, Feng L, Du C, Jian S, Yang W, et al. Wood-derived biochar as thick electrodes for high-rate performance supercapacitors. *Biochar*. 2022 Dec 1;4(1).
23. Zheng S, Zhang J, Deng H, Du Y, Shi X. Chitin derived nitrogen-doped porous carbons with ultrahigh specific surface area and tailored hierarchical porosity for high performance supercapacitors. *Journal of Bioresources and Bioproducts*. 2021 May 1;6(2):142–51.
24. Correia LB, Fiuza RA, de Andrade RC, Andrade HMC. CO₂ capture on activated carbons derived from mango fruit (*Mangifera indica* L.) seed shells: A TG study. *J Therm Anal Calorim*. 2018 Jan 1;131(1):579–86.
25. Rahman SS, Salomon M, Dembélé S. Towards scanning electron microscopy image denoising: a state-of-the-art overview, benchmark, taxonomies, and future direction. *Machine Vision and Applications*. 2024 Jul;35(4):87.
26. Brodusch N, Brahimi SV, Barbosa De Melo E, Song J, Yue S, Piché N, Gauvin R. Scanning Electron Microscopy versus Transmission Electron Microscopy for Material Characterization: A Comparative Study on High-Strength Steels. *Scanning*. 2021;2021(1):5511618.
27. Mensah-Darkwa K, Zequine C, Kahol PK, Gupta RK. Supercapacitor energy storage device using biowastes: A sustainable approach to green energy. *Sustainability*. 2019 Jan 15;11(2):414.
28. Armonio JV, Caragdag IJ, Escorpizo JA, Miranda KM, Raymundo AJ, Roque E. Production of activated carbon from corn cobs and mango kernels via H₃PO₄ activation and mediated hydrothermal treatment. In *MATEC Web of Conferences 2019* (Vol. 268, p. 06020). EDP Sciences.
29. Krishna DN, Philip J. Review on surface-characterization applications of X-ray photoelectron spectroscopy (XPS): Recent developments and challenges. *Applied Surface Science Advances*. 2022 Dec 1;12:100332.
30. Sahlabji T, El-Nemr MA, Nemr AE, Ragab S, Alghamdi MM, El-Zahhar AA, Idris AM, Said TO. High surface area microporous activated carbon from *Pisum sativum* peels for

- hexavalent chromium removal from aquatic environment. *Toxin Reviews*. 2022 Apr 3;41(2):639-49.
31. Schlumberger C, Scherdel C, Kriesten M, Leicht P, Keilbach A, Ehmman H, Kotnik P, Reichenauer G, Thommes M. Reliable surface area determination of powders and meso/macroporous materials: Small-angle X-ray scattering and gas physisorption. *Microporous and Mesoporous Materials*. 2022 Jan 1;329:111554.
 32. López-Pérez L, Zarubina V, Melián-Cabrera I. The Brunauer–Emmett–Teller model on alumino-silicate mesoporous materials. How far is it from the true surface area?. *Microporous and Mesoporous Materials*. 2021 May 1;319:111065.
 33. Schlumberger C, Thommes M. Characterization of hierarchically ordered porous materials by physisorption and mercury porosimetry—a tutorial review. *Advanced Materials Interfaces*. 2021 Feb;8(4):2002181.
 34. Gong Y, Chen X, Wu W. Application of fourier transform infrared (FTIR) spectroscopy in sample preparation: Material characterization and mechanism investigation. *Advances in Sample Preparation*. 2024 Aug 1;11:100122.
 35. Arshanitsa A, Jashina L, Pals M, Ponomarenko J, Akishin Y, Zake M. Characteristics of the Main-and Side-Stream Products of Microwave Assisted Torrefaction of Lignocellulosic Biomass of Different Origination. *Energies*. 2022 Mar 2;15(5):1857.
 36. Jain A, Ghosh M, Krajewski M, Kurungot S, Michalska M. Biomass-derived activated carbon material from native European deciduous trees as an inexpensive and sustainable energy material for supercapacitor application. *Journal of Energy Storage*. 2021 Feb 1;34:102178.
 37. Rawat S, Mishra RK, Bhaskar T. Biomass derived functional carbon materials for supercapacitor applications. *Chemosphere*. 2022 Jan 1;286:131961.
 38. Major GH, Fernandez V, Fairley N, Smith EF, Linford MR. Guide to XPS data analysis: applying appropriate constraints to synthetic peaks in XPS peak fitting. *Journal of Vacuum Science & Technology A*. 2022 Dec 1;40(6).
 39. Ketenoglu D. A general overview and comparative interpretation on element-specific X-ray spectroscopy techniques: XPS, XAS, and XRS. *X-Ray Spectrometry*. 2022 Sep 1;51(5–6):422–43.
 40. Wang Q, Ran X, Shao W, Miao M, Zhang D. High performance flexible supercapacitor based on metal-organic-framework derived CoSe₂ nanosheets on carbon nanotube film. *Journal of Power Sources*. 2021 Apr 1;490:229517.
 41. Huo S, Zhang X, Liang B, Zhao Y, Li K. Synthesis of interconnected hierarchically porous carbon networks with excellent diffusion ability based on NaNO₃ crystal-assisted strategy for high performance supercapacitors. *Journal of Power Sources*. 2020 Feb 29;450:227612.
 42. Singh M, Gupta A, Sundriyal S, Dubey P, Jain K, Dhakate SR. Activated green carbon-based 2-D nanofabric mats for ultra-flexible all-solid-state supercapacitor. *J Energy Storage [Internet]*. 2022;49:104193.
 43. Dubey P, Shrivastav V, Singh M, Maheshwari PH, Sundriyal S, Dhakate SR. Electrolytic Study of Pineapple Peel Derived Porous Carbon for All-Solid-State Supercapacitors. *ChemistrySelect*. 2021 Nov 15;6(42):11736–46.

44. Ahmed F, Almutairi G, Hasan PM, Rehman S, Kumar S, Shaalan NM, Aljaafari A, Alshoaibi A, AlOtaibi B, Khan K. Fabrication of a biomass-derived activated carbon-based anode for high-performance li-ion batteries. *Micromachines*. 2023 Jan 12;14(1):192.
45. Irzalinda AD, Gunlazuardi J, Wibowo R. Development of a non-enzymatic urea sensor based on a Ni/Au electrode. In *Journal of Physics: Conference Series 2020* (Vol. 1442, No. 1, p. 012054). IOP Publishing.
46. Ma F, Ding S, Ren H, Liu Y. Sakura-based activated carbon preparation and its performance in supercapacitor applications. *RSC Adv*. 2019;9(5):2474–83.
47. Liang YZ, Hsu TY, Su YS. Tailoring the Size of Reduced Graphene Oxide Sheets to Fabricate Silicon Composite Anodes for Lithium-Ion Batteries. *ACS Applied Materials and Interfaces*. 2024 Jun 5;16(22):29226–34.
48. Yarramsetti S, Girirajan M, Kalluri S, Sangaraju S, Maram PS. Multifunctional activated carbon derived from novel biomass for high-performance energy storage applications: A sustainable alternative to fossil-fuel-derived carbon. *Materials Chemistry and Physics*. 2024 Jul 1;320:129424.
49. Azad UP, Chandra P. *Handbook of Nanobioelectrochemistry: Application in Devices and Biomolecular Sensing*. Handbook of Nanobioelectrochemistry: Application in Devices and Biomolecular Sensing. Springer; 2023. 1–950.
50. Lazanas AC, Prodromidis MI. *Electrochemical Impedance Spectroscopy—A Tutorial*. Vol. 3, ACS Measurement Science Au. American Chemical Society; 2023. 162–93.
51. Zhang L, Dai Y, Li C, Dang Y, Zheng R, Wang Z, Wang Y, Cui Y, Arandiyani H, Shao Z, Sun H. Recent advances in electrochemical impedance spectroscopy for solid-state batteries. *Energy Storage Materials*. 2024 Apr 26:103378.
52. Chen J, Lee PS. Electrochemical supercapacitors: from mechanism understanding to multifunctional applications. *Advanced Energy Materials*. 2021 Feb;11(6):2003311.
53. Strange LE, Li X, Wornyo E, Ashaduzzaman M, Pan S. Scanning electrochemical microscopy for chemical imaging and understanding redox activities of battery materials. *Chemical & Biomedical Imaging*. 2023 Mar 23;1(2):110-20.
54. Mozhzhukhina N, Flores E, Lundström R, Nyström V, Kitz PG, Edström K, et al. Direct Operando Observation of Double Layer Charging and Early Solid Electrolyte Interphase Formation in Li-Ion Battery Electrolytes. *Journal of Physical Chemistry Letters*. 2020 May 21;11(10):4119–23.

Chapter **3**

**CASHEW NUTSHELL-DERIVED
ACTIVATED CARBON FOR EFFECTIVE
SUPERCAPACITOR APPLICATIONS**

Some of the contents of this chapter have been published in

- I. Merin, P., Jimmy Joy, P., Muralidharan, M. N., Veena Gopalan, E., & Seema, A. (2021). Biomass-derived activated carbon for high-performance supercapacitor electrode applications. *Chemical Engineering & Technology*, 44(5), 844-851.
- II. Pulikkottil, M., Antony, H., Muralidharan, M. N., Gopalan, E. V., & Ansari, S. (2022). Cashew Nut Shell Derived Porous Activated Carbon Electrodes for “Water-in-Salt” Electrolyte Based Symmetric Supercapacitor. *Chemistryselect*, 7(23), e202200984.

3.1 Introduction

Activated carbon (AC) is an efficient material with multifaceted applications. Owing to its high porosity, good electrical conductivity, excellent chemical stability, and improved specific surface area, there is significant research interest in AC-related applications.(1) However, conventional sources of AC such as coal, petroleum coke, and pitch are raising a significant challenge for the sustainable environment.(2) The natural and environmentally friendly biomass-derived activated carbon (BDAC) can address this challenge effectively.

In this study, cashew nut shell waste (CNS) is utilised as a precursor for the preparation of BDAC. CNS has a highly porous structure similar to a soft honeycomb matrix. This unique structure has several pores, which are desirable for preparing AC with a large specific surface area.(3,4) The extensive surface area of activated carbon derived from cashew nut shells (CNSAC) is crucial for various applications, including water purification and heavy metal impurity removal. CNSAC has received substantial attention in this field as a low-cost alternative to conventional adsorbents.(5,6) The large surface area and excellent porous nature of CNSAC are suitable for supercapacitors, especially electrochemical double-layer capacitors (EDLC). Furthermore, CNSAC has benefits such as ease of availability, environmental friendliness, low cost, higher porosity, and ease of handling. An extensive literature survey confirmed that CNSAC-based electrode materials for supercapacitors are not an extensively explored area.(7,8) The present chapter discusses the preparation of CNSAC and the fabrication of highly efficient supercapacitors using CNSAC as electrode material. As electrolytes also have an inevitable role in improving the value of specific capacitance in EDLCs, the performance of CNSAC electrode material is studied with conventional 'salt in water' aqueous electrolyte (1M Na₂SO₄) and 'water in salt' aqueous electrolyte (10 m NaNO₃).

3.2 Experimental details

3.2.1 Preparation of Cashew Nutshell-derived Activated Carbon

CNS were crushed into small pieces of dimension 4–6 mm with a stainless-steel mortar. The excess cashew nut oil and other impurities in CNS were removed through

thorough washing using deionised water. These cleaned and crushed CNS were then dried overnight at a temperature of 80 °C. This dried sample served as the precursor for preparing CNSAC. Chemical activation followed by carbonisation was employed for this synthesis. The detailed methodology is schematically displayed in Figure 3.1. The dried CNS precursor was chemically activated with KOH in weight ratios of 1:1, 1:2, and 1:3 (CNS: KOH) while continuously stirring for 3 hours. Afterwards, the mixture was dried in an air oven at 100 °C for 24 hours. The activated samples were carbonised in a tubular furnace at a heating rate of 5 °C min⁻¹, starting from room temperature and reaching various carbonisation temperatures of 600, 700, and 800 °C. This process was conducted under a flow of argon gas at a rate of 2 L min⁻¹ and maintained for one hour. After carbonisation, the samples were washed with 0.1 M HCl and deionised water until the pH of the filtered liquid reached approximately 7. The resulting samples were then dried for 24 hours at a temperature of 120 °C under vacuum and ground into fine powders. The samples were labelled as CNSAC-X-Y, where X represents the corresponding activation ratio (1, 2, or 3) and Y denotes the carbonisation temperature (600, 700, or 800 °C).

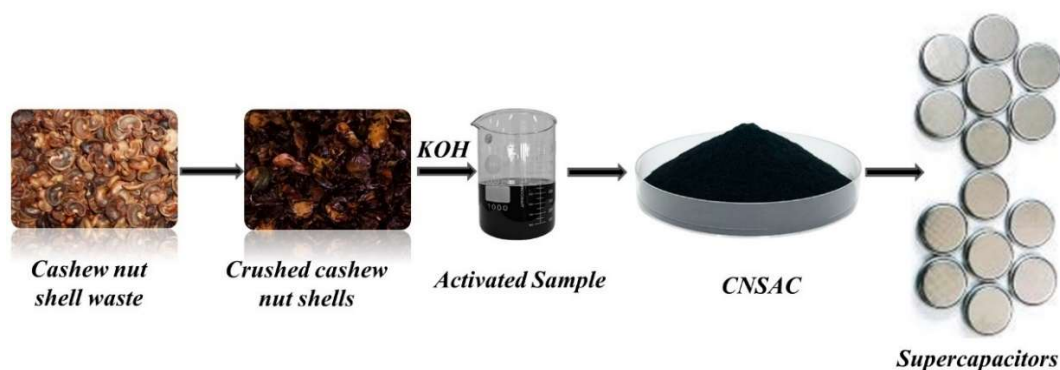


Figure 3.1 Schematic representation of methodology

3.2.2 Preparation of Electrode

A homogeneous slurry was made by mixing active material, conducting material (carbon black), binder (PVDF), and N-methyl pyrrolidone (NMP) as the solvent. The composition CNSAC-X-Y, carbon black, and PVDF was optimised to a mass ratio of 8:1:1. Electrochemical studies of the CNSAC-X-Ys were conducted using a three-electrode system, which included an Ag/AgCl reference electrode and a platinum rod as the counter electrode. A 2 µL sample of the prepared slurry was evenly

applied to a glassy carbon working electrode and dried for 5 minutes under an infrared lamp. The active electrode material was coated with a mass loading of approximately 4 mg cm^{-2} .

3.2.3 Fabrication of Symmetric Supercapacitors (SSCs)

SSCs were fabricated with CNSAC-based electrodes. The as-prepared slurry was coated on an aluminium current collector using the tape-casting method. A porous cellulose membrane was used as the separator. The SSCs were fabricated by placing the separator soaked in electrolyte between the electrodes. This arrangement is enclosed in coin cells of type 2025 ($20 \times 2.5 \text{ mm}$ dimension). $1 \text{ M Na}_2\text{SO}_4$ ('salt in water' aqueous electrolyte) and 10 m NaNO_3 ('water in salt' aqueous electrolyte) were used in the SSCs. They were respectively named SSC- Na_2SO_4 and SSC- NaNO_3 .

3.3 Results and Discussions

CNSACs were synthesised through chemical activation, followed by carbonisation. The structure of CNSAC is determined by two major parameters: activation ratio and carbonisation temperature. These factors are optimised based on results from various material and electrochemical studies. The surface area and other structural features of the synthesised CNSACs were analysed using material characterisation techniques including XRD, FTIR, SEM and BET analysis. The electrochemical performance is studied using techniques such as CV, GCD, etc. Furthermore, linear sweep voltammetry (LSV) is utilised to determine the potential window feasible for the WIS electrolytes being studied. These results are used to optimise the activation ratio and carbonisation temperature. The feasibility of CNSAC for practical supercapacitor applications was validated by fabricating SSC systems with 'salt in water' and 'water in salt' electrolytes.

3.3.1 Material characterisations

3.3.1.1 XRD analysis

The XRD pattern of CNSACs (Figure 3.2) displays an intense broad peak around 24.2° and an inconspicuous broad peak around 43.5° . These peaks correspond to the (002) and (100) diffraction planes in the graphitic framework and are indexed

with ICDD No. 01-075-1621. They indicate the presence of graphitic carbon and interlayer condensation, respectively.(9) The formation of this graphitic structure during carbonisation is beneficial for the excellent electrochemical efficiency of the electrode material. The presence of the graphitic structure enhances the electrochemical activity of CNSAC, indicating its potential as an effective electrode material. However, the broadness of the peaks also suggests the amorphous nature of the materials.(10)

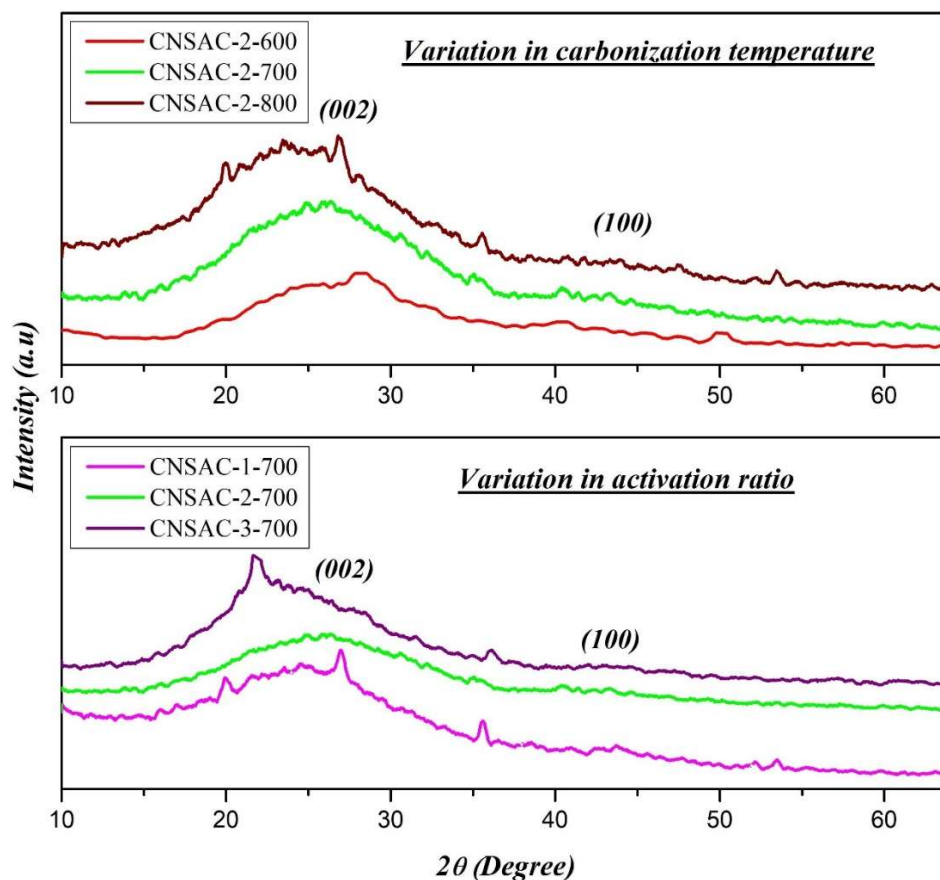


Figure 3.2 Comparison of XRD patterns of CNSAC-X-Ys.

The XRD patterns of CNSAC-1-700, CNSAC-2-700, and CNSAC-3-700 suggest that the peaks become broader and less intense with increasing activation ratio. This broadening of the peaks is attributed to the decreased degree of graphitisation in the electrode materials. Additionally, the reduction in intensity of the (002) diffraction peak at higher carbonisation temperatures suggests a decrease in interlayer spacing as carbonisation temperature increases.(11)

3.3.1.2 FTIR analysis

The surface chemistry of AC-based electrode materials significantly affects their electrical conductivity, which increases as the concentration of surface functional groups diminishes. FTIR spectroscopy is employed to understand the surface chemistry of CNSACs. Figure 3.3 displays the FTIR spectrum of CNSAC-X-Ys. The vibrations observed in all five samples were similar, with four weak peaks located at approximately 1055, 1200, 1593, and 3461 cm^{-1} , suggesting the presence of a graphitic structure in the spectra.(6)

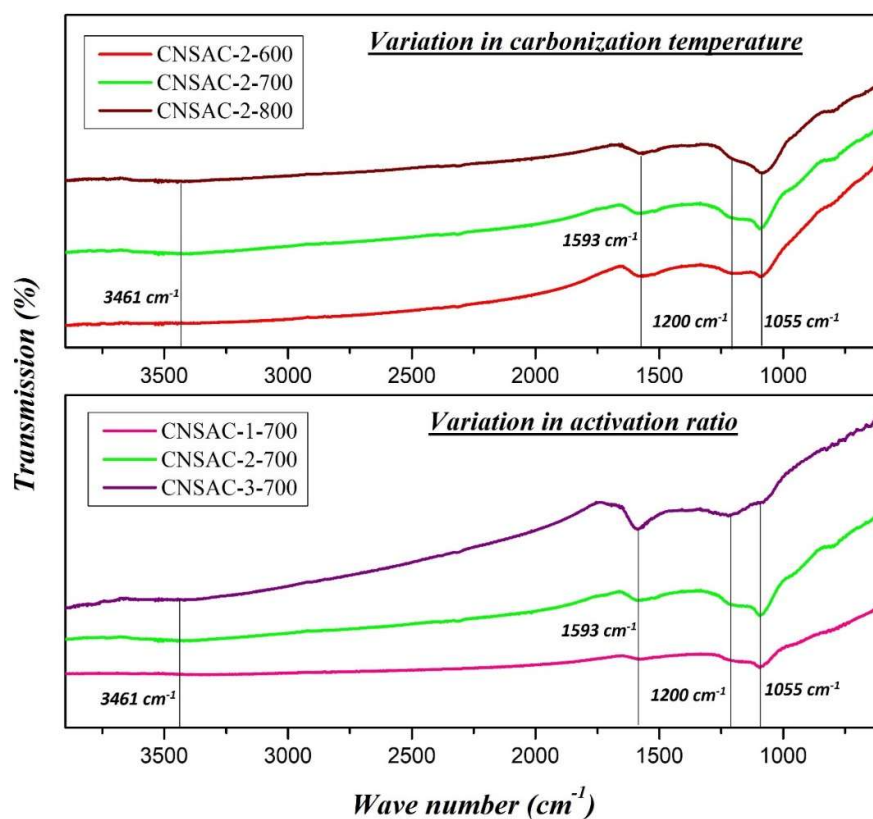


Figure 3.3 FTIR spectra of CNSAC-X-Ys

C–H bending vibrations can be identified from peaks at 1055 cm^{-1} . The band located around 1593 cm^{-1} represents C=C stretching vibrations, while the broad band around 3461 cm^{-1} indicates the O–H vibrations. The absorption peak at 1200 cm^{-1} corresponds to C–O stretching vibrations.(12) These functional groups significantly

impact the electrochemical performance of the prepared AC and are advantageous for enhancing charge storage, specific capacitance and other surface properties.(13)

The impact of activation ratio and carbonisation temperature in determining the functional groups present in their structure is confirmed by the FTIR spectra of these materials. As shown in FTIR spectra, the intensity of all peaks corresponding to C=C and C–O stretching vibrations increases with an increase in the activation ratio. The activation ratio is crucial in developing oxygen-containing functional groups within AC. Furthermore, the intensity of peaks in CNSACs decreases with a rise in carbonisation temperature. This indicates that the increased carbonisation temperature may lead to a more tightly packed graphitic structure with fewer functional groups.(12)

3.3.1.3 SEM analysis

The morphology and microstructure of porous AC promote the efficient charge storage and electrolyte transport in supercapacitors. The morphology of as-prepared CNSACs was studied using SEM analysis, and EDAX was employed for elemental analysis. Figure 3.4 (a)-(j) displays SEM images of CNSAC-X-Ys. All CNSACs exhibit honeycomb-like, highly porous structures with several cavities on the surface. This structure, composed of numerous pores, may be assigned to the intercalation and removal of metallic potassium during AC synthesis. These interconnected pores improve the accessible surface area for electrolytes and facilitate effective ion transmission. Such a porous structure can serve as an ion-buffering reservoir for electrolytes, create additional interfaces for charge storage, and improve both their capacitive properties and electrochemical efficiency.(14,15)

The SEM images illustrate the effect of activation ratio on the development of porous structure in AC. The pore size increases with increasing KOH activation ratio due to increased KOH etching. However, this effect is not predominant after the 1:2 activation ratio. A further increase in the activation ratio to 1:3 results in a reduction in the number of pores. The distribution of pores is highly related to the temperature during the carbonisation process. The number and size of pores increase with a rise in carbonisation temperature.

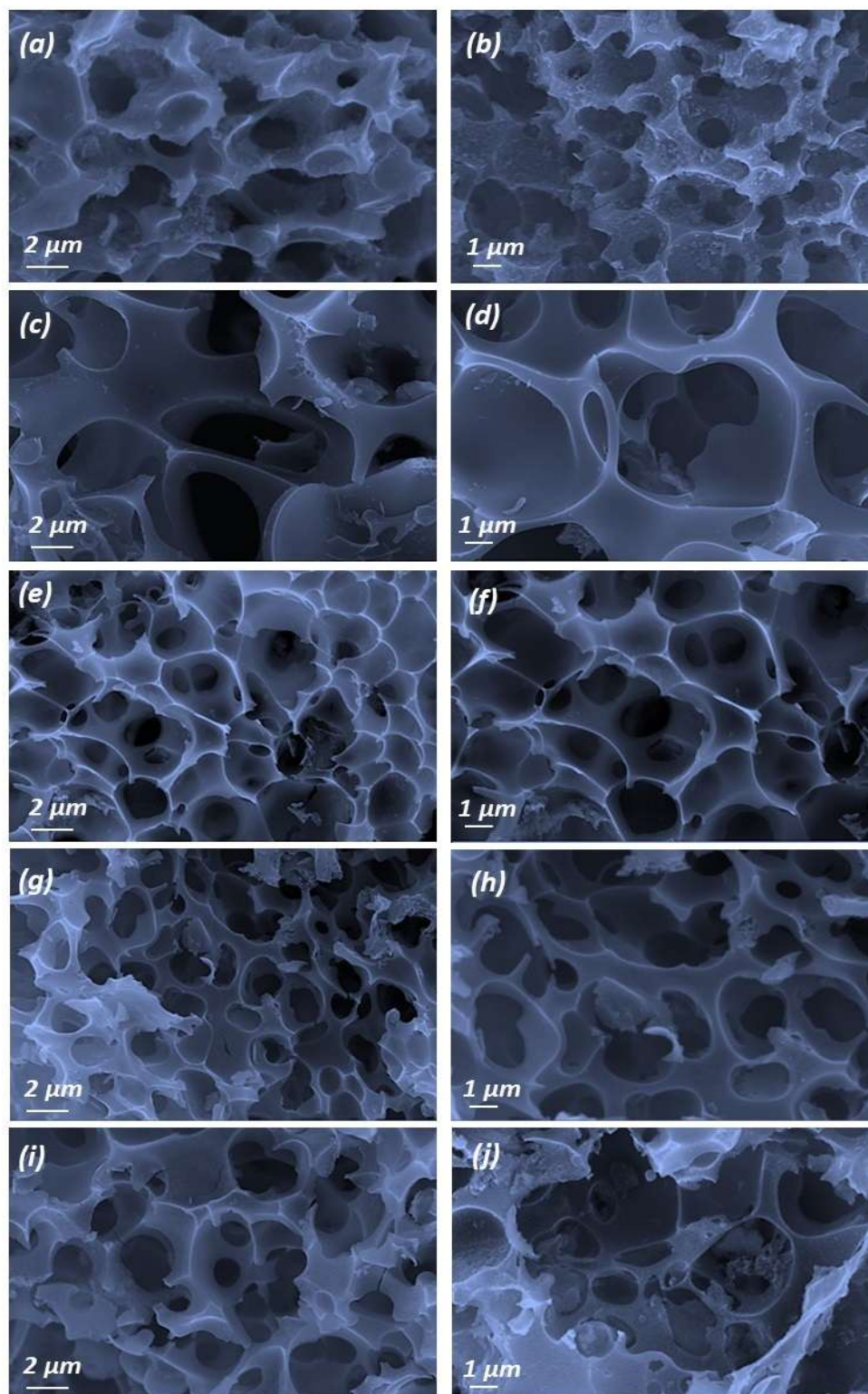


Figure 3.4 SEM images of (a, b) CNSAC-1-700, (c, d) CNSAC-2-700, (e, f) CNSAC-3-700, (g, h) CNSAC-2-600 and (i, j) CNSAC-2-800 at a magnification of 15000 and 20000 X, respectively.

Table 3.1 Elemental analysis of CNSAC-X-Ys

Weight percentage	CNSAC-1-700	CNSAC-2-700	CNSAC-3-700	CNSAC-2-600	CNSAC-2-800
C	85.21	87.43	86.38	86.60	88.68
O	14.79	12.57	13.62	13.40	11.32

The pores become well-defined and evenly distributed as the temperature varies between 600 °C and 700 °C. However, when the temperature increases to 800 °C, the number of macropores increases and causes structural collapse in CNSACs. Even though CNSAC-2-800 shows a higher degree of graphitisation, the accessible surface area and porosity are significantly reduced. Among all the prepared CNSACs, CNSAC-2-700 has a highly developed porous structure with the majority of micropores and a few mesopores. This porous distribution facilitates ion transport and improves the electrochemical efficiency of the material.(16) The SEM analysis confirms the feasibility of CNSAC-2-700 for supercapacitor applications. The results from the EDAX analysis are tabulated in the Table. 3.1. The analysis indicates the presence of carbon (C) and oxygen (O) in all CNSAC samples. The C content of the material is much higher than the O content. These observations from EDAX analysis are consistent with the results obtained from FTIR spectra and XRD.

3.3.1.4 Raman Spectroscopy

The Raman spectra of CNSAC-X-Ys are presented in Figure 3.5. The spectra show two distinct peaks corresponding to the D (defect) and G (graphite) bands in graphitic carbon. The D band around 1355 cm^{-1} reflects the A_{1g} vibrational mode, representing defective or disordered sites in carbon materials. In contrast, the G band (1580 cm^{-1}) is associated with E_{2g} symmetric phonon vibrations of C-C bond stretching. These peaks can be ascribed to the crystalline graphite and disordered carbon.(17) The ratio of the intensities of the D and G bands (I_D/I_G) reflects the degree of graphitisation in the AC structure. A higher I_D/I_G indicates more defects in the graphitic structure. The I_D/I_G values for CNSAC-1-700, CNSAC-2-700, and CNSAC-3-700 were 0.94, 0.95,

and 0.93, respectively. These values indicate incomplete graphitisation and deformation of the graphitic structure in lower and higher KOH activation ratios. The I_D/I_G values for CNSAC-2-600, CNSAC-2-700, and CNSAC-2-800 were 0.89, 0.92, and 0.96, respectively. These I_D/I_G values suggest an enhancement in the structural defects with rising carbonisation temperature.(10)

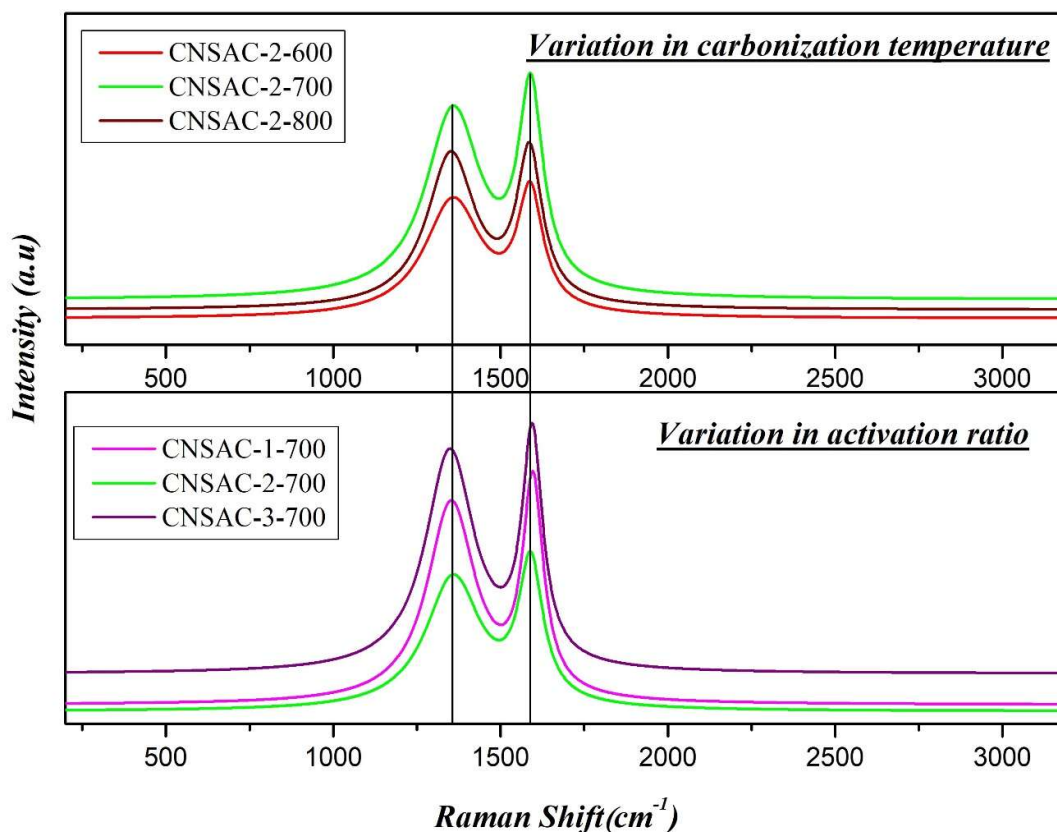


Figure 3.5 Raman spectra of CNSAC-X-Ys

3.3.1.5 Surface area analysis

The N_2 adsorption-desorption isotherm of CNSAC-X-Ys (Figure 3.6) shows a sharp increase at the lower relative pressure region (below 0.5) and a plateau at the higher relative pressure region. According to IUPAC classification, these isotherms are categorised as a type I isotherm indicating the microporous nature of the materials. The type H4 hysteresis in these isotherms suggests a broader pore size distribution with wider micropores and smaller mesopores. This type of isotherm is common for materials with pore diameters less than 2.5 nm.(18,19)

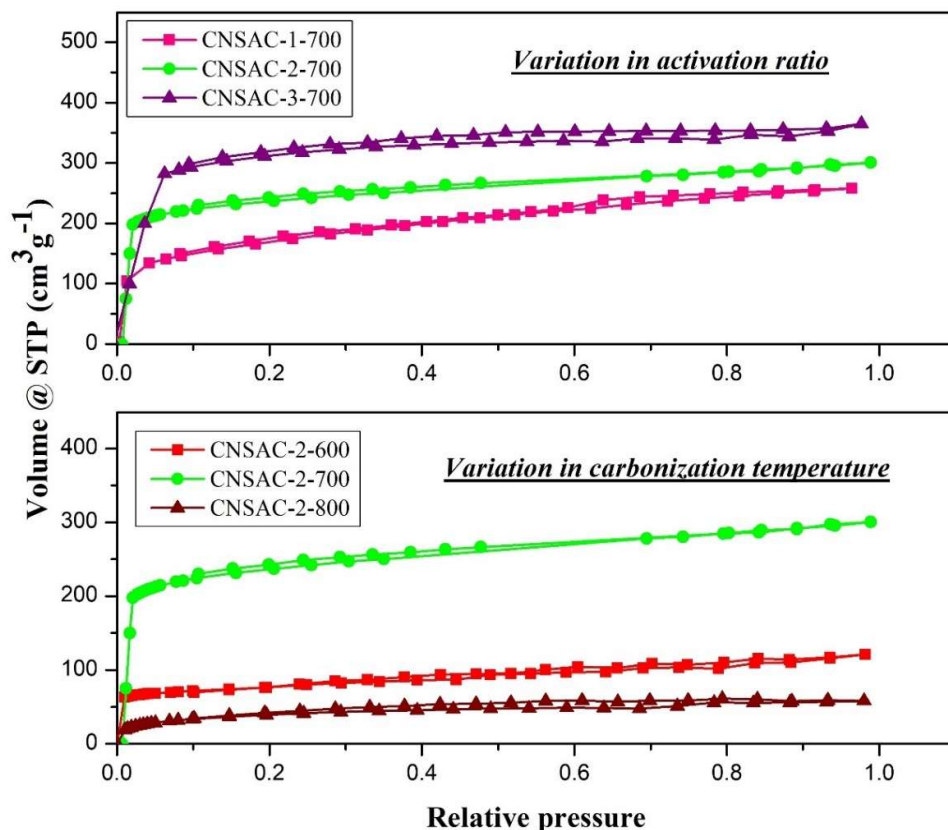


Figure 3.6 N₂ adsorption-desorption isotherm of CNSAC-X-Ys

The larger micropores and smaller mesopores in the structure of AC are desirable for supercapacitor electrode applications. The slight increase in adsorption in the higher relative pressure region (close to 1) reflects traces of macropores in the structure. The nature of these isotherms suggests several significant conclusions. CNSAC-2-700 has a structure with both micropores and mesopores. The isotherm indicates a higher concentration of mesopores and macropores in CNSAC-3-700, which may be attributed to the structural collapse on excessive addition of KOH. The carbonisation temperature significantly affects the porous structure of CNSACs. The enlargement of the hysteresis loop with an increase in carbonisation temperature reflects the expansion of micropores, which may lead to structural collapse in the material.(20)

The activation ratio and temperature at which carbonisation occurs significantly impact pore distribution and other structural parameters. The BET theory, t-plot method, and BJH theory were employed to calculate structural parameters such as

surface area and pore volume, which are tabulated in Table 3.2. All these values align well with the nature of the above N₂ adsorption-desorption isotherms. Total surface area and pore volume increase as KOH concentration rises. These results suggest the availability of micropores in the structure of AC that may be attributed to effective KOH activation. Micropores are responsible for improving the surface area of CNSAC-X-Ys. These structures enhance the accessible surface area for electrolytes and facilitate rapid ion transport.(21) The higher value of average pore diameter in CNSAC-3-700 may be attributed to the number of mesopores in it. The surface area and pore volume values increase with a rise in carbonisation temperature. However, a further increase in carbonisation temperature to 800 °C negatively affects the surface area and pore volume of CNSAC.

Table 3.2 Pore structure parameters of CNSAC-X-Ys

Sample Name	Surface area [m ² g ⁻¹]			Pore volume [cm ³ g ⁻¹]			Diameter (nm)
	Micro pores	Meso pore	Total	Micro pores	Meso pore	Total	
CNSAC-1-700	449	115	771	0.19	0.14	0.25	0.54
CNSAC-2-700	704	65	835	0.37	0.07	0.40	0.97
CNSAC-3-700	880	94	1150	0.41	0.06	0.56	1.96
CNSAC-2-600	466	17	601	0.24	0.02	0.25	0.58
CNSAC-2-800	274	109	448	0.27	0.16	0.27	1.51

3.3.2 Electrochemical characterisations

Electrochemical properties of CNSAC-X-Ys were studied using a three-electrode configuration with 1 M Na₂SO₄ as electrolyte.

3.3.2.1 Cyclic voltammetry (CV)

CV was carried out to study the electrochemical efficiency of the material at different scan rates from 1 to 100 mV s^{-1} over a potential window of 0- 0.8V. Figure 3.7 shows cyclic voltammograms of CNSACs at a scan rate of 10 mV s^{-1} , which are symmetric and have highly reversible charging and discharging curves. This quasi-rectangular nature of these curves reflects the formation of an electrochemical double layer and is ideal for efficient supercapacitor electrode material.(22)

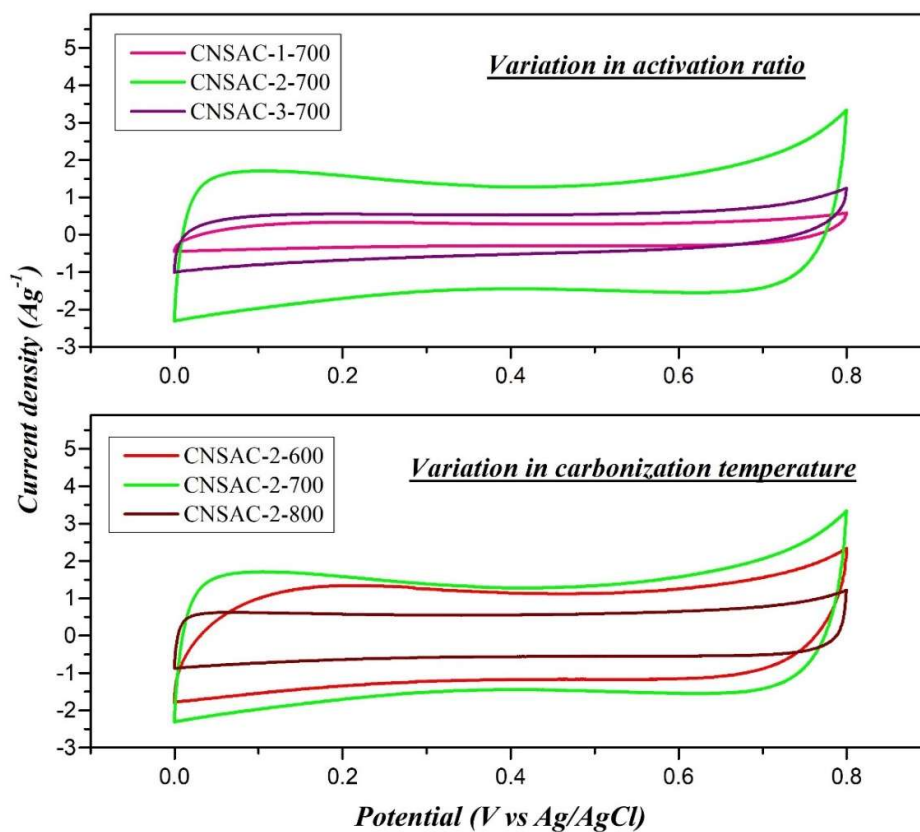


Figure 3.7 Cyclic voltammogram of CNSAC-X-Ys

The integral area of the CV curves reflects the system's specific capacitance. The capacitive properties of CNSACs are highly influenced by the activation ratio and carbonisation temperature used during the synthesis of CNSACs, and the variation in the value of specific capacitance with activation ratio and carbonisation temperature can be identified from these curves. The area under the cyclic voltammogram first increases and then decreases with an increase in activation ratio and carbonisation temperature. The larger curve area of CNSAC-2-700 suggests its better capacitive

properties among CNSAC-X-Ys and indicates its great potential as a viable electrode material.(23) The value of activation ratio and carbonisation temperature is optimized as 1:2 and 700 °C.

The CV curves of CNSAC-2-700 at different scan rates are shown in Figure 3.8. The curves maintain their quasi-rectangular shape even at higher scan rates, which is an ideal characteristic of EDLCs. This also suggests rapid charging and discharging across the carbon network. The gradual distortion of CV curves with an increasing scan rate is related to the higher fraction of micropores in CNSAC-2-700. Higher ion diffusion resistance causes a reduction in charge accumulation on the electrode surface at higher scan rates.(24) This, in turn, decreases the specific capacitance value of CNSAC-2-700.

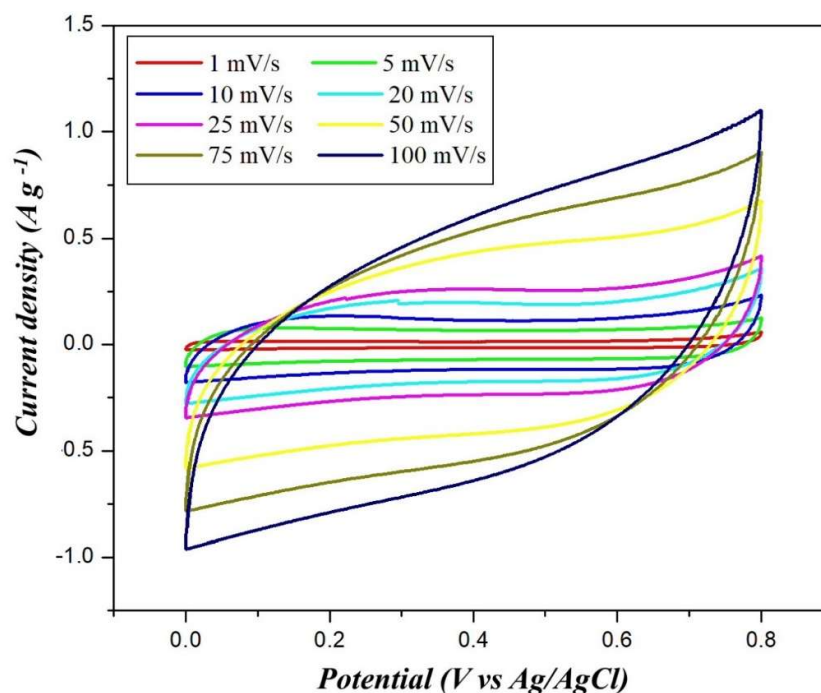


Figure 3.8 Cyclic voltammogram of CNSAC-2-700 at different scan rates

3.3.2.2 Galvanostatic charge-discharge (GCD)

GCD analysis is used to further evaluate the electrochemical performance of CNSAC-X-Ys. Figure 3.9 illustrates GCD curves of CNSAC-X-Ys at a current density of 1 A g^{-1} . The symmetrical and triangular nature of the curves reflects remarkable

electrochemical reversibility and coulombic efficiency of the materials. Additionally, the negligible voltage drops at turning points represent the minimal internal resistance of the materials. These are desirable features for efficient electrode materials with good capacitive behaviour.(24,25) The significantly longer discharge curve of CNSAC-2-700 indicates its higher specific capacitance value than other samples. The GCD curves reflect the effect of activation ratio and carbonisation temperature on determining the efficiency of the electrode materials. These results go hand in hand with the observations of CV curves. The specific capacitance was found to increase up to an activation ratio of 1:2 and a carbonisation temperature of 700 °C, then drops again with further increase in activation ratio and carbonisation temperature.

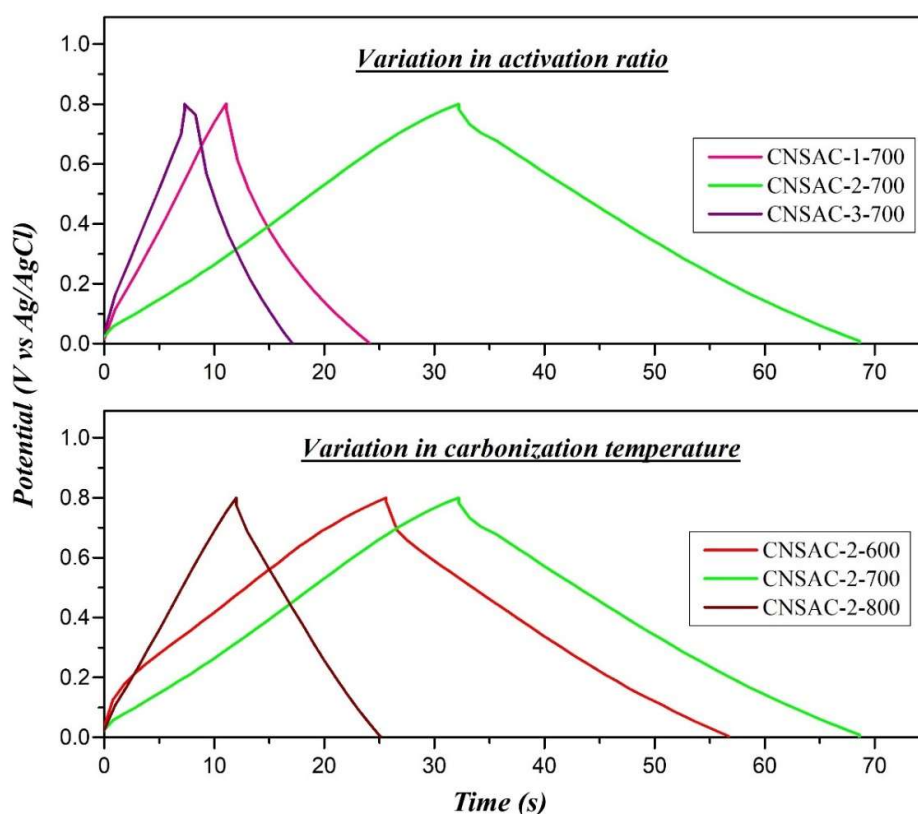


Figure 3.9 Galvanostatic charge-discharge curves of CNSAC-X-Ys

The variation of the charging-discharge behaviour of CNSAC-2-700 with an increasing current density can be identified in Figure 3.10. As current density increases, charging and discharging times reduce, which is a typical characteristic of EDLCs. The

gravimetric capacitance values of CNSACs were calculated using the following equation.

$$C_{sp} = \frac{I \times \Delta t}{m \times \Delta v} \quad 3.1$$

In equation 3.1, I , m , Δt , and Δv represent the current, active material's mass, discharge time, and potential range, respectively.(26) The values of C_{sp} for CNSAC-X-Ys are tabulated in Table 3.3. These results are consistent with those of BET analysis. Moreover, the available accessible surface area in electrode materials has a considerable impact on determining their electrochemical efficiency.

Table 3.3 Specific capacitance values of CNSAC-X-Ys

	CNSAC-1-700	CNSAC-2-700	CNSAC-3-700	CNSAC-2-600	CNSAC-2-800
Specific capacitance @ 1Ag ⁻¹ (Fg ⁻¹)	197	214	138	150	109

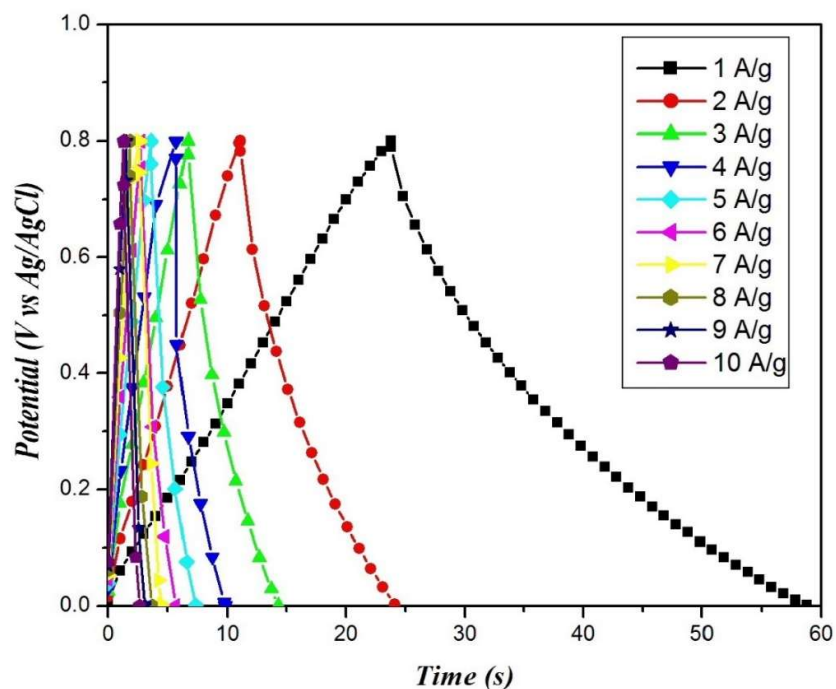


Figure 3.10 GCD curves of CNSAC-2-700 at different current rates

Figure 3.11 shows variation in the specific capacitance value of CNSAC-2-700 at different current densities. The reduction in these values at higher current density indicates the formation of EDLC in the system.

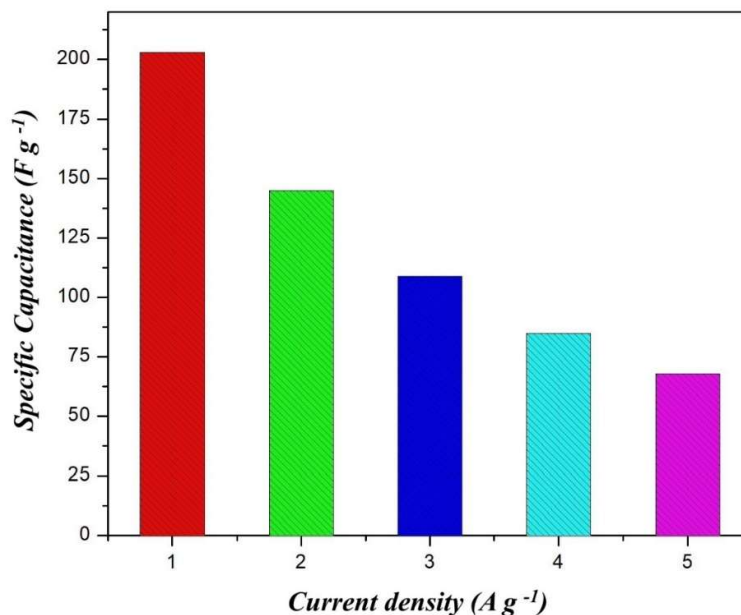


Figure 3.11 Dependence of specific capacitance on current densities

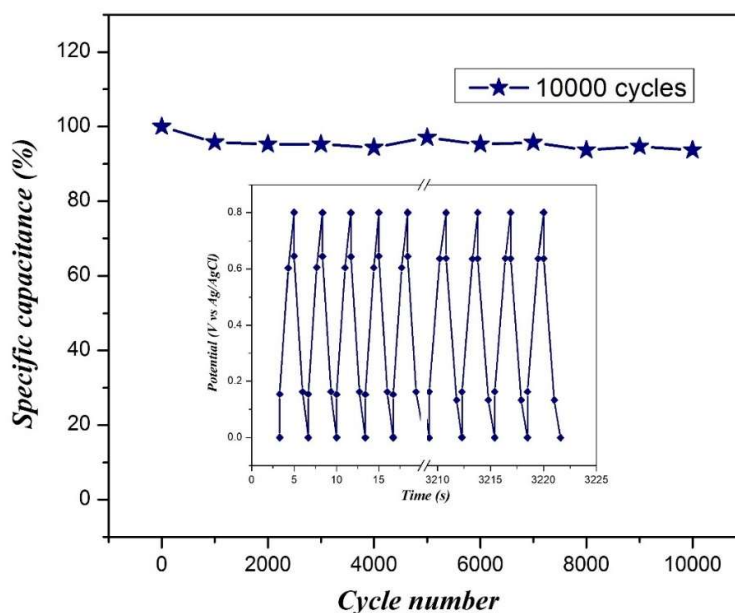


Figure 3.12 Cycle life test of CNSAC-2-700 at a current density of $10 Ag^{-1}$

Cycling stability is a critical factor to be analysed for understanding the viability of electrode material for practical supercapacitor applications. 10000 cycles of

charging and discharging at a current density of 10 A g^{-1} were carried out to study the cycling stability of CNSAC-2-700. Figure 3.12 represents the cycling performance of CNSAC-2-700 over 10000 GCD cycles, with the first and last five charge-discharge cycles in the inset. The material retains a capacitance of 94% after 10000 charging and discharging cycles. The GCD curves in the inset are remarkably comparable, further confirming better capacitive retention of the material. The large surface area and microporous structure may be responsible for this. These factors facilitate rapid ion diffusion by creating an adequate electrode-electrolyte interface and increasing the accessible surface area for electrolyte ion transport.(27) The remarkable value of specific capacitance and excellent cycling stability are essential for an effective supercapacitor electrode material. All these results confirm the significant potential of CNSAC-2-700 for supercapacitor applications.

Table 3.4. Comparison of electrochemical properties of different activated carbon materials.

Precursor material	Activation	Specific capacitance [F g^{-1}]	Current density [A g^{-1}]	Electrolyte	Ref.
Corn cob	KOH	153	1	0.5 M H_2SO_4	(22)
Rice husk	H_3PO_4	176	0.05	6 M KOH	(25)
Sakura flower	KOH	265.8	0.2	6 M KOH	(28)
Banana peel	ZnCl_2	74	0.02	1 M Na_2SO_4	(29)
Green tea waste	KOH	165	0.5	1 M H_2SO_4	(30)
Coconut husk	Steam	141	1	6 M KOH	(31)
Commercial AC	-	60	1	1 M H_2SO_4	(32)
Commercial AC	-	200	0.05	1 M H_2SO_4	(33)
Cashew nut shell	KOH	214	1	1 M Na_2SO_4	Present work

The specific capacitance values of various AC electrode materials in different electrolyte systems are summarized in Table 3.4. Based on these references, the potential of CNSAC-2-700 for an efficient supercapacitor system is validated. The table also suggests remarkable specific capacitance value of the material in comparison with previously reported values.

3.3.2.3 Electrochemical impedance spectroscopy (EIS)

EIS analysis was conducted to investigate the frequency response and capacitive behaviours in supercapacitor systems. The analysis was carried out in 1 M Na_2SO_4 aqueous solution for a frequency ranging from 10^{-2} to 10^5 Hz. The frequency response of CNSAC-X-Ys is represented as Nyquist plots, as shown in Figure 3.13.

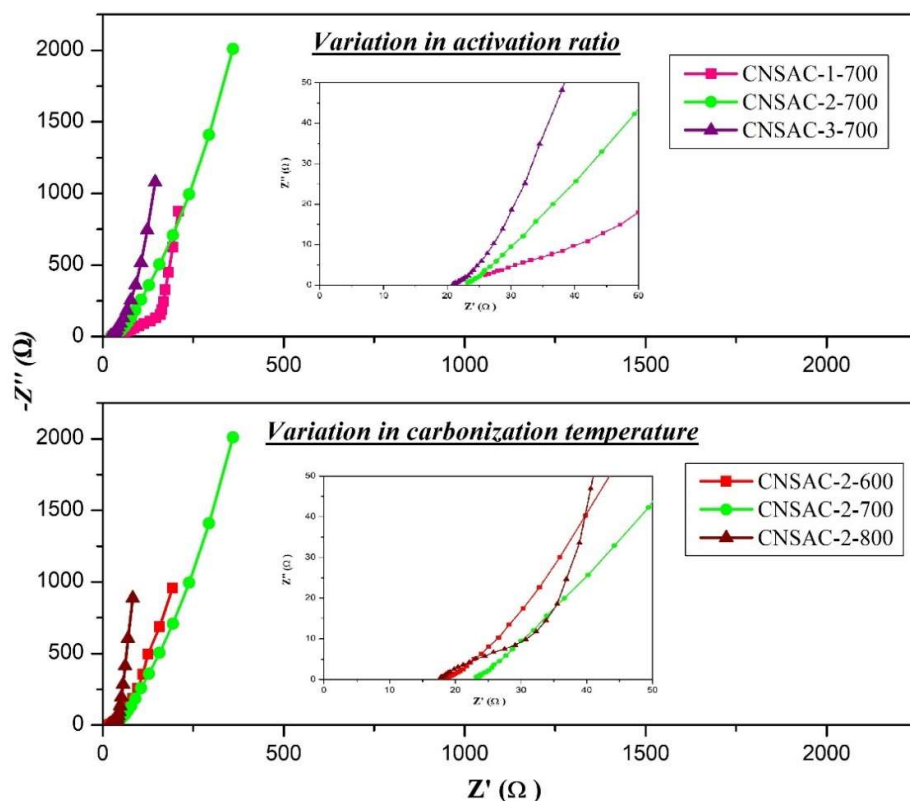


Figure 3.13 Nyquist plot for a frequency range 10^5 Hz to 10^{-3} Hz (the enlarged curves at a high frequency range are given as an inset)

The Nyquist plot of an ideal supercapacitor will be a vertical curve. However, for practical supercapacitors, the Nyquist plot generally consists of a semicircle in the

high-frequency region, followed by straight lines with a slope of 45° and with a slope of more than 45° in the low-frequency region. The semi-circle in the higher frequency region indicates the faradaic process of charge transfer occurring at the electrode-electrolyte interface.(34)

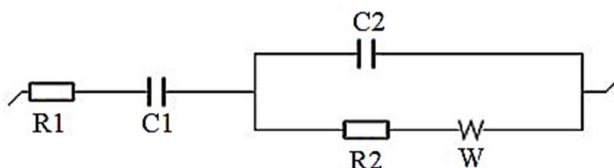


Figure 3.14 Equivalent circuit diagram of CNSAC-X-Ys

The EIS curve with a negligible semicircle in the higher frequency region reflects fast charge transfer in these systems. The frequency-dependent ionic diffusion in the electrolyte (Warburg element) is represented by the region after the faradaic region.(35) The longer straight line of slope close to 1 in the extreme low-frequencies in the Nyquist plot of CNSAC-2-700 validates a faster ion transfer rate in it. The lower intersection of the curve indicates the equivalent series resistance (ESR) of the system.(36) Figure 3.14 displays the equivalent circuit diagram of CNSAC-X-Ys. Table 3.5 gives the values of R1, R2, C1, C2 and W elements in the fitted equivalent circuit.

Table 3.5 The values of elements in the equivalent circuit of CNSACs

Sample	R ₁ [Ω]	R ₂ [Ω]	C ₁ [F]	C ₂ [μF]	W [Ω.s ^{-1/2}]
CNSAC-1-700	14.44	22.76	0.036	24.96	95.94
CNSAC-2-700	16.77	23.24	0.089	41.86	69.88
CNSAC-3-700	15.23	21.74	0.016	5.28	27.02
CNSAC-2-600	18.63	20.01	0.097	2.5	232.9
CNSAC-2-800	19.11	19.25	0.014	0.84	15.37

3.3.3 The electrochemical characterisations of symmetric supercapacitors (SSC- Na_2SO_4 , SSC- NaNO_3)

The viability of CNSAC-2-700-based electrode material was evaluated using two-electrode configurations. SSCs were fabricated with 1 M Na_2SO_4 , named SSC- Na_2SO_4 . CV analysis of SSC- Na_2SO_4 was carried out for a potential range of 0 to 1.2 V at scan rates varying from 1 to 100 mV s^{-1} . The CV curves of SSC- Na_2SO_4 are displayed in Figure 3.15. The nearly rectangular CV curves, with no redox peaks, are typical for EDLCs. The curves retain their quasi-rectangular shape, even at higher scan rates.

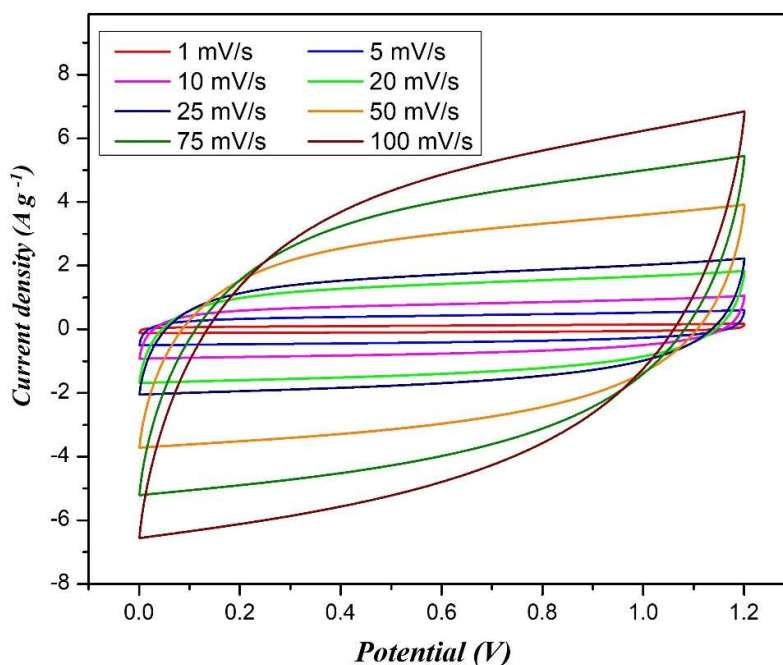


Figure 3.15 CV curves of SSC- Na_2SO_4 at different scan rates (1 to 100 mV s^{-1})

The GCD studies of SSC- Na_2SO_4 were carried out by varying current densities across a voltage window of 0-1.2 V. Figure 3.16 shows GCD curves of SSC- Na_2SO_4 . The curves are linear, symmetrical and triangular representing the reversibility of EDLCs. The specific capacitance of the discharge curve gives the measure of specific capacitance.

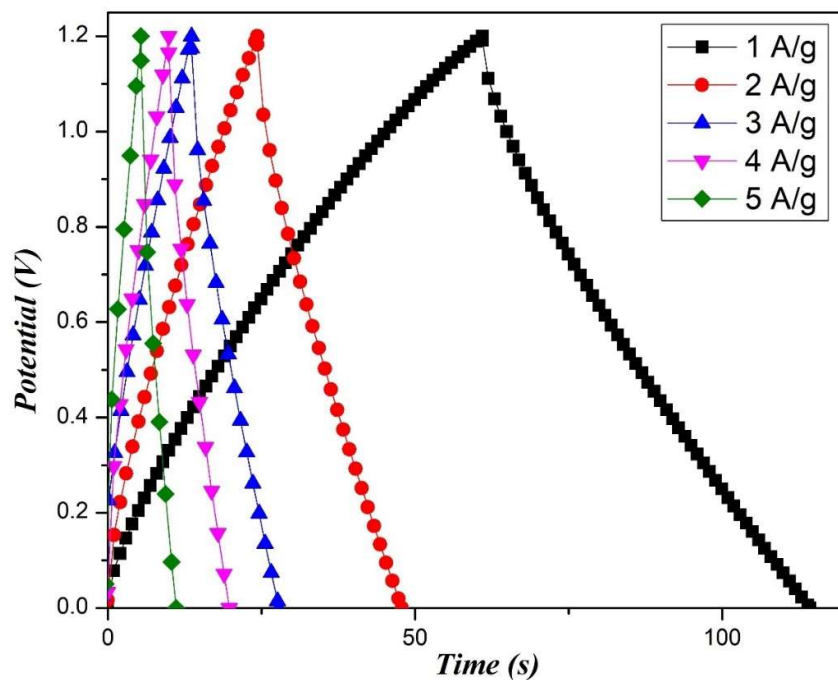


Figure 3.16 GCD curves of SSC- Na_2SO_4 at current densities from 1 to 5 A/g^{-1}

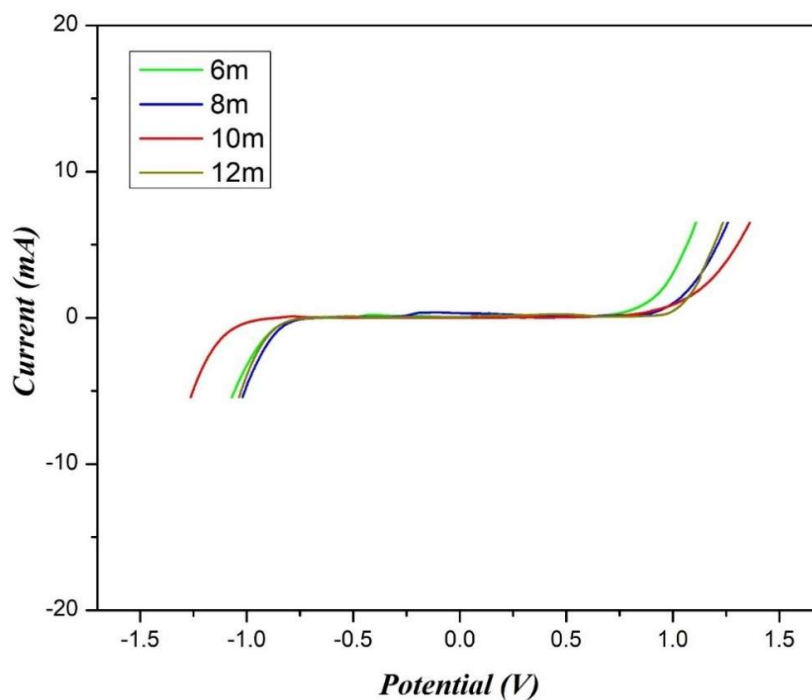


Figure 3.17 LSV curves with different concentrations of SSC- NaNO_3

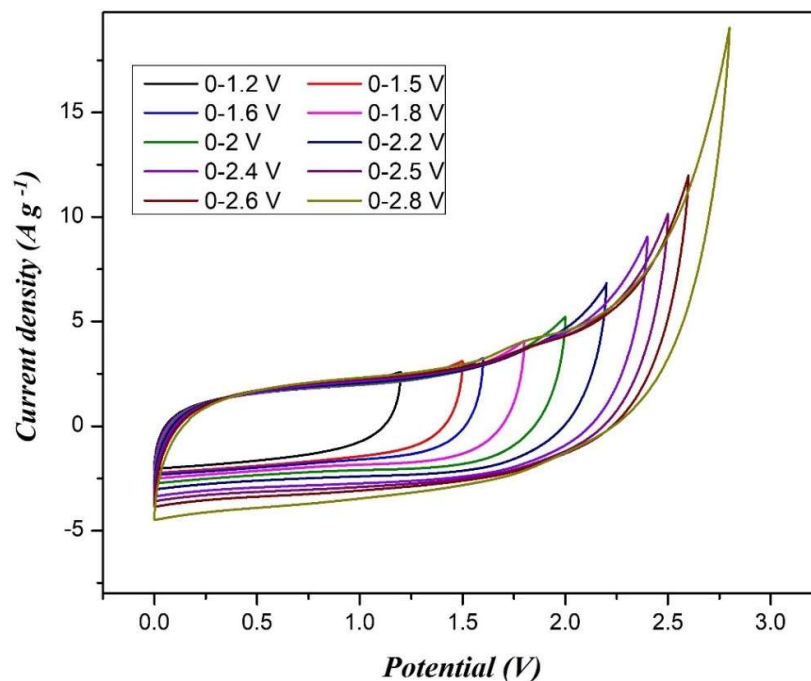


Figure 3.18 CV curves at different ESWs

NaNO_3 WIS electrolyte was used to understand its potential to address the lower potential range of conventional aqueous electrolytes. The electrochemical performance of WIS electrolytes mainly depends on the concentration of salt in them. LSV at a scan rate of 5 mV s^{-1} was performed for different concentrations of NaNO_3 (6 m, 8 m, 10 m, and 12 m). The optimum salt concentration of the WIS electrolyte was determined based on LSV results. Figure 3.17 shows the dependence of the electrochemical stability window (ESW) on the concentration of NaNO_3 electrolyte. Stainless steel electrodes are used as working and counter electrodes. Ag/AgCl is employed as the reference electrode.⁽³⁷⁾ ESW was found to be maximum (0-2 V) for 10 m NaNO_3 . SSC was fabricated using 10 m NaNO_3 to ensure maximum performance and was denoted as SSC- NaNO_3 .

The stability of the potential window is further demonstrated by CV curves at different potential ranges (Figure 3.18) with a scan rate of 50 mV s^{-1} . These curves validate that the ESW of SSC- NaNO_3 is 0- 2V. Figure 3.19 displays the variation in the cyclic voltammogram of as-fabricated SSC- NaNO_3 at different scan rates ranging

from 1 to 100 mV s^{-1} . The superior rate capability of SSC- NaNO_3 is shown by the quasi-rectangular shape of its CV curve at higher scan rates.

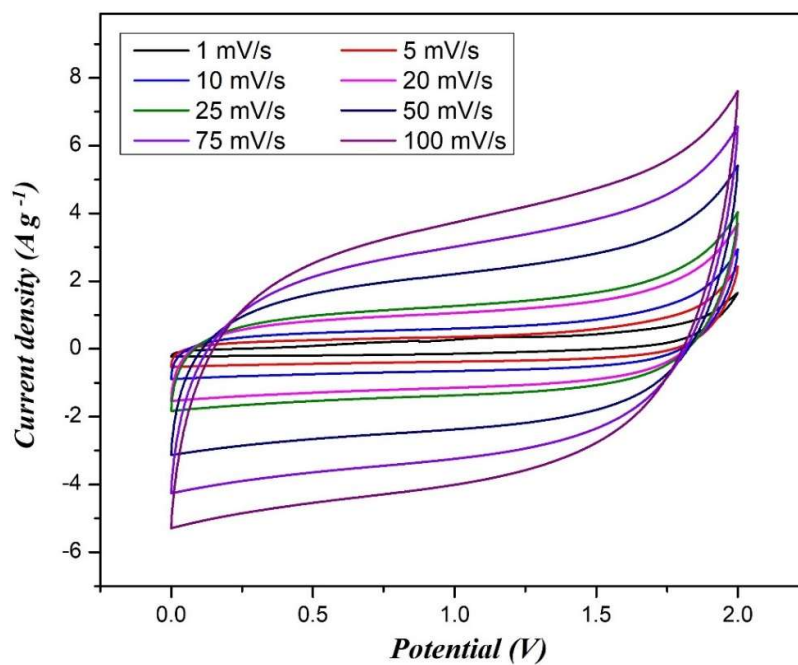


Figure 3.19 CV curves of SSC- NaNO_3 at different scan rates (1 to 100 mV s^{-1})

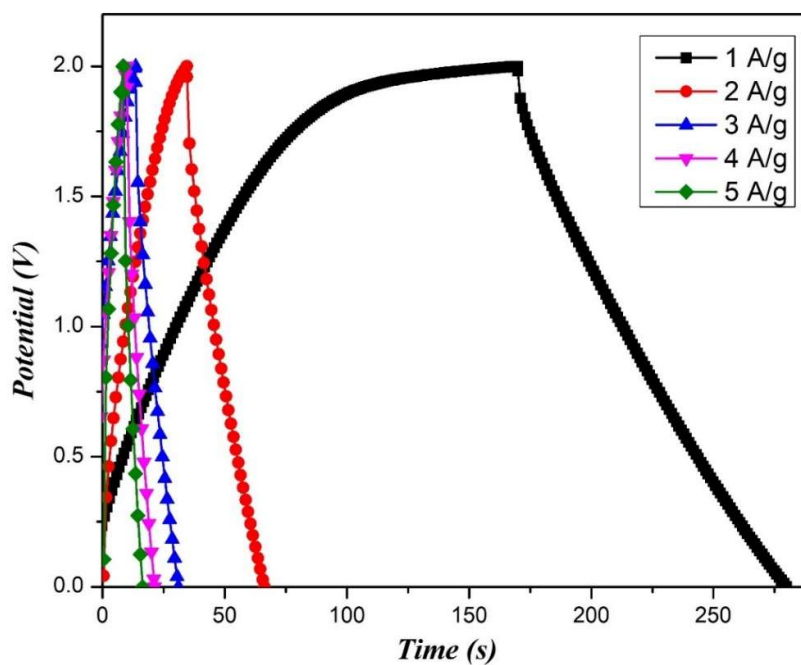


Figure 3.20 GCD curves of SSC- NaNO_3 at current densities from 1 to 5 A g^{-1}

The GCD analysis of SSC- NaNO_3 was performed for different current densities. The GCD curves in Figure 3.20 have a characteristic triangular shape, indicating an electrochemically reversible system. The capacitive behaviour and negligible internal resistance of SSC- NaNO_3 is well demonstrated by ideal triangular pattern of the GCD curves and is consistent with the CV results.

The performance of SSC- Na_2SO_4 and SSC- NaNO_3 is compared using CV, GCD and EIS analysis. CV at a scan rate of 50 mV s^{-1} displayed in Figure 3.21. The CV curve of SSC- NaNO_3 exhibit wider potential window and has a larger integral area indicating its higher specific capacity than SSC- Na_2SO_4 . The enhanced specific capacity of SSC- NaNO_3 can be attributed to the effect of increased conductivity.(38)

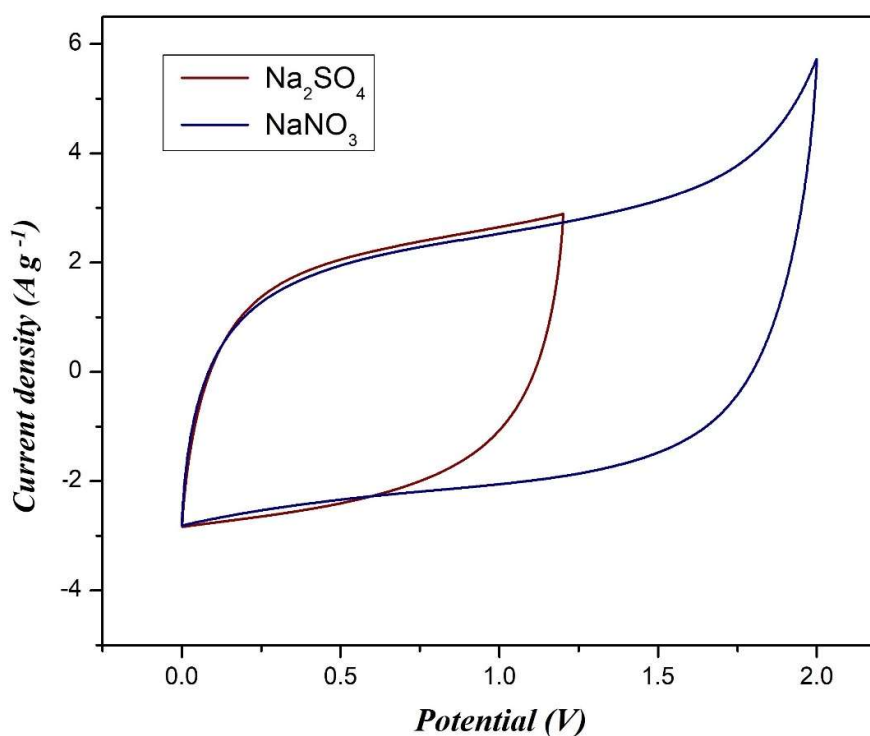


Figure 3.21 CV curves of SSCs at a scan rate of 50 mV s^{-1}

Figure 3.22 represents the observations of GCD analysis carried out for a potential range of 0-1.2 V for SSC- Na_2SO_4 and 0-2 V for SSC- NaNO_3 at a current density of 2 Ag^{-1} . SSC- NaNO_3 has a larger discharging time and a smaller IR drop. The larger discharge time indicates greater specific capacitance of SSC- NaNO_3 as the discharge time in the GCD curve represents its specific capacitance value.

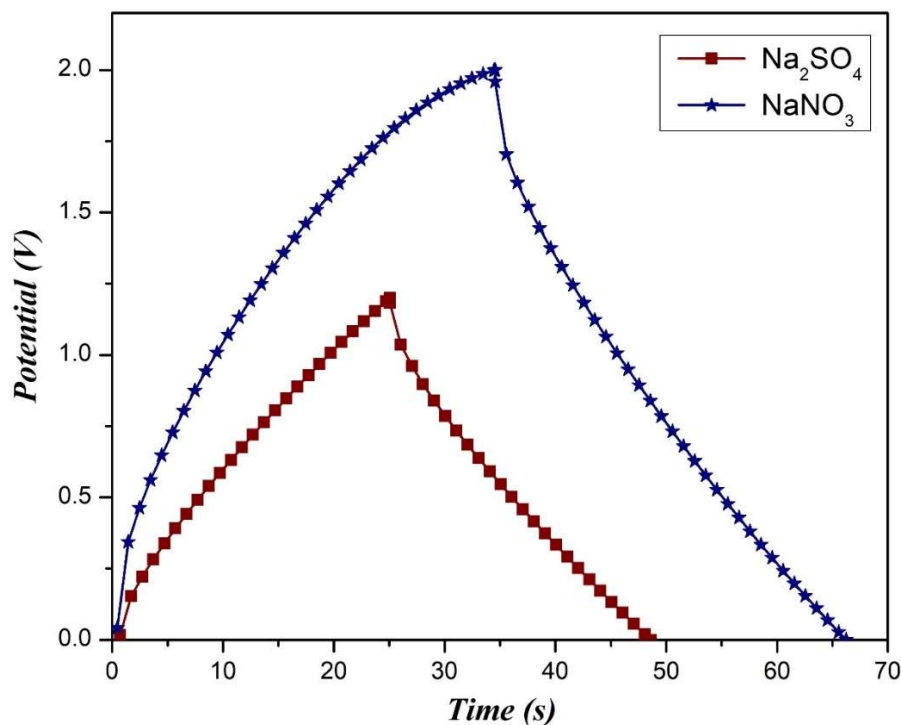


Figure 3.22 GCD curves of SSCs at the current density of 2 Ag^{-1}

The specific capacitance value is calculated using Equation 3.2.

$$C_{sp} = \frac{4 \times I \times \Delta t}{m \times \Delta v} \quad 3.2$$

In equation 3.2, C_{sp} , ΔV , I , Δt , and m represent specific capacitance, voltage difference between the beginning and end of discharge curves, current, time taken for complete discharge, and the total weight of the two electrodes used, respectively. (39) The values of specific capacitance of SSC- NaNO_3 and SSC- Na_2SO_4 are 110 Fg^{-1} and 90 Fg^{-1} respectively at a current density of 1 Ag^{-1} . Thus, an improved specific capacitance and a wider potential window of SSC confirm the superiority of WIS electrolytes over conventional SSCs.

A decrease in specific capacitance values is observed for both SSCs as current density increases. Figure 3.23 reflects the dependence of specific capacitance on the value of applied current densities. GCD tests at a current density of 10 Ag^{-1} for 10000 cycles are carried out to further evaluate the long-term cycle stability of SSCs, as shown in Figure 3.24. The capacitive retention of SSC- Na_2SO_4 and SSC- NaNO_3 is found to

be 74% and 83% over 10000 cycles of charging and discharging. The greater capacitive retention of SSC- NaNO_3 indicates better efficiency of the WIS electrolyte.

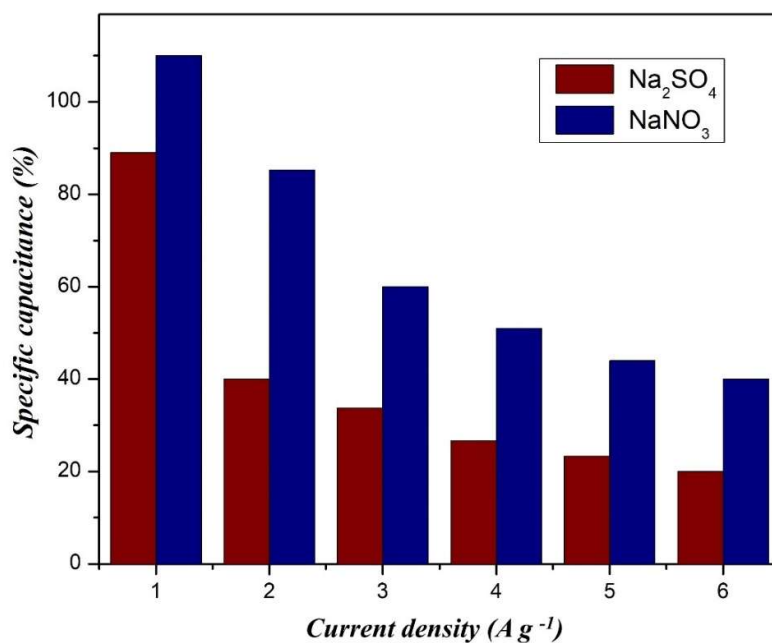


Figure 3.23 Variation in the value of specific capacitance with current density

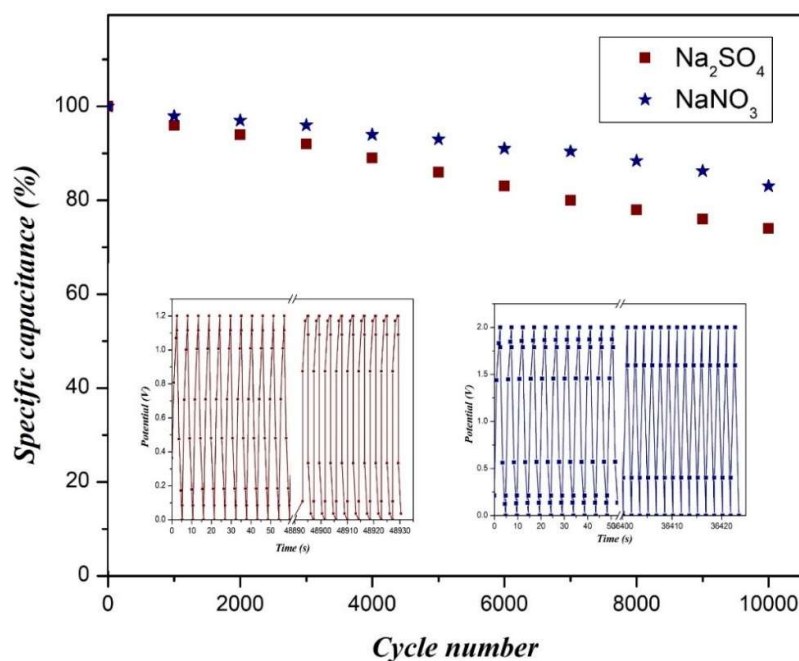


Figure 3.24 Cycle test of SSCs at a current density of 10 Ag^{-1} for 10000 cycles

The Nyquist plots in Figure 3.25 are further used to explore the capacitive behaviour of both SSC systems. The curves are enlarged at higher frequency ranges, and the equivalent circuit diagram is shown as an inset. The EIS curves exhibit a characteristic straight line in the lower frequency region, confirming the presence of an electric double layer at the electrode–electrolyte interfaces. The vertical line in the Nyquist plot of the SSC- NaNO_3 is significantly longer than that of SSC- Na_2SO_4 , which could be related to the enhanced capacitive nature of SSC- NaNO_3 . The semicircle with a smaller diameter in the Nyquist plot of SSC- NaNO_3 confirms the improved capacitance due to the WIS electrolyte.(40) The ESR value for the SSC- NaNO_3 is found to be smaller than that of SSC- Na_2SO_4 , which indicates an increase in conductivity of the material with WIS electrolyte. The values of components in equivalent circuits of SSCs are tabulated in Table 3.6. Impedance analysis results are also consistent with those of other electrochemical characterisations.

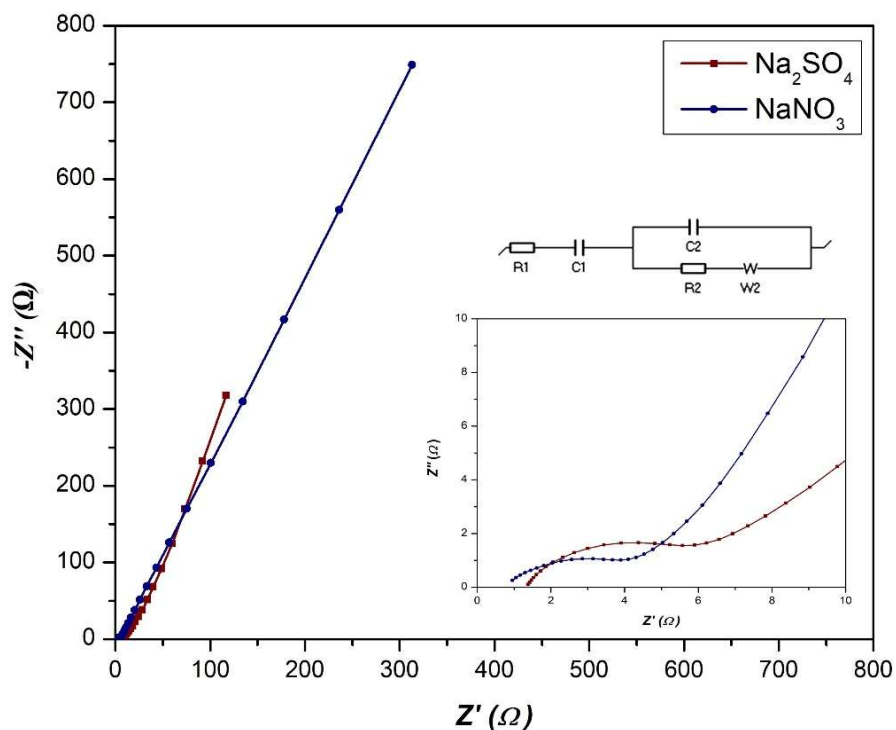


Figure 3.25 Nyquist plots of SSC- Na_2SO_4 and SSC- NaNO_3 (the inset shows the enlarged curves in a high frequency range and the equivalent circuit diagram).

Table 3.6. The values of elements in the equivalent circuit of two SSCs

SSC	ESR [Ω]	R1 [Ω]	R2 [Ω]	C1 [F]	C2 [μ F]	W2 [$\Omega.s^{(1/2)}$]
SSC-Na ₂ SO ₄	1.30	1.54	3.453	0.07	24.51	24.84
SSC-NaNO ₃	0.64	0.75	0.93	0.05	15.49	31.52

Table 3.7. Comparison of electrochemical properties of activated carbon electrode materials in various WIS-based SSC systems.

Electrode Material	Specific capacitance [Fg ⁻¹]	Current density [Ag ⁻¹]	WIS Electrolyte	Ref.
Ground grain hull-derived AC	59	0.5	17m NaClO ₄	(40)
Commercial AC	32.68	1	12m NaNO ₃	(41)
Rose petal-derived AC	63	0.5	20m LiTFSI	(42)
Commercial AC	33	1	17m NaClO ₄	(43)
Commercial AC	31.9	1	17m NaClO ₄	(44)
Prosopisjuliflora	101	0.05	35M NaFSI+3M NaOAc	(45)
Commercial AC	27.8	1	21m LiTFSI/H ₂ O/ACN	(46)
Cashew nut shell	110	1	10m NaNO ₃	Present work

The electrochemical performance of activated carbon in several WIS-based SSC systems is compared in Table 3.7. The table summarises the specific capacitance obtained with various WIS electrolytes. CNSAC has a supreme specific capacitance

value, which is even better than the previously reported AC-based SSCs with WIS electrolytes. These results conclude the greater feasibility of SSC with CNSAC as electrode material and NaNO_3 WIS electrolyte.

3.4 Conclusion

The preparation of CNSAC was done using a cost-effective and environmentally friendly method. SEM, XRD, surface area analysis, adsorption-desorption isotherms and FTIR studies validated the presence of hierarchical pore distribution in CNSAC, which facilitates fast ion transport in the system. The cyclic voltammogram displayed a reversible quasi-rectangular shape indicative of the formation of an electric double layer at the electrode-electrolyte interface. The highest specific capacitance value achieved for CNSAC-2-700 is 214 F g^{-1} at a current density of 1 Ag^{-1} . Based on these results, the optimal activation ratio and carbonisation temperature for preparing efficient CNSAC were found to be 1:2 and 700°C , respectively. The high specific capacitance and excellent capacitance retention are appropriate for practical supercapacitor applications. The SSC with CNSAC electrodes and WIS electrolyte demonstrates superior performance, achieving a high specific capacitance of 110 Fg^{-1} . It offers a wider potential window (0- 2V) and excellent cycle stability, with 83% capacitance retention. Additionally, it features lower ESR compared to conventional aqueous electrolyte-based SSC systems. In conclusion, cashew nut shell waste has the potential to be developed into a highly valuable product for supercapacitor electrode applications, making it a sustainable choice for energy storage solutions.

References

1. Ahmed MB, Hasan Johir MA, Zhou JL, Ngo HH, Nghiem LD, Richardson C, et al. Activated carbon preparation from biomass feedstock: Clean production and carbon dioxide adsorption. *J Clean Prod.* 2019 Jul 10;225:405–13.
2. Yan B, Zheng J, Feng L, Du C, Jian S, Yang W, et al. Wood-derived biochar as thick electrodes for high-rate performance supercapacitors. *Biochar.* 2022 Dec 1;4(1).
3. Aina EO, Adisa AF, Olayanju TMA, ismaila SO. Performance Evaluation of a Developed Cashew Nut Shell Liquid Expeller. *Agricultural Engineering.* 2018 Jul 1;22(2):5–19.

4. Subramaniam R, Kumar Ponnusamy S. Novel adsorbent from agricultural waste (cashew NUT shell) for methylene blue dye removal: Optimization by response surface methodology. *Water Resour Ind.* 2015 Sep 1;11:64–70.
5. Prabu D, Parthiban R, Senthil Kumar P, Kumari N, Saikia P. Adsorption of copper ions onto nano-scale zero-valent iron impregnated cashew nut shell. *Desalination Water Treat.* 2016 Mar 21;57(14):6487–502.
6. Spagnoli AA, Giannakoudakis DA, Bashkova S. Adsorption of methylene blue on cashew nut shell based carbons activated with zinc chloride: The role of surface and structural parameters. *J Mol Liq.* 2017 Mar 1;229:465–71.
7. Maity S, BMN, Kella T, Shee D, Das PP, Mal SS. Activated carbon- supported Vanadonickelate (IV) based hybrid materials for energy application. *J Energy Storage.* 2021 Aug 1;40.
8. Sekar S, Kim DY, Lee S. Excellent oxygen evolution reaction of activated carbon-anchored nio nanotablets prepared by green routes. *Nanomaterials.* 2020 Jul 1;10(7):1–13.
9. Singh M, Gupta A, Sundriyal S, Jain K, Dhakate SR. Kraft lignin-derived free-standing carbon nanofibers mat for high-performance all-solid-state supercapacitor. *Mater Chem Phys.* 2021 May 1;264.
10. Jain A, Ghosh M, Krajewski M, Kurungot S, Michalska M. Biomass-derived activated carbon material from native European deciduous trees as an inexpensive and sustainable energy material for supercapacitor application. *J Energy Storage.* 2021 Feb 1;34.
11. Dizbay-Onat M, Vaidya UK, Lungu CT. Preparation of industrial sisal fiber waste derived activated carbon by chemical activation and effects of carbonization parameters on surface characteristics. *Ind Crops Prod.* 2017 Jan 1;95:583–90.
12. Arshanitsa A, Jashina L, Pals M, Ponomarenko J, Akishin Y, Zake M. Characteristics of the Main-and Side-Stream Products of Microwave Assisted Torrefaction of Lignocellulosic Biomass of Different Origination. *Energies.* 2022 Mar 2;15(5):1857.
13. Hassan MF, Sabri MA, Fazal H, Hafeez A, Shezad N, Hussain M. Recent trends in activated carbon fibers production from various precursors and applications—A comparative review. Vol. 145, *Journal of Analytical and Applied Pyrolysis.* Elsevier B.V.; 2020.
14. Rajesh M, Manikandan R, Park S, Kim BC, Cho WJ, Yu KH, et al. Pinecone biomass-derived activated carbon: the potential electrode material for the development of symmetric and asymmetric supercapacitors. *Int J Energy Res.* 2020 Sep 1;44(11):8591–605.
15. Awasthi GP, Bhattarai DP, Maharjan B, Kim KS, Park CH, Kim CS. Synthesis and characterizations of activated carbon from *Wisteria sinensis* seeds biomass for energy storage applications. *Journal of Industrial and Engineering Chemistry.* 2019 Apr 25;72:265–72.
16. Veeramani V, Sivakumar M, Chen SM, Madhu R, Alamri HR, Alothman ZA, et al. Lignocellulosic biomass-derived, graphene sheet-like porous activated carbon for electrochemical supercapacitor and catechin sensing. *RSC Adv.* 2017;7(72):45668–75.

17. Sesuk T, Tammawat P, Jivaganont P, Somton K, Limthongkul P, Kobsiriphat W. Activated carbon derived from coconut coir pith as high performance supercapacitor electrode material. *J Energy Storage*. 2019 Oct 1;25.
18. Bai P, Liu W, Yang C, Wei S, Xu L. Boosting electrochemical performance of activated carbon by tuning effective pores and synergistic effects of active species. *J Colloid Interface Sci*. 2021 Apr 1;587:290–301.
19. Yang S, Zhang K. Converting corncob to activated porous carbon for supercapacitor application. *Nanomaterials*. 2018 Apr 1;8(4).
20. Zheng S, Zhang J, Deng H, Du Y, Shi X. Chitin derived nitrogen-doped porous carbons with ultrahigh specific surface area and tailored hierarchical porosity for high performance supercapacitors. *Journal of Bioresources and Bioproducts*. 2021 May 1;6(2):142–51.
21. Dubey P, Shrivastav V, Singh M, Maheshwari PH, Sundriyal S, Dhakate SR. Electrolytic Study of Pineapple Peel Derived Porous Carbon for All-Solid-State Supercapacitors. *ChemistrySelect*. 2021 Nov 15;6(42):11736–46.
22. Yang S, Zhang K. Converting corncob to activated porous carbon for supercapacitor application. *Nanomaterials*. 2018 Apr 1;8(4).
23. Wei H, Wang H, Li A, Li H, Cui D, Dong M, et al. Advanced porous hierarchical activated carbon derived from agricultural wastes toward high performance supercapacitors. *J Alloys Compd*. 2020 Apr 15;820.
24. Feng L, Yan B, Zheng J, Chen J, Wei R, Jiang S, et al. Soybean protein-derived N, O co-doped porous carbon sheets for supercapacitor applications. *New Journal of Chemistry*. 2022;46(22):10844–53.
25. Charoensook K, Huang CL, Tai HC, Lanjapalli VVK, Chiang LM, Hosseini S, et al. Preparation of porous nitrogen-doped activated carbon derived from rice straw for high-performance supercapacitor application. *J Taiwan Inst Chem Eng*. 2021 Mar 1;120:246–56.
26. Li YT, Pi YT, Lu LM, Xu SH, Ren TZ. Hierarchical porous active carbon from fallen leaves by synergy of K₂CO₃ and their supercapacitor performance. *J Power Sources*. 2015 Dec 20;299:519–28.
27. Li Y, Wang G, Wei T, Fan Z, Yan P. Nitrogen and sulfur co-doped porous carbon nanosheets derived from willow catkin for supercapacitors. *Nano Energy*. 2016 Jan 1;19:165–75.
28. Ma F, Ding S, Ren H, Liu Y. Sakura-based activated carbon preparation and its performance in supercapacitor applications. *RSC Adv*. 2019;9(5):2474–83.
29. Taer E, Taslim R, Aini Z, Hartati SD, Mustika WS. Activated carbon electrode from banana-peel waste for supercapacitor applications. In: *AIP Conference Proceedings*. American Institute of Physics Inc.; 2017.
30. Peng C, Yan X Bin, Wang RT, Lang JW, Ou YJ, Xue QJ. Promising activated carbons derived from waste tea-leaves and their application in high performance supercapacitors electrodes. *Electrochim Acta*. 2013 Jan 1;87:401–8.

31. Taer E, Taslim R, Putri AW, Apriwandi A, Agustino A. Activated carbon electrode made from coconut husk waste for supercapacitor application. *Int J Electrochem Sci*. 2018 Dec 1;13(12):12072–84.
32. Huo S, Zhang X, Liang B, Zhao Y, Li K. Synthesis of interconnected hierarchically porous carbon networks with excellent diffusion ability based on NaNO₃ crystal-assisted strategy for high performance supercapacitors. *J Power Sources*. 2020 Feb 29;450.
33. Li B, Dai F, Xiao Q, Yang L, Shen J, Zhang C, et al. Nitrogen-doped activated carbon for a high energy hybrid supercapacitor. *Energy Environ Sci*. 2016 Jan 1;9(1):102–6.
34. Yadav N, Yadav N, Hashmi SA. High-Energy-Density Carbon Supercapacitors Incorporating a Plastic-Crystal-Based Nonaqueous Redox-Active Gel Polymer Electrolyte. *ACS Appl Energy Mater*. 2021 Jul 26;4(7):6635–49.
35. Shabeeba P, Thayyil MS, Pillai MP, Soufeena PP, Niveditha C V. Electrochemical Investigation of Activated Carbon Electrode Supercapacitors. *Russian Journal of Electrochemistry*. 2018 Mar 1;54(3):302–8.
36. Alipoori S, Torkzadeh MM, Mazinani S, Aboutalebi SH, Sharif F. Performance-tuning of PVA-based gel electrolytes by acid/PVA ratio and PVA molecular weight. *SN Appl Sci*. 2021 Mar 1;3(3).
37. Mahankali K, Thangavel NK, Ding Y, Putatunda SK, Arava LMR. Interfacial behavior of water-in-salt electrolytes at porous electrodes and its effect on supercapacitor performance. *Electrochim Acta*. 2019 Dec 5;326.
38. Zhang M, Li Y, Shen Z. “Water-in-salt” electrolyte enhanced high voltage aqueous supercapacitor with all-pseudocapacitive metal-oxide electrodes. *J Power Sources*. 2019 Feb 28;414:479–85.
39. Ye B, Gong C, Huang M, Tu Y, Zheng X, Fan L, et al. Improved performance of a CoTe//AC asymmetric supercapacitor using a redox additive aqueous electrolyte. *RSC Adv*. 2018;8(15):7997–8006.
40. Sundaram MM, Appadoo D. Traditional salt-in-water electrolyte: Vs. water-in-salt electrolyte with binary metal oxide for symmetric supercapacitors: Capacitive vs. faradaic. *Dalton Transactions*. 2020 Sep 7;49(33):11743–55.
41. Guo J, Ma Y, Zhao K, Wang Y, Yang B, Cui J, et al. High-Performance and Ultra-Stable Aqueous Supercapacitors Based on a Green and Low-Cost Water-In-Salt Electrolyte. *ChemElectroChem*. 2019 Oct 31;6(21):5433–8.
42. Xu SW, Zhang MC, Zhang GQ, Liu JH, Liu XZ, Zhang X, et al. Temperature-dependent performance of carbon-based supercapacitors with water-in-salt electrolyte. *J Power Sources*. 2019 Nov 30;441.
43. Bu X, Su L, Dou Q, Lei S, Yan X. A low-cost “water-in-salt” electrolyte for a 2.3 V high-rate carbon-based supercapacitor. *J Mater Chem A Mater*. 2019;7(13):7541–7.
44. Dou Q, Lu Y, Su L, Zhang X, Lei S, Bu X, et al. A sodium perchlorate-based hybrid electrolyte with high salt-to-water molar ratio for safe 2.5 V carbon-based supercapacitor. *Energy Storage Mater*. 2019 Dec 1;23:603–9.

45. Sennu P, Chua R, Dintakurti SSH, Hanna J V., Ramabhadran RO, Aravindan V, et al. Supersaturated “water-in-salt” hybrid electrolyte towards building high voltage Na-ion capacitors with wide temperatures operation. *J Power Sources*. 2020 Oct 1;472.
46. Xiao D, Dou Q, Zhang L, Ma Y, Shi S, Lei S, et al. Optimization of Organic/Water Hybrid Electrolytes for High-Rate Carbon-Based Supercapacitor. *Adv Funct Mater*. 2019 Oct 1;29(42).

Chapter 4

EFFICIENT SOLID-STATE SUPERCAPACITOR WITH MAHOGANY FRUIT SHELL-BASED POROUS ELECTRODE

Some of the contents of this chapter have been published in

- I. P. Merin, T. Anitta, E. G. Veena, M. N. Muralidharan, A. Seema, **Highly Efficient Solid-state Supercapacitor with Porous Electrode Material, Energy Technology, (2023), 11 (9), 2300398.**

4.1 Introduction

Electrolytes are crucial in determining the electrochemical stability window of electrochemical double layer capacitors (EDLCs), directly affecting their energy density. Consequently, developing efficient electrolyte systems for high-performance EDLCs with increased energy densities has become a prominent research focus in recent years. Conventional liquid electrolytes that exhibit high ionic conductivity, high-rate capability, and excellent electrode-electrolyte interfacial properties are commonly used in supercapacitors.(1) Nevertheless, electrolyte leakage, low energy and power densities, corrosion, and limited cycle life restrict the broader application of EDLCs.(2,3)

Solid-state electrolytes, especially gel polymer electrolytes (GPEs), have recently received considerable attention owing to their advantages, such as a wide electrochemical window, relatively high ionic conductivity, ease of handling, high cycling performance, and safety.(4) Furthermore, flexible GPEs have the potential to fulfill the demand for flexible solid-state supercapacitors (FSCs) in the domain of portable and wearable electronics. GPEs generally consist of liquid electrolytes and polymer matrices, such as poly(vinyl alcohol) (PVA), poly(ethylene oxide), poly(methyl methacrylate), polyacrylonitrile, and poly(vinyl pyrrolidone).(5,6) PVA-based aqueous GPEs are widely recognised owing to their considerable merits, including ease of fabrication, low cost, biodegradability, excellent flexibility, nontoxicity, high chemical stability, and high dielectric constant.(7) The addition of salts to the polymer can further enhance the ionic conductivity of GPEs because the free ions act as charge carriers.(8)

Furthermore, an appropriate choice of electrode material can further improve the capacitance, which enhances the energy and power densities of FSCs.(9) The activated carbon (AC) derived from mahogany fruit shells can be a potential candidate for electrode applications in FSCs, owing to its well-defined mesoporous structure and unique surface properties.(10,11) In this study, the activation ratio and carbonisation temperature for the preparation of porous mahogany fruit shell-derived AC (MSAC) were optimised based on their structural and electrochemical properties. Subsequently, highly efficient FSCs were fabricated with MSAC-based electrodes and the rarely

investigated PVA|Na₂SO₄ GPE. The flexibility of the as-prepared FSCs was also validated in different bending conditions to ensure the feasibility of the fabricated FSCs for real-world applications.

4.2 Experimental details

4.2.1 Preparation of Mahogany Fruit Shell-derived Activated Carbon

MSAC was prepared through the chemical activation of mahogany fruit shells (MFS) using KOH as the activating agent. The MFS were cleaned and crushed into powder-like form before the activation process. The precursor was mixed with KOH at different activation ratios (weight ratio of MFS: KOH = 1, 2, and 3). Figure 4.1 represents the detailed methodology used for electrode material preparation in FSC fabrication. Then carbonisation of these activated samples was carried out in a tubular furnace at various carbonisation temperatures (500 °C, 600 °C, 700 °C and 800 °C) with a heating rate of 5 °C min⁻¹. The sample was carbonised for 1 h under continuous Ar (99.99%) supply (flow rate: 1 L min⁻¹). The carbonised materials were washed with 0.1 M HCl and dried overnight at 100 °C.^(12,13) The prepared AC materials were accordingly denoted as MSAC-X-Y, where X denotes the corresponding activation ratio (1, 2, 3), and Y represents the carbonisation temperature (500, 600, 700, and 800 °C).



Figure 4.1 Schematic representation of methodology

4.2.2 Conductivity studies of PVA|Na₂SO₄ GPEs

PVA|Na₂SO₄ GPEs were prepared using various weight ratios of PVA and Na₂SO₄. The ionic conductivity of the PVA|Na₂SO₄ GPEs was measured using EIS analysis in the frequency range of 100–10⁶ Hz at a signal amplitude of 10 mV. The

prepared GPEs were placed between two stainless steel plates of dimensions $1 \times 1 \text{ cm}^2$ and subjected to this conductivity measurement. The ionic conductivities (σ) of the electrolytes were calculated using the following equation:

$$\sigma = \frac{T}{R \times A} \quad 4.1$$

where T is the thickness of the film (cm), R is the bulk resistance (Ω), and A is the contact area of the symmetric electrodes (cm^2). The x -intercept of the Nyquist plot gives the value of R .(14,15)

4.2.3 Preparation of flexible solid-state supercapacitors (FSCs)

The FSCs were fabricated using MSAC-2-700 as the electrode material and PVA|Na₂SO₄ GPE as the electrolyte. A homogeneous slurry was prepared by mixing MSAC-2-700, carbon black, and PVDF at a weight ratio of 8:1:1 in NMP with a magnetic stirrer. The slurry was then coated onto a flexible aluminum current collector using a tape-casting method with a mass loading of 2-4 mg cm⁻¹. The PVA|Na₂SO₄ GPE was sandwiched between prepared electrodes and was subjected to various electrochemical characterisation techniques to understand its electrochemical efficiency.

4.3 Results and Discussions

The structural and electrochemical properties of MSACs are crucial in enhancing their performance as electrode material in FSCs. Their material properties are evaluated using various physicochemical characterisation techniques, including XRD, Raman spectroscopy, TEM, SEM, FTIR and TGA analyses. The electrochemical performance of these materials is further assessed using techniques such as CV, GCD, and EIS. The results obtained from these analyses help to optimise the preparation conditions for MSAC-X-Ys. Additionally, the potential of MSACs for practical wearable supercapacitor applications has been validated through the fabrication of FSC systems.

4.3.1 Material characterisations

4.3.1.1 XRD analysis

Figure 4.2 shows the XRD patterns of MSAC-X-Ys with two broad characteristic peaks at $2\theta = 24^\circ$ and 43° that were assigned to the (002) and (100) planes in the graphitic carbon structure, respectively. The XRD patterns obtained were compared with those in the ICDD catalog No. 01-075-1621.(13,16) The peaks at 24° indicate a better regularity of crystalline structure in the materials. However, the inconspicuous broad peak at 43° is related to interlayer condensation. These results confirm the evident graphitic nature and excellent surface cavities of MSACs.(17)

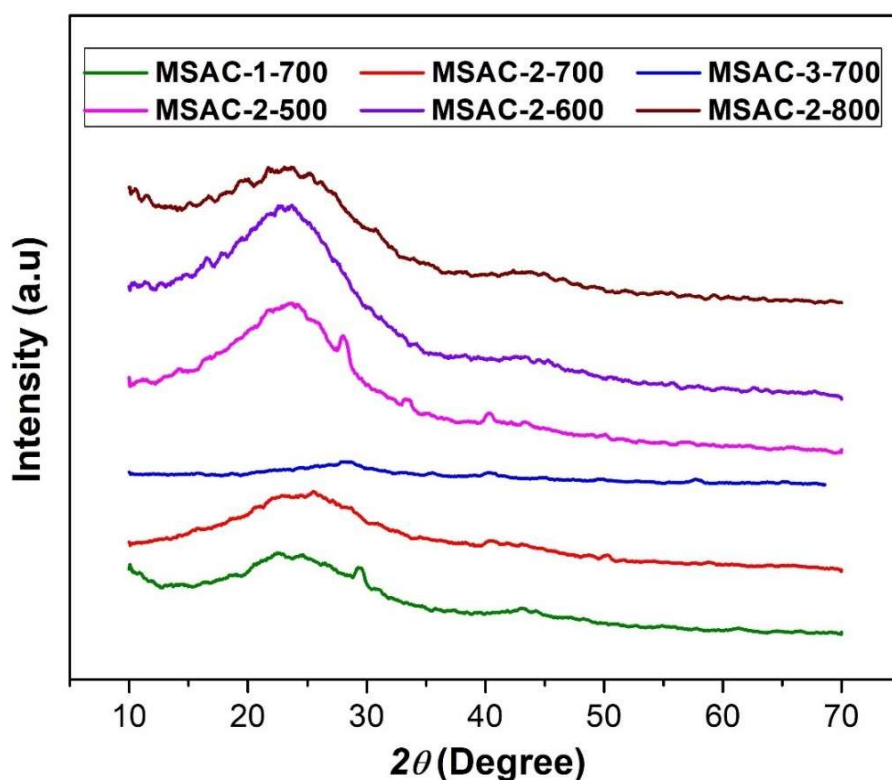


Figure 4.2 XRD patterns of MSAC-X-Ys.

Moreover, the broadness of these peaks suggests the amorphous nature of MSAC-X-Ys. The peak intensity increases initially and then decreases as the carbonisation temperature rises. The influence of the activation ratio on carbon structure formation is evident from the XRD patterns obtained.(18) Additionally, the XRD pattern of MSAC-3-700 does not show characteristic peaks associated with the

graphitic structure, which signifies the structural deformation occurring at higher activation ratios.(16)

4.3.1.2 Raman Spectroscopy

Raman spectra of MSAC-X-Ys are shown in Figure 4.3. All spectra display two well-defined, broad peaks at approximately 1355 and 1580 cm^{-1} . These peaks are attributed to the D (defect) and G (graphite) bands in graphitic carbon.(19) The D band is related to the A_{1g} vibrational mode and represents the defective or disordered sites in carbon materials. In contrast, the G band is associated with E_{2g} symmetric phonon vibrations of C–C bond stretching.(18) These results confirm the presence of crystalline graphite and disordered carbon in the samples.

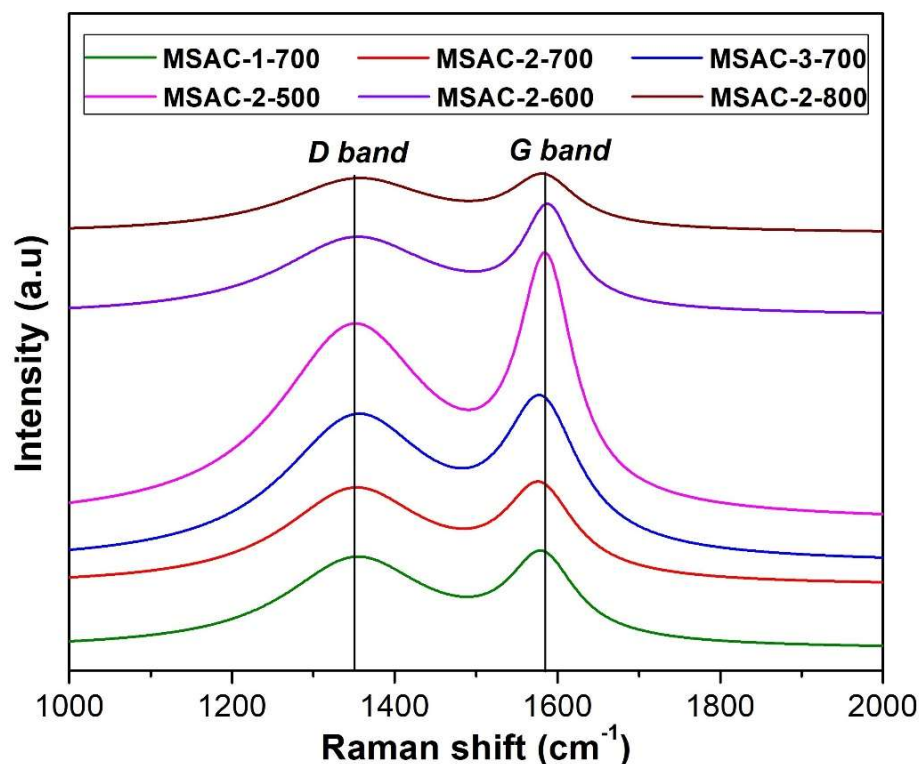


Figure 4.3 Raman spectra of MSAC-X-Ys

The degree of graphitisation was evaluated from the intensity ratio of D and G bands (I_D/I_G), with a higher ratio indicating more defects in the graphitic structure. The I_D/I_G values for MSAC-1-700, MSAC-2-700, and MSAC-3-700 were 0.93, 0.96 and 0.92, respectively. These values represent the presence of localised sp^3 defects within

the sp^2 (C=C) network, which can be related to incomplete graphitisation and deformation of the graphitic structure at lower and higher KOH activation ratios.(16) 0.82, 0.92, 0.96 and 0.99 are the I_D/I_G values of MSAC-2-500, MSAC-2-600, MSAC-2-700, and MSAC-2-800. These typical values of I_D/I_G reflect the increase in structural defects with an increase in carbonisation temperature.(20)

4.3.1.3 TGA analysis

The TGA curve shown in Figure 4.4 illustrates the mass degradation of pristine MFS across a temperature range of 0-1000 °C. The significant components in MFS, including hemicellulose, cellulose, and lignin, are prominently visible in the TGA curve. In this curve, the initial weight loss of 3% at approximately 120 °C is attributed to the evaporation of water and the breakdown of highly volatile compounds from pristine MFS.(5)

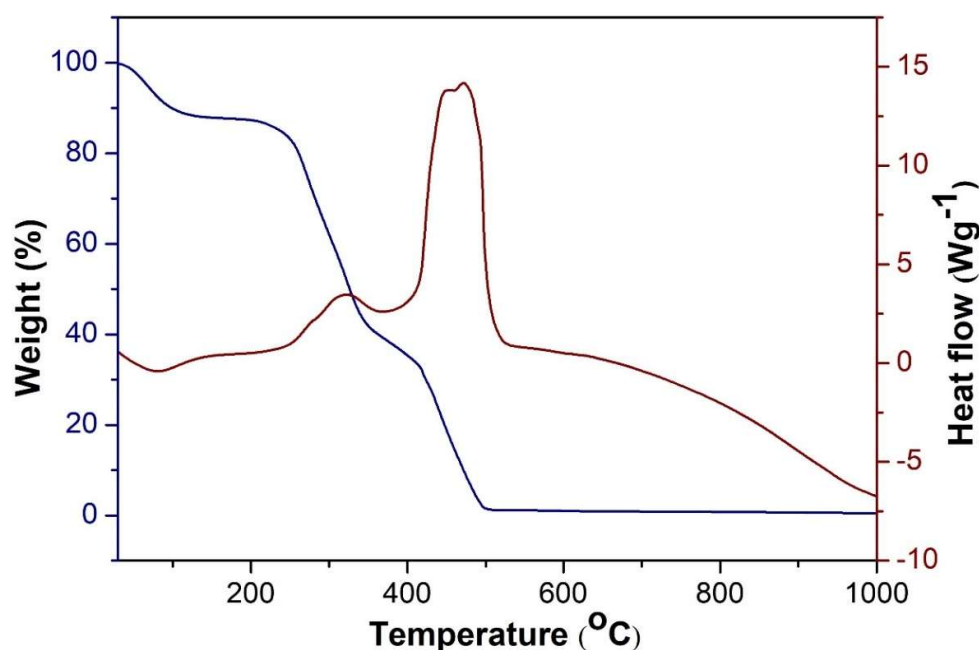


Figure 4.4 TGA curve of pristine mahogany fruit shell

The thermal mass degradation from 120 to 250 °C can be ascribed to the decomposition of hemicellulose. Cellulose, the primary component in lignocellulosic biomass, undergoes decomposition above 250 °C. Significant mass loss occurs between 400 and 500 °C due to lignin degradation, which is thermally stable.(4)

4.3.1.4 SEM analysis

SEM analysis was conducted to investigate the structural morphology of pristine MFS and MSAC samples. The SEM image of pristine MFS is shown in Figure 4.5. The images suggest that the rigid and porous structure of MFS enhances its potential for the preparation of AC with a well-developed pore distribution.

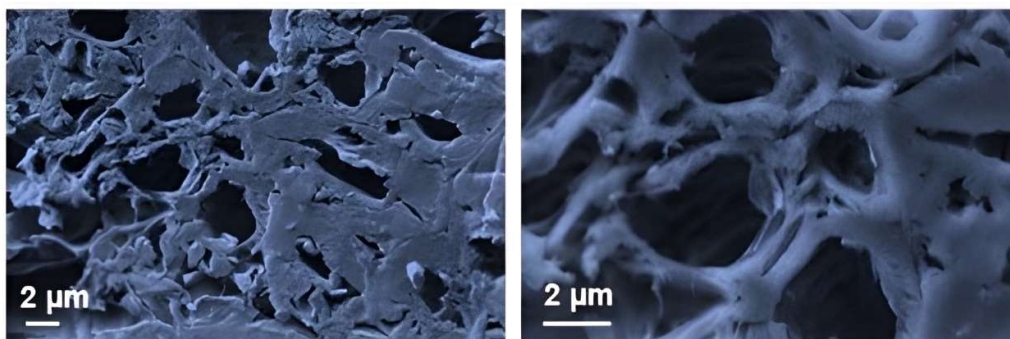


Figure 4.5 SEM images of pristine mahogany fruit shell at 5000 and 10000 X magnification, respectively.

The well-distributed pores are visible in the SEM micrographs (Figure 4.6) of MSACs. These electrode materials typically exhibit an interconnected porous structure, which facilitates the rapid diffusion of the electrolyte and acts as an ion-buffering reservoir.⁽¹³⁾ The porous structure can be attributed to the efficient KOH etching of the biomass waste. Comparing the SEM images of pristine MFS and MSAC-X-Ys confirms this. This unique porous structure is beneficial for increasing the accessible surface area and improving the electrochemical performance of electrode materials.⁽²¹⁾ The SEM results confirm the significant impact of the activation ratio and carbonisation temperature on the structure formation of biomass-derived AC. The number of pores increased with an increase in the activation ratio, which, in turn, increased the surface area of the material. However, the SEM image of MSAC-3-700 indicates the structural collapse associated with excessive addition of the activating agent.⁽¹²⁾ Moreover, the pores became more defined and well-distributed as the carbonisation temperature increased from 600 to 700 °C. Although a high degree of porosity was observed for MSAC-2-800, this also results in the thinning of the structural walls of the MSAC.^(22,23)

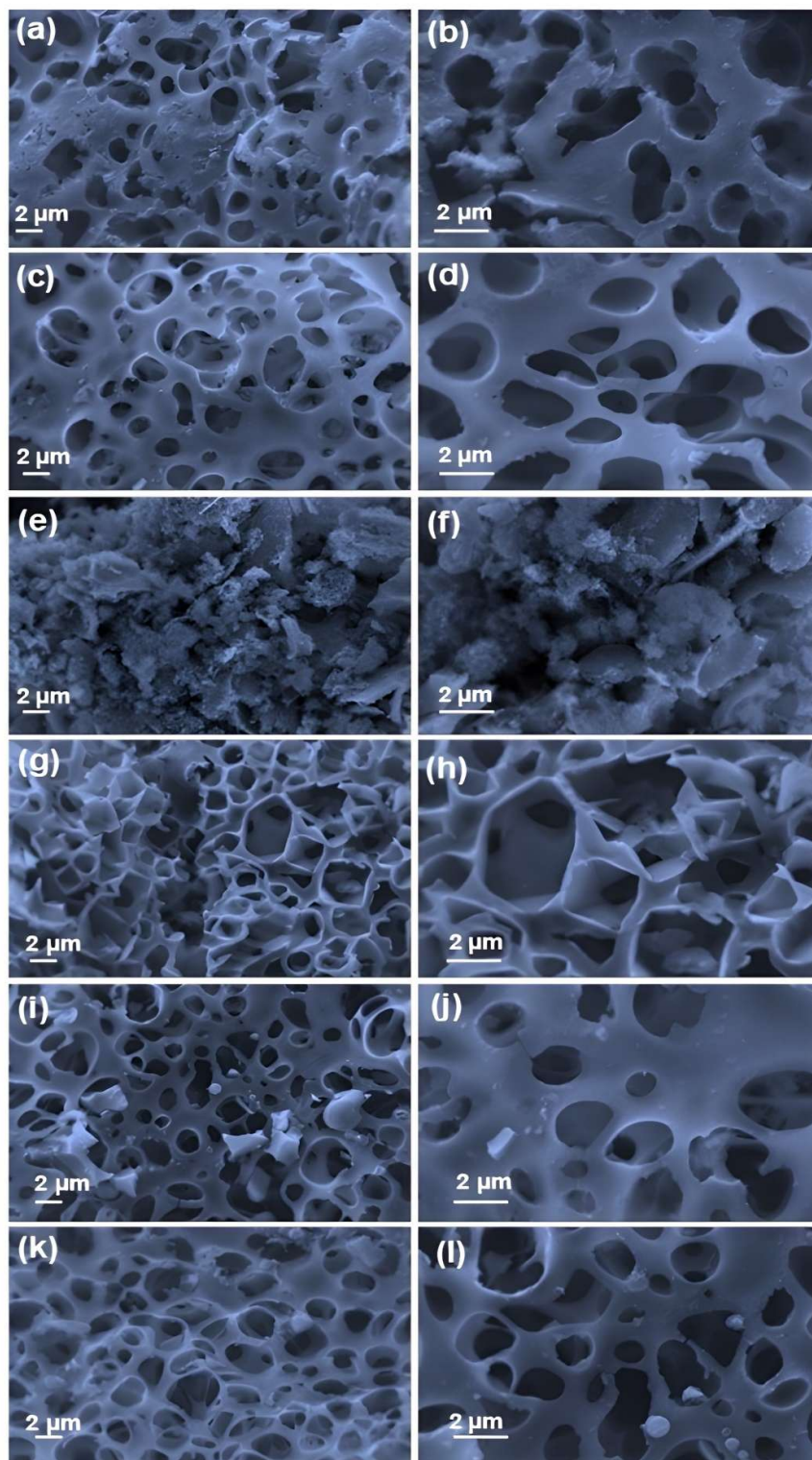


Figure 4.6 SEM images of (a, b) MSAC-1-700, (c, d) MSAC-2-700, (e, f) MSAC-3-700, (g, h) MSAC-2-500, (i, j) MSAC-2-600, and (k, l) MSAC-2-800 at a magnification of 10000 and 20000 X, respectively.

EDAX was used to perform elemental analysis of the prepared electrode materials, and the results are consolidated in Table 4.1. In the samples, the ratio of carbon predominates over oxygen. Compared to other MSAC-X-Ys, MSAC-2-700 shows a higher carbon content.

Table 4.1 Elemental analysis of MSAC-X-Ys

Weight percentage	MSAC-1-700	MSAC-2-700	MSAC-3-700	MSAC-2-500	MSAC-2-600	MSAC-2-800
C	85.1	92.4	89.3	83.6	86.1	90.3
O	14.9	7.6	10.7	16.4	13.9	9.7

4.3.1.5 Surface area analysis

The surface area and pore size distribution of the electrode materials play a vital role in improving the performance of FSCs. As shown in Figure 4.7, MSAC-X-Ys exhibit the type-I nitrogen adsorption–desorption isotherms.(20,24)

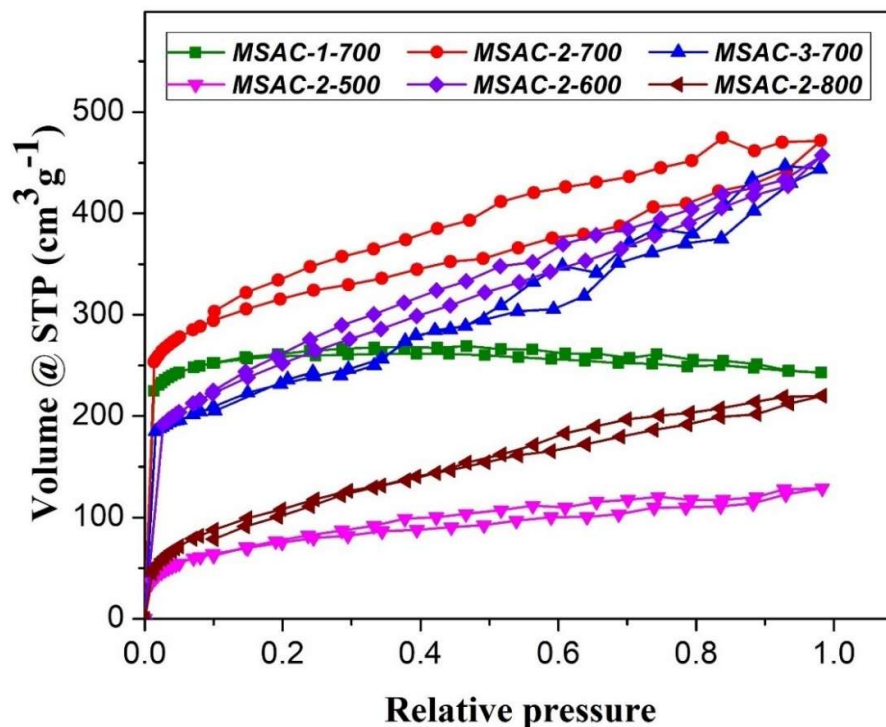


Figure 4.7 N₂ adsorption–desorption isotherms of MSACs

The type-I isotherm shows a sharp increase in the volume adsorbed at a relative pressure of approximately 0.01, followed by a relatively flat region in the higher relative pressure values.(25) These isotherms are usually associated with the micropores present in the electrode materials. The availability of micro pores can be ascribed to the intercalation and deintercalation of metallic K during chemical activation and carbonisation, respectively. In addition, the H4-type hysteresis loop in the curves is usually associated with the mesopores in the samples.(26) The largest hysteresis loop of MSAC-2-700 suggests that it has the largest surface area among all the MSAC-X-Ys.

Table 4.2 Pore structure parameters of MSAC-X-Ys

Sample Name	Surface area [m^2g^{-1}]			Pore volume [cm^3g^{-1}]			Diameter (nm)
	Micro pores	Meso pore	Total	Micro pores	Meso pore	Total	
MSAC-1-700	761	338	1072	0.462	0.328	0.726	3.15
MSAC-2-700	103	202	1022	0.397	0.101	0.376	8.35
MSAC-3-700	341	161	429	0.586	0.2018	0.896	1.47
MSAC-2-500	846	195	1028	0.693	0.365	0.913	3.55
MSAC-2-600	515	279	807	0.291	0.471	0.686	3.40
MSAC-2-800	526	213	898	0.405	0.266	0.707	2.70

The Brunauer–Emmett–Teller (BET) method is employed for calculating surface areas of all the samples, which were summarised in Table 4.2. The surface area of the materials increases with an increase in the activation ratio from 1 to 2, followed by a slight decrease as the activation ratio increases from 2 to 3. However, the surface area of MSAC rises as the carbonisation temperature increases up to 700 °C. A further increase in the carbonisation temperature to 800 °C reduces the surface area, which can be attributed to the structural collapse at higher temperatures.(20)

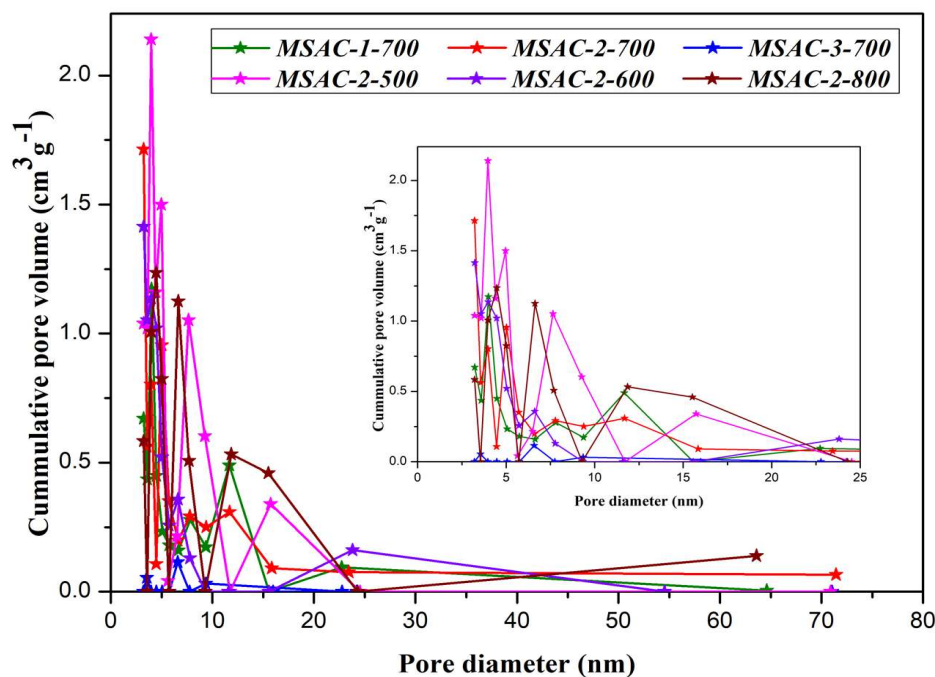


Figure 4.8 Pore size distributions of MSACs (the inset shows the enlarged curves at smaller pore diameters)

Figure 4.8 shows the pore size distribution in MSACs. The Barrett–Joyner–Halenda (BJH) method is used to understand the pore distribution in MSACs. The enlarged curves at smaller pore diameters are shown in the inset. The values of corresponding pore volumes are also tabulated in Table 4.2. The results confirm the largest surface area of MSAC-2-700 and the availability of both micropores and mesopores in its structure. This may be associated with the effective etching using KOH activation. These results align with all other characterisations and indicate the material's potential for efficient electrochemical charge storage.(20,24)

4.3.1.6 FTIR analysis

FTIR spectra displayed in Figure 4.9 represent the functional groups present in MSACs. All the samples show similar peaks around 1055, 1200, 1593, and 3461 cm^{-1} . These are characteristic peaks associated with the graphitic structure in the materials.(27) C–H bending vibrations are related to the peaks at 1055 cm^{-1} . The band near 1593 cm^{-1} is associated with C=C stretching vibrations, whereas the broad band around 3461 cm^{-1} can be ascribed to O–H vibrations. C–O stretching vibrations present

in the material are suggested by the absorption peak at 1200 cm^{-1} .(28) These functional groups are advantageous for enhancing charge storage, specific capacitance and other surface properties in MSAC-based FSC electrodes.(29)

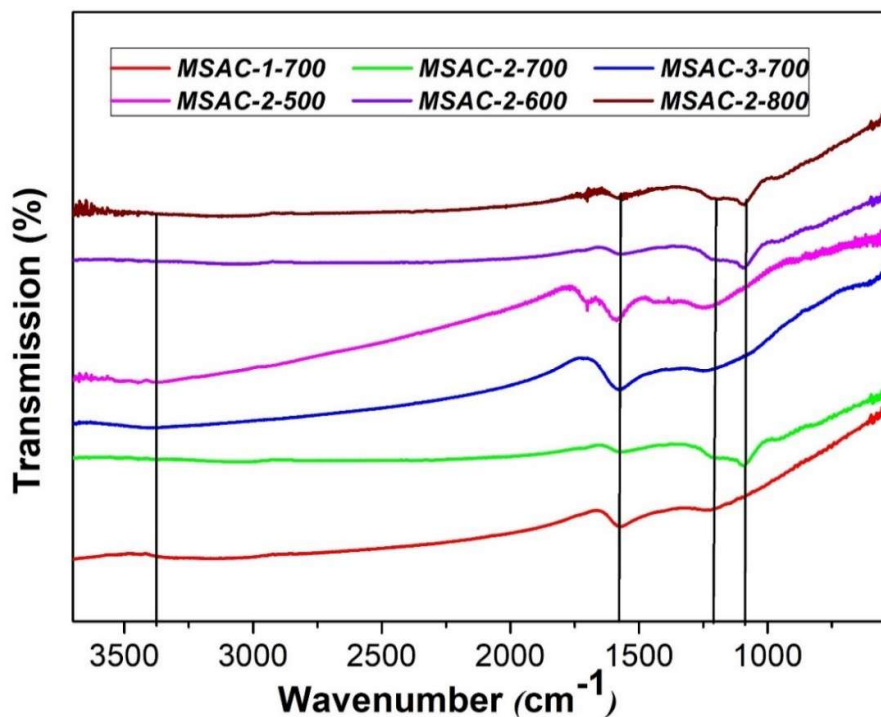


Figure 4.9 FTIR spectra of MSAC-X-Ys

The reduction in the intensity of peaks with the rise in carbonisation temperature indicates the formation of a more tightly packed graphitic structure with fewer functional groups. The spectra further validate the effect of activation ratio in improving the functional groups in the materials.(28)

4.3.1.7 TEM analysis

The porous distribution of ACMS-2-700 was further validated using high-resolution TEM analysis. Figure 4.10 shows structural micrographs of ACMS-2-700 at different resolutions. A well-defined pore distribution in the material with micropores ($< 2\text{ nm}$), mesopores ($2\text{-}50\text{ nm}$), and macropores ($> 50\text{ nm}$) is visible from the TEM images.(20)

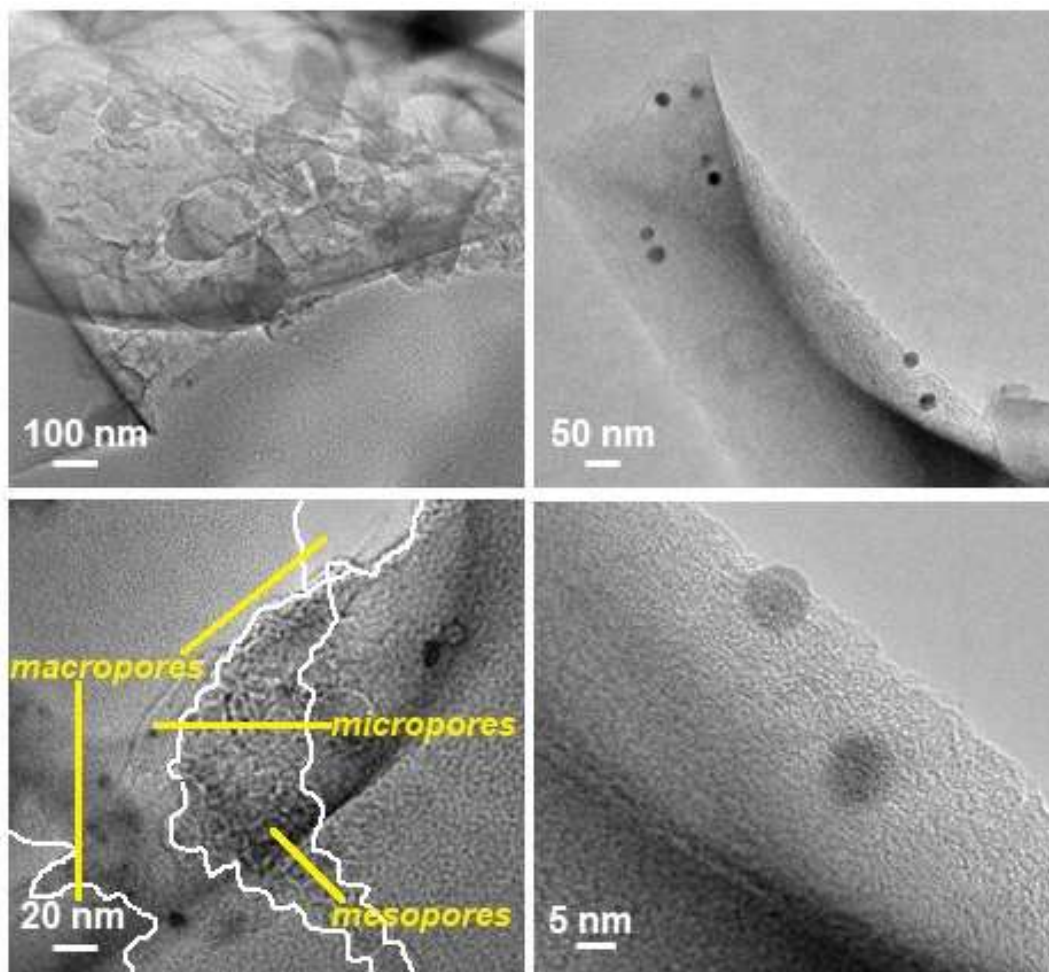


Figure 4.10 TEM images of the MSAC-2-700 at various magnifications showing porous structures with micro, meso, and macropores.

The availability of mesopores and micropores is advantageous for fast ion transport and facilitates the capacitive properties of AC, which are favourable for electrode applications.(29)

4.3.2 Electrochemical characterisation of MSAC-X-Ys

Electrochemical performance of MSAC-X-Ys was evaluated using a three-electrode configuration, including a working electrode, a reference electrode and a counter electrode with 1 M KOH as the electrolyte.

4.3.2.1 Cyclic voltammetry (CV)

CV was carried out at different scan rates over a potential window from -1 to 0 V. Figure 4.11 illustrates the CV response of MSAC-X-Ys at a scan rate of 1 mV s^{-1} . The CV curves show no redox peaks, even at low scan rates, indicating the formation of an ideal electric double layer in the supercapacitor systems. Additionally, these reversible curves indicate a fast electrochemical response of the materials.(17,30)

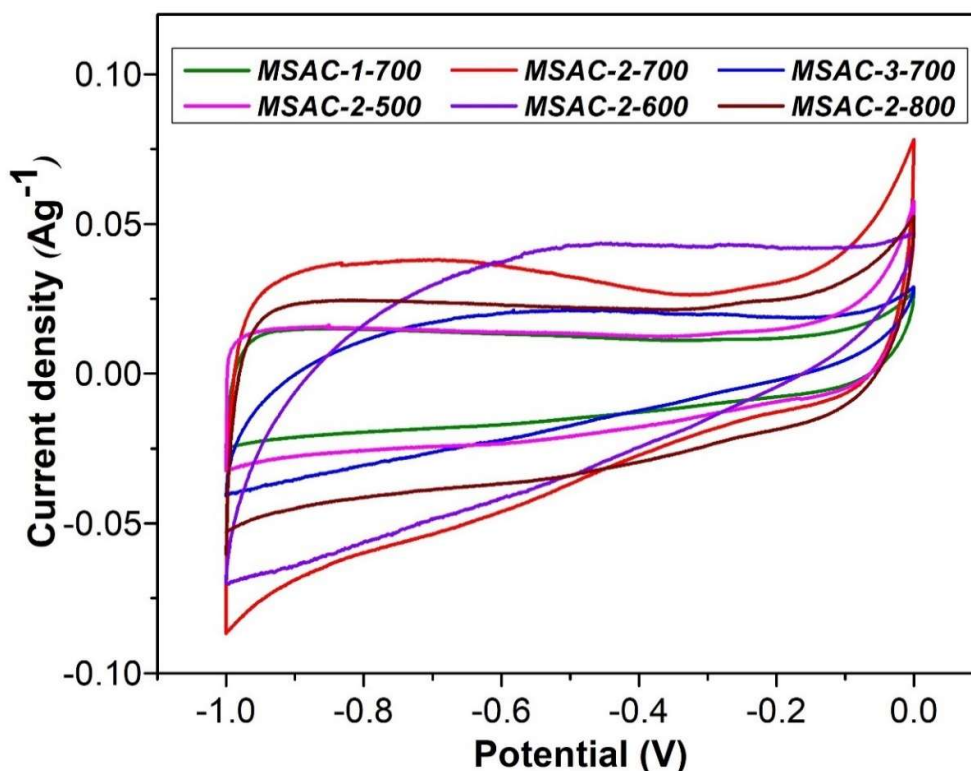


Figure 4.11 CV curves of MSAC-X-Ys at a scan rate of 1 mV s^{-1}

Activation ratio and carbonisation temperature significantly affect the CV response. The CV curve area of MSAC-2-700 was higher than that of all other electrode materials, reflecting its higher specific capacitance and electrochemical performance.(31) The CV curves of MSAC-2-700 obtained at various scan rates are shown in Figure 4.12. At lower scan rates, the CV curves of MSAC-X-Y are quasi-rectangular, suggesting the suitability of MSAC-2-700 as a supercapacitor material. In contrast, the distorted CV curves at higher scan rates indicate that the electrolyte

diffuses inefficiently into the internal pores of the electrode material, resulting in reduced charge accumulation on the electrode surface.(18)

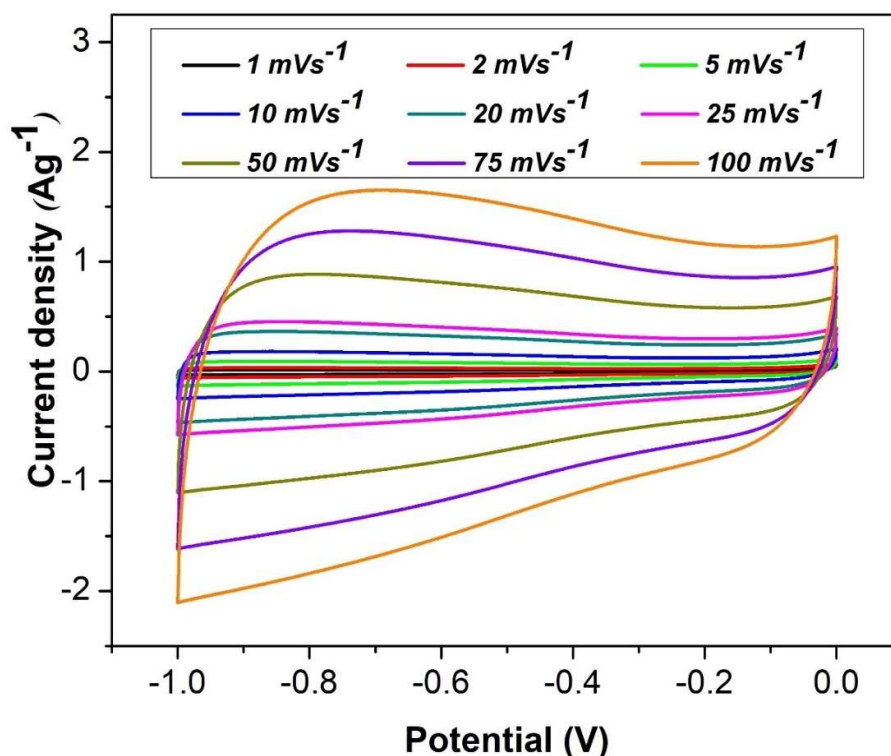


Figure 4.12 CV curves of MSAC-2-700 at different scan rates

4.3.2.2 Galvanostatic charge-discharge (GCD)

GCD measurements were performed at different current densities to further evaluate the electrochemical properties of the as-prepared electrode materials. GCD response of these electrode materials at a current density of 1 A g^{-1} is compared in Figure 4.13. The curves are almost triangular and symmetrical, indicating the reversible behaviour of the electrode material.(23) In addition, the negligible voltage drop in the discharge curves reflects low internal resistance and reasonable electrical conductivity of the electrode materials. MSAC-2-700 has a longer discharge curve, suggesting its better capacitive properties and a faradaic efficiency of $>100\%$.

The value of specific capacitance was calculated using the following equation:

$$C_{sp} = \frac{I \times \Delta t}{\Delta V \times m} \quad 4.1$$

where C_{sp} is the specific capacitance, I is the current density, Δt is the discharge time, ΔV is the potential window, and m is the mass of the active material in the electrode. (32,33)

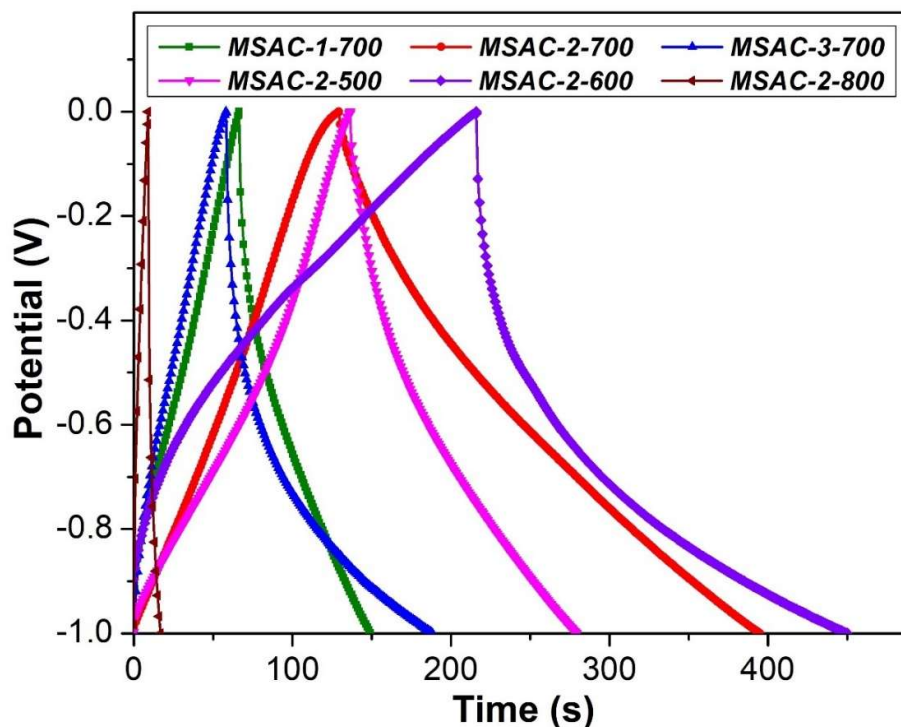


Figure 4.13 GCD curves of MSAC-X-Ys at a current density of 1 A g^{-1}

The specific capacitance values of the electrode materials are listed in Table 4.3. MSAC-2-700 has the highest specific capacitance value among all MSAC-X-Ys. The results signify the effect of the accessible surface area on the electrochemical capacitance and are consistent with the SEM and surface area analysis results. The improvement in the capacitance values is attributed to the rapid ion diffusion and effective electrolyte ion transport inside the electroactive material.

Table 4.3 Specific capacitance values of MSAC-X-Ys.

Sample	MSAC-1-700	MSAC-2-700	MSAC-3-700	MSAC-2-500	MSAC-2-600	MSAC-2-800
$C_{sp} [\text{F g}^{-1}]$	144	267	129	142	234	112
IR drop [mV]	1.68	0.24	1.65	0.62	1.26	5.17

Figure 4.14 shows the GCD curves of MSAC-2-700 at different current densities ranging from 1 to 5 A g⁻¹. The GCD curves are straight and symmetrical at low current densities of 1 and 2 A g⁻¹, indicating the reversible electrochemical behaviour and high coulombic efficiency of MSAC-2-700.(31) The discharge time and specific capacitance of MSAC-2-700 decreased with an increase in the current density.

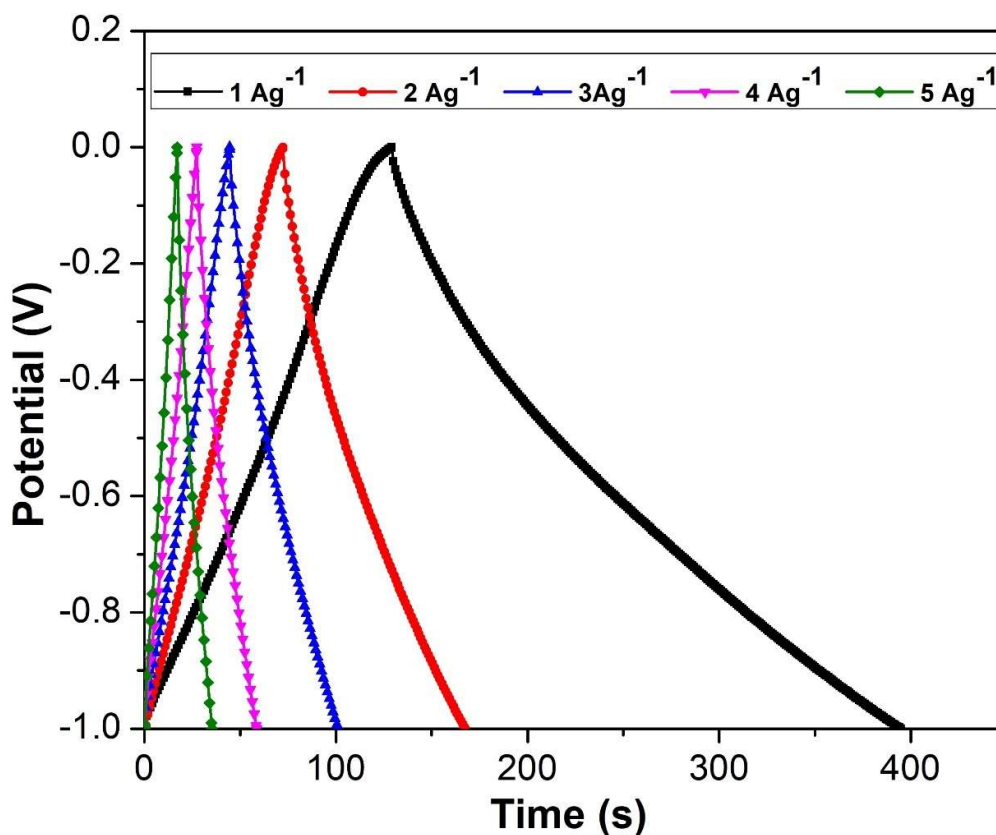


Figure 4.14 GCD curves of MSAC-2-700 at various current densities

Figure 4.15 displays the variation in the specific capacitance and IR drop with an increase in current density for MSAC-2-700. A small IR drop observed at higher current densities confirms the significant capacitive nature of the material.(32,33) The stability of MSAC-2-700 was studied by performing 10,000 charging and discharging cycles at a current density of 20 A g⁻¹ (Figure 4.16). The material showed high capacitance retention of approximately 97%. The specific capacitance values of various biomass-derived AC electrode materials are listed in Table 4.4. The specific capacitance of MSAC is comparable to or even higher than those reported in previous studies.

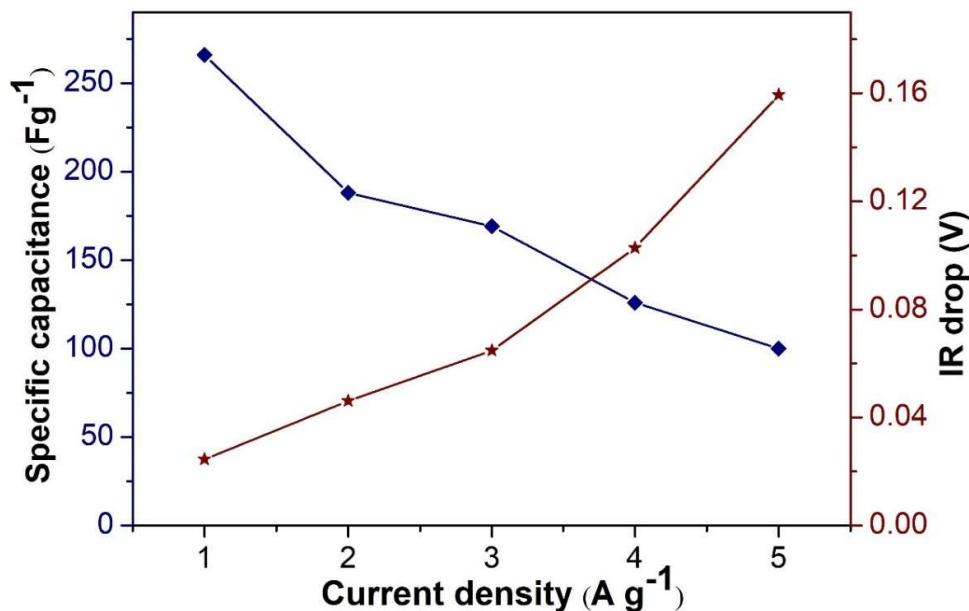


Figure 4.15 Dependence of specific capacitance and IR drop on the current density for MSAC-2-700

The specific energy density (E) and power density (P) of MSAC-2-700 were calculated using equations 4.2 and 4.3:

$$E(\text{Whkg}^{-1}) = \frac{0.5 \times C_{sp} \times V^2}{3.6} \quad 4.2$$

$$P(\text{Wkg}^{-1}) = \frac{3600 \times E}{t} \quad 4.3$$

where C_{sp} is the specific capacitance (F g^{-1}), V is the voltage change during the discharge after the reduction of the IR drop (V), and t is the discharge time (s). (34)

Figure 4.17 shows the Ragone plot for MSAC-2-700 that represents the variation in energy density depending on the power density of the electrode material. The power density and energy density of various biomass-derived AC electrode materials are illustrated in the figure. The Ragone curve further validates the potential of MSAC-2-700 for FSC applications as it displays high energy density and remarkable power density, which are ideal for highly efficient electrode material. (35–39)

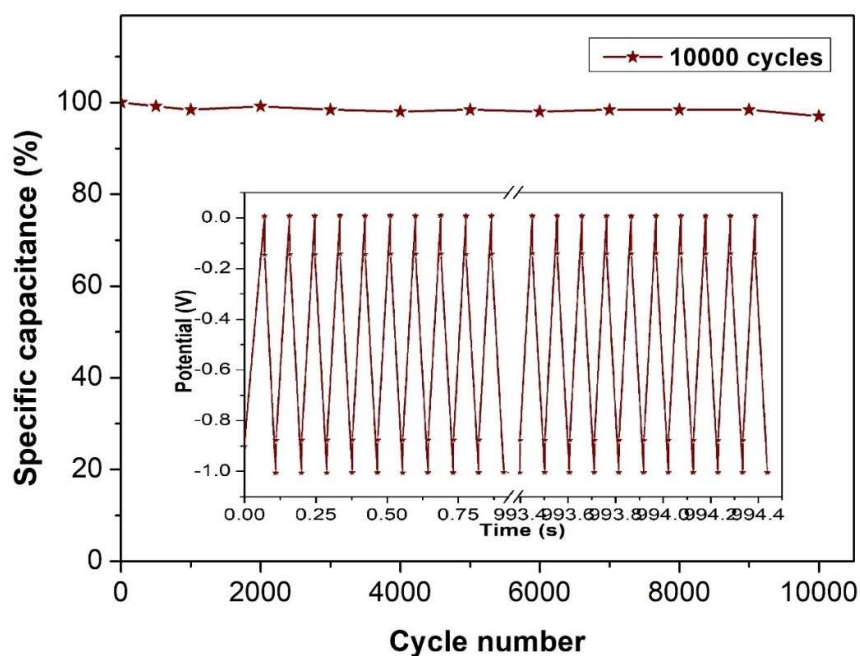


Figure 4.16 Cycle life of MSAC-2-700 at a current density of 20 A g^{-1} for 10,000 cycles with the first and last five charge-discharge cycles in the inset

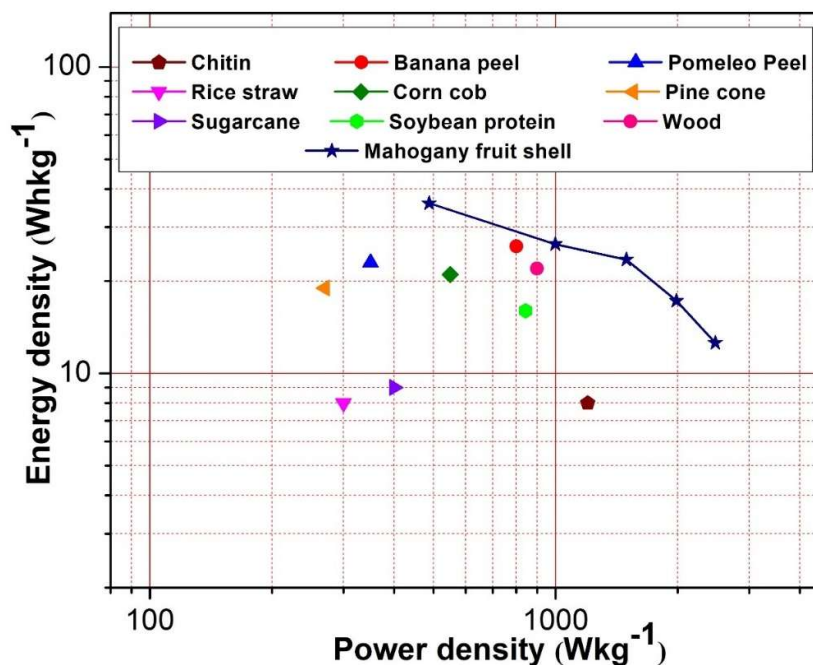


Figure 4.17 Ragone plot of MSAC-2-700 compared with various biomass-derived AC electrode materials

Table 4.4 Comparison of specific capacitance of different biomass-derived AC materials.

Precursor Material	Activating agent	Specific capacitance [F g ⁻¹]	Current density [A g ⁻¹]	Electrolyte	Energy density [W h kg ⁻¹]	Power density [W kg ⁻¹]	Cycle Test @ 10 A g ⁻¹	Ref.
Cashew nutshell	KOH	194	1	0.5 M Na ₂ SO ₄	--	--	94 % after 10000 cycles	(12)
Coconut coir pith	NaOH	120	1	1 M H ₂ SO ₄	18	271	----	(20)
Pine cone	KOH	185	0.5	1 M H ₂ SO ₄	16	454	96 % after 10000 cycles	(22)
Sakura flower	KOH	231	1	6 M KOH	--	--	95 % after 5000 cycles	(30)
Corn cob	KOH	299	1	6 M KOH	--	--	90 % after 2000 cycles	(33)
Banana peel	H ₃ PO ₄	199	1	1 M KOH	23	342	90 % after 11000 cycles	(34)
Soybean protein	ZnCl ₂	210	1	6 M KOH	16	844	93 % after 10000 cycles	(36)
Wood	KOH	175	0.05	6 M KOH	22	900	76% after 20000 cycles	(37)
Chitin	NaOH	227	0.5	1 M H ₂ SO ₄	8	1200	98 % after 10000 cycles	(38)
Cucumis melo fruit peel	KOH	245	0.5	1 M KOH	29	279	91 % after 10000 cycles	(40)
Pomelo peels	KOH	103	1	1 M Na ₂ SO ₄	20	500	99 % after 4000 cycles	(41)
Mahogany fruit shell	KOH	267	1	1 M KOH	27	990	97 % after 10000 cycles	Present work

4.3.2.3 Electrochemical impedance spectroscopy (EIS)

The charge transfer and ion diffusion properties of the MSAC-X-Ys were evaluated using EIS analysis. Figure 4.18 illustrates the Nyquist plot of the MSAC-X-

Ys in the high-frequency region. The Nyquist plots of MSAC-X-Y show a semicircle in the high-frequency region and a straight line in the low-frequency region.

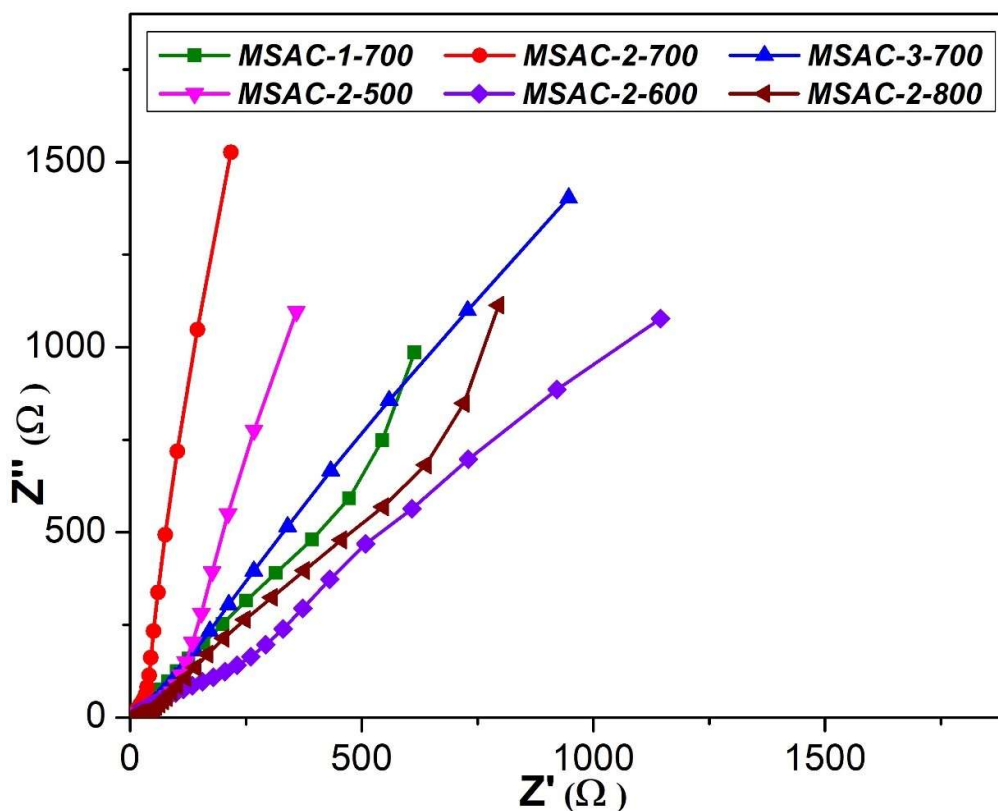


Figure 4.18 Nyquist plot of the electrode materials (the enlarged curves at the high-frequency range and equivalent circuit diagram are shown in the insets)

The EIS curves were fitted to the equivalent circuit (as inset) consisting of internal resistance (R_s), charge transfer resistance (R_{ct}), double-layer capacitance (C_{dl}), and Warburg resistance (Z_w). The value of the equivalent series resistance (ESR) can be found from the value of the lower intersection of the semicircle in the high-frequency region of the Nyquist plot. The value of R_s consists of the contact resistance between the current collector and active material, solution resistance, and the intrinsic resistance of the electrode material. The vertical line may be attributed to the low diffusive resistance associated with the fast ion transport in the system.(42,43) Table 4.5 lists the values of R_s , R_{ct} , C_{dl} , and Z_w . The ion diffusion resistance between the

electrolyte and active material is represented by R_{ct} . Z_w and C_{dl} are associated with the electrochemical reaction rate and the charge accumulation at the interface, respectively.

Table 4.5 Fitted values of components in equivalent circuit derived from the EIS curves for MSAC-X-Ys.

Sample Name	R_s [Ω]	R_{ct} [Ω]	C_{dl} [μF]	W [$\Omega \cdot \text{s}^{-1/2}$]
MSAC-1-700	5.12 ± 0.37	7.31 ± 0.39	7.15 ± 1.78	150.6 ± 0.06
MSAC-2-700	6.02 ± 0.21	8.74 ± 0.12	4.81 ± 0.34	250.7 ± 1.18
MSAC-3-700	5.65 ± 0.38	7.23 ± 0.91	9.46 ± 0.21	454.5 ± 0.05
MSAC-2-500	5.68 ± 0.44	5.60 ± 0.39	13.11 ± 3.93	124.8 ± 0.46
MSAC-2-600	8.21 ± 0.30	20.94 ± 0.45	17.61 ± 1.06	291.5 ± 0.06
MSAC-2-800	6.47 ± 0.34	14.93 ± 0.39	10.55 ± 1.18	239.7 ± 0.05

4.3.3 Electrochemical analysis of gel polymer-based flexible solid-state supercapacitors (FSCs)

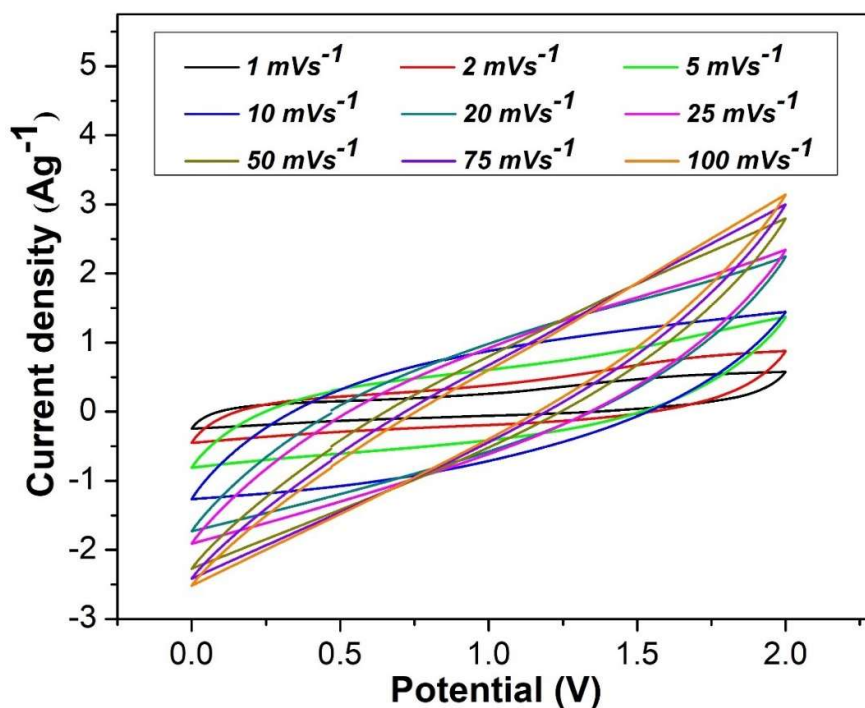


Figure 4.19 CV curves of the FSC at different scan rates from 1 to 100 mV s^{-1}

The ionic conductivity of the gel polymer plays a crucial role in determining the electrochemical performance of the FSC system.(14) Conductivity studies of the as-prepared GPEs were carried out to identify the optimal ratios of PVA and Na₂SO₄ for preparing PVA|Na₂SO₄ GPEs. The ionic conductivity values were calculated using the bulk resistance (Ω) obtained from EIS analysis. The as-prepared GPE with 10 weight percent PVA and 0.1 M Na₂SO₄ had the maximum ionic conductivity of 1.2468 mS cm⁻¹. FSCs were fabricated using GPEs with the composition mentioned above.

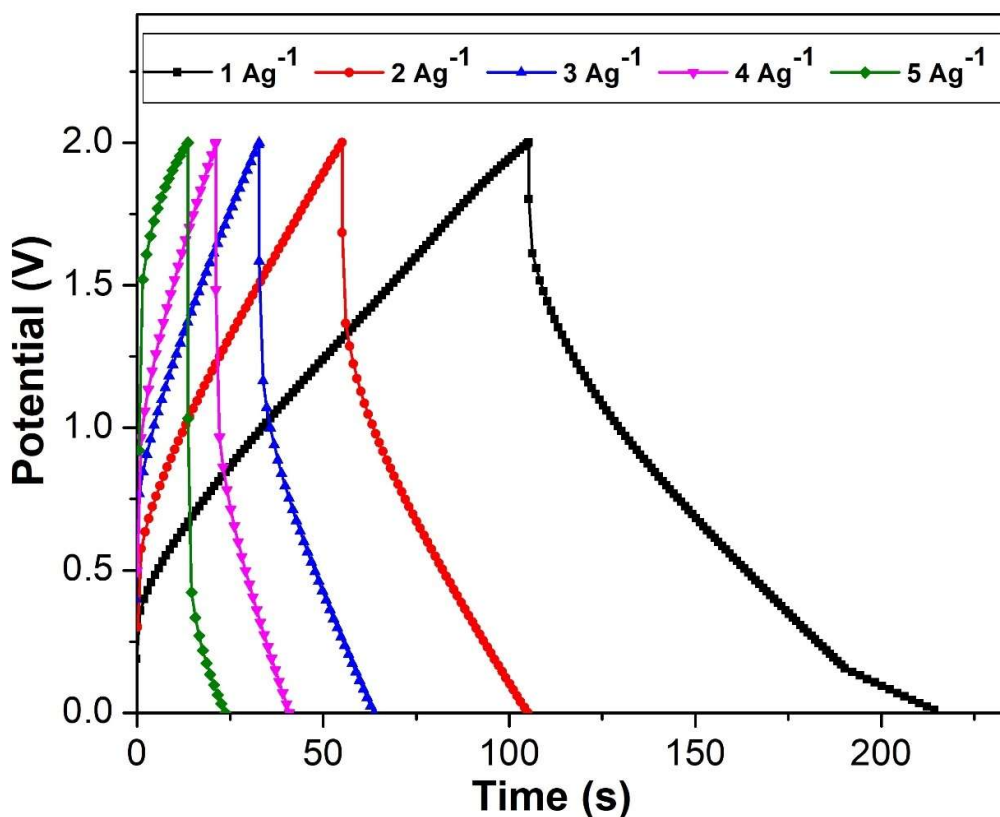


Figure 4.20 GCD curves of the FSC at current densities from 1 to 5 A g⁻¹

The CV tests were carried out at different scan rates (1, 2, 5, 10, 20, 25, 50, 75, and 100 mV s⁻¹) over a larger potential window of 0–2 V (Figure 4.19). The almost rectangular CV curves underpin the formation of a perfect double layer resulting from the high reversibility of both charging and discharging curves at a pseudo-constant rate

without the presence of any redox element. The CV curves were slightly distorted at higher scan rates, which is typical for EDLCs. (17)

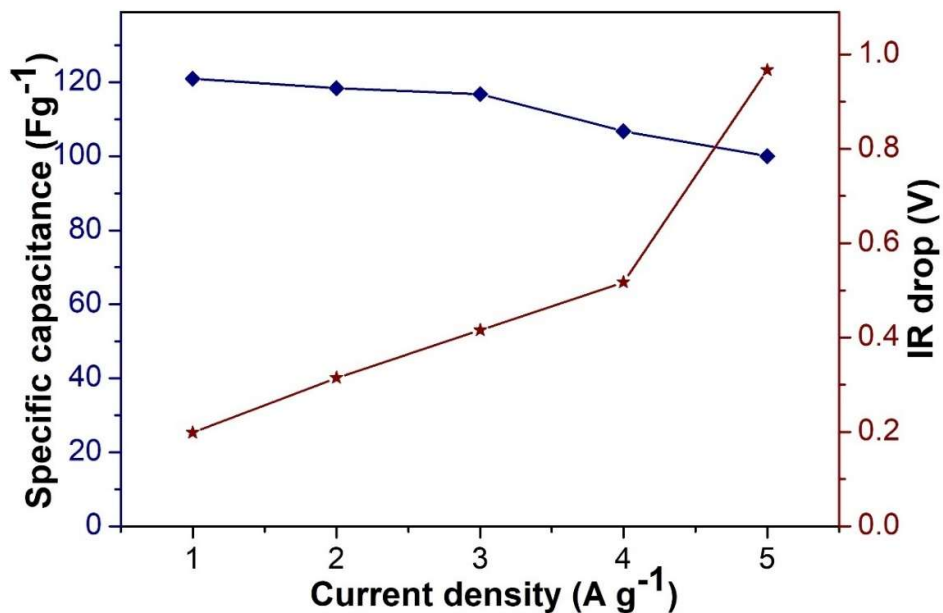


Figure 4.21 Dependence of specific capacitance and IR drop on the current density of FSC

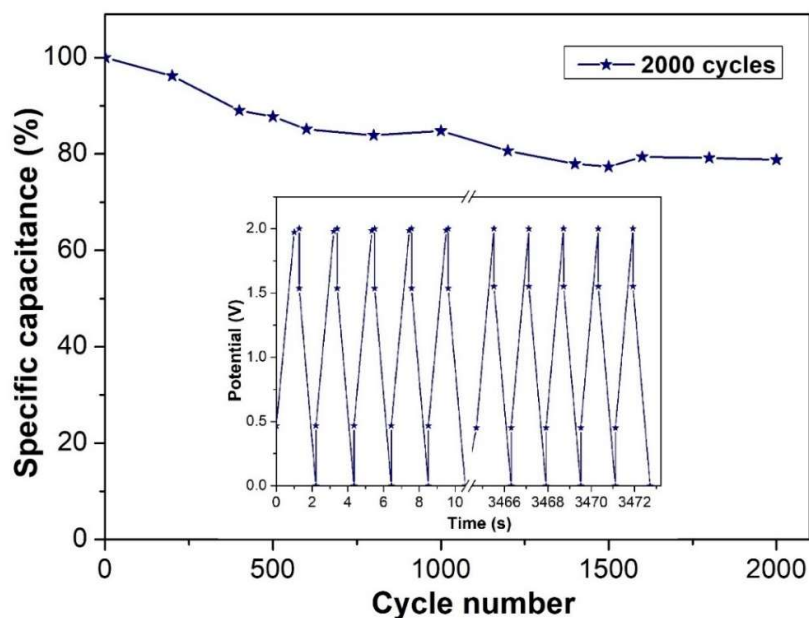


Figure 4.22 Cycle life of the FSC at a current density of 20 A g⁻¹ for 2,000 cycles with the first and last five charge-discharge cycles in the inset

Figure 4.20 represents the GCD curves of FSC obtained for different current densities. The curves are triangular and electrochemically reversible, representing the pure capacitive behaviour of FSC. As expected, the discharge time and specific capacitance of the FSC decreased with increasing current density.(23) The specific capacitance of the FSC was calculated using equation (4.4):

$$C_{sp} = \frac{2 \times I \times \Delta t}{\Delta V \times m} \quad 4.4$$

where C_{sp} is the specific capacitance, I is the current density, Δt is the discharge time, ΔV is the potential window, and m is the total mass of the active electrode material in FSC.(26) The FSC exhibited a high specific capacitance of 121 F g^{-1} at a current density of 1 A g^{-1} .

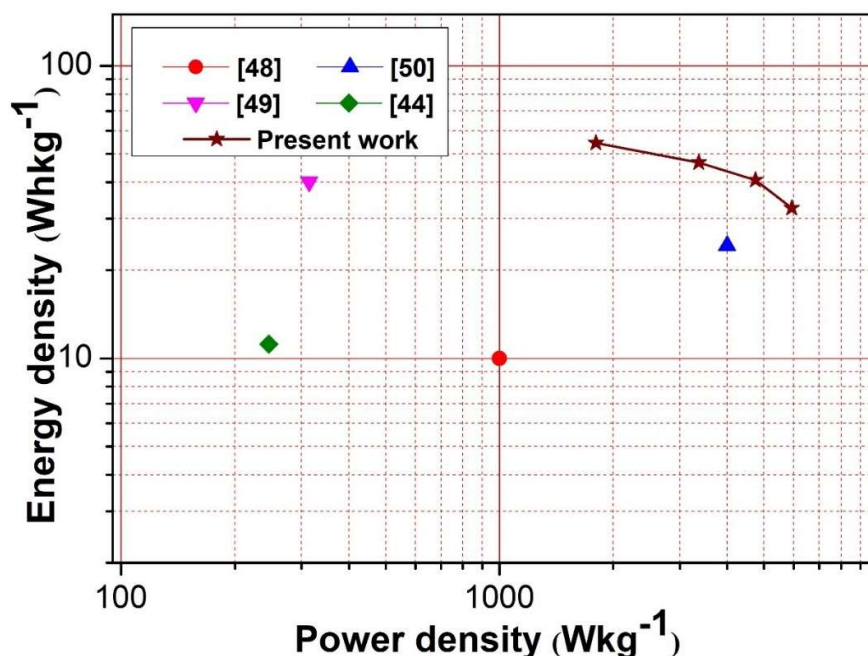


Figure 4.23 Ragone plot of the FSC in comparison with previously reported values

Figure 4.21 illustrates a reduction in specific capacitance and an increase in IR voltage drop as current density rises, which are typical characteristics of EDLCs. In addition, as shown in Figure 4.22, FSC exhibits capacitance retention of 78% after 2,000 cycles at 20 A g^{-1} . The energy and power densities of FSC were calculated using

equations 4.2 and 4.3, which were comparable to or even better than the values reported earlier, as shown in the Ragone plot (Figure 4.23).

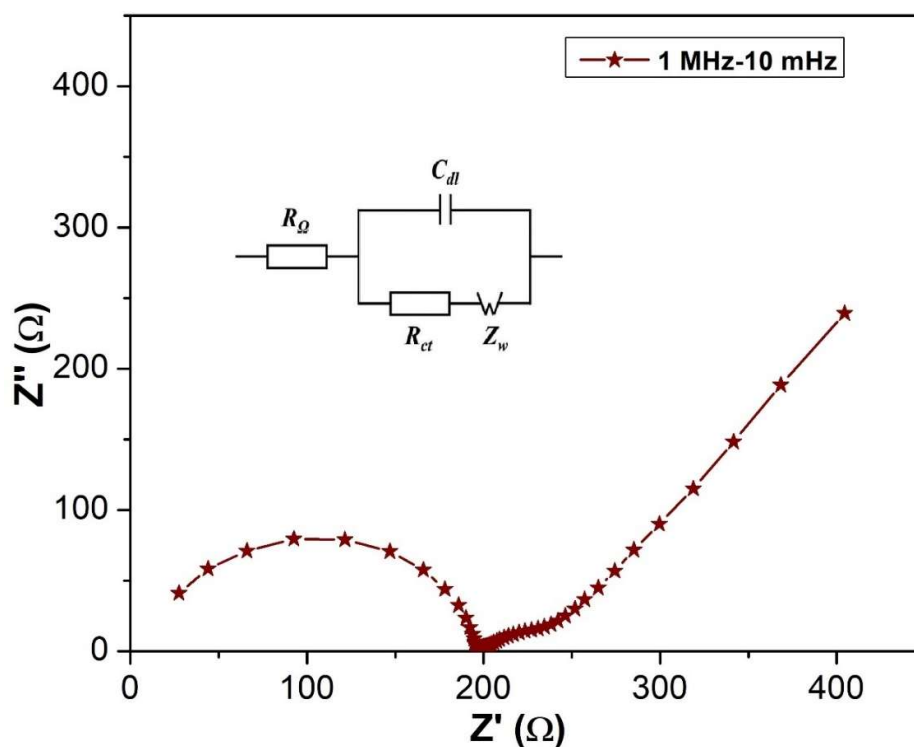


Figure 4.24 Nyquist plot of the FSC (the equivalent circuit diagram is shown as an inset)

The Nyquist plot of the FSC (Figure 4.24) is similar to the characteristic curve of an ideal supercapacitor and was further analysed using equivalent circuits. The values of R_s , R_{ct} , C_{dl} , and W were determined to be 21.5 Ω , 179 Ω , 0.57 μF , and 66.07 $\Omega \cdot \text{s}^{-1/2}$, respectively. These results indicate the viability of FSC fabrication employing MSAC as the electrode material and PVA| Na_2SO_4 GPE as the electrolyte.(37,41)

The major application of FSC lies in the field of wearable devices. So, to confirm the feasibility of FSC for practical applications has to be evaluated. The fabricated FSC was subjected to bending from 0° to 180° . CV curves of FSC at various bending angles are displayed in Figure 4.25. The CV curves show only a slight shift in bending, indicating considerable flexibility and ease of bending at different angles without compromising its electrochemical performance.

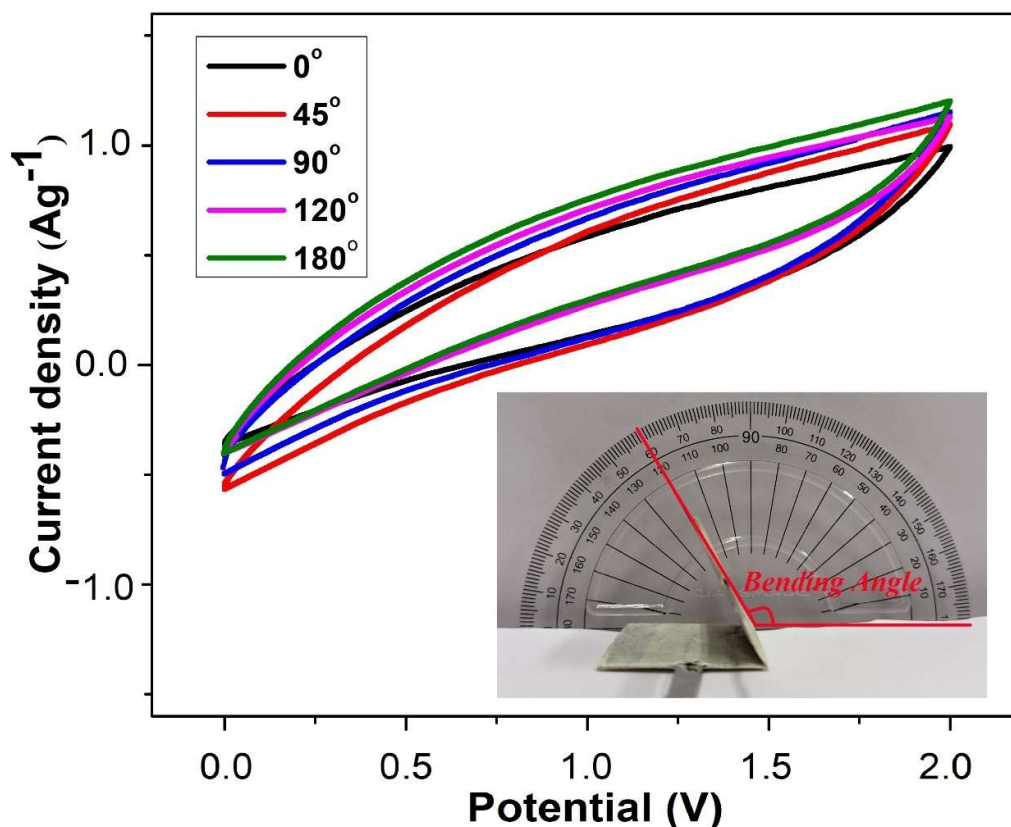


Figure 4.25 CV curves of FSC subjected to bending at various angles; scan rate: 20 mV s^{-1} (inset displays the bending angle)

4.4 Conclusion

Different MSACs were prepared via the low-cost KOH chemical activation method. The optimal activation ratio of mahogany fruit shell waste to KOH and carbonisation temperature for preparing highly porous MSACs with a large surface area were determined to be 1:2 and $700 \text{ }^\circ\text{C}$ (MSAC-2-700), respectively. Based on the results obtained from electrochemical characterisation, MSAC-2-700 also exhibited the highest specific capacitance of 267 F g^{-1} at a current density of 1 A g^{-1} and excellent stability with capacitance retention of 97% over 10,000 charge–discharge cycles. The applicability of MSAC-2-700 as an electrode material in the FSC was further validated by fabricating a GPE-based FSC. The as-prepared FSC exhibited a high specific capacitance of 121 F g^{-1} at a current density of 1 A g^{-1} with significant capacitance retention of 78% over 2,000 charge–discharge cycles. The improved potential window

with a high specific capacitance of the GPE-based FSC suggests its excellent energy and power densities. This study confirms the potential of MSACs as electrode materials for supercapacitors and the superiority of the fabricated FSC over conventional FSCs.

References

1. Zhu S, Sheng J, Chen Y, Ni J, Li Y. Carbon nanotubes for flexible batteries: recent progress and future perspective. *Natl Sci Rev.* 2021 May 13;8(5).
2. Pal B, Yang S, Ramesh S, Thangadurai V, Jose R. Electrolyte selection for supercapacitive devices: A critical review. *Nanoscale Adv.* 2019;1(10):3807–35.
3. Zhang Q, Yan B, Feng L, Zheng J, You B, Chen J, Zhao X, Zhang C, Jiang S, He S. Progress in the use of organic potassium salts for the synthesis of porous carbon nanomaterials: Microstructure engineering for advanced supercapacitors. *Nanoscale.* 2022;14(23):8216–44.
4. Redda HG, Nikodimos Y, Su WN, Chen RS, Jiang SK, Abrha LH, et al. Enhancing the electrochemical performance of a flexible solid-state supercapacitor using a gel polymer electrolyte. *Mater Today Commun.* 2021 Mar 1;26.
5. Cheng X, Pan J, Zhao Y, Liao M, Peng H. Gel polymer electrolytes for electrochemical energy storage. *Advanced Energy Materials.* 2018 Mar;8(7):1702184.
6. Singh M, Gupta A, Sundriyal S, Dubey P, Jain K, Dhakate SR. Activated green carbon-based 2-D nanofabric mats for ultra-flexible all-solid-state supercapacitor. *Journal of Energy Storage.* 2022 May 1;49:104193.
7. Dubey P, Shrivastav V, Singh M, Maheshwari PH, Sundriyal S, Dhakate SR. Electrolytic Study of Pineapple Peel Derived Porous Carbon for All-Solid-State Supercapacitors. *ChemistrySelect.* 2021 Nov 15;6(42):11736–46.
8. Alipoori S, Mazinani S, Aboutalebi SH, Sharif F. Review of PVA-based gel polymer electrolytes in flexible solid-state supercapacitors: Opportunities and challenges. *journal of energy storage.* 2020 Feb 1;27:101072.
9. Singh M, Gupta A, Sundriyal S, Jain K, Dhakate SR. Kraft lignin-derived free-standing carbon nanofibers mat for high-performance all-solid-state supercapacitor. *Mater Chem Phys.* 2021 May 1;264.
10. John B, Magoling A, Angeles-Macalalad AA. Mahogany Fruit Husk-derived Activated Carbon for Removal of Cr (VI) from Aqueous Solution. *Int J Sci Eng Res [Internet].* 2019;10(6).
11. Pranolo SH, Waluyo J, Paryanto, Susanti AD, Permana RB, Erwanda I, et al. Feasible tar cleaning method of producer gas from palm kernel shell and mahogany fruit shell gasification. *Mater Today Proc.* 2022 Jan 1;63:S237–43.
12. Pulikkottil M, Antony H, Muralidharan MN, Gopalan EV, Ansari S. Cashew Nut Shell Derived Porous Activated Carbon Electrodes for “Water-in-Salt” Electrolyte Based Symmetric Supercapacitor. *ChemistrySelect.* 2022 Jun 20;7(23).

13. Merin P, Jimmy Joy P, Muralidharan MN, Veena Gopalan E, Seema A. Biomass-derived activated carbon for high-performance supercapacitor electrode applications. *Chemical Engineering & Technology*. 2021 May;44(5):844-51.
14. Alipoori S, Torkzadeh MM, Mazinani S, Aboutalebi SH, Sharif F. Performance-tuning of PVA-based gel electrolytes by acid/PVA ratio and PVA molecular weight. *SN Appl Sci*. 2021 Mar 1;3(3).
15. Hai A, Bharath G, Babu KR, Taher H, Naushad M, Banat F. Date seeds biomass-derived activated carbon for efficient removal of NaCl from saline solution. *Process Safety and Environmental Protection*. 2019 Sep 1;129:103–11.
16. Jain A, Ghosh M, Krajewski M, Kurungot S, Michalska M. Biomass-derived activated carbon material from native European deciduous trees as an inexpensive and sustainable energy material for supercapacitor application. *J Energy Storage*. 2021 Feb 1;34.
17. Zhang J, Gao J, Chen Y, Hao X, Jin X. Characterization, preparation, and reaction mechanism of hemp stem based activated carbon. *Results in physics*. 2017 Jan 1;7:1628-33.
18. Dizbay-Onat M, Vaidya UK, Lungu CT. Preparation of industrial sisal fiber waste derived activated carbon by chemical activation and effects of carbonization parameters on surface characteristics. *Ind Crops Prod*. 2017 Jan 1;95:583–90.
19. Ghosh A, Razzino C do A, Dasgupta A, Fujisawa K, Vieira LHS, Subramanian S, et al. Structural and electrochemical properties of babassu coconut mesocarp-generated activated carbon and few-layer graphene. *Carbon N Y*. 2019 Apr 1;145:175–86.
20. Sesuk T, Tammawat P, Jivaganont P, Somton K, Limthongkul P, Kobsiriphat W. Activated carbon derived from coconut coir pith as high performance supercapacitor electrode material. *J Energy Storage*. 2019 Oct 1;25.
21. Agrawal LL, Awadhia A. DSC and conductivity studies on PVA based proton conducting gel electrolytes. *Bulletin of Materials Science*. 2004 Dec;27:523-7.
22. Rajesh M, Manikandan R, Park S, Kim BC, Cho WJ, Yu KH, et al. Pinecone biomass-derived activated carbon: the potential electrode material for the development of symmetric and asymmetric supercapacitors. *Int J Energy Res*. 2020 Sep 1;44(11):8591–605.
23. Awasthi GP, Bhattarai DP, Maharjan B, Kim KS, Park CH, Kim CS. Synthesis and characterizations of activated carbon from *Wisteria sinensis* seeds biomass for energy storage applications. *Journal of Industrial and Engineering Chemistry*. 2019 Apr 25;72:265–72.
24. Du W, Wang X, Sun X, Zhan J, Zhang H, Zhao X. Nitrogen-doped hierarchical porous carbon using biomass-derived activated carbon/carbonized polyaniline composites for supercapacitor electrodes. *Journal of Electroanalytical Chemistry*. 2018 Oct 15;827:213–20.
25. Muhammad FF, Aziz SB, Hussein SA. Effect of the dopant salt on the optical parameters of PVA:NaNO₃ solid polymer electrolyte. *Journal of Materials Science: Materials in Electronics*. 2015 Jan 1;26(1):521–9.
26. Dubey P, Shrivastav V, Maheshwari PH, Sundriyal S. Recent advances in biomass derived activated carbon electrodes for hybrid electrochemical capacitor applications: Challenges and opportunities. *Carbon*. 2020 Dec 1;170:1-29.

27. Spagnoli AA, Giannakoudakis DA, Bashkova S. Adsorption of methylene blue on cashew nut shell based carbons activated with zinc chloride: The role of surface and structural parameters. *J Mol Liq.* 2017 Mar 1;229:465–71.
28. Arshanitsa A, Jashina L, Pals M, Ponomarenko J, Akishin Y, Zake M. Characteristics of the Main-and Side-Stream Products of Microwave Assisted Torrefaction of Lignocellulosic Biomass of Different Origination. *Energies.* 2022 Mar 2;15(5):1857.
29. Hassan MF, Sabri MA, Fazal H, Hafeez A, Shezad N, Hussain M. Recent trends in activated carbon fibers production from various precursors and applications—A comparative review. *Journal of Analytical and Applied Pyrolysis.* 2020 Jan 1;145:104715.
30. Ma F, Ding S, Ren H, Liu Y. Sakura-based activated carbon preparation and its performance in supercapacitor applications. *RSC Adv.* 2019;9(5):2474–83.
31. Yu F, Huang M, Wu J, Qiu Z, Fan L, Lin J, et al. A redox-mediator-doped gel polymer electrolyte applied in quasi-solid-state supercapacitors. *J Appl Polym Sci.* 2014 Jan 15;131(2).
32. Daud WM, Ali WS, Sulaiman MZ. The effects of carbonization temperature on pore development in palm-shell-based activated carbon. *Carbon.* 2000 Jan 1;38(14):1925–32.
33. Yang S, Zhang K. Converting corncob to activated porous carbon for supercapacitor application. *Nanomaterials.* 2018 Apr 1;8(4).
34. Nguyen TN, Le PA, Phung VBT. Facile green synthesis of carbon quantum dots and biomass-derived activated carbon from banana peels: synthesis and investigation. *Biomass Convers Biorefin.* 2022 Jul 1;12(7):2407–16.
35. Ma G, Li J, Sun K, Peng H, Mu J, Lei Z. High performance solid-state supercapacitor with PVA-KOH-K₃[Fe(CN)₆] gel polymer as electrolyte and separator. *J Power Sources.* 2014 Jun 15;256:281–7.
36. Feng L, Yan B, Zheng J, Chen J, Wei R, Jiang S, et al. Soybean protein-derived N, O co-doped porous carbon sheets for supercapacitor applications. *New Journal of Chemistry.* 2022;46(22):10844–53.
37. Yan B, Zheng J, Feng L, Du C, Jian S, Yang W, et al. Wood-derived biochar as thick electrodes for high-rate performance supercapacitors. *Biochar.* 2022 Dec 1;4(1).
38. Zheng S, Zhang J, Deng H, Du Y, Shi X. Chitin derived nitrogen-doped porous carbons with ultrahigh specific surface area and tailored hierarchical porosity for high performance supercapacitors. *Journal of Bioresources and Bioproducts.* 2021 May 1;6(2):142–51.
39. Feng L, Yan B, Zheng J, Zhang Q, Wei R, Zhang C, et al. Chemical foaming-assisted synthesis of N, O co-doped hierarchical porous carbon from soybean protein for high rate performance supercapacitors. *Diam Relat Mater.* 2023 Mar;133:109767.
40. Elaiyappillai E, Srinivasan R, Johnbosco Y, Devakumar P, Murugesan K, Kesavan K, et al. Low cost activated carbon derived from Cucumis melo fruit peel for electrochemical supercapacitor application. *Appl Surf Sci.* 2019 Aug 30;486:527–38.
41. Peng C, Lang J, Xu S, Wang X. Oxygen-enriched activated carbons from pomelo peel in high energy density supercapacitors. *RSC Adv.* 2014;4(97):54662–7.

42. Yadav N, Yadav N, Hashmi SA. Ionic liquid incorporated, redox-active blend polymer electrolyte for high energy density quasi-solid-state carbon supercapacitor. *J Power Sources*. 2020 Mar 1;451.
43. Yadav N, Yadav N, Hashmi SA. High-Energy-Density Carbon Supercapacitors Incorporating a Plastic-Crystal-Based Nonaqueous Redox-Active Gel Polymer Electrolyte. *ACS Appl Energy Mater*. 2021 Jul 26;4(7):6635–49.

Chapter **5**

SUITABILITY OF NUTMEG SHELL- DERIVED ACTIVATED CARBON FOR APPLICATIONS IN Li-ION BATTERIES AND SUPERCAPACITORS

Some of the contents of this chapter have been published in

1. **M. Pulikkottil, R.R. Baby, A. Seema, Impact of the Stable Solid-Electrolyte Interphase in Sustainable and High-Performance Lithium-Ion Battery Anodes, Batteries & Supercaps, (2025) 2500228.**

5.1 Introduction

The demand for supercapacitors and lithium-ion batteries (LIBs) is continually increasing as they drive the transition toward a greener future in transportation. However, conventional electrode materials have limitations, such as high costs, limited resources, and environmental concerns. (1,2) Activated carbon (AC) is a widely recognised sustainable alternative to address these issues. The unique combination of high surface area, tunable porosity, and excellent electrical conductivity makes biomass-derived activated carbon (BDAC) an ideal platform for enhancing the electrochemical performance of these energy storage devices, as they determine key aspects such as energy density, power density, and cycle life.(3,4) Motivated by this, the present study aimed to develop a versatile electrode material using BDAC, particularly nutmeg shell, for applications in supercapacitors and LIBs.

In this work, the nutmeg shell waste was used as the precursor for the preparation of BDAC due to its inherent lignocellulosic nature. The shells contain lignin (50–59%), cellulose (11–28%), and hemicellulose (9–16%) in their total dry weight. This specific composition is advantageous for producing BDAC with a well-developed pore distribution.(5–7) Thus, this nutmeg-derived AC (ACNM) has better structural properties, which are beneficial for electrode applications in supercapacitors and LIBs.(8–10) Additionally, ACNM offers a sustainable and environmentally friendly approach to utilising nutmeg waste material and a cost-effective alternative to commercially available AC, which is often derived from non-renewable sources.(9)

Nevertheless, the structural properties of anode materials are crucial in forming and stabilising the solid electrolyte interface (SEI) on the surface of the anode material in LIBs. A stable SEI ensures long-term cycling stability, minimal active material loss, improved safety, and enhanced performance of LIBs.(10–12) Anode materials with high surface areas often result in thicker and nonuniform SEI layers due to an increased availability of active sites for electrolyte decomposition. Consequently, large surface area and high porosity in AC often result in a thicker SEI during the initial charging and discharging cycles.(13) This limitation can be addressed by optimising the porous distribution and surface area in the AC-based anode material. A controlled

porous structure in AC-based anodes can limit excessive formation of SEI, reduce initial capacity loss, and enhance the cycle life of LIBs.(14)

In the following sections, we shall discuss the development of porous ACNMs and insights into their remarkable material and electrochemical properties. Further, emphasis is given to optimising the activation ratio and carbonisation temperature to prepare ACNM and ensure efficient performance as an electrode in supercapacitors and LIBs.

5.2 Experimental details

5.2.1 Preparation of Nutmeg Shell-derived Activated Carbon

In this study, the KOH-based chemical activation of nutmeg shell waste is done at various activation ratios (weight% of nutmeg shells: KOH = 1, 2, and 3). The activated samples were carbonised in a tubular furnace at temperatures of 500 °C, 600 °C, 700 °C and 800 °C for one hour. Continuous Ar (99.99%) supply was provided throughout carbonisation. 0.1 M HCl and distilled water were used to wash the carbonised samples to maintain a neutral pH of the prepared samples.(15–17) The as-prepared ACNM samples were dried overnight at 100 °C and labeled as ACNM-1-700, ACNM-2-700, ACNM-3-700, ACNM-2-500, ACNM-2-600, ACNM-2-800, where (1, 2, 3) represents the activation ratio and (500, 600, 700, and 800 °C) represents carbonisation temperature.

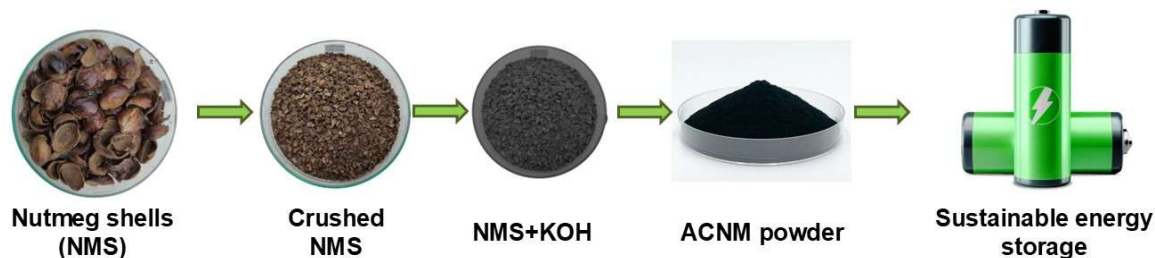


Figure 5.1 Methodology for preparing ACNM-based sustainable electrodes

5.2.2 Preparation of ACNM-based electrode material

The active electrode material was prepared by mixing ACNM-X-Y, carbon black, and PVDF at an 8:1:1 weight ratio in the solvent NMP, where X denotes the activation ratio and Y denotes the carbonisation temperature. The active material loading on the modified glassy carbon electrode was maintained at 10-20 mg cm⁻².

The anodes for LIBs were prepared using the homogeneous slurry mentioned above. The slurry was applied to the copper current collector (40 µm) employing the tape casting method. The casted anode tape was punched into a circular shape with a mass loading of 2 mg cm⁻².

5.2.3 Half-cell preparation and performance testing

The anode half cells were prepared by assembling lithium foil of thickness 45 µm and ACNM as the electrodes in the coin cell of type CR2025. Solupor® separator soaked in the electrolyte 1.0 M LiPF₆ in a 1:1 (V/V) mixture of ethylene carbonate (EC) and dimethyl carbonate (DMC) is also used in the fabrication to ensure constant contact between electrode and electrolyte. The assembling of half cells was carried out inside a glovebox filled with argon gas. This precise fabrication method ensures that the anode half-cells are correctly fabricated and optimised for subsequent electrochemical evaluation.

5.3 Results and Discussions

The structural and electrochemical properties of ACNMs are evaluated using various physicochemical characterisation techniques, including XRD, Raman spectroscopy, TEM, SEM, FTIR, XPS, and TGA analyses. The electrochemical performance of these materials is further assessed using techniques such as CV, GCD, and EIS. The results obtained from these analyses help to optimise the preparation conditions for ACNM-X-Ys. Additionally, the interface studies with scanning electrochemical microscopy (SECM) highlight the formation of the SEI layer on the anode surface and its subsequent impact on battery performance. Overall, these studies provide insights into the potential of ACNMs for practical applications in supercapacitor and LIB systems.

5.3.1 Material characterisations

5.3.1.1 XRD analysis

XRD spectra of ACNMs are displayed in Figure 5.2. All the samples exhibit identical XRD patterns, indicating the presence of a graphitic nature alongside remarkable surface cavities. The spectra contain two broad peaks around $2\theta = 24^\circ$ and 43° . These characteristic peaks represent (002) and (100) planes of carbon as referenced in the ICDD database (ICDD PDF No: 01-075-1621).^(17,18) These planes indicate interlayer condensation and a significant regularity in crystalline structure, respectively. These features suggest the suitability for supercapacitor electrode applications.

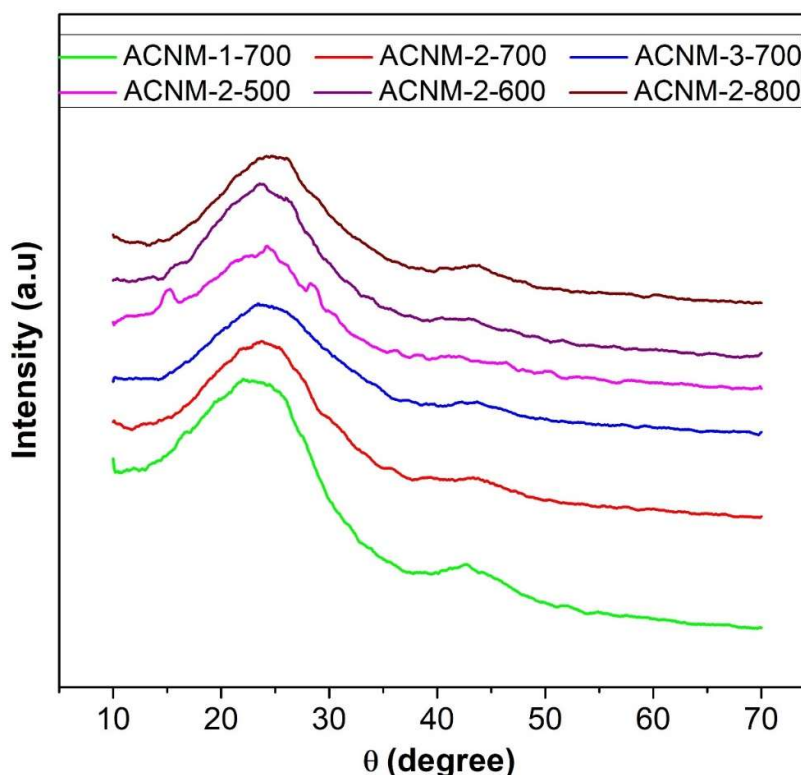


Figure 5.2 XRD patterns of ACNM-X-Ys.

Additionally, this structure contributes positively to the formation of a stable SEI. However, the broadness of these peaks is related to the amorphous nature of the as-prepared AC, which provides a large surface area and active sites for electrolyte decomposition. This may lead to the formation of a heterogeneous SEI layer. Since

ACNM-2-700 has the lowest FWHM value, it is more likely to develop a stable SEI layer than the other ACNM-X-Ys.(19,20)

5.3.1.2 Raman Spectroscopy

Figure 5.3 shows the Raman spectra of developed ACNMs that provide essential insights into the structural characteristics of as-prepared AC. All spectra are identical and display characteristic peaks corresponding to graphitic carbon. The peak around 1355 cm^{-1} represents the D band corresponding to the disordered sites in the sample. Whereas, the E_{2g} symmetric phonon vibrations can be identified from the G band around 1580 cm^{-1} . Raman spectra of ACNMs represent the availability of graphite and disordered carbon structures.(21,22)

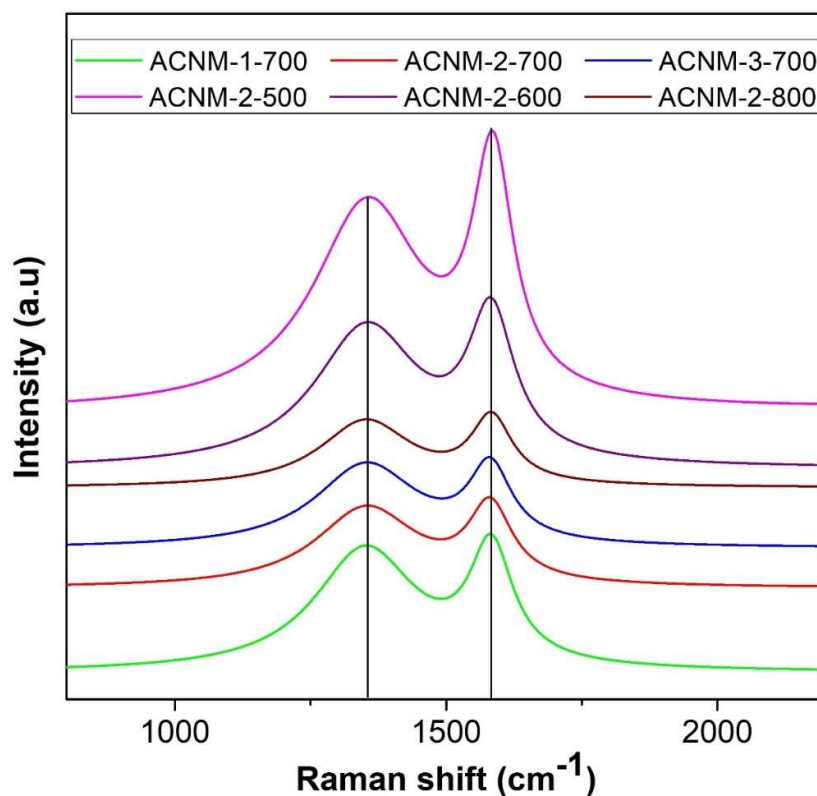


Figure 5.3 Raman spectra of ACNM-X-Ys

The intensity ratios (I_D/I_G) for ACNM-1-700, ACNM-2-700, and ACNM-3-700 were 0.94, 1.05, and 1.11, respectively. The rise in I_D/I_G ratio indicates that the activation ratio is responsible for defects in the graphitic structure. ACNM-2-500,

ACNM-2-600, ACNM-2-700, and ACNM-2-800 have I_D/I_G values of 0.87, 0.98, 1.05, and 1.01, respectively, that represent the incomplete graphitisation at lower temperatures and distorted graphitic structure at higher carbonisation temperatures.(23,24) This structure is related to the limited atomic mobility of carbon atoms at lower temperatures and the rapid movement of carbon atoms at higher temperatures. Ultimately, this structure leads to a higher concentration of disordered sites.(8) These available defects are desirable to improve the number of active sites and accessible surface area in the ACNM-based electrode material for supercapacitors.

The presence of defects and disordered sites in AC significantly influences the performance of LIB systems, with the I_D/I_G ratio serving as a key quantitative indicator. A higher I_D/I_G ratio represents a higher level of disorder that may lead to capacity fading during cycling and reduced rate capability. In contrast, a lower I_D/I_G ratio is related to an ordered structure, which may limit the storage capacity. Therefore, a moderate I_D/I_G value can offer additional lithium storage, sufficient capacity and a stable cycle life.(25) Moreover, a higher I_D/I_G is typically associated with the chances of forming a thick and unstable SEI layer. ACNM-3-700 and ACNM-2-800 exhibit large I_D/I_G ratios, indicating thicker SEI layer formation and irreversible loss in capacity when used as anodes in LIBs.(26,27) These results suggest the potential of ACNM-2-700 as an anode material with an optimum I_D/I_G value.

5.3.1.3 TGA analysis

The pristine nutmeg shells (NMS) were subjected to TGA-DTA analysis to explore thermal degradation with the temperature rise. TGA-DTA curves shown in Figure 5.4 represent three distinct portions of mass loss stages, indicating the presence of hemicelluloses, lignin, and cellulose in NMS.(9,28) Around 120 °C, highly volatile compounds undergo breakdown along with water evaporation and cause initial weight loss. The thermal decomposition of hemicellulose occurs in the temperature range of 120 to 250 °C. For a temperature above 250 °C, cellulose undergoes decomposition. The most significant mass loss occurs between 360 °C and 550 °C, which represents the degradation of lignin.(16,29)

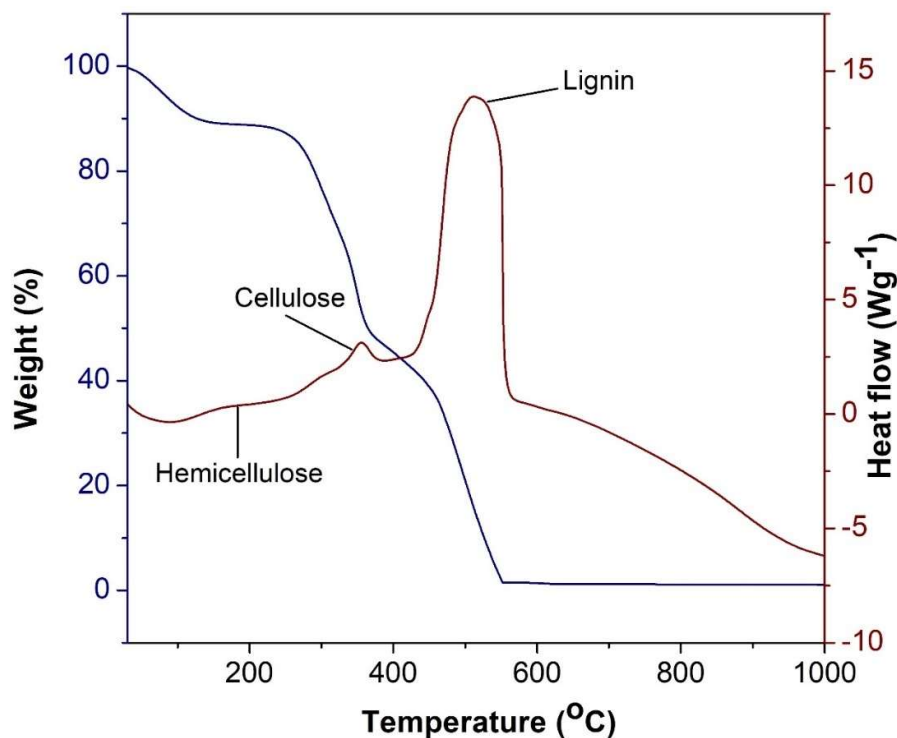


Figure 5.4 TGA curve of pristine nutmeg shell

5.3.1.4 SEM analysis

The surface morphology of ACNMs was identified using SEM analysis. The interconnected porous structure was evident from the SEM images shown in Figure 5.5. This well-distributed porous structure improves the accessible surface area, enabling rapid electrolyte diffusion. Consequently, this increases the electrochemical efficiency of the electrode material.(30,31) The SEM images demonstrate the significant effect of activation ratio and carbonisation temperature on the formation of pore structure during the synthesis of ACNM. In addition, the porous distribution became more defined with the rise in carbonisation temperature.(21,32) However, further increases in temperature above 700 °C cause a high degree of porosity along with thin structural walls.(28)

Energy dispersive spectroscopy (EDS) was performed for elemental analysis of ACNMs, and results are presented in Table 5.1. In all the ACNMs, the ratio of carbon predominates over that of oxygen.

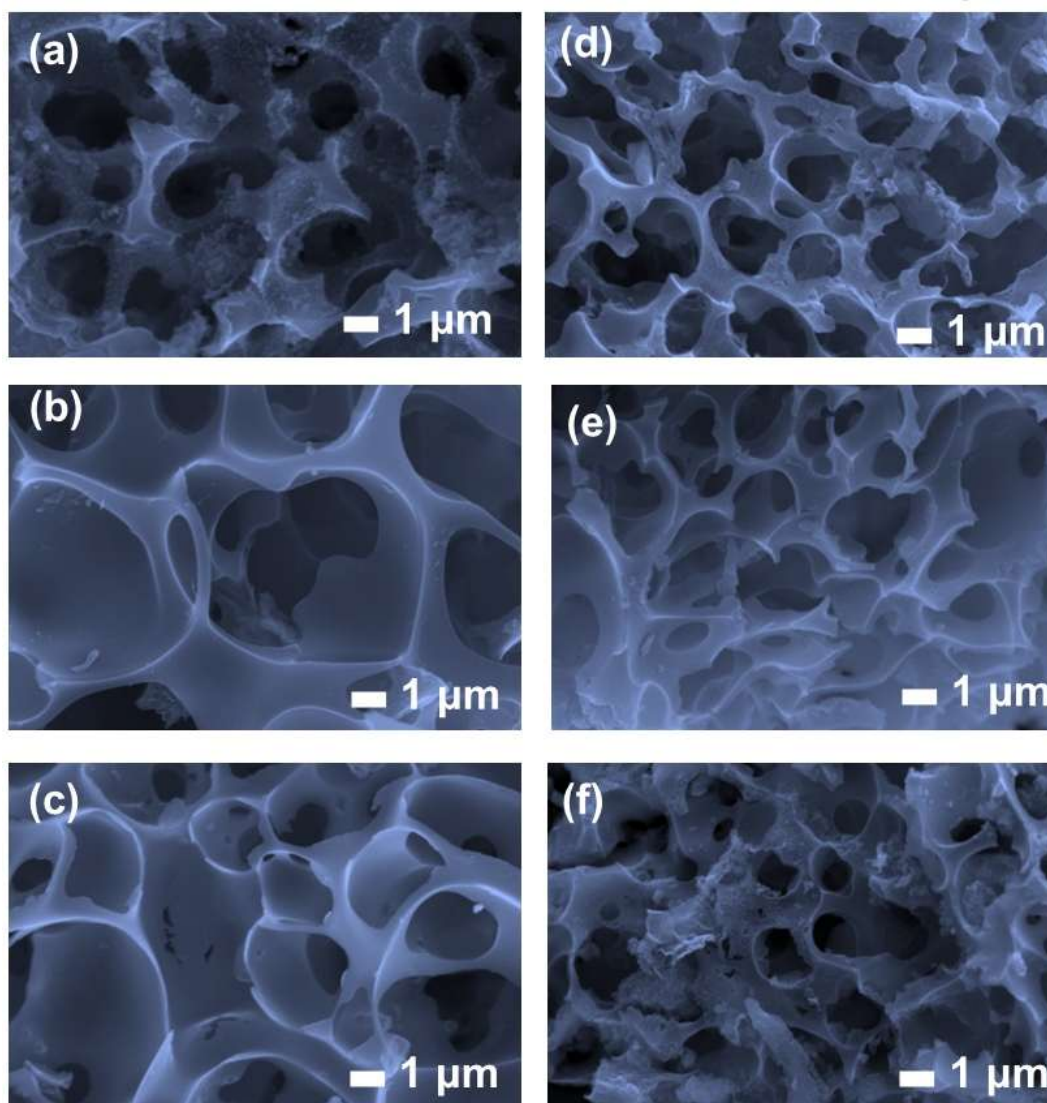


Figure 5.5 SEM images of (a) ACNM-1-700, (b) ACNM-2-700, (c) ACNM-3-700, (d) ACNM-2-500, (e) ACNM-2-600, and (f) ACNM-2-800 at 20,000 X magnification.

Table 5.1 Elemental analysis of ACNM-X-Ys

Weight percentage	ACNM-1-700	ACNM-2-700	ACNM-3-700	ACNM-2-500	ACNM-2-600	ACNM-2-800
C	88.3	91.7	92.3	82.5	90.2	91.3
O	11.73	8.3	7.7	17.5	9.8	8.7

5.3.1.5 Surface area analysis

The pore distribution in electrode materials determines their energy storage efficiency for supercapacitor and LIB applications. The nitrogen adsorption-desorption isotherms were studied to identify the porous structure in ACNMs, which is displayed in Figure 5.6. All the materials show type-I isotherms, indicating the microporous nature of the electrode materials. In the lower relative pressure region, the volume adsorbed rises sharply and remains unchanged in the higher relative pressure region. The development of micropores in ACNMs may be due to the intercalation and deintercalation of potassium. The H4-type hysteresis loop in the isotherms can be related to the availability of mesopores in their structure.(33,34)

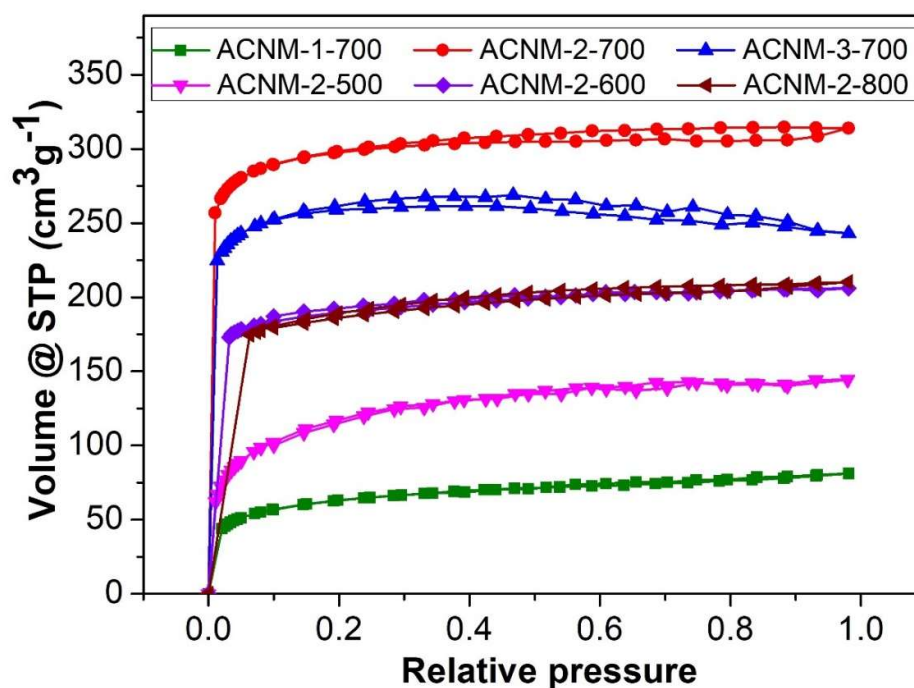


Figure 5.6 N₂ adsorption–desorption isotherms of ACNMs

Figure 5.7 represents the distribution of the pores in ACNMs. The surface areas and pore volume of ACNMs were tabulated in Table 5.2. These data confirm that lignin content in precursor material significantly contributes to the micropores in ACNMs. The surface area of ACNM-X-Y increases as the activation ratio rises from 1 to 3. The carbonisation temperature also plays a superior role in determining the porosity of these materials. The surface area of the as-prepared AC rises with

carbonisation temperature up to 700 °C, and beyond this temperature, the surface area is reduced.(15,35) The carbonisation temperature aids in the surface area till the temperature reaches 700 °C.

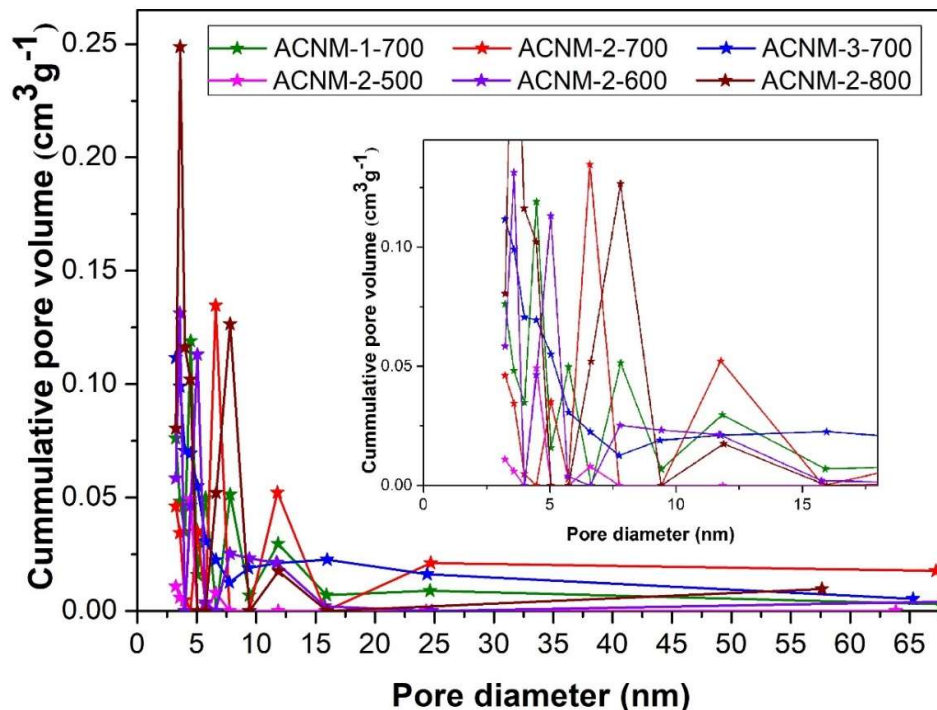


Figure 5.7 Pore size distributions of ACNMs (the inset shows the enlarged curves at smaller pore diameters)

As the carbonisation temperature further increases, the surface area of the as-prepared AC reduces.(15,36) This indicates hierarchical pore structure formation followed by structural collapse at higher temperatures. The results show that ACNM-3-700 has the largest surface area, primarily due to its microporous structure. However, the availability of micropores and mesopores in ACNM-2-700 facilitates the accessible surface area and improves electrochemical charge storage.(37) All these unique characteristics help improve the electrochemical performance of ACNMs.

Additionally, the surface area analysis of anode material is a highly reliable tool for predicting the feasibility of SEI formation in LIBs. The micropores available in the anode material can lead to excessive SEI formation and electrolyte

decomposition. Meanwhile, the presence of mesopores creates a more stable and uniform SEI.(13,38)

Table 5.2 Pore structure parameters of ACNM-X-Ys

Sample Name	Surface area [m^2g^{-1}]			Pore volume [cm^3g^{-1}]			Diameter (nm)
	Micro pores	Meso pore	Total	Micro pores	Meso pore	Total	
ACNM-1-700	170	20	230	0.073	0.028	0.126	2.18
ACNM-2-700	851	50	1011	0.239	0.770	0.960	3.24
ACNM-3-700	1092	9	1177	0.426	0.023	0.486	1.65
ACNM-2-500	123	3	256	0.101	0.004	0.160	2.50
ACNM-2-600	691	19	764	0.262	0.026	0.318	1.66
ACNM-2-800	342	35	432	0.173	0.047	0.224	2.06

Even though the large surface area and pore volume improve lithium-ion intercalation, they can also lead to extensive SEI layer formation and capacity loss.(11) On comparing the as-prepared anode materials, ACNM-2-700 shows the highest contribution of mesopores, which benefits lithium storage efficiency due to its high surface area and helps minimise excessive SEI formation.(39) This observation is also consistent with Raman spectroscopy and XRD analysis of ACNMs.

5.3.1.6 FTIR analysis

FTIR spectra of ACNMs displayed in Figure 5.8 illustrate the available functional groups in the materials. All the spectra exhibit similar peaks around 1055, 1200, 1593, and 3461 cm^{-1} . These peaks indicate the graphitic structure in the materials.(40) The peaks at 1055 cm^{-1} can be ascribed to the C–H bending vibrations in the materials. The broad bands near 1593 cm^{-1} and 3461 cm^{-1} are associated with C=C stretching and O–H vibrations. The absorption peak at 1200 cm^{-1} is related to the C–O stretching vibrations present in them.(28) These functional groups are advantageous for enhancing charge storage, specific capacitance and other surface properties in MSAC-based FSC electrodes.(41)

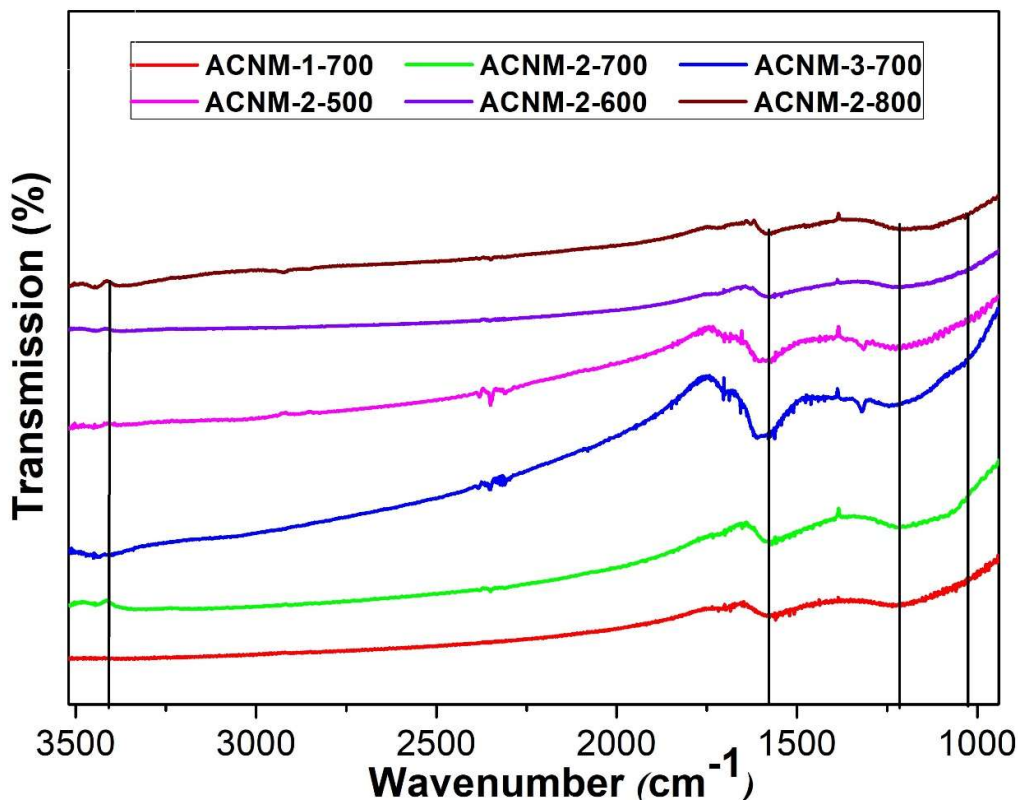


Figure 5.8 FTIR spectra of ACNM-X-Ys

The reduction in the intensity of peaks with the rise in carbonisation temperature indicates a more tightly packed graphitic structure with fewer functional groups. The spectra further validate the effect of activation ratio in improving the functional groups in the materials.(28)

5.3.1.7 XPS analysis

The XPS survey spectrum (Figure 5.9 (a)) identifies elements such as oxygen and carbon. Figures 5.9 (b) and (c) show the C1s and O1s spectra of ACNMs. The C 1s spectrum displays three characteristic peaks at approximately 284.6 eV, 285.68 eV, and 288.8 eV. These peaks correspond to the C–C bond, the C–O bond, and the O=C–O bond, respectively. The highest intensity of the C–C bond suggests that most of the carbon atoms in ACNM are arranged in a conjugated honeycomb structure.(42)

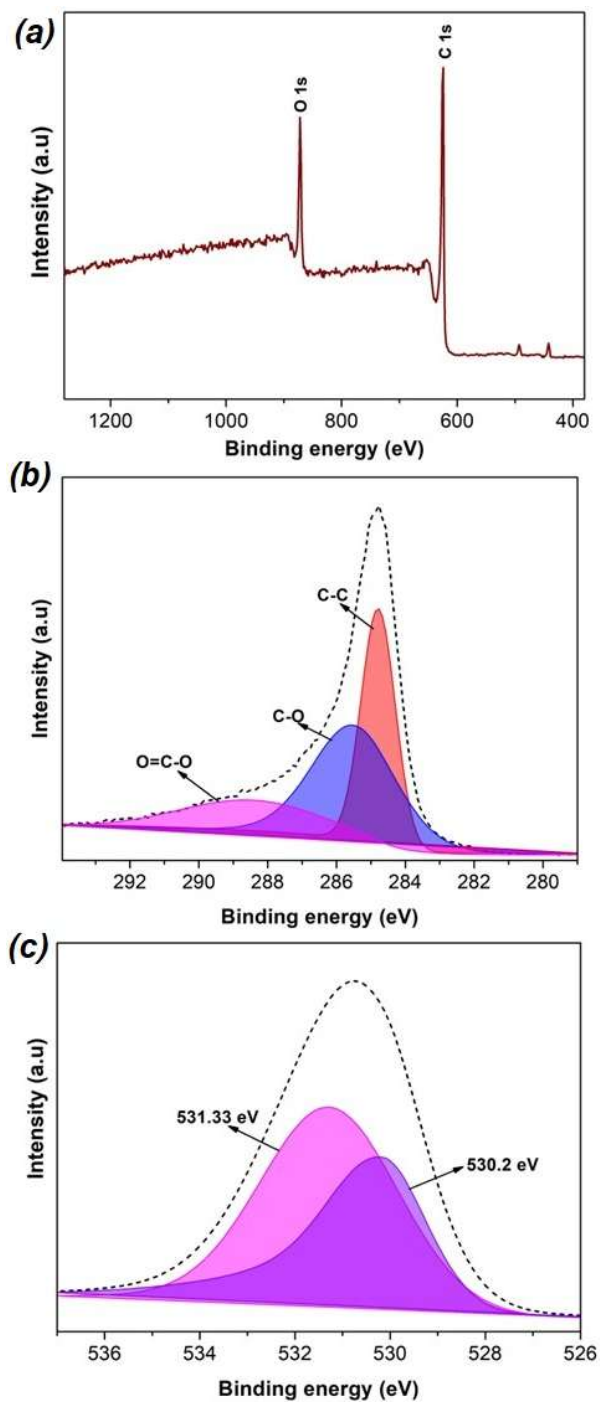


Figure 5.9 (a) XPS Survey spectrum, (b) C 1s spectrum, and (c) O 1s spectrum of ACNM.

Figure 5.9 (c) shows the O 1s spectra, which display two deconvoluted peaks at 530.2 eV and 531.33 eV. These peaks indicate the presence of various oxygen-containing functional groups and oxygen vacancies, respectively. The aromatic

structure present in the lignin may be responsible for these oxygen-containing functional groups. These functional groups are favourable for increasing the number of active sites. In addition, these groups can lead to more reactive sites for electrolyte decomposition and result in a thicker or less stable SEI layer. However, these groups can also enhance the surface wettability of the anode material and adhesion of the electrolyte, which is advantageous for improving ion transport and SEI uniformity.(43) These results are also consistent with the observations made in the Raman spectra.

5.3.1.8 TEM analysis

The structural micrograms obtained from high-resolution TEM are shown in Figure 5.10, illustrating the disordered porous structure present in the material.

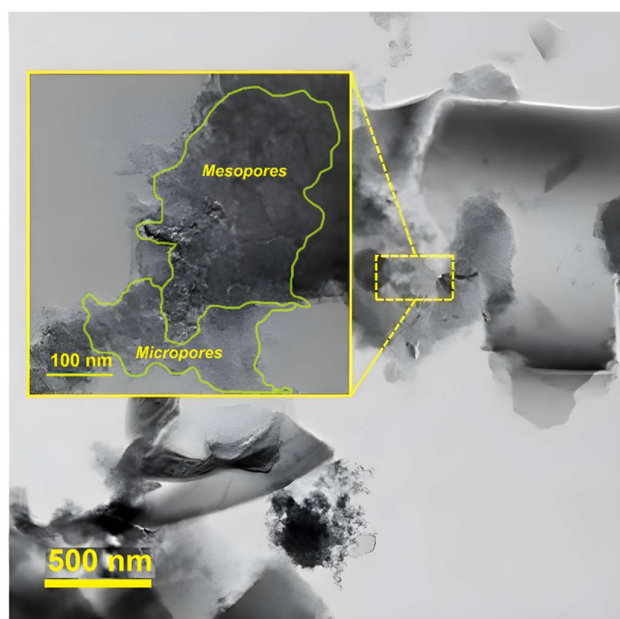


Figure 5.10 TEM images of the ACNM-2-700 at various magnifications showing porous structures with micro, meso, and macropores.

The availability of micropores and mesopores over the surface of the anode material is beneficial for extensive charge storage capacity.(42) Additionally, an adequate distribution of mesopores is visible from the TEM images, facilitating better electrolyte wetting and ion transport. The availability of mesopores and micropores is advantageous for fast ion transport and facilitates the capacitive properties of AC,

which are favourable for supercapacitor electrode applications.(41) Furthermore, such a pore distribution is also favourable for the development of a stable and uniform SEI in the anode material. The TEM images are consistent with the surface area analysis and suggest the feasibility of ACNM for anode applications in LIBs.(43) .

5.3.2 Electrochemical characterisation of ACNM-X-Ys

The electrochemical efficiency of ACNM-X-Ys was evaluated using a three-electrode configuration, including a working electrode, a reference electrode and a counter electrode. The counter and reference electrodes were platinum and calomel electrodes, respectively. 1 M KOH was used for electrochemical analysis over a potential window ranging from -1V to 0V.

5.3.2.1 Cyclic voltammetry (CV)

CV was performed at different scan rates from 1 to 100 mV s^{-1} over a potential window from -1 to 0 V. CV curves of ACNMs at a scan rate of 1 mV s^{-1} are compared in Figure 5.11. The CV curves are quasi-rectangular in shape and reversible in nature, indicating fast electrochemical response of the electrode materials.

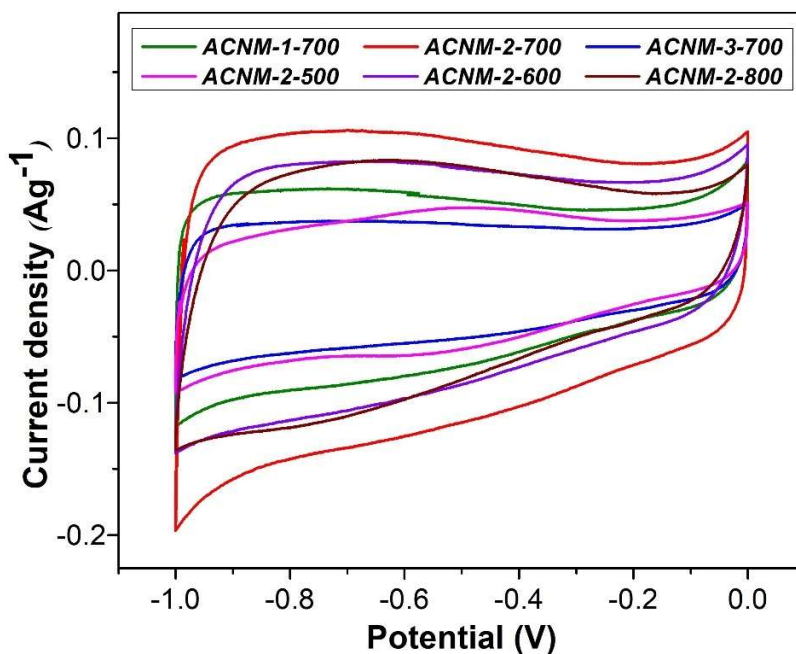


Figure 5.11 CV curves of ACNM-X-Ys at a scan rate of 1 mV s^{-1}

The activation ratio and carbonisation temperature have a significant role in the formation of pores that facilitate efficient charge transport in the system. The CV curves also validate the effect of these parameters on the specific capacitance of the as-prepared electrode materials. The larger CV curve area of ACNM-2-700 than that of all other electrode materials, indicating its higher specific capacitance and better electrochemical performance.(15)

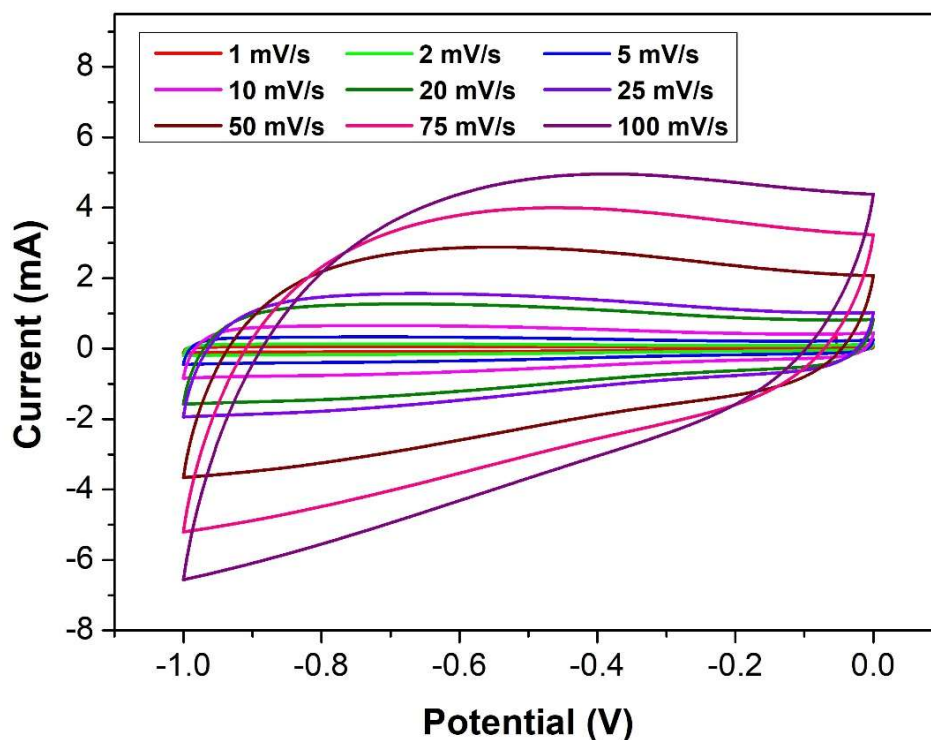


Figure 5.12 CV curves of ACNM-2-700 at different scan rates

Figure 5.12 displays the influence of scan rate on the value of ACNM-2-700's specific capacitance. The quasi-rectangular shape of the CV curves is maintained even at higher scan rates, which indicates effective diffusion of the electrolyte into the internal pores of the ACNM-2-700 electrode material.(44,45) This further validates its potential as an effective electrode material for energy storage applications.

5.3.2.2 Galvanostatic charge-discharge (GCD)

GCD analysis was performed at different current densities to explore the charging and discharging behaviour of the electrode materials. The charging-discharging characteristic of ACNMs at a current density of 1 A g^{-1} is displayed in Figure 5.13.

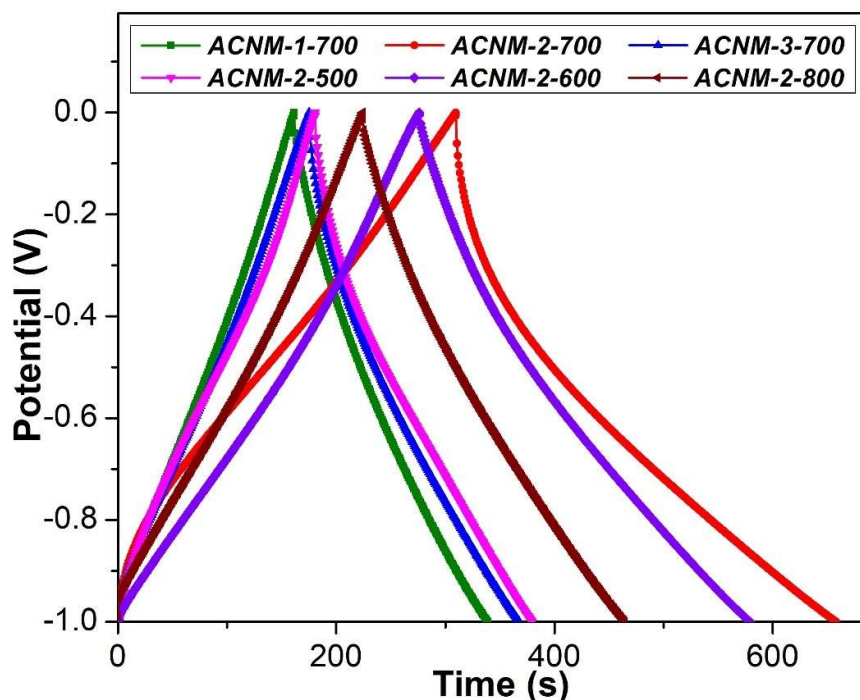


Figure 5.13 GCD curves of ACNM-X-Ys at a current density of 1 A g^{-1}

The triangular and symmetrical nature of the GCD curves indicates the reversible behaviour of the electrode material with low internal resistance and reasonable electrical conductivity.(46,47) By showing a longer discharge curve, ACNM-2-700 demonstrates superior faradaic efficiency compared to other electrode materials. This makes it a potential choice for applications where performance and reliability are paramount.

The GCD curves of MSAC-2-700 (Figure 5.14) at different current densities show a reduction in the discharge time and specific capacitance with an increase in current density. This is ideal for a perfect EDLC system.

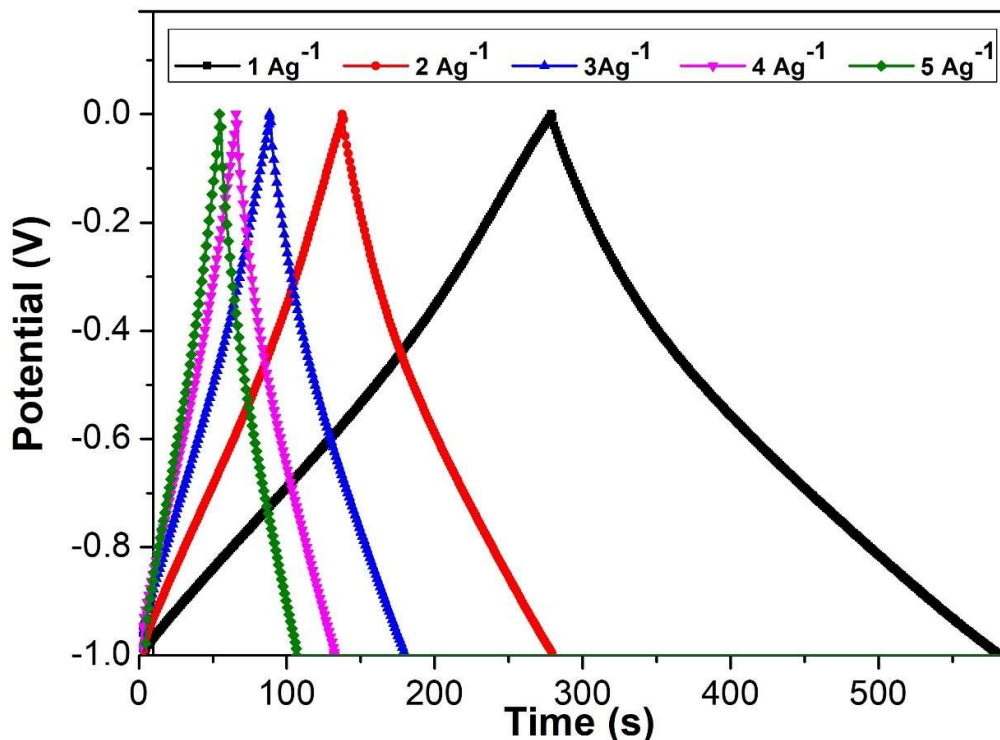


Figure 5.14 GCD curves of ACNM-2-700 at various current densities

The specific capacitance of the materials was calculated using the equation:

$$C_{sp} = \frac{I \times \Delta t}{\Delta V \times m} \quad 5.1$$

where C_{sp} is the specific capacitance, I is the current density, Δt is the discharge time, ΔV is the potential window, and m is the mass of the active material in the electrode(48).

The specific capacitance values of the electrode materials are displayed in Figure 5.15. ACNM-2-700 exhibits the highest specific capacitance of 314 Fg^{-1} . Moreover, it shows a better rate capability than other ACNMs. These observations confirm that ACNM-2-700 has the most accessible surface area among all ACNMs, further validating the predictions from the SEM and surface area analyses. The better capacitance values can be assigned to the availability of porous distribution that consists of both micropores and mesopores, which facilitate rapid ion diffusion and effective electrolyte ion transport in an electrochemical system(49).

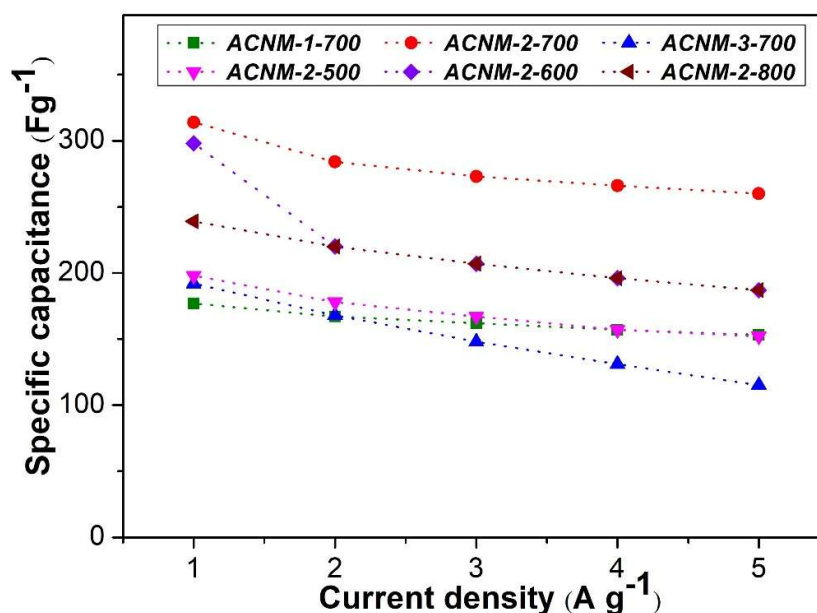


Figure 5.15 Dependence of specific capacitance on the current density

Ten thousand charging-discharging cycles at a current density of 20 A g⁻¹ were carried out to understand the cycle stability of ACNM-2-700. Figure 5.16 displays the capacitive retention for 10,000 cycles with the first and last ten charging and discharging cycles as an inset. The capacitance retention of the electrode material is found to be approximately 96%. The state-of-the-art specific capacitance values of various BDAC electrode materials are listed and compared with the present ACNM-2-700 in Table 5.3. The satisfactory specific capacitance value of as-prepared ACNM shows its potential as an electrode material for supercapacitor applications.

Equations 5.2 and 5.3 were used for calculating the specific energy density (E) and power density (P) of ACNM-2-700.

$$E(\text{Whkg}^{-1}) = \frac{0.5 \times C_{sp} \times V^2}{3.6} \quad 5.2$$

$$P(\text{Wkg}^{-1}) = \frac{3600 \times E}{t} \quad 5.3$$

where C_{sp} is the specific capacitance ($F g^{-1}$), V is the voltage change during the discharge after the reduction of the IR drop (V), and t is the discharge time (s) (50).

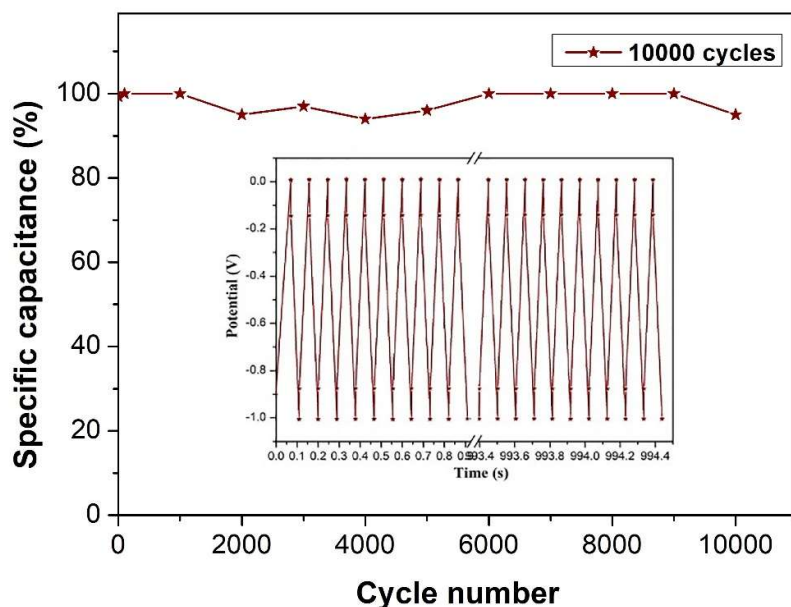


Figure 5.16 Cycle life of ACNM-2-700 at a current density of $20 A g^{-1}$ for 10,000 cycles with the first and last ten charge–discharge cycles in the inset

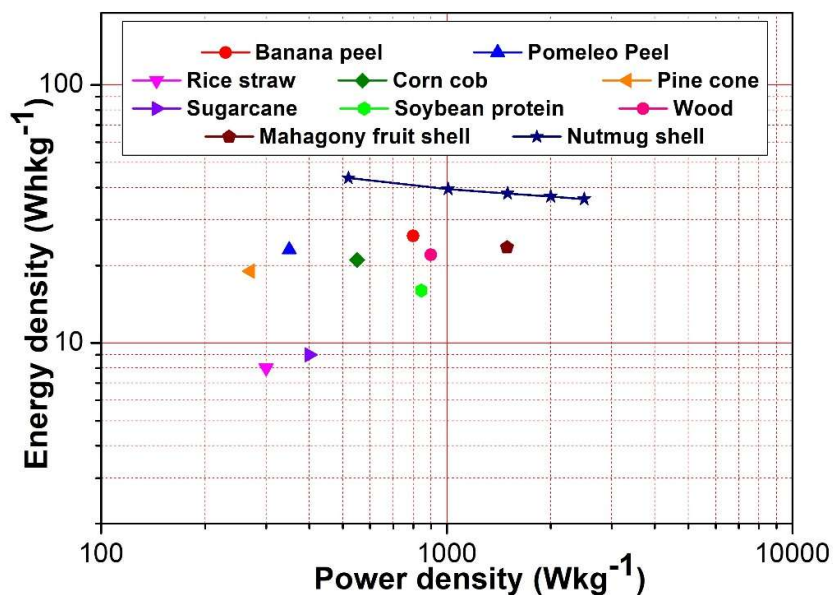


Figure 5.17 Ragone plot of ACNM-2-700 compared with various BDAC electrode materials

Table 5.3 Comparison of specific capacitance of different BDAC materials.

Precursor Material	Activating agent	Specific capacitance [F g ⁻¹]	Current density [A g ⁻¹]	Electrolyte	Energy density [Wh kg ⁻¹]	Power density [W kg ⁻¹]	Cycle Test @ 10 A g ⁻¹	Ref.
Coconut coir pith	NaOH	120	1	1 M H ₂ SO ₄	18	271	----	(37)
Pine cone	KOH	185	0.5	1 M H ₂ SO ₄	16	454	96 % after 10000 cycles	(31)
Pomelo peels	KOH	103	1	1 M Na ₂ SO ₄	20	500	99 % after 4000 cycles	(51)
Chitin	NaOH	227	0.5	1 M H ₂ SO ₄	8	1200	98 % after 10000 cycles	(52)
Cashew nutshell	KOH	194	1	0.5 M Na ₂ SO ₄	--	--	94 % after 10000 cycles	(16)
Mahogany fruit shell	KOH	267	1	1 M KOH	27	990	97 % after 10000 cycles	(15)
Wood	KOH	175	0.05	6 M KOH	22	900	76% after 20000 cycles	(53)
Cucumis melo fruit peel	KOH	245	0.5	1 M KOH	29	279	91 % after 10000 cycles	(54)
Sakura flower	KOH	231	1	6 M KOH	--	--	95 % after 5000 cycles	(55)
Banana peel	H ₃ PO ₄	199	1	1 M KOH	23	342	90 % after 11000 cycles	(56)
Soybean protein	ZnCl ₂	210	1	6 M KOH	16	844	93 % after 10000 cycles	(57)
Nutmeg shell	KOH	314	1	1 M KOH	43	519	96 % after 10000 cycles	Present work

The Ragone plot of various BDAC electrode materials (Figure 5.17) shows that the prepared electrode material has a high energy density with remarkable power density, which is ideal for highly efficient electrode materials in EDLCs.

5.3.2.3 Electrochemical impedance spectroscopy (EIS)

The EIS technique was used to explore the charge transfer and ion diffusion properties of the ACNMs. The EIS was done for a frequency range from 10^{-2} to 10^5 Hz with an AC perturbation of 10 mV. The Nyquist plots of ACNM-X-Y (Figure 5.18) have a semicircle in the high-frequency region, followed by a straight line in the low-frequency region.

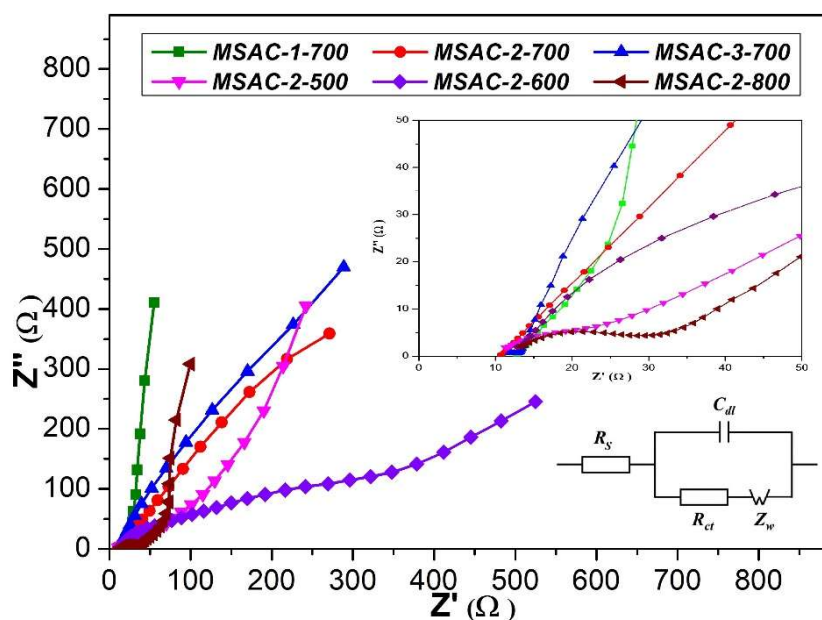


Figure 5.18 Nyquist plot of the electrode materials (the enlarged curves at the high-frequency range and equivalent circuit diagram are shown in the insets)

The Nyquist plots were further analysed using a fitted equivalent circuit with components such as internal resistance (R_s), charge transfer resistance (R_{ct}), double-layer capacitance (C_{dl}), and Warburg resistance (Z_w) (19,35). The intersection of the semicircle in the high-frequency region of the Nyquist plot gives the value of the equivalent series resistance (ESR), R_s . The vertical line in the low-frequency region can be assigned to the low diffusive resistance associated with the fast ion transport in

the electrochemical system. Table 5.4 lists the values of R_s , R_{ct} , C_{dl} , and Z_w . The element R_s represents the sum of contact resistance between the current collector and active material, solution resistance, and intrinsic resistance of the electrode material. Whereas R_{ct} is associated with the ion diffusion resistance between the electrolyte and active material. The electrochemical reaction rate and the charge accumulation at the interface are given by Z_w and C_{dl} , respectively (3,31).

Table 5.4 Fitted values of R_s , R_{ct} , C_{dl} , and Z_w derived from the EIS curves for ACNM-X-Ys.

Sample Name	R_s [Ω]	R_{ct} [Ω]	C_{dl} [μF]	W [$\Omega \cdot \text{S}^{-1/2}$]
ACNM-1-700	11.63 ± 0.25	24.98 ± 0.23	13.16 ± 2.94	127.60 ± 1.84
ACNM -2-700	9.88 ± 0.11	19.96 ± 0.12	39.04 ± 0.43	43.06 ± 1.78
ACNM -3-700	11.31 ± 0.20	20.29 ± 0.21	12.99 ± 0.12	34.90 ± 3.40
ACNM -2-500	11.26 ± 0.39	19.4 ± 0.39	9.93 ± 1.11	145.60 ± 23.3
ACNM -2-600	11.66 ± 0.41	27.02 ± 0.48	3.29 ± 1.19	124.60 ± 3.46
ACNM -2-800	13.36 ± 0.42	24.97 ± 0.96	8.96 ± 0.93	38.38 ± 7.10

5.3.3 Study of the suitability of ACNMs as LIB anode material

Anode half-cells were fabricated with lithium metal and ACNMs as cathode and anode material, respectively. The fabricated half-cells were then subjected to various electrochemical analyses to understand the lithium storage properties of ACNMs in LIBs. CV measurements at a scan rate of 0.1 mV s^{-1} , for a potential window of 0-3 V vs. $\text{Li}^+|\text{Li}$, were carried out to evaluate the capacity of the fabricated anode half-cells. Galvanostatic cycling tests were also performed at various C rates for the same voltage range. The suitability of ACNM electrodes in LIBs was subsequently studied by combining the CV and GCD measurements. EIS is carried out from 10 mHz to 100 kHz, with a voltage of 10 mV.

Figure 5.19 represents the cyclic voltammograms of ACNM-based anode half-cells at a scan rate of 0.1 mV s^{-1} in the potential window of 0-3 V vs. $\text{Li}^+|\text{Li}$. The CV

scan is repeated for five cycles, which resembles that of traditional amorphous carbon materials.(58) The curves are irreversible and the first cycle shows a significant difference from the subsequent cycles, which is a typical characteristic of the carbon-based anodes in LIBs.(59) The first cycle shows a broad peak extending below 1.0 V vs. $\text{Li}^+|\text{Li}$ and a small signal at about 0.7 V followed by a tilted line extending to 0.01 V vs. $\text{Li}^+|\text{Li}$. This irreversible nature of the first cycle can be assigned to the partial electrolyte decomposition and SEI layer formation at the electrode/electrolyte interphase.(58,60) The irreversible reduction peaks observed in the first cycle of CV measurement demonstrate the formation of SEI and the loss of lithium ions associated with it.(61)

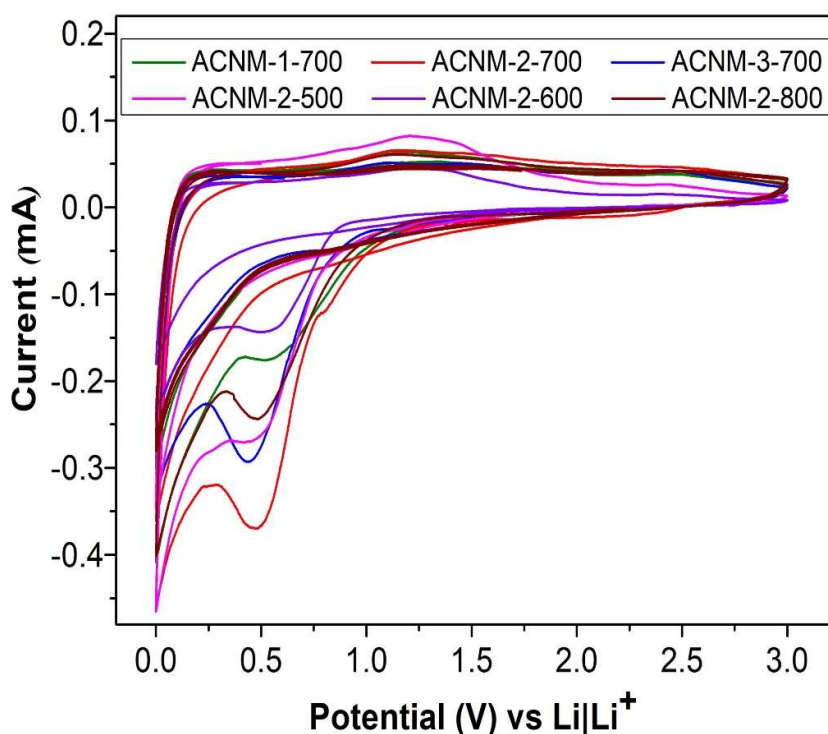


Figure 5.19 Cyclic voltammogram of anode half-cell at a scan rate of 0.1 mV s^{-1}

The subsequent cycles are reversible and have a progressively overlapping profile with peaks around 0.01 V vs. $\text{Li}^+|\text{Li}$ as the SEI has already formed. Additionally, the diminishing peaks in these subsequent cycles indicate the intercalation and deintercalation of the lithium ions into the disordered carbon along

with lithium plating/stripping into the pores present in the active materials without further SEI formation.(13,26) A slight shift and broadening of redox peaks may be ascribed to the increased resistance at the SEI layer. These overlapping cycles further indicate the irreversible electrolyte decomposition and the presence of a well-formed SEI in the half-cell.(62) The absence of additional irreversible processes in subsequent CV curves also validates the stability of the SEI formed. This stability trend further demonstrates that the anode material's high surface area and well-defined porous structure make it ideal for LIBs, as it offers sufficient sites for insertion of lithium ions.(63,64)

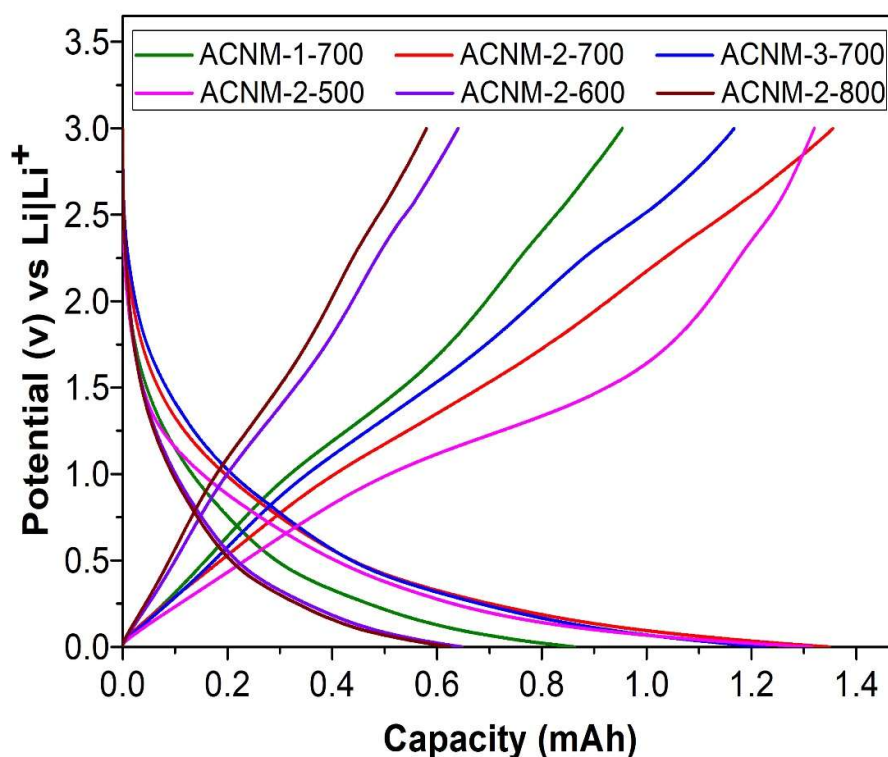


Figure 5.20 The charge-discharge profile of the half-cell at a current rate of 0.1C

The specific capacity of the anode cells is calculated using the equation given below.

$$Q \text{ (mAhg}^{-1}\text{)} = \int_{V_2}^{V_1} i(V)dV / (2 \times 3.6 \times m \times v) \quad 5.4$$

where Q is the specific capacity (mAhg⁻¹), $\int_{V_2}^{V_1} i(V)dV$ is the total charge storage, m

and v represent the mass of active material and scan rate respectively. The capacity of a system is directly related to the area under the CV curve. When the CV curve area decreases after the first cycle, it can lead to significant capacity loss. This initial capacity loss further validates the formation of SEI. After the first cycle, the CV curves overlap, indicating a stable system with perfect reversible capacity, even though there is a considerable irreversible capacity loss in the first cycle.(63,65) The value of specific capacity calculated from CV is tabulated in Table 5.5.

Table 5.5 Values of specific capacity of ACNMs.

Sample name	Capacity (mAh)		Specific capacity (mAhg ⁻¹)	
	From CV	From GCD	From CV	From GCD
ACNM-1-700	0.80	0.92	333	383
ACNM -2-700	1.32	1.52	574	610
ACNM -3-700	0.96	1.31	291	397
ACNM -2-500	1.17	1.44	344	422
ACNM -2-600	0.52	0.67	326	416
ACNM -2-800	0.48	0.65	302	404

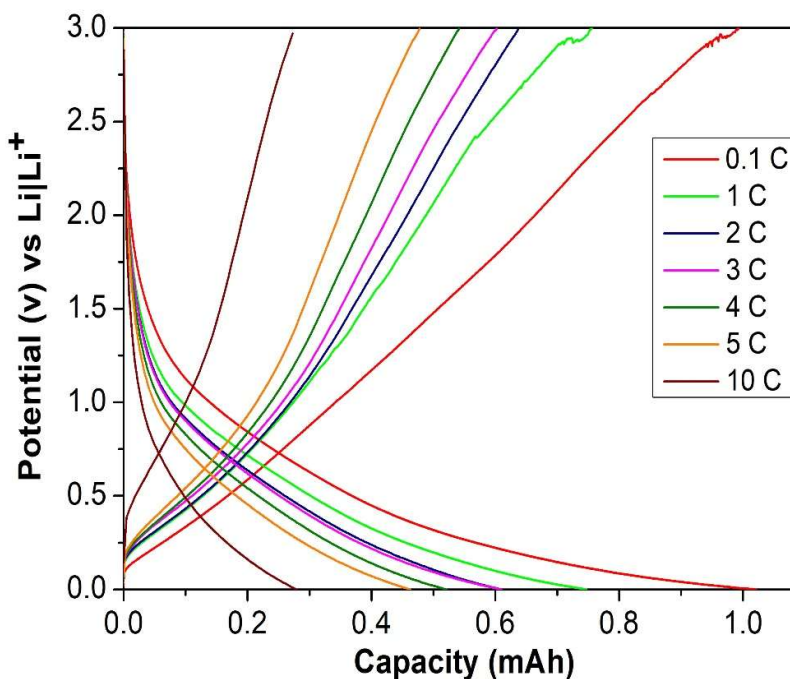


Figure 5.21 GCD profile of the half-cell at various current rates

ACNM-based half-cells were further investigated galvanostatically at different current rates. The GCD cycling was carried out over the voltage range 0-3.0 V vs. $\text{Li}^+|\text{Li}$. The charge-discharge profile of fabricated half-cells, at a current rate of 0.1C, is displayed in Figure 5.20. ACNM-2-700 shows the highest capacity of 610 mAh g^{-1} at a C rate of 0.1C. This remarkable reversible capacity value can be attributed to the well-developed porous structure and excellent surface area in the anode material.

Table 5.6. Specific capacity values of sustainable AC anode materials

Precursor Material	Activating agent	Specific capacity [mAh g^{-1}]	Current rate	Cycle Test	Ref.
Jute fiber	ZnCl ₂	534	0.2 C	79 % @ C/5 after 100 cycles	(1)
Pine cone	KOH	370	0.1 C	83 % @ C/3 after 100 cycles	(13)
Cherry pits	KOH	320	0.1 C	84 % @ C/3 after 200 cycles	(62)
Rice husk	NaOH	477	0.2 C	68 % @ C/5 after 100 cycles	(66)
Coffee waste	Air	359	0.2 C	72 % @ C/5 after 100 cycles	(52)
Pistachio shell	KOH	317	0.1 C	85 % @ 2C after 500 cycles	(67)
Nutmeg shell	KOH	610	0.1C	84 % @ 2C after 200 cycles	Present work

The values of specific capacity of all samples from GCD analysis were consolidated in Table 5.5. The presence of SEI significantly influences the GCD characteristics of an anode half-cell. The lithium loss occurred during the formation of SEI is evident from the higher discharge capacity in the first GCD cycle than that in subsequent cycles. The state of art specific capacity values of previously reported BDAC materials are compared with the present ACNM-2-700 and represented in the

Table 5.6. These values confirm the remarkable capacity of the ACNM-based LIB system.

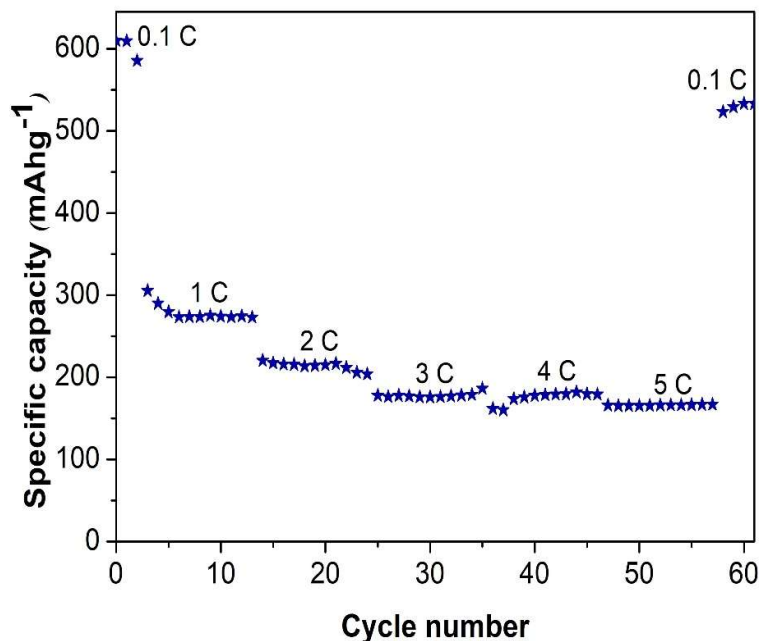


Figure 5.22 Variation in capacity during rate capability test

Further stability tests show that the anode half-cell shows excellent rate capability and cycling stability. The relationship between the capacity values of the fabricated half-cell and the current rate is displayed in Figure 5.21. The capacity value exhibits a consistent decreasing trend with an increase in the current rate.

The rate capability test of the half-cell is carried out at different current rates for 10 cycles each. Figure 5.22 represents the capacity at current rates of 0.1 C, 1 C, 2 C, 3 C, 4 C, 5 C, and 0.1 C. The reversible capacities are 610 mAhg⁻¹, 307 mAhg⁻¹, 211 mAhg⁻¹, 186 mAhg⁻¹, 169 mAhg⁻¹, and 557 mAhg⁻¹ respectively. The capacity retention is found to be 91% after the rate capability test. The decrease in cell capacity at higher current rates is likely due to restricted lithium-ion diffusion through SEI, as the increased resistance from the SEI typically results in a significant capacity drop. However, the remarkable capacity retention observed here suggests efficient ion transport, indicating the presence of a well-formed SEI.(68)

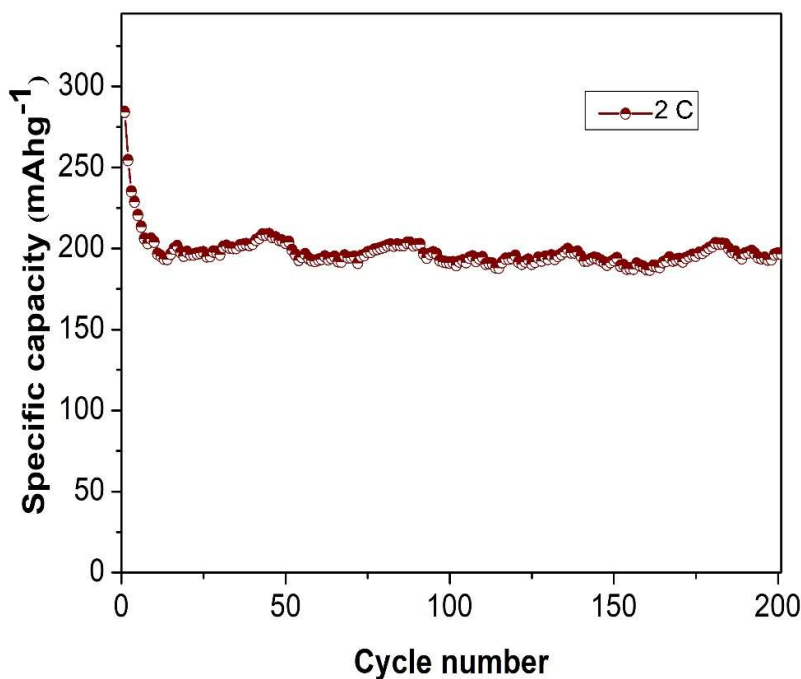


Figure 5.23 Cycling performance of the anode half-cell at a current rate of 2C for 200 cycles

A stable SEI facilitates regular charging and discharging without electrolyte decomposition, which in turn improves the cycle stability of LIBs and ensures better capacity retention and slower capacity loss during cycling. Figure 5.23 represents a cycle test of the system at a current rate of 2 C for 200 cycles. The cycling performance is also very impressive, as the capacity value of 200 mAhg⁻¹ is maintained even after 200 cycles. However, the value of specific capacity gradually decreases until the 33rd cycle. This may be due to the irreversible surface reactions and the hierarchical porous nature of the material.(69)

The volume of the material expands as lithium ions are embedded during the cycling process, and slightly subsides when the ions are released. Compared to bulk material, the structural collapse of hierarchical porous material occurs more frequently. In subsequent cycles, the material stabilises and maintains discharge capacity. This can also be attributed to a stable SEI layer formed at the interface between the anode and the electrolyte.(70)

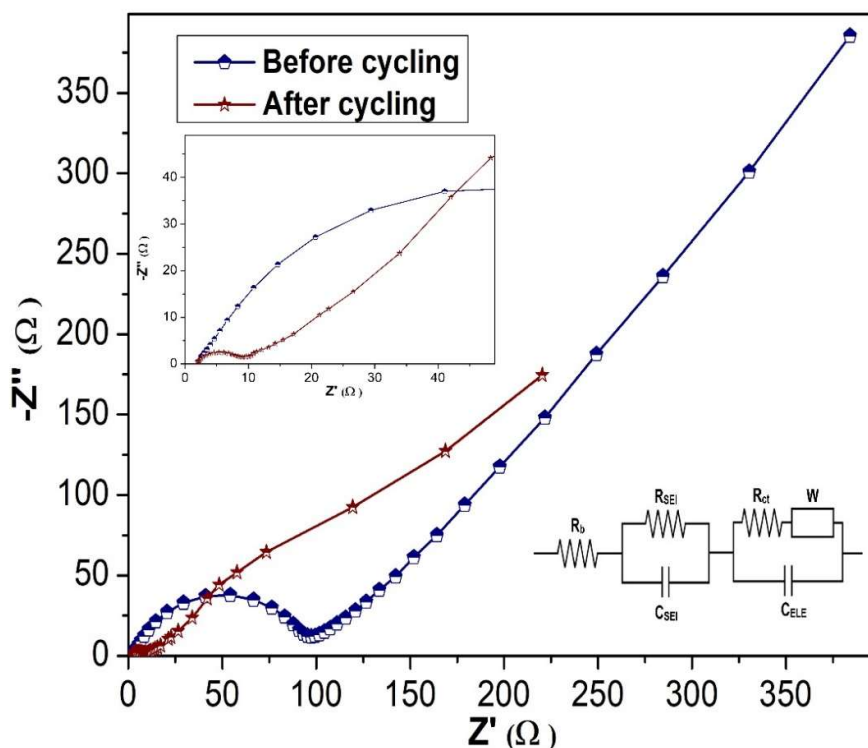


Figure 5.24 Nyquist plot of ACNM-2-700 based anode half cells before and after cycling with higher frequency region and equivalent circuit as inset

The Nyquist plot (Figure 5.24) is used to study the formation of SEI and other electrochemical behavior of fabricated LIBs. The higher frequency region of the Nyquist plot reflects electrolyte resistance in the fabricated system. The deeply convoluted semicircle in the middle-to-high frequency reflects resistance associated with charge transfer resistance and the SEI layer present in the electrode/ electrolyte interface of the LIB half-cell. Warburg element represented by a tilted line with a slope around 45° in the low-frequency indicates the semi-infinite diffusion.(39) The curve contains a semicircle with a small diameter, indicating lower SEI resistance and suggesting a well-formed SEI. This stable SEI enhances the performance of LIB. The curves can be related to an equivalent circuit consisting of elements such as R_b , R_{SEI} , C_{SEI} , R_{ct} , C_{ELE} , and W . Where R_b represents the bulk resistance. The resistance due to charge transfer is given by R_{ct} . The resistance and capacitance of SEI are given by R_{SEI}

and C_{SEI} . The values of C_{ELE} and W are related to the double-layer capacitance and lithium-ion diffusion on the anode material, respectively.

Table 5.7 Components in the equivalent circuits of the anode half-cell

	R_b [Ω]	C_{SEI} [μF]	R_{SEI} [Ω]	R_{ct} [Ω]	C_{ELE} [μF]	W [$\Omega S^{-1/2}$]
Before cycling	2.12±0.1	3.84±0.2	79.50±0.2	5.03±0.2	2.14±2.9	79.98±1.8
After cycling	2.42±0.2	1.05±0.1	108.60±0.1	5.77±0.1	21.1±0.4	18.30±1.7

Table 5.7 contains the values of these components before and after cycling experiments. The lower R_b and R_{ct} values demonstrate the formation of a stable SEI. Moreover, the reduction in ohmic and activation polarization during lithiation/delithiation processes is evident from these values. The effect of cycling is also clear from these Nyquist plots. A slight increase in R_b value suggests the ageing of LIB over prolonged cycling. The smaller diameter of the semicircle after cycling may be ascribed to the decrease in charge transfer resistance. In the Nyquist plots, the Warburg element of the anode half cell after cycling decreases, also confirming the presence of a thin SEI.(71,72) These observations are consistent with those of CV and GCD.

5.3.4 Mapping of SEI layer on the surface of anode with SECM

SECM is used to study the formation of SEI on ACNM-based anode electrodes. SECM analysis was performed on pristine and cycled (after the first cycle and after 200 cycles) anode electrodes with an ultramicroelectrode of diameter $\sim 15 \mu m$ in a three-electrode configuration. $Fe(CN)_6^{3-}/Fe(CN)_6^{4-}$ is employed as a redox mediator for the analysis. Figure 5.25 represents the schematic illustration of the SECM experimental setup.

Here, the SECM area scan is used to investigate the surface of anodes and understand the changes associated with the formation of SEI. The information related to the surface is obtained from the tip current, which is a function of the tip position. The approach method was employed to identify the closest distance for receiving

current feedback, and the z-position was fixed before starting the area scan in the x-y direction. The current profile obtained reflects the surface of the anode under study and is associated with the electrochemical behaviour of the surfaces. This data is represented as a colour pattern, with each colour corresponding to the respective current value.(73,74)

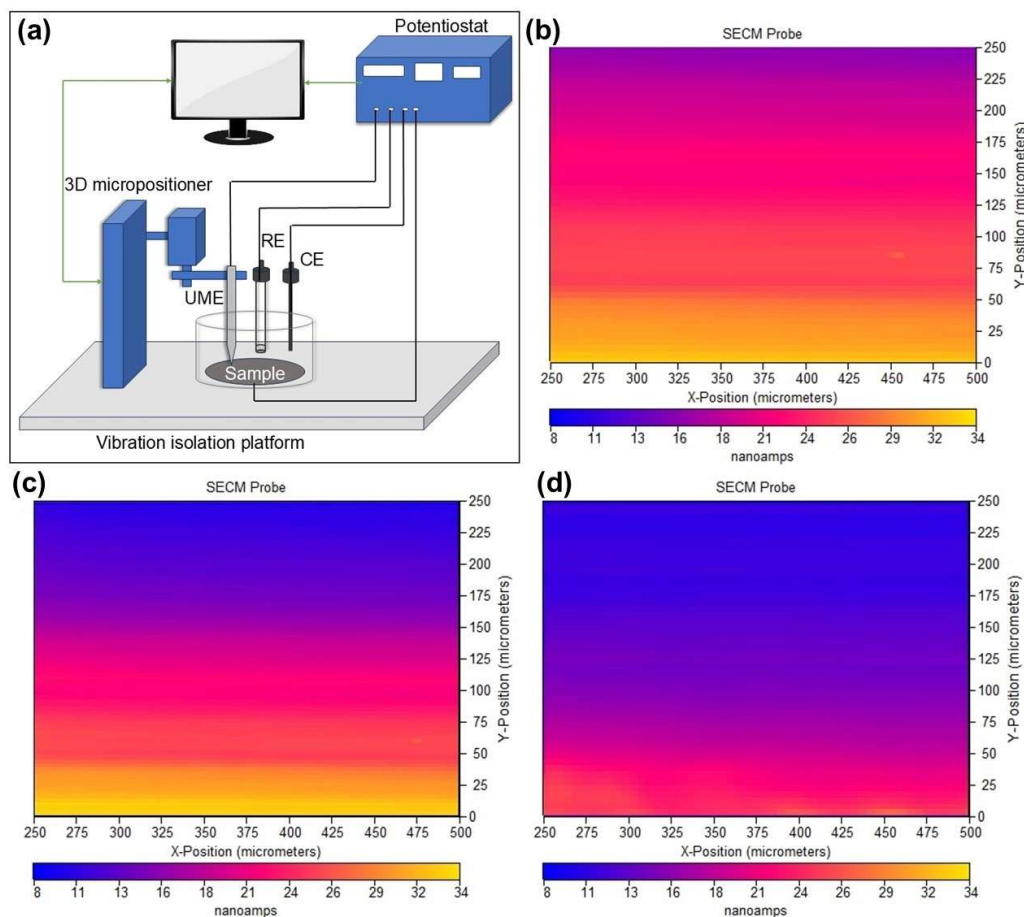


Figure 5.25 (a) Schematic illustration of SECM experimental setup, SECM area scan measurement of (b) pristine anode, (c) after the first cycle, and (d) after 200 cycles of charging and discharging

The SECM was recorded in positive feedback mode in an area scan of $250 \mu\text{m} \times 250 \mu\text{m}$. Figure 5.25 (b)-(d) illustrates the area scan of pristine anode, after the first cycle and after 200 cycles, respectively. These figures reveal a randomly distributed SEI layer, which may be attributed to the high surface area and porosity in the anode material.(75) The pristine anode (Figure 5.25 (b)) has a relatively uniform

current profile with minor variations corresponding to the local topography. However, after cycling, SEI is randomly distributed across the electrode surface. (14) Figure 5.25 (c) displays the heterogeneous evolution of the interface on the anode after the first cycle. The SECM image obtained for cycled anode material (Figure 5.25 (d)) indicates insulating SEI regions, which are unevenly distributed across the surface. (76) Significant reductions in the current profile after cycling further confirm the formation of a well-defined SEI. The SECM analysis is also consistent with the electrochemical behavior of the obtained CV curves. The irreversible capacity loss associated with the first cycle charging and discharging is also validated from the observations of SECM analysis. (77) Overall, ACNM has demonstrated remarkable performance in terms of specific capacity, cyclability, availability of well-formed SEI, and rate capability, making it a promising anode material for LIBs.

5.4 Conclusion

In conclusion, we have developed AC with an enhanced surface area and hierarchical porous structure from nutmeg shell waste through chemical activation using KOH, followed by carbonisation. By fine-tuning the activation ratio and carbonisation temperature, a total of 6 samples were prepared, in which sample ACNM-2-700 ended up with a large surface area of $1011 \text{ m}^2\text{g}^{-1}$ and pore volume of $0.960 \text{ cm}^3\text{g}^{-1}$. The observations from physicochemical analyses suggest a hierarchical pore distribution that facilitates effective ion transport and improves charge storage in ACNM-based electrodes. Additionally, the availability of mesopores and micropores in ACNM-2-700 is beneficial in effective lithium storage as well as the formation of stable SEI. The hierarchical porous structure yielded into highly efficient electrode material with a specific capacitance of 314 Fg^{-1} at a current density of 1 Ag^{-1} . It has also showcased excellent capacitance retention of 96% over 10000 charge-discharge cycles, suggesting the developed ACNM is a promising candidate for supercapacitor electrode application.

Anode half cells were fabricated using all electrode materials to assess their suitability for LIB applications. A high specific capacity of 610 mAhg^{-1} at a current rate of 0.1 C was obtained for the ACNM-2-700-based anode. Moreover, the material displayed better stability over 200 cycles for a current rate of 2 C. The rate capability

test further validated the efficiency of the anode material for LIBs. SECM scanning of the pristine and cycled anodes validated the effective formation of SEI in a fabricated half-cell. The results of structural and electrochemical characterisations are in agreement. All the reported approach for fabricating electrode material is a straightforward and cost-effective route and thus offer great promise for future energy storage applications.

References

1. Dou Y, Liu X, Wang X, Yu K, Liang C. Jute fiber based micro-mesoporous carbon: A biomass derived anode material with high-performance for lithium-ion batteries. *Mater Sci Eng B Solid State Mater Adv Technol*. 2021 Mar 1;265.
2. Xing B, Shi F, Jin Z, Zeng H, Qu X, Huang G, Zhang C, Xu Y, Chen Z, Lu J. A facile ice-templating-induced puzzle coupled with carbonization strategy for kilogram-level production of porous carbon nanosheets as high-capacity anode for lithium-ion batteries. *Carbon Energy*. 2024 Dec;6(12):e633.
3. Rish K, Tahmasebi A, Wang R, Dou J, Yu J. Novel composite nano-materials with 3D multilayer-graphene structures from biomass-based activated-carbon for ultrahigh Li-ion battery performance. *Electrochim Acta*. 2021 Sep 10;390.
4. Zhao W, Yan B, Chen D, Chen J, Zhang Q, Jiang L, et al. Free-standing carbon network with enhanced capacitive performance synthesized via green H₂O₂ activation. *Colloids Surf A Physicochem Eng Asp*. 2023 Jul;668:131425.
5. Thangaselvabai T, Sudha KR, Selvakumar T, Balakumbahan R. Nutmeg (*Myristica fragrans* Houtt)-the twin spice-a review. *Agricultural Reviews*. 2011;32(4):283-93.
6. Kapoor IPS, Singh B, Singh G, De Heluani CS, De Lampasona MP, Catalan CAN. Chemical composition and antioxidant activity of essential oil and oleoresins of nutmeg (*Myristica fragrans* Houtt.) fruits. *Int J Food Prop*. 2013 Jul 4;16(5):1059–70.
7. Anooj ES, Suganthi V, Praseetha PK. Synthesis and characterization of graphene quantum dots from turmeric powder (*Berberis aristata*) and its biomedical applications. *Scopus Ijphrd Citation Score*. 2019 Jul;10(7):1239.
8. Khan M, Yan S, Ali M, Mahmood F, Zheng Y, Song X, et al. From longan peel waste to energy storage: Porous activated carbon as a cathode matrix for advanced Li/Na-selenium batteries. *Progress in Natural Science: Materials International* . 2024 Apr 1;34(2):329–37.
9. Yarramsetti S, Girirajan M, Kalluri S, Sangaraju S, Maram PS. Multifunctional activated carbon derived from novel biomass for high-performance energy storage applications: A sustainable alternative to fossil-fuel-derived carbon. *Mater Chem Phys*. 2024 Jul 1;320.
10. Astuti Y, Insani RR, Ekaningsih AZ, Nurhasanah I, Lestariningsih T, Suseno A. Synthesis, characterization and electrochemical performance of Bi₂S₃/rice husk-based activated carbon composites as lithium ion battery anodes. *Results in Engineering*. 2024 Dec 1;24:103211.

11. Chu Y, Shen Y, Guo F, Zhao X, Dong Q, Zhang Q, Li W, Chen H, Luo Z, Chen L. Advanced characterizations of solid electrolyte interphases in lithium-ion batteries. *Electrochemical energy reviews*. 2020 Mar;3:187-219.
12. Nandihalli N. A Review of Nanocarbon-Based Anode Materials for Lithium-Ion Batteries. *Crystals*. 2024 Sep 10;14(9):800.
13. Zhang T, Mao J, Liu X, Xuan M, Bi K, Zhang XL, et al. Pinecone biomass-derived hard carbon anodes for high-performance sodium-ion batteries. *RSC Adv*. 2017;7(66):41504–11.
14. Hernández-Rentero C, Marangon V, Olivares-Marín M, Gómez-Serrano V, Caballero Á, Morales J, Hassoun J. Alternative lithium-ion battery using biomass-derived carbons as environmentally sustainable anode. *Journal of colloid and interface science*. 2020 Aug 1;573:396-408.
15. Pulikkottil M, Thomas A, Malamal Neelanchery M, Gopalan Elavumkal V, Ansari S. Highly Efficient Solid-State Supercapacitor with Porous Electrode Material. *Energy Technology*. 2023 Sep 1;11(9).
16. Pulikkottil M, Antony H, Muralidharan MN, Gopalan EV, Ansari S. Cashew Nut Shell Derived Porous Activated Carbon Electrodes for “Water-in-Salt” Electrolyte Based Symmetric Supercapacitor. *ChemistrySelect*. 2022 Jun 20;7(23).
17. Merin P, Jimmy Joy P, Muralidharan MN, Veena Gopalan E, Seema A. Biomass-derived activated carbon for high-performance supercapacitor electrode applications. *Chemical Engineering & Technology*. 2021 May;44(5):844-51.
18. Shi Z, Jin Y, Han T, Yang H, Gond R, Subasi Y, et al. Bio-based anode material production for lithium-ion batteries through catalytic graphitization of biochar: the deployment of hybrid catalysts. *Sci Rep*. 2024 Dec 1;14(1).
19. Dizbay-Onat M, Vaidya UK, Lungu CT. Preparation of industrial sisal fiber waste derived activated carbon by chemical activation and effects of carbonization parameters on surface characteristics. *Ind Crops Prod*. 2017 Jan 1;95:583–90.
20. Yang S, Zhang K. Converting corncob to activated porous carbon for supercapacitor application. *Nanomaterials*. 2018 Apr 1;8(4).
21. Ghosh S, Santhosh R, Jeniffer S, Raghavan V, Jacob G, Nanaji K, et al. Natural biomass derived hard carbon and activated carbons as electrochemical supercapacitor electrodes. *Sci Rep*. 2019 Dec 1;9(1).
22. Kok MV, Ozgur E. Characterization of lignocellulose biomass and model compounds by thermogravimetry. *Energy Sources, Part A: Recovery, Utilization and Environmental Effects*. 2017 Jan 17;39(2):134–9.
23. García JR, Sedran U, Zaini MAA, Zakaria ZA. Preparation, characterization, and dye removal study of activated carbon prepared from palm kernel shell. *Environmental Science and Pollution Research*. 2018 Feb 1;25(6):5076–85.
24. Nuriskasari I, Syahril AZ, Ivandini TA, Sumboja A, Priyono B, Yan Q, Destyorini F, Priyono S. Synthesis of graphitic carbon from empty palm oil fruit bunches through single-step graphitization process using K₂FeO₄-KOH catalyst as lithium ion battery anode. *Results in Engineering*. 2024 Dec 1;24:103273.

25. Liang YZ, Hsu TY, Su YS. Tailoring the Size of Reduced Graphene Oxide Sheets to Fabricate Silicon Composite Anodes for Lithium-Ion Batteries. *ACS Applied Materials and Interfaces*. 2024 Jun 5;16(22):29226–34.
26. Gajan A, Lecourt C, Torres Bautista BE, Fillaud L, Demeaux J, Lucas IT. Solid electrolyte interphase instability in operating lithium-ion batteries unraveled by enhanced-Raman spectroscopy. *ACS Energy Letters*. 2021 Apr 12;6(5):1757-63.
27. Mozhzhukhina N, Flores E, Lundström R, Nyström V, Kitz PG, Edström K, et al. Direct Operando Observation of Double Layer Charging and Early Solid Electrolyte Interphase Formation in Li-Ion Battery Electrolytes. *Journal of Physical Chemistry Letters*. 2020 May 21;11(10):4119–23.
28. Arshanitsa A, Jashina L, Pals M, Ponomarenko J, Akishin Y, Zake M. Characteristics of the Main-and Side-Stream Products of Microwave Assisted Torrefaction of Lignocellulosic Biomass of Different Origination. *Energies*. 2022 Mar 2;15(5):1857.
29. Redda HG, Nikodimos Y, Su WN, Chen RS, Jiang SK, Abrha LH, et al. Enhancing the electrochemical performance of a flexible solid-state supercapacitor using a gel polymer electrolyte. *Mater Today Commun*. 2021 Mar 1;26.
30. Liu Y, Zhang H, Li X, Wang L, Dong Y, Li W, et al. Solvent-assisted synthesis of N-doped activated carbon-based catalysts for acetylene hydrochlorination. *Appl Catal A Gen*. 2021 Feb 5;611.
31. Rajesh M, Manikandan R, Park S, Kim BC, Cho WJ, Yu KH, et al. Pinecone biomass-derived activated carbon: the potential electrode material for the development of symmetric and asymmetric supercapacitors. *Int J Energy Res*. 2020 Sep 1;44(11):8591–605.
32. Martínez-Casillas DC, Mascorro-Gutiérrez I, Arreola-Ramos CE, Villafán-Vidales HI, Arancibia-Bulnes CA, Ramos-Sánchez VH, et al. A sustainable approach to produce activated carbons from pecan nutshell waste for environmentally friendly supercapacitors. *Carbon N Y*. 2019 Jul 1;148:403–12.
33. Dubey P, Shrivastav V, Singh M, Maheshwari PH, Sundriyal S, Dhakate SR. Electrolytic Study of Pineapple Peel Derived Porous Carbon for All-Solid-State Supercapacitors. *ChemistrySelect*. 2021 Nov 15;6(42):11736–46.
34. Singh M, Gupta A, Sundriyal S, Jain K, Dhakate SR. Kraft lignin-derived free-standing carbon nanofibers mat for high-performance all-solid-state supercapacitor. *Mater Chem Phys*. 2021 May 1;264.
35. Du W, Wang X, Sun X, Zhan J, Zhang H, Zhao X. Nitrogen-doped hierarchical porous carbon using biomass-derived activated carbon/carbonized polyaniline composites for supercapacitor electrodes. *Journal of Electroanalytical Chemistry*. 2018 Oct 15;827:213–20.
36. Vo TN, Dang NK, Le ML, Nguyen VH, Tran VM, Nguyen MT, Tran NH, Nguyen TL, Kim IT. ZnCl₂-based activation for converting spent coffee grounds into a robust anode for Li-ion batteries. *Biomass and Bioenergy*. 2024 Feb 1;181:107058.
37. Sesuk T, Tammawat P, Jivaganont P, Somton K, Limthongkul P, Kobsiriphat W. Activated carbon derived from coconut coir pith as high performance supercapacitor electrode material. *J Energy Storage*. 2019 Oct 1;25.

38. Aktekin B, Riegger LM, Otto SK, Fuchs T, Henss A, Janek J. SEI growth on Lithium metal anodes in solid-state batteries quantified with coulometric titration time analysis. *Nat Commun.* 2023 Dec 1;14(1).
39. Zhang Y, Qiao R, Nie Q, Zhao P, Li Y, Hong Y, et al. Synergetic regulation of SEI mechanics and crystallographic orientation for stable lithium metal pouch cells. *Nat Commun.* 2024 Dec 1;15(1).
40. Spagnoli AA, Giannakoudakis DA, Bashkova S. Adsorption of methylene blue on cashew nut shell based carbons activated with zinc chloride: The role of surface and structural parameters. *J Mol Liq.* 2017 Mar 1;229:465–71.
41. Hassan MF, Sabri MA, Fazal H, Hafeez A, Shezad N, Hussain M. Recent trends in activated carbon fibers production from various precursors and applications—A comparative review. *Journal of Analytical and Applied Pyrolysis.* 2020 Jan 1;145:104715.
42. Deng B, Huang Q, Zhang W, Liu J, Meng Q, Zhu Z, et al. Design high performance biomass-derived renewable carbon material for electric energy storage system. *J Clean Prod.* 2021 Aug 1;309.
43. Senthil C, Park JW, Shaji N, Sim GS, Lee CW. Biomass seaweed-derived nitrogen self-doped porous carbon anodes for sodium-ion batteries: Insights into the structure and electrochemical activity. *Journal of Energy Chemistry.* 2021 Jan 1;64:286–95.
44. Sharma K, Arora A, Tripathi SK. Review of supercapacitors: Materials and devices. *Journal of Energy Storage.* 2019 Feb 1;21:801-25.
45. Grebel H. Asymmetric Supercapacitors: Optical and Thermal Effects When Active Carbon Electrodes Are Embedded with Nano-Scale Semiconductor Dots. *C (Basel).* 2021 Jan 15;7(1):7.
46. Fukuhara M, Kuroda T, Hasegawa F, Hashida T, Takeda M, Fujima N, et al. Amorphous cellulose nanofiber supercapacitors. *Sci Rep.* 2021 Dec 1;11(1).
47. Shabeeba P, Thayyil MS, Pillai MP, Soufeena PP, Niveditha C V. Electrochemical Investigation of Activated Carbon Electrode Supercapacitors. *Russian Journal of Electrochemistry.* 2018 Mar 1;54(3):302–8.
48. Qin H, Liu P, Chen C, Cong HP, Yu SH. A multi-responsive healable supercapacitor. *Nat Commun.* 2021 Dec 1;12(1).
49. Rawat S, Mishra RK, Bhaskar T. Biomass derived functional carbon materials for supercapacitor applications. *Chemosphere.* 2022 Jan 1;286.
50. Maity S, BM N, Kella T, Shee D, Das PP, Mal SS. Activated carbon- supported Vanadonickelate (IV) based hybrid materials for energy application. *J Energy Storage.* 2021 Aug 1;40.
51. Peng C, Lang J, Xu S, Wang X. Oxygen-enriched activated carbons from pomelo peel in high energy density supercapacitors. *RSC Adv.* 2014;4(97):54662–7.
52. Zheng S, Zhang J, Deng H, Du Y, Shi X. Chitin derived nitrogen-doped porous carbons with ultrahigh specific surface area and tailored hierarchical porosity for high performance supercapacitors. *Journal of Bioresources and Bioproducts.* 2021 May 1;6(2):142–51.

53. Yan B, Zheng J, Feng L, Du C, Jian S, Yang W, et al. Wood-derived biochar as thick electrodes for high-rate performance supercapacitors. *Biochar*. 2022 Dec 1;4(1).
54. Elaiyappillai E, Srinivasan R, Johnbosco Y, Devakumar P, Murugesan K, Kesavan K, et al. Low cost activated carbon derived from Cucumis melo fruit peel for electrochemical supercapacitor application. *Appl Surf Sci*. 2019 Aug 30;486:527–38.
55. Ma F, Ding S, Ren H, Liu Y. Sakura-based activated carbon preparation and its performance in supercapacitor applications. *RSC Adv*. 2019;9(5):2474–83.
56. Nguyen TN, Le PA, Phung VBT. Facile green synthesis of carbon quantum dots and biomass-derived activated carbon from banana peels: synthesis and investigation. *Biomass Convers Biorefin*. 2022 Jul 1;12(7):2407–16.
57. Feng L, Yan B, Zheng J, Chen J, Wei R, Jiang S, et al. Soybean protein-derived N, O co-doped porous carbon sheets for supercapacitor applications. *New Journal of Chemistry*. 2022;46(22):10844–53.
58. Nzereogu PU, Omah AD, Ezema FI, Iwuoha EI, Nwanya AC. Anode materials for lithium-ion batteries: A review. *Applied Surface Science Advances*. 2022 Jun 1;9:100233.
59. Kim T, Choi W, Shin HC, Choi JY, Kim JM, Park MS, Yoon WS. Applications of voltammetry in lithium ion battery research. *Journal of Electrochemical Science and Technology*. 2020;11(1):14-25.
60. Chen L, Zhang Y, Lin C, Yang W, Meng Y, Guo Y, et al. Hierarchically porous nitrogen-rich carbon derived from wheat straw as an ultra-high-rate anode for lithium ion batteries. *J Mater Chem A Mater*. 2014 Jul 7;2(25):9684–90.
61. Edström K, Herstedt M, Abraham DP. A new look at the solid electrolyte interphase on graphite anodes in Li-ion batteries. *Journal of Power Sources*. 2006 Feb 28;153(2):380-4.
62. Hernández-Rentero C, Marangon V, Olivares-Marín M, Gómez-Serrano V, Caballero Á, Morales J, et al. Alternative lithium-ion battery using biomass-derived carbons as environmentally sustainable anode. *J Colloid Interface Sci*. 2020 Aug 1;573:396–408.
63. Vu DL, Seo JS, Lee HY, Lee JW. Activated carbon with hierarchical micro-mesoporous structure obtained from rice husk and its application for lithium-sulfur batteries. *RSC Adv*. 2017;7(7):4144–51.
64. Lee SY, Choi Y, Kim JK, Lee SJ, Bae JS, Jeong ED. Biomass-garlic-peel-derived porous carbon framework as a sulfur host for lithium-sulfur batteries. *Journal of Industrial and Engineering Chemistry*. 2021 Feb 25;94:272–81.
65. Mai TT, Vu DL, Huynh DC, Wu NL, Le AT. Cost-effective porous carbon materials synthesized by carbonizing rice husk and K₂CO₃ activation and their application for lithium-sulfur batteries. *Journal of Science: Advanced Materials and Devices*. 2019 Jun 1;4(2):223–9.
66. Yu K, Li J, Qi H, Liang C. High-capacity activated carbon anode material for lithium-ion batteries prepared from rice husk by a facile method. *Diamond and Related Materials*. 2018 Jun 1;86:139-45.
67. Baskar AV, Singh G, Ruban AM, Davidraj JM, Bahadur R, Sooriyakumar P, Kumar P, Karakoti A, Yi J, Vinu A. Recent progress in synthesis and application of biomass-

- based hybrid electrodes for rechargeable batteries. *Advanced Functional Materials*. 2023 Jan;33(3):2208349.
68. Steinhauer M, Diemant T, Heim C, Jürgen Behm R, Wagner N, Andreas Friedrich K. Insights into solid electrolyte interphase formation on alternative anode materials in lithium-ion batteries. *J Appl Electrochem*. 2017 Feb 1;47(2):249–59.
 69. Xie L, Tang C, Bi Z, Song M, Fan Y, Yan C, Li X, Su F, Zhang Q, Chen C. Hard carbon anodes for next-generation Li-ion batteries: review and perspective. *Advanced Energy Materials*. 2021 Oct;11(38):2101650.
 70. Li Z, Li S, Wang T, Yang K, Zhou Y, Tian Z. Facile Fabrication of High-Performance Li-Ion Battery Carbonaceous Anode from Li-Ion Battery Waste. *J Electrochem Soc*. 2021 Sep 1;168(9):090513.
 71. Xie F, Zhao S, Bo X, Li G, Fei J, Ahmed EAMA, et al. A robust solvothermal-driven solid-to-solid transition route from micron SnC₂O₄ to tartaric acid-capped nano-SnO₂ anchored on graphene for superior lithium and sodium storage. *J Mater Chem A Mater*. 2022 Nov 21;11(1):53–67.
 72. Pięłowska M, Kurc B, Rymaniak Ł. Modeling of Diffusion of Metal Ions in Carbon Electrodes for Lithium-Ion Cells. *Waste Biomass Valorization*. 2023 Jul 1;14(7):2401–17.
 73. Strange LE, Li X, Wornyo E, Ashaduzzaman M, Pan S. Scanning Electrochemical Microscopy for Chemical Imaging and Understanding Redox Activities of Battery Materials. Vol. 1, *Chemical and Biomedical Imaging*. American Chemical Society; 2023. p. 110–20.
 74. Chen J, Lee PS. Electrochemical Supercapacitors: From Mechanism Understanding to Multifunctional Applications. *Adv Energy Mater*. 2021 Feb 1;11(6).
 75. Peled E, Menkin S. Review—SEI: Past, Present and Future. *J Electrochem Soc*. 2017;164(7):A1703–19.
 76. Strange LE, Li X, Wornyo E, Ashaduzzaman M, Pan S. Scanning electrochemical microscopy for chemical imaging and understanding redox activities of battery materials. *Chemical & Biomedical Imaging*. 2023 Mar 23;1(2):110-20.
 77. Barruna AE, Naufal RM, Nugraha MR, Subiyanto I, Tinaprilla N, Subhan A, Chairul H. Material characteristics and electrochemical performance of lithium-ion capacitor with activated carbon cathode derived from sugarcane bagasse. In *IOP Conference Series: Earth and Environmental Science* 2021 Feb 1 (Vol. 673, No. 1, p. 012018). IOP Publishing.

Chapter **6**

HIGH-PERFORMANCE NON-ENZYMATIC UREA SENSOR WITH AC/NiO COMPOSITE MATERIAL

Some of the contents of this chapter have been published in

- I. P. Merin, M. N. Muralidharan, A. Seema, **High-Performance Nonenzymatic Urea Sensors with Cost-Effective Electrode Material.** (Manuscript Submitted)

6.1 Introduction

Accurate detection of urea is essential for ensuring quality and safety in critical areas such as medical diagnostics, environmental monitoring, and agricultural applications.(1,2) Conventional measurement techniques have several drawbacks, such as high cost, complex instrumentation, and time-consuming sample pretreatments.(3) Additionally, they are not suitable for on-site monitoring of urea levels. In this context, electrochemical sensors have received considerable attention for the quantitative measurement of urea, as they effectively address the limitations of conventional methods. Moreover, these sensors provide unique advantages such as higher sensitivity, affordability, quicker response times, and simplicity.(4)

Electrochemical sensors usually employ enzymatic or non-enzymatic approaches for urea detection. However, owing to their stability and resistance to environmental factors like temperature and pH, non-enzymatic electrochemical sensors have gained more interest than enzymatic sensors. Despite this, the wide application of non-enzymatic urea sensors is limited by several challenges that can affect their performance. One major limitation is the selectivity of these sensors in distinguishing between urea and interfering substances, which is crucial for ensuring their efficiency. Additionally, the factors such as sensitivity, reproducibility, and repeatability are relevant for the practical feasibility of these sensors.(5) Furthermore, the real-world applicability of these sensors poses a significant challenge, as most research has been conducted in laboratory settings. These challenges can be addressed by implementing surface modifications in the electrode materials to enhance selectivity, sensitivity, and durability.(6)

NiO is a widely used electrode material for sensing applications owing to its chemical stability, good conductivity, and high surface area. The redox activity of $\text{Ni}^{2+}/\text{Ni}^{3+}$ facilitates urea oxidation and is employed for urea sensors. The availability of NiO also enhances electron transfer at the interface during urea detection. However, the intrinsic catalytic efficiency of NiO may limit the detection of low urea concentrations in real-world samples.(7,8) Materials such as activated carbon (AC), which possess well-defined porous structures and high surface areas, can enhance the active sites for sensing applications involving NiO.(9) Furthermore, the porous

structure improves both the adsorption of urea molecules on the surface and the stability of the sensor. Additionally, AC offers an efficient pathway for electron transport during the analysis and enhances the mass transport of urea and hydroxide ions.(10) Overall, AC/NiO composite-based electrodes for urea sensing offer significant advantages. The high surface area of AC enhances the effective adsorption of urea, while the presence of NiO increases the number of active sites for interaction. These characteristics of AC/NiO composites make them suitable candidates for urea sensors, offering high sensitivity, low detection limits, and enhanced stability.(11)

In this study, the coprecipitation method is adopted for the preparation of AC/NiO composites. This technique ensures a uniform distribution of NiO nanoparticles on the AC surface, enhances surface characteristics such as area and the number of active sites, thereby improving the reactivity and overall performance of the electrode material. Moreover, the process is scalable, cost-effective, and simple, making it suitable for large-scale applications.(12,13) The prepared composite materials were then subjected to various material and structural characterisations. The urea sensing capability of the AC/NiO composite was assessed using different electrochemical analysis techniques with 0.1 M KOH as supporting electrolyte. The lower detection limits, improved limit of quantification, and a wider linear detection range of the prepared material demonstrate a strong response to urea sensing. Additionally, this work highlights the feasibility of the electrode material for real-life applications by providing insights into selectivity, repeatability, and reproducibility.

6.2 Experimental details

6.2.1 Synthesis of AC/NiO composites

The AC/NiO composite is prepared through the co-precipitation method and is schematically represented in Figure 6.1. The AC derived from nutmeg shell waste was used in this study.(14–16) Initially, AC and $\text{Ni}(\text{NO}_3)_2$ solution were mixed in a beaker to form a homogeneous dispersion, followed by NaOH in $\text{Ni}(\text{NO}_3)_2$: NaOH=1:2 weight ratio. The mixture is then washed and dried in an air oven at 120 °C. These samples were subjected to calcination in a tubular furnace at temperatures of 300 °C, 400 °C, and 500 °C for one hour, with a continuous supply of Ar (99.99%). The as-prepared AC/NiO composites were then ground into fine powder and used for further

studies. Various AC/NiO composites were prepared having AC: NiO ratios of 70:30, 80:20, and 90:10. The prepared electrode material were named ACNiO_7:3_400, ACNiO_8:2_400, ACNiO_9:1_400, ACNiO_8:2_300, and ACNiO_8:2_500 where (7:3, 8:2, 9:1) represents the ratios of AC to NiO and (300, 400, and 500 °C) indicate the temperature at which calcination was carried out.

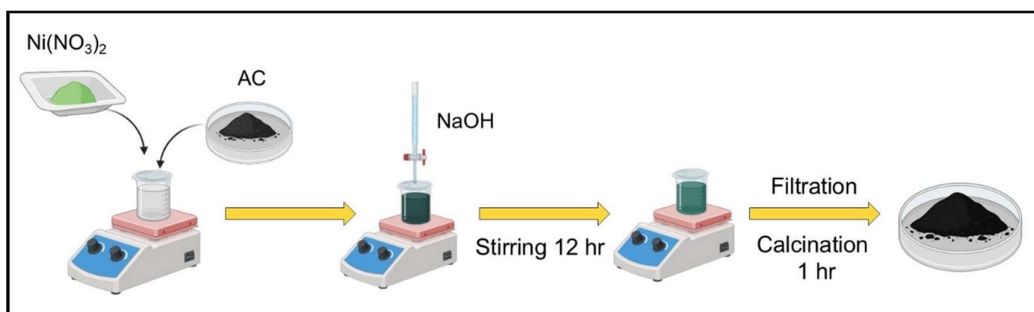


Figure 6.1 Schematic representation of the preparation of the AC/NiO composite

6.2.2 Analysis of the electrochemical performance of AC/NiO for sensing applications

A modified glassy carbon electrode (MGCE) was utilised to evaluate the electrochemical performance of as-prepared AC/NiO composites. A homogenous slurry was prepared with AC/NiO composite and PVDF in a 90:10 weight ratio. NMP was used as a solvent with a loading of 20%. This active material was then coated onto the glassy carbon electrode using a micropipette and dried with an infrared lamp. The mass loading of active material on MGCE is kept between 5 and 10 mg cm⁻² to ensure optimal efficiency and performance. A three-electrode configuration comprising the MGCE, an Ag/AgCl, and a platinum rod as the working electrode, reference electrode, and counter electrode, respectively, was used for this study. Different electrochemical analyses were performed using 0.1 M KOH as the supporting electrolyte for a potential window of 0-0.8 V for various scan rates. The calibration curve was derived from the variation in peak current with different concentrations of urea added to the supporting electrolyte.

6.3. Results and Discussions

The structural properties of AC/NiO composite materials have a significant impact on the performance of urea sensors. In this study, various physicochemical characterisation techniques were employed, including XRD, Raman spectroscopy, TEM, SEM, XPS and TGA. The effectiveness of these materials for urea sensing applications was further evaluated using different electrochemical methods. Additionally, the potential of the prepared composite materials was discussed, emphasising their feasibility for use in real-world samples.

6.3.1 Material characterisations

6.3.1.1 TGA analysis

TGA analysis was performed under nitrogen flow to study the NiO content of the AC/NiO composite. The TGA curve obtained for ACNiO_8:2_400 is represented in Figure 6.2.

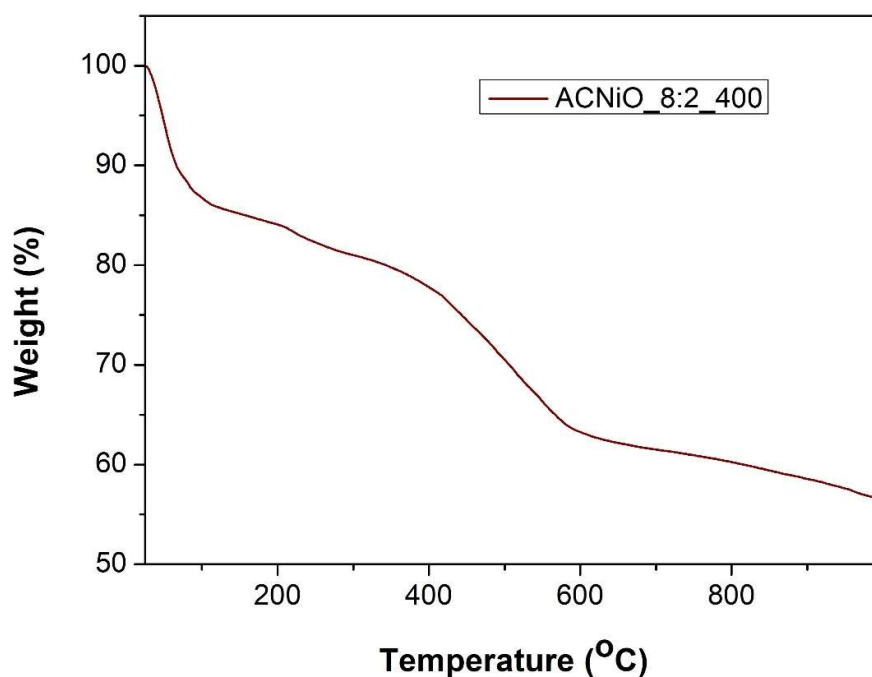


Figure 6.2 TGA curve of AC/NiO

The initial weight loss observed at the lower temperature (up to ~200 °C) can be ascribed to the desorption of moisture and other volatile compounds. The mass loss

in the temperature range from 200 °C to 400 °C indicates the decomposition of functional groups on the surface of AC.(17) As the temperature increases above 500 °C, a significant mass loss occurs, which is associated with a reduction reaction that produces nickel metal and releases gases such as CO and CO₂.(18) Stable NiO is formed at 400°C, minimising carbon decomposition, which confirms that this is the optimal calcination temperature for preparing the AC/NiO composite. The residue value, approximately 30%, mainly represents the remaining NiO content. The curve also illustrates the predicted compositions of AC and NiO. (13,19)

6.3.1.2 XRD analysis

Figure 6.3 shows that all composite materials show similar XRDs with characteristic peaks corresponding to AC and NiO. The AC material exhibits a wide peak around $2\theta=26^\circ$ representing (002) diffraction planes (ICDD No. 01-075-1621), which is also present in all the composite materials. The presence of this peak suggests the availability of disordered carbon in the structure and highlights the porous nature of these materials.(11,20)

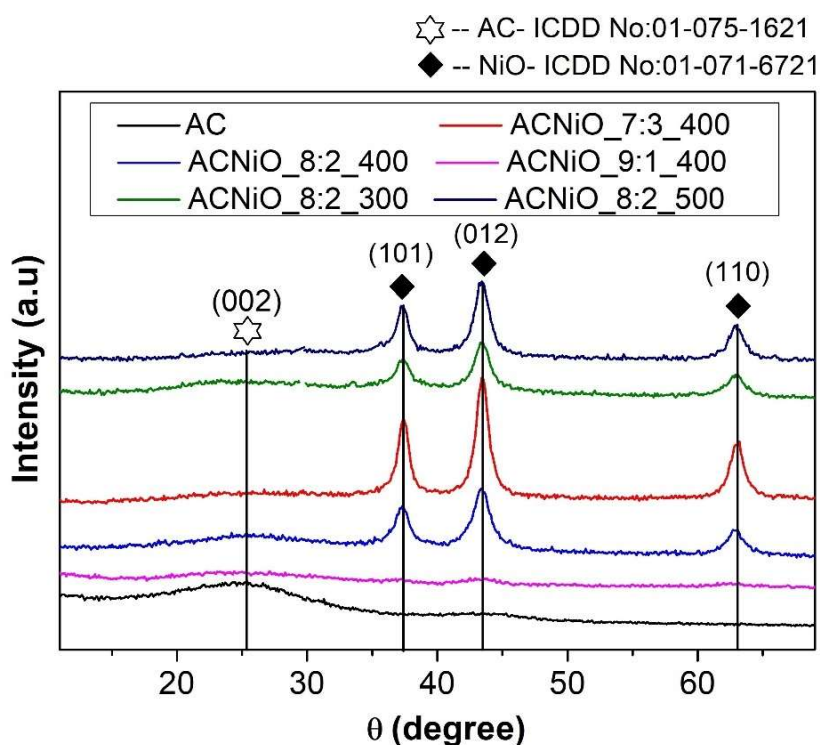


Figure 6.3 XRDs of AC/NiO composite materials

These materials also show intense peaks around $2\theta=37.2^\circ$, 43.3° , and 62.9° corresponding to (101), (012), and (110) diffraction planes, respectively. These characteristic peaks indicate the presence of NiO in the composites and are matched with the ICDD card No. 01-071-6721. The intensities of these peaks increase with higher NiO composition and calcination temperature.(6,10) These observations from XRDs are consistent with previous studies.

6.3.1.3 Raman Spectroscopy

The Raman spectra of prepared AC/NiO composite materials are shown in Figure 6.4. All the curves exhibit two broad characteristic peaks at 1346, 1600, and 2895 cm^{-1} , representing D, G, and 2D bands of the AC structure, respectively.(7) The band around 498 cm^{-1} indicates the presence of NiO in the material. This peak is particularly prominent in the ACNiO_7:3_400 sample, as it contains a higher ratio of NiO than the other samples.(21)

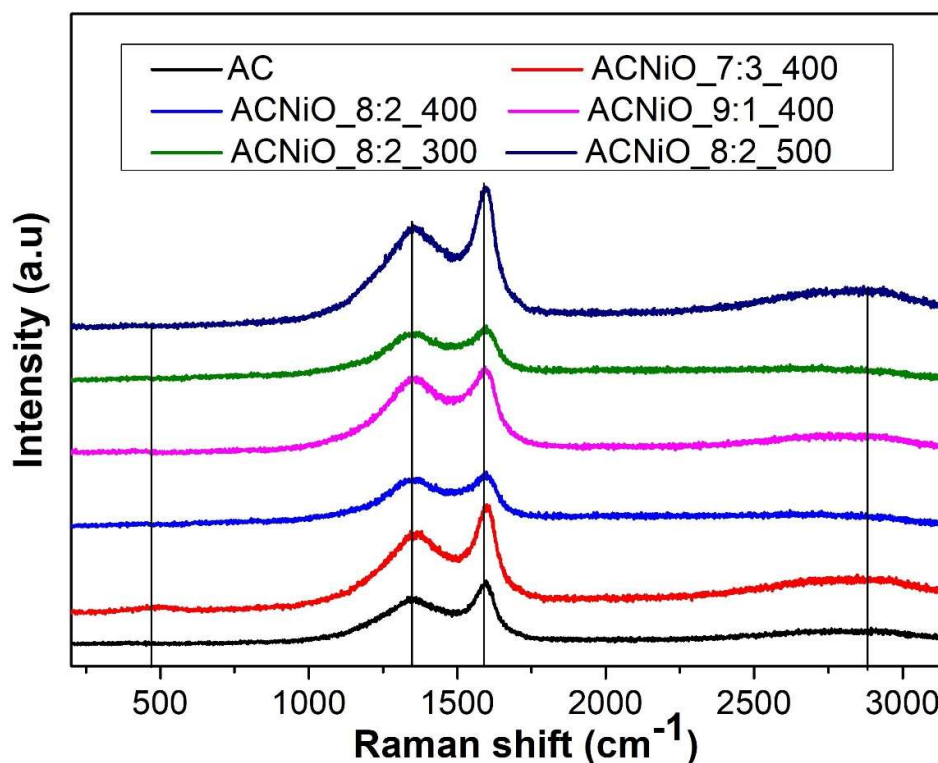


Figure 6.4 Raman spectra of AC/NiO composite materials

6.3.1.4 SEM analysis

SEM micrographs of AC/NiO composites are displayed in Figure 6.5. These images reveal the hierarchical porous structure present in them. The NiO particles were grown as clusters of heterogeneous particle sizes on the walls of these pores in the materials.(12) These clusters provide a larger active surface area, which enhances urea adsorption and increases the number of oxidation sites. Additionally, these porous NiO clusters improve the sensitivity and reaction kinetics of the electrodes by facilitating reactant diffusion and reducing charge transfer resistance.

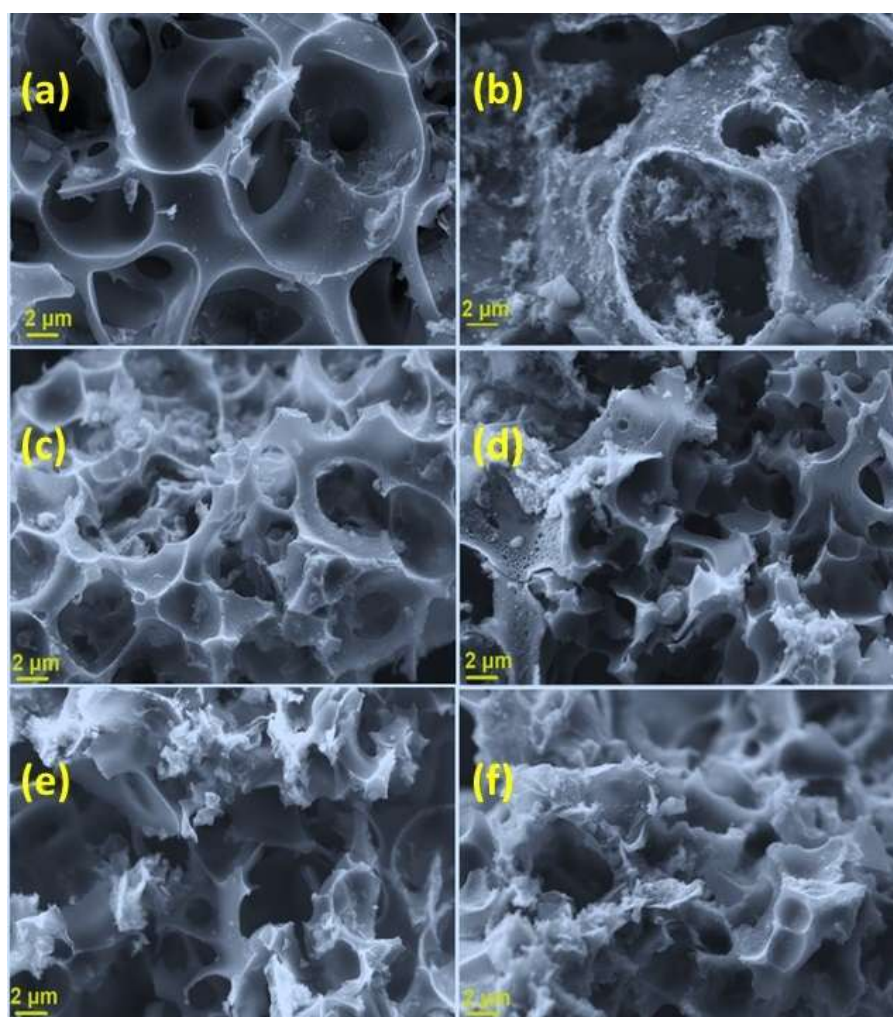


Figure 6.5 SEM images of (a) AC, (b) ACNiO_9:1_400, (c) ACNiO_8:2_400, (d) ACNiO_7:3_400, (e) ACNiO_8:2_300, and (f) ACNiO_8:2_500 at 15,000 X magnification.

The remarkable effect of calcination temperature and AC to NiO composition in determining the morphology of the composites is visible from the SEM images. This porous structure is beneficial in facilitating easy electrolyte access during the redox reaction, which in turn improves the sensitivity of the electrode material for electrochemical sensing applications.(8)

Table 6.1 Elemental analysis of AC/NiO composites

Sample Name	Elemental analysis [Wt%]		
	C	O	Ni
ACNiO_7:3_400	49.6	24.0	26.4
ACNiO_8:2_400	38.6	22.9	38.5
ACNiO_9:1_400	80.9	13.7	5.4
ACNiO_8:2_300	71.9	19.3	8.8
ACNiO_8:2_500	53.6	24.1	22.3
AC	91.7	8.3	-

The EDAX values in Table 6.1 further confirm the presence of NiO in the materials, and these values align with those reported in the literature. Among these composite materials, ACNiO_8:2_400 has optimum C content and a higher Ni mass fraction. The elemental analysis indicates that the Ni mass fraction increases initially and then decreases with rising calcination temperature. Furthermore, from these results, the optimum calcination temperature for preparing the AC/NiO composite is identified as 400 °C. The SEM analysis and EDAX results indicate that AC/NiO is suitable for sensing applications due to its highly active NiO content and well-developed porous structure.

6.3.1.5 Surface area analysis

Figure 6.6 illustrates the nitrogen adsorption-desorption isotherms of the prepared composite materials. The isotherm of AC reflects the typical type I isotherm, indicating the availability of a well-defined porous structure with a majority of micropores.(12) Whereas, the isotherms corresponding to the composite material exhibit a combination of type I and type IV isotherms, confirming the existence of

mesopores and micropores.

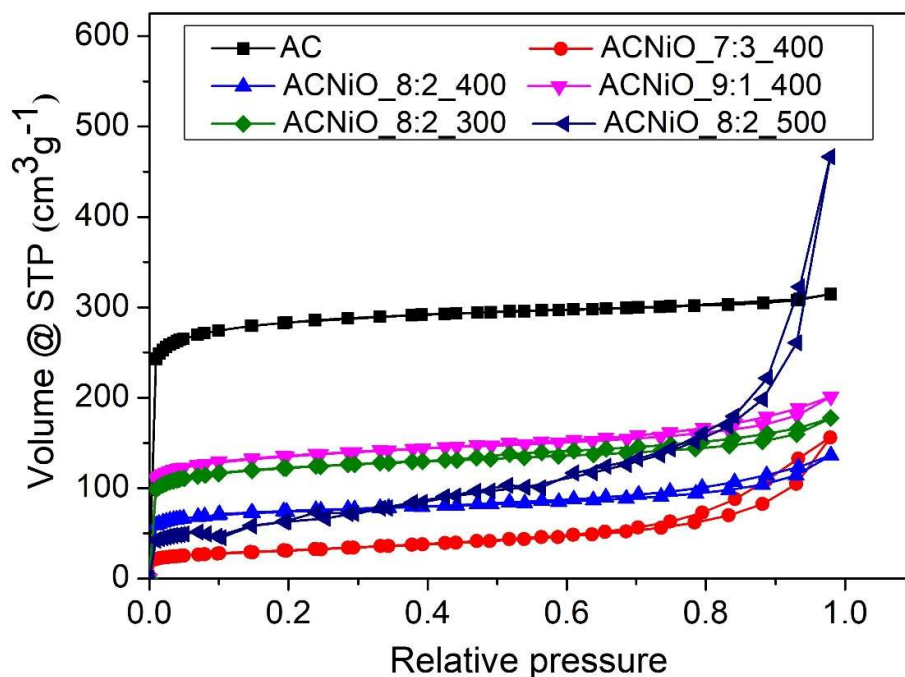


Figure 6.6 N₂ adsorption-desorption isotherms of AC/NiO composite materials

Table 6.2 Pore structure parameters of AC/NiO composites

Sample Name	Surface area [m ² g ⁻¹]			Pore volume [cm ³ g ⁻¹]			Diameter [nm]
	Micro pores	Meso pores	Total	Micro pores	Meso pores	Total	
ACNiO_7:3_400	27	68	109	0.117	0.218	0.241	8.81
ACNiO_8:2_400	218	47	280	0.112	0.108	0.210	3.00
ACNiO_9:1_400	422	47	513	0.204	0.112	0.311	2.42
ACNiO_8:2_300	386	49	465	0.155	0.098	0.274	2.35
ACNiO_8:2_500	226	18	226	0.092	0.695	0.721	1.27
AC	1026	26	1111	0.403	0.048	0.187	1.75

The reduction in surface area and pore volume with the incorporation of NiO

in the AC is visible in the figure, which can be ascribed to the blocking effect of NiO particles on active sites in the AC.(22,23) The values of various structural parameters of the materials are consolidated in Table 6.2. These readings are in agreement with observations of isotherms. The surface area of the composite materials increases with an increase in NiO, while it decreases as the calcination temperature rises. These observations are consistent with previous reports and suggest the surface area of prepared materials is significant for sensing applications. In ACNiO_8:2_400, the contributions from micropores and mesopores to the total pore volume are equal, which indicates the presence of more active sites and accessible area suitable for sensing applications.

6.3.1.6 XPS analysis

Detailed elemental information and the oxidation state of the composite material ACNiO_8:2_400 were obtained through XPS analysis. The XPS survey spectrum is displayed in Figure 6.7 (a), identifying the elements such as nickel, oxygen, and carbon present in the sample.

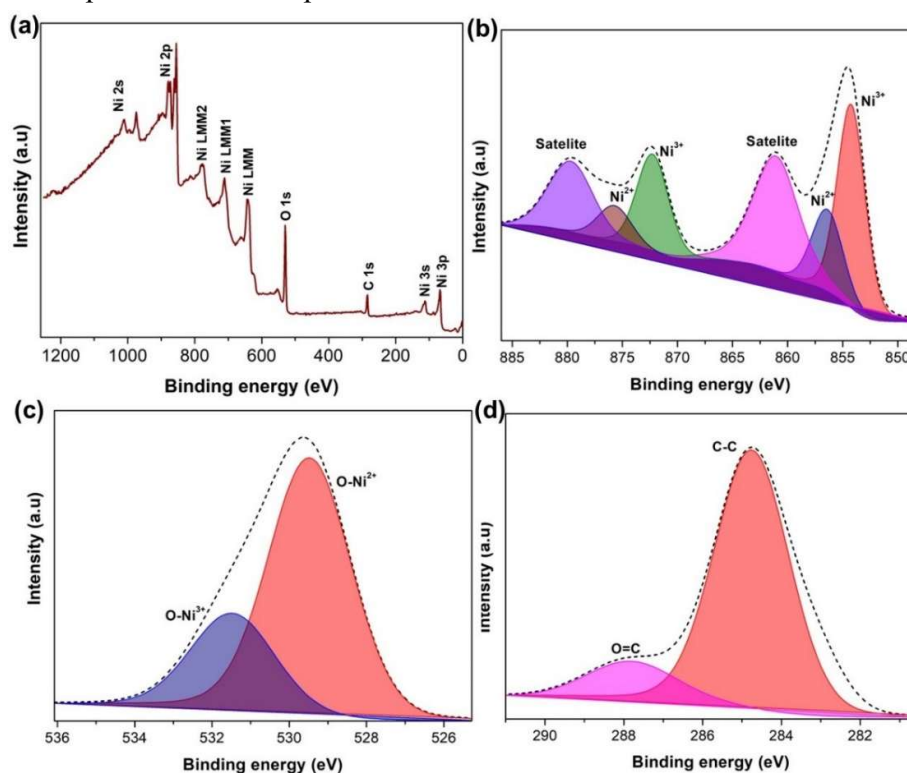


Figure 6.7 XPS spectra of ACNiO_8:2_400: (a) Survey spectrum, (b) Ni 2p, (c) O 1s (d) C 1s.

Figure 6.7 (b)-(d) represents Ni 2p, O 1s, and C 1s spectra respectively. In the Ni 2p spectrum, two edge splits due to spin-orbital coupling are visible. The spectrum shows 2 $p_{3/2}$ main peaks and their satellites around 854 eV and 861 eV, respectively. Meanwhile, the peaks around 872 eV and 879 eV reflect the 2 $p_{1/2}$ main peak and its satellite. These characteristic peaks confirm the presence of NiO in the sample.(24)

Furthermore, the C 1s spectrum displays two characteristic peaks that reveal the C-C bond associated with sp^2 hybridized carbon around 284.7 eV and the other corresponding to the C=O bond in carboxyl or ketone groups around 288.9 eV. The spectrum suggests the presence of a carbon network which enhances the accessible surface area of the electrode material, promoting effective adsorption of analytes. Additionally, the O 1s spectrum confirms the presence of various oxygen-containing bonds, with two peaks at approximately 529.5 eV and 531.3 eV. These peaks are ascribed to O-Ni²⁺ bonds, corresponding to pure stoichiometric NiO, and O-Ni³⁺ bonds, which relate to defects in NiO.(25)

6.3.1.7 TEM analysis

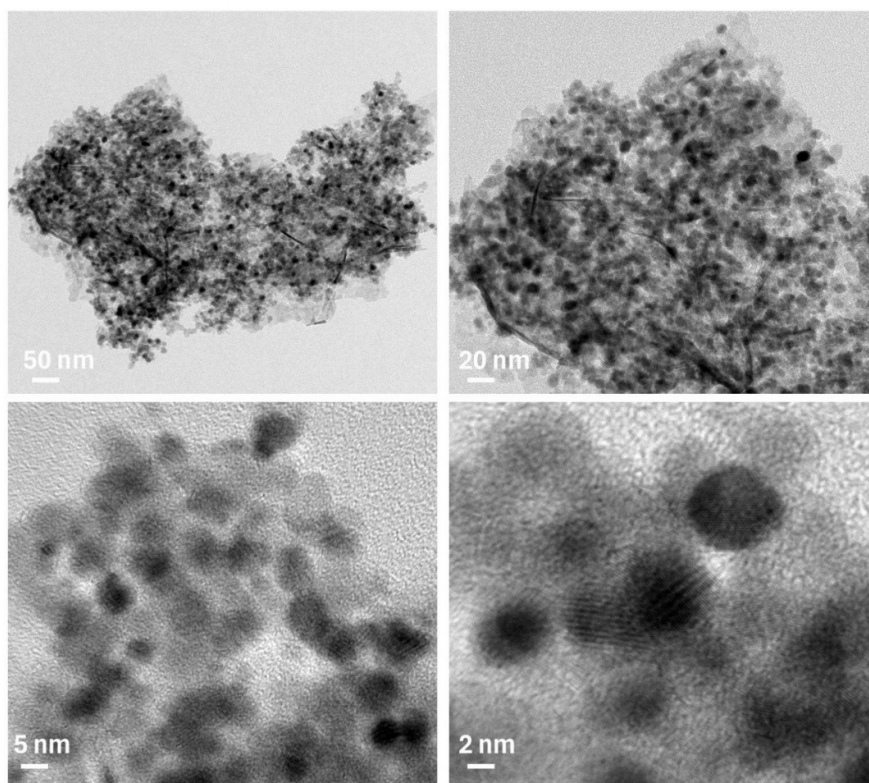


Figure 6.8 TEM images of the AC/NiO composites at various magnifications

The surface morphology of ACNiO_8:2_400 was further validated using high-resolution TEM analysis. Figure 6.8 presents TEM images of the electrode material at various resolutions. Well-dispersed NiO nanoparticles are evident in the TEM micrographs. The material also shows mild agglomeration throughout its structure. This agglomeration may have resulted from several factors, including heat generated during the combustion process and the subsequent formation of gas, low density, weak interparticle forces, and magnetic interactions among the particles.(26) The porous structure of the carbon is also clearly visible in the TEM images. The availability of mesopores and micropores is advantageous for fast ion transport and facilitates the urea adsorption, which is favourable for electrochemical sensor applications.(27) The observations in TEM structural analysis align well with the SEM images obtained for the composites.

6.3.2 Electrochemical investigation of urea with AC-NiO-based sensors

The electrochemical performance of the as-prepared AC/NiO composites was studied using CV analysis at a scan rate of 20 mV s^{-1} for a potential window of 0-0.8 V. The measurement was carried out with a glassy carbon working electrode modified with as-prepared composite materials with 0.05 mM urea in 0.1 M KOH (pH=13). The counter and reference electrodes were platinum and Ag/AgCl electrodes, respectively.

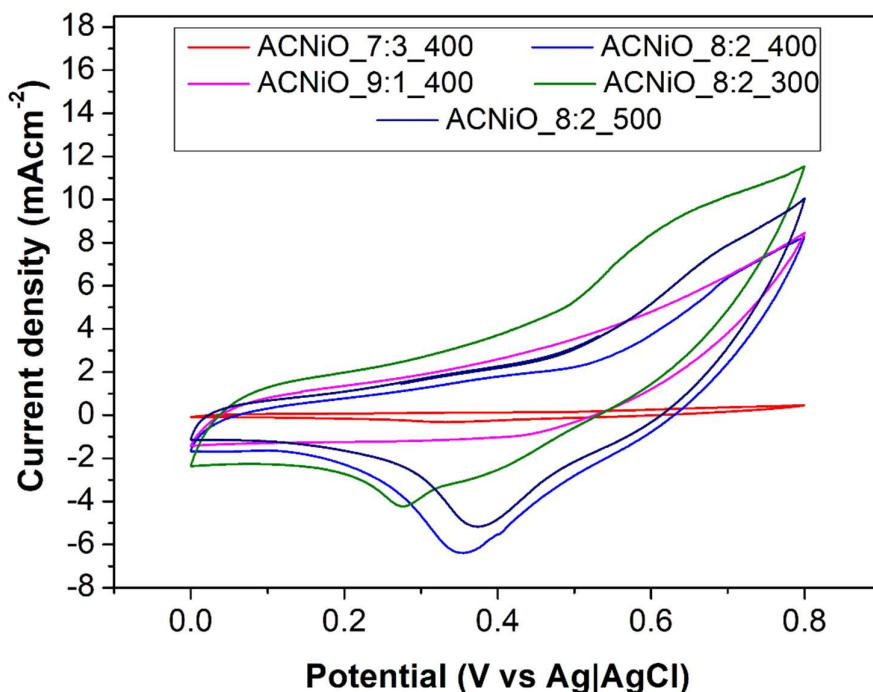
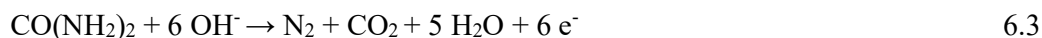
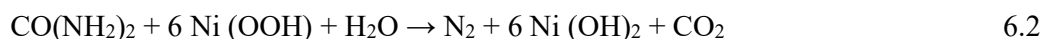


Figure 6.9 CV curves of AC/NiO composite materials at a scan rate of 20 mV s^{-1}

The OH^- ions in the supporting electrolyte (KOH) are essential reactants for the electrochemical generation of the active NiOOH phase from $\text{Ni}(\text{OH})_2$, and they are consumed during the overall reaction. Equations 6.1 to 6.3 outline the complete mechanism for urea sensing.(28) KOH provides the alkaline medium that oxidises Ni^{2+} to Ni^{3+} , as described in Equation 6.1. The highly reactive Ni^{3+} then oxidises urea and is reduced to Ni^{2+} during the reverse scan (Equation 6.2). Equation 6.3 describes the overall reaction.



The reduction peak observed in the CV curve (Figure 6.9) indicates the electrochemical activity of various composite electrode materials. Additionally, the cyclic voltammograms illustrate how the optimal ratio of AC to NiO influences the electrochemical performance of the composite materials. The value of peak current density increases and then decreases with increasing AC concentration and calcination temperature.(1) The CV curve indicates that the electrode material ACNiO_8:2_400 exhibits better electrochemical efficiency than other composite materials.

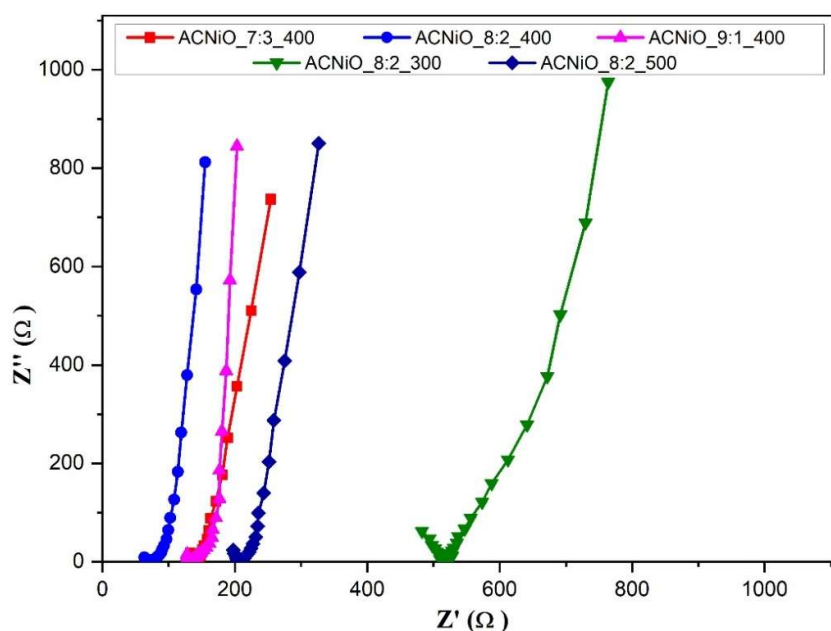


Figure 6.10 Nyquist plots of AC/NiO electrode materials

The electrochemical performance of the prepared materials was further evaluated using EIS. The charge transfer resistance (R_{ct}), determined by analyzing the data from the Nyquist plot (Figure 6.10) and fitting it to an equivalent circuit, indicates the resistance to electron flow at the electrode-electrolyte interface during a Faradaic (redox) reaction. The circuit elements are tabulated in Table 6.3. Lower R_{ct} values signify faster electron transfer during these reactions. Among the prepared electrode materials, the ACNiO-8:2_400 exhibited the lowest R_{ct} value, indicating that it is the best-performing material. This finding aligns with the results obtained from the CV analysis. Consequently, ACNiO_8:2_400-based electrode is utilized in further studies to assess its viability as an electrode material for urea sensors.(39)

Table 6.3 Fitted values of R_s , R_{ct} , C_{dl} , and Z_w derived from the EIS curves

Sample Name	R_s [Ω]	R_{ct} [$\times 10^{-6} \Omega$]	C_{dl} [$\times 10^{-3} F$]	W [$\Omega \cdot S^{-1/2}$]
ACNiO_7:3_400	142.4	80.5	5.344	1163
ACNiO_8:2_400	73.27	52.4	21.96	375.4
ACNiO_9:1_400	137.2	67.69	151.8	514.4
ACNiO_8:2_300	523	75.59	4.914	741.2
ACNiO_8:2_500	212.2	138.3	3.345	2210

The performance of urea sensors is significantly influenced by pH levels. The CV curves obtained at various pH values (pH = 10, 11, 12, and 13) of the supporting electrolyte are shown in Figure 6.11. These CV curves reveal that the generation of the active NiOOH species is highly dependent on pH. A strongly alkaline environment (pH = 13) is crucial for the efficient operation of the urea sensor, as it provides the necessary OH^- as reactants, facilitating the formation of active NiOOH.(36)

Figure 6.12 illustrates the dependence of scan rate on the efficiency of the electrochemical process occurring at the electrode surface. The CV analysis was performed at various scan rates: 10, 20, 25, 50, 75, 100, 150, and 200 $mV s^{-1}$, with 0.05 mM urea in the supporting electrolyte. The CV curves illustrate that the reduction peak current increases with increasing scan rate. The variation in peak current and the square

root of the scan rate is depicted in Figure 6.13. The curve displays strong linearity, suggesting diffusion-controlled mass transport. The R^2 value is calculated as 0.9937.(2)

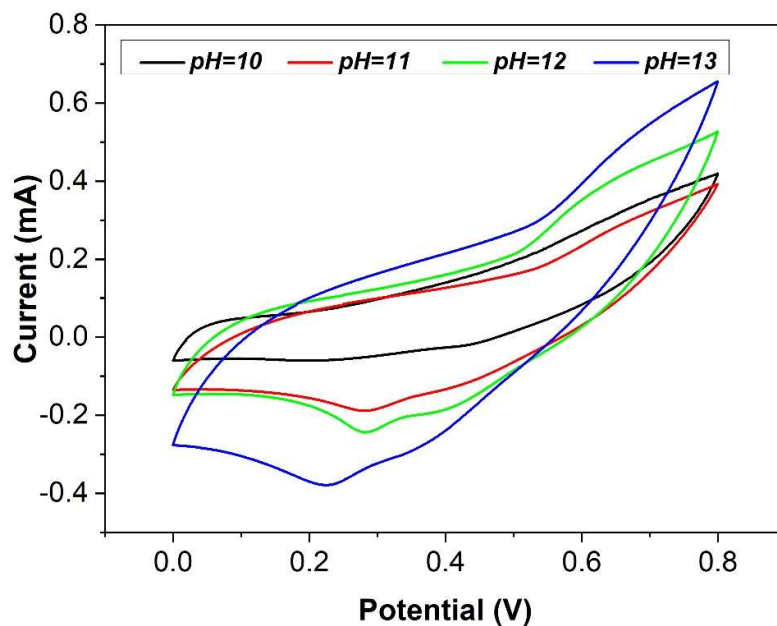


Figure 6.11 CV curves at various pH values of the supporting electrolyte

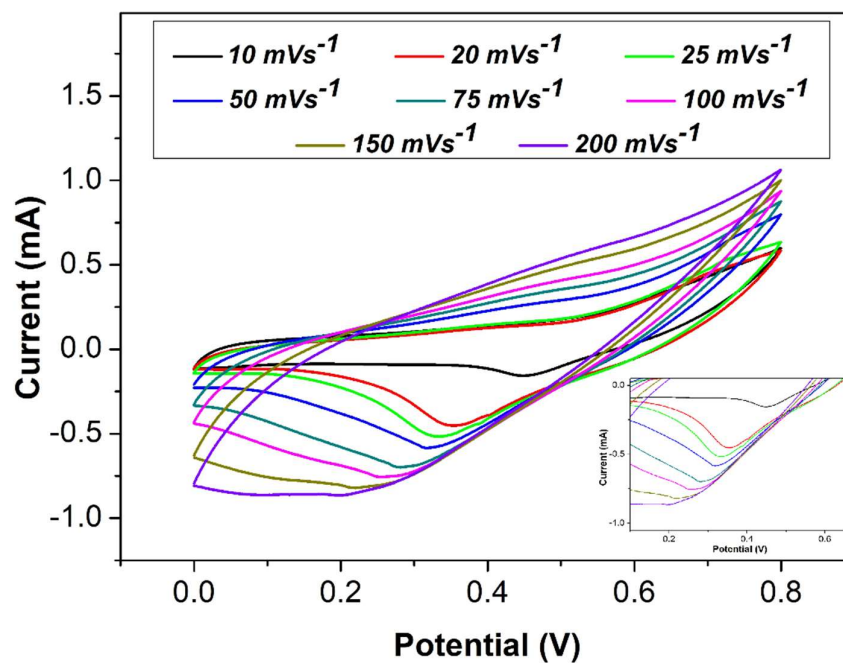


Figure 6.12 CV curves of ACNiO_{8:2_400} at different scan rates with enlarged anodic peak as an inset

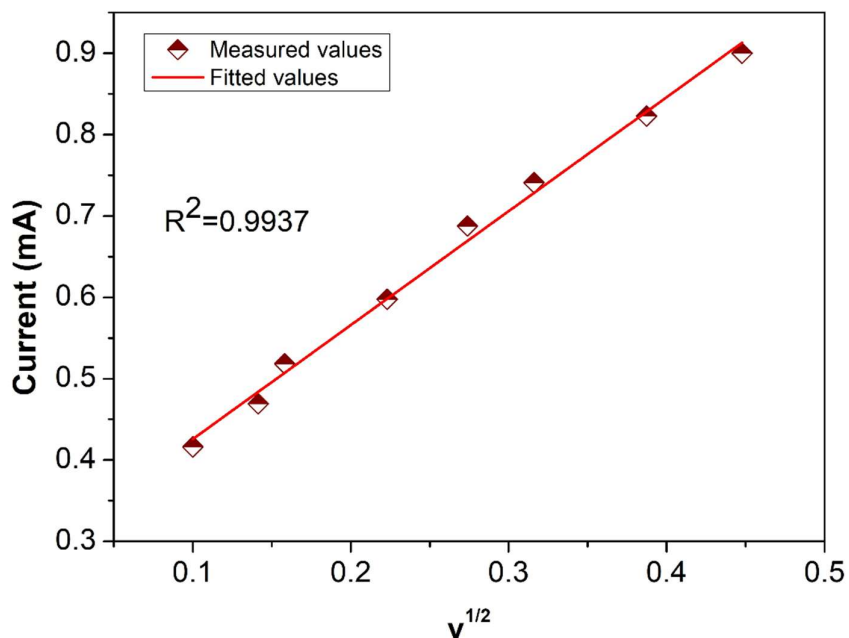


Figure 6.13 Variation of anodic peak current with scan rate.

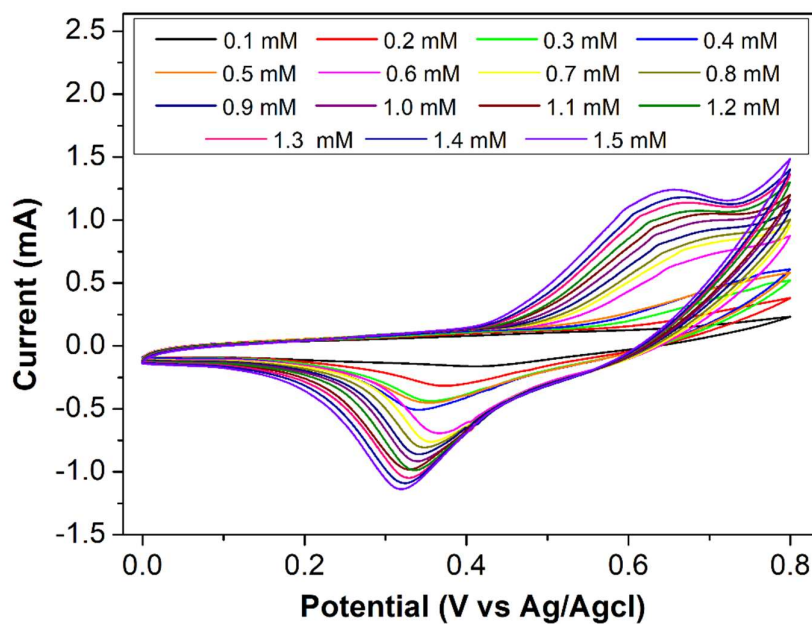


Figure 6.14 CV curve with varying urea concentrations

The CV curves were recorded at various concentrations of urea with a scan rate of 20 mV s^{-1} , as displayed in Figure 6.14. As the concentration of urea increased from 0.1 mM to 1.5 mM, the peak current exhibited a gradual increase. Figure 6.15

shows the dependence of peak current on the concentration of urea. This calibration curve indicates a linear relationship between the redox peak current and urea concentration, with an R^2 value of 0.9953. The separation between the oxidation and reduction peak potentials appears to be relatively constant (0.3 V), which is greater than the theoretical 59 mV for a perfectly reversible, one-electron transfer system. This suggests the system is quasi-reversible, indicating fast electron transfer kinetics.

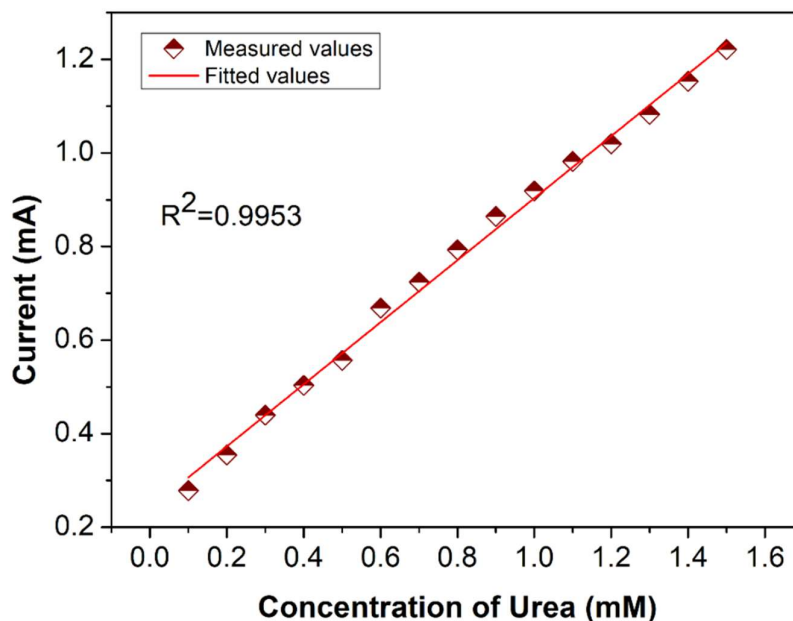


Figure 6.15 Calibration curve of anodic peak current against the concentration of urea

The effectiveness of the prepared electrode material for urea sensing applications was further validated at micromolar concentrations of urea. Differential pulse voltammetry (DPV) was carried out for various concentrations of urea ranging from 10 to 80 μM , as illustrated in Figure 6.16. As expected, the peak current increased linearly with the increase in urea concentration.⁽⁴²⁾ Additionally, Figure 6.17 shows the linear relationship between peak current and urea concentration within the measurement range.

The fitted curve can be used to predict the lower limit of detection (LOD), limit of quantification (LOQ), and sensitivity of the sensor. Equations 6.3, 6.4, and 6.5 are utilised for these calculations.

$$LOD = \frac{3 \times S}{m} \quad 6.3$$

$$LOQ = \frac{10 \times S}{m} \quad 6.4$$

$$Sensitivity = \frac{m}{A} \quad 6.5$$

where S is the standard deviation of the response, m is the slope of the calibration plot, and A is the surface area of the GCE.(29,30)

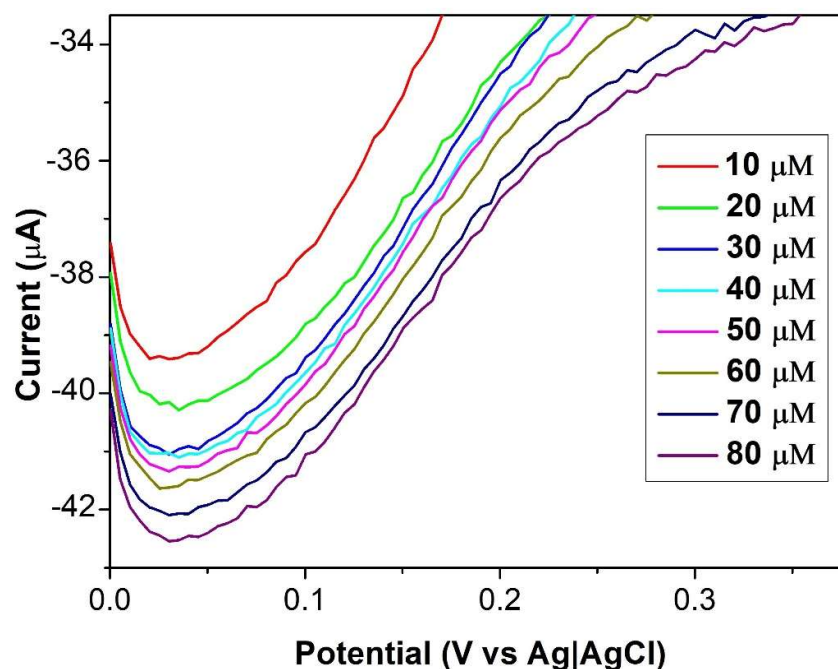


Figure 6.16 DPV curves for different concentrations of urea (10–80 μM)

The values of LOD, LOQ, and sensitivity are calculated as 2.9 μM , 9.6 μM , and 1620.1 $\mu\text{A mM}^{-1} \text{cm}^{-2}$, respectively. The performance of the prepared AC/NiO composites was compared with similar works previously reported in the literature. The details of these studies are summarised in Table 6.4, which suggests the significant potential of AC/NiO composite material for urea sensing applications.

Repeatability tests are essential for ensuring the long-term stability of electrodes used for urea sensing. The sensor's performance over time was validated by carrying out CV analysis for 25 cycles at the scan rate of 20 mV s^{-1} . The current

responses obtained are illustrated in Figure 6.18. The CV curves are nearly overlapping, with only a slight deviation observed throughout the analysis. Moreover, the reduction peak current remains nearly constant throughout the twenty-five cycles, confirming the stability of the fabricated sensor.(41)

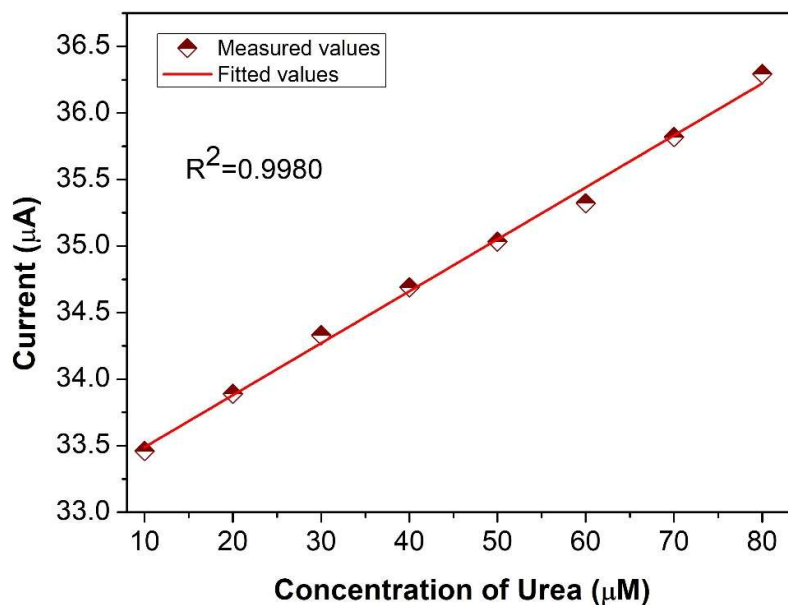


Figure 6.17 Variation in the reduction peak current against concentration

Table 6.4 Comparison of various electrodes used for urea sensing.

Electrode material	LOD (μM)	Linear range (mM)	Sensitivity (μA mM ⁻¹ cm ⁻²)	References
NiO-MWCNT	160	0.2-1.2	436.3	(31)
NiO-Carbon paste	26.7	0.2-5.8	392	(32)
NiO/GCE	22	0.1-5	13.9	(33)
Graphene-PANi/GCE	8.8	0.01-2	226.9	(34)
Ni@NiMn	18.7	1-9	-	(35)
CuO/MWCNT/GCE	160	2-8	-	(36)
Ni-MOF nanobelts	2.23	0.01-7	118.7	(37)
NiO	10	0.1-1.1	-	(38)
NiS/GO/MGCE	3.79	0.1-1.0	-	(39)
NiO nanoflakes	20	1-9	-	(40)
AC-NiO	2.9	0.1-1.5	1620.1	Present work

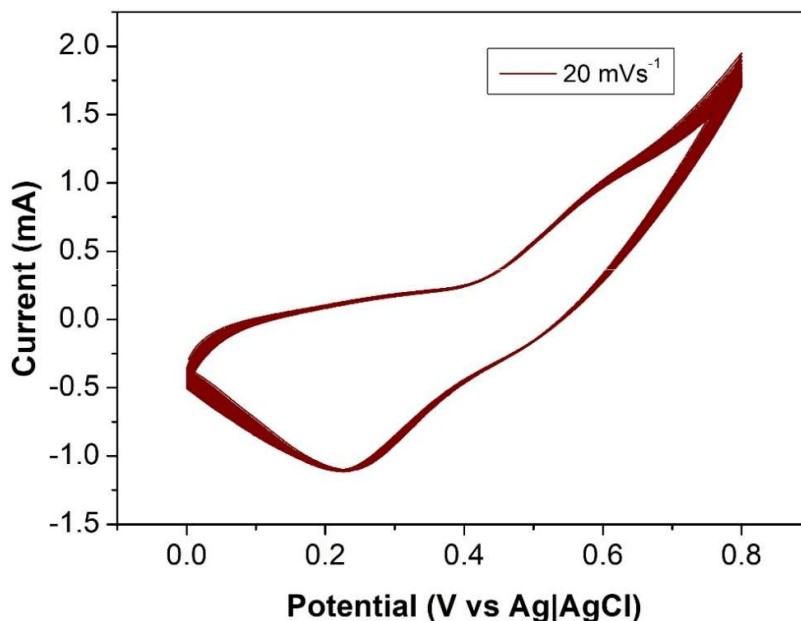


Figure 6.18 CV curves obtained with a 0.1 mM urea in the presence of 0.1 M KOH for 25 repetitive cycles at a scan rate of 20 mV s⁻¹

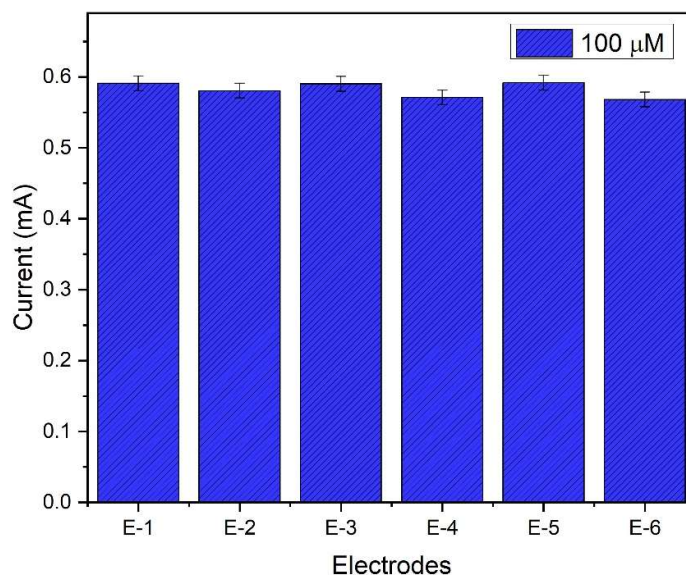


Figure 6.19 CV curves at various pH values of the supporting electrolyte

The reproducibility of the urea sensor across multiple fabricated electrodes is also crucial for its feasibility for various environmental monitoring and biological applications. The detection of an equal concentration of urea (100 μM urea in 0.1 M KOH) was conducted with six different electrodes that were prepared following the same optimized protocol. The variation in reduction peak current for each electrode is

represented in Figure 6.19. Upon analyzing the results, the variation in the current response of urea is very low, with a mean current of 0.58 ± 0.01 mA, corresponding to a relative standard deviation (RSD) of 1.5 % (n=6). This low RSD value demonstrates excellent inter-electrode reproducibility of the modified working electrode using the AC/NiO composite material for urea detection.(42)

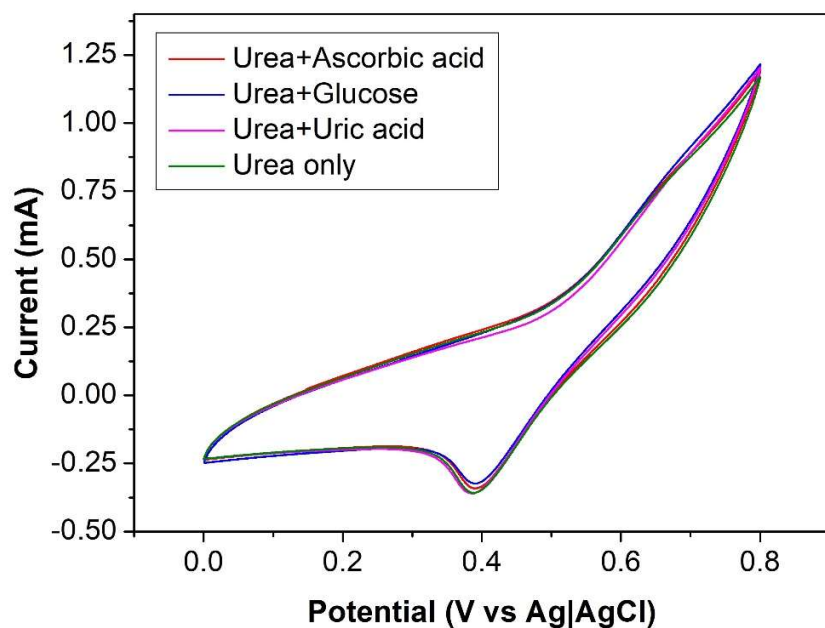


Figure 6.20 CV curves obtained for urea with different interfering species

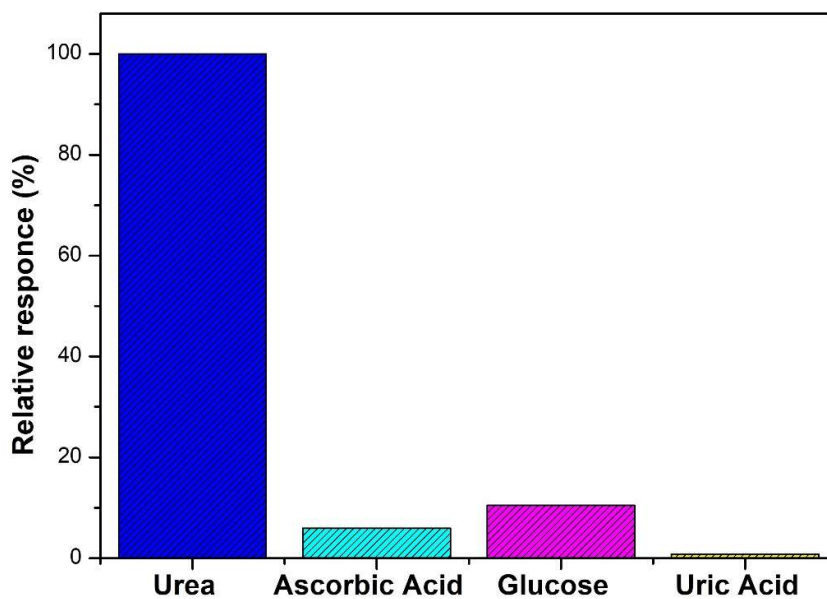


Figure 6.21 Relative response of interferents

The influence of interfering molecules is crucial for the performance of electrochemical sensors. To evaluate the selectivity of AC/NiO composite towards urea sensing applications, analysis at a scan rate of 20 mV s^{-1} with 0.1 mM of urea in the presence of various interfering molecules. In this work, the selectivity test was conducted using equimolar concentrations of potential interfering molecules such as uric acid, glucose and ascorbic acid. Figure 6.20 displays the CV curve obtained for different interfering molecules and the findings are shown in Table 6.5. No significant variation in the current profile was found across all cases. The relative response of all molecules is shown in Figure 6.21. The observations indicate negligible interference from other ions, demonstrating the high selectivity of the prepared electrode material for urea. These results confirm that the prepared electrode material is suitable for monitoring urea in real samples.(26)

Table 6.5 The influence of other interfering species on the detection of urea.

Interference	Concentration (mM)	Change in Current (%)
Ascorbic Acid	1	5.9
Glucose	1	10.5
Uric Acid	1	0.8

Table 6.6 Real sample analysis of urea

Concentration of Urea (μM)	Recovered Concentration (μM)	Percentage of recovery (%)
100	102.5 ± 2.0	102.50
200	203.9 ± 1.4	101.96
500	505.6 ± 3.7	101.12
1000	1008 ± 4.5	100.80

The suitability of these sensors for real sample applications was examined using tap water with varying concentrations of urea. The urea recovery data is summarised in Table 6.6. The percentage of urea recovery ranges from 100.8-102.5%. These significant recovery values indicate that the electrode material is suitable for real sample applications, with minimal interference from the various impurities present in

these samples.(42) This work can be further expanded to the biological samples, including blood, urine, serum, etc.

6.4. Conclusion

This study focused on the preparation of activated carbon (AC) and nickel oxide (NiO) composites using a cost-effective coprecipitation method. The efficiency of these materials for urea sensing applications was evaluated through cyclic voltammetry and differential pulse voltammetry analysis. This non-enzymatic sensor demonstrated a characteristic linear dependence on the scan rate. The performance of the prepared material for urea sensing was validated across various concentrations of urea. It exhibited a sensitivity of $1620 \mu\text{A mM}^{-1} \text{cm}^{-2}$, which is superior to previously reported values. The values of the limit of detection and limit of quantification were obtained as $1.69 \mu\text{M}$ and $9.6 \mu\text{M}$, respectively. These values further highlight the performance of the prepared electrode material for urea sensing applications. Additionally, the significant recovery percentage of urea in tap water samples indicates the practicality of using the prepared electrodes in real-world applications. This study can be further expanded for effective urea detection in biological samples. The electrode also demonstrated excellent selectivity against other interfering species, a wide linear range for urea detection, and good reproducibility, with a high recovery percentage for real samples ranging from 100.8% to 102.5%. Overall, the AC/NiO composite shows remarkable efficiency and sensitivity making it a promising, cost-effective material for urea sensing applications in various fields, including dairy industries, clinical diagnostics, and environmental monitoring.

References

1. Sunil Kumar Naik TS, Saravanan S, Sri Saravana KN, Pratiush U, Ramamurthy PC. A non-enzymatic urea sensor based on the nickel sulfide / graphene oxide modified glassy carbon electrode. *Mater Chem Phys*. 2020 Apr 15;245.
2. Kumar V, Kaur I, Arora S, Mehla R, Vellingiri K, Kim KH. Graphene nanoplatelet/graphitized nanodiamond-based nanocomposite for mediator-free electrochemical sensing of urea. *Food Chem*. 2020 Jan 15;303.

3. Sha R, Komori K, Badhulika S. Graphene–Polyaniline composite based ultra-sensitive electrochemical sensor for non-enzymatic detection of urea. *Electrochim Acta*. 2017 Apr 10;233:44–51.
4. Zhu J, Yin H, Gong J, Al-Furjan MSH, Nie Q. Easy one pot synthesis of NiO/Nitrogen doped carbon spheres for highly sensitive enzyme free amperometric glucose sensors. *Appl Surf Sci*. 2018 Jun 30;444:56–64.
5. Kim J, Sung GY, Park M. Efficient portable urea biosensor based on urease immobilized membrane for monitoring of physiological fluids. *Biomedicines*. 2020 Dec 1;8(12):1–11.
6. Xie A, Du J, Zhang J, Xiong Z, Shao F, Luo S. A High-Performance Nonenzymatic Urea Sensor Based on Graphene-NiO-Polyaniline. *J Electrochem Soc*. 2019;166(6):B456–63.
7. Sekar S, Kim DY, Lee S. Excellent oxygen evolution reaction of activated carbon-anchored nio nanotablets prepared by green routes. *Nanomaterials*. 2020 Jul 1;10(7):1–13.
8. Chennah A, Khan MA, Zbair M, Ait Ahsaine H. NiO/AC Active Electrode for the Electrosorption of Rhodamine B: Structural Characterizations and Kinetic Study. *Catalysts*. 2023 Jun 1;13(6).
9. Bhat VS, S. S, Hegde G. Review—Biomass Derived Carbon Materials for Electrochemical Sensors. *J Electrochem Soc*. 2020 Jan 2;167(3):037526.
10. Khaleed AA, Bello A, Dangbegnon JK, Momodu DY, Madito MJ, Ugbo FU, et al. Effect of activated carbon on the enhancement of CO sensing performance of NiO. *J Alloys Compd*. 2017;694:155–62.
11. Kumar V, Kaur I, Arora S, Mehla R, Vellingiri K, Kim KH. Graphene nanoplatelet/graphitized nanodiamond-based nanocomposite for mediator-free electrochemical sensing of urea. *Food Chem*. 2020 Jan 15;303.
12. Avinash B, Ravikumar CR, Kumar MRA, Santosh MS, Pratapkumar C, Nagaswarupa HP, et al. NiO bio-composite materials: Photocatalytic, electrochemical and supercapacitor applications. *Applied Surface Science Advances*. 2021 Mar 1;3.
13. Olán Ramos M, Del Angel Meraz E, Rojo JM, Pacheco-Catalán DE, Pantoja Castro MA, Mora Ortiz RS. Activated carbons from coconut shell and NiO-based composites for energy storage systems. *Journal of Materials Science: Materials in Electronics*. 2021 Feb 1;32(4):4872–84.
14. Pulikkottil M, Thomas A, Malamal Neelanchery M, Gopalan Elavumkal V, Ansari S. Highly Efficient Solid-State Supercapacitor with Porous Electrode Material. *Energy Technology*. 2023 Sep 1;11(9).
15. Pulikkottil M, Antony H, Muralidharan MN, Gopalan EV, Ansari S. Cashew Nut Shell Derived Porous Activated Carbon Electrodes for “Water-in-Salt” Electrolyte Based Symmetric Supercapacitor. *ChemistrySelect*. 2022 Jun 20;7(23).
16. Merin P, Joy PJ, Muralidharan MN, Gopalan EV, Seema A. Biomass-Derived Activated Carbon for High-Performance Supercapacitor Electrode Applications. *Chem Eng Technol [Internet]*. 2021 May 1 [cited 2021 Sep 23];44(5):844–51. Available from: <https://onlinelibrary.wiley.com/doi/full/10.1002/ceat.202000450>

17. Almeida C, Jackson P, Vicentini R, Pereira EL, Santos E, Morais L, et al. Charge and energy storage properties of NiO-AC composites in organic electrolyte using operando Raman and distributed capacitance analyses in the time domain [Internet]. Available from: <https://ssrn.com/abstract=5088141>
18. Madhu R, Veeramani V, Chen SM, Veerakumar P, Liu S Bin. Functional porous carbon/nickel oxide nanocomposites as binder-free electrodes for supercapacitors. *Chemistry - A European Journal*. 2015 May 1;21(22):8200–6.
19. Cao JP, He S, Wu Y, Zhao XY, Wei XY, Takarada T. Synthesis of NiO/activated carbon composites and their application as electrode materials for capacitors. *Int J Electrochem Sci*. 2017 Apr 1;12(4):2704–18.
20. Xie A, Du J, Zhang J, Xiong Z, Shao F, Luo S. A High-Performance Nonenzymatic Urea Sensor Based on Graphene-NiO-Polyaniline. *J Electrochem Soc*. 2019;166(6):B456–63.
21. Mansurov ZA, Smagulova GT, Imash AA, Taurbekov AT, Elouadi B, Kaidar BB. Carbon/NiO Compositional Fibers. *Eurasian Chemico-Technological Journal*. 2022;24(2):59–67.
22. Abioye AM, Faraji S, Ani FN. Effect of heat treatment on the characteristics of electroless activated carbon-nickel oxide nanocomposites. *J Teknol*. 2017;79(7–3):61–7.
23. Taeño M, Maestre D, Ramírez-Castellanos J, Li S, Lee PS, Cremades A. Towards control of the size, composition and surface area of nio nanostructures by sn doping. *Nanomaterials*. 2021 Feb 1;11(2):1–13.
24. Huang W, Ding S, Chen Y, Hao W, Lai X, Peng J, et al. 3D NiO hollow sphere/reduced graphene oxide composite for high-performance glucose biosensor. *Sci Rep*. 2017 Dec 1;7(1).
25. Ivanova T, Harizanova A, Shipochka M, Vitanov P. Nickel Oxide Films Deposited by Sol-Gel Method: Effect of Annealing Temperature on Structural, Optical, and Electrical Properties. *Materials*. 2022 Mar 1;15(5).
26. Arain M, Nafady A, Sirajuddin, Ibupoto ZH, Hussain Sherazi ST, Shaikh T, et al. Simpler and highly sensitive enzyme-free sensing of urea via NiO nanostructures modified electrode. *RSC Adv*. 2016;6(45):39001–6.
27. Hassan MF, Sabri MA, Fazal H, Hafeez A, Shezad N, Hussain M. Recent trends in activated carbon fibers production from various precursors and applications—A comparative review. Vol. 145, *Journal of Analytical and Applied Pyrolysis*. Elsevier B.V.; 2020.
28. Vedharathinam V, Botte GG. Direct evidence of the mechanism for the electro-oxidation of urea on Ni (OH) 2 catalyst in alkaline medium. *Electrochimica Acta*. 2013 Oct 1;108:660-5.
29. Arain M, Nafady A, Sirajuddin, Ibupoto ZH, Hussain Sherazi ST, Shaikh T, et al. Simpler and highly sensitive enzyme-free sensing of urea via NiO nanostructures modified electrode. *RSC Adv*. 2016;6(45):39001–6.
30. Morales-Cruz M, Solis-Marcano NE, Binder C, Priest C, Cabrera CR. Electrochemical *Proteus vulgaris* whole cell urea sensor in synthetic urine. *Curr Res Biotechnol*. 2019 Nov 1;1:22–7.

31. Dong Q, Ryu H, Lei Y. Metal oxide based non-enzymatic electrochemical sensors for glucose detection. *Electrochimica acta*. 2021 Feb 20;370:137744.
32. Pitiphattharabun S, Auewattanapun K, Htet TL, Thu MM, Panomsuwan G, Techapiesancharoenkij R, et al. Reduced graphene oxide/zinc oxide composite as an electrochemical sensor for acetylcholine detection. *Sci Rep*. 2024 Dec 1;14(1).
33. Agnihotri AS, Varghese A, M N. Transition metal oxides in electrochemical and bio sensing: A state-of-art review. *Applied Surface Science Advances*. 2021 Jun 1;4.
34. Babitha KB, Soorya PS, Peer Mohamed A, Rakhi RB, Ananthakumar S. Development of ZnO@rGO nanocomposites for the enzyme free electrochemical detection of urea and glucose. *Mater Adv*. 2020;1(6):1939–51.
35. G P, Rathi BS, Kumar PS, Rangasamy G. Electrochemical sensor for urea determination using structural c-multiwall carbon nanotubes decorated CuO hybrid nanocomposite: Application in rice water samples. *Desalination Water Treat*. 2024 Oct 1;320.
36. Magar HS, Hassan RYA, Abbas MN. Non-enzymatic disposable electrochemical sensors based on CuO/Co₃O₄@MWCNTs nanocomposite modified screen-printed electrode for the direct determination of urea. *Sci Rep*. 2023 Dec 1;13(1).
37. Botewad SN, Gaikwad DK, Girhe NB, Thorat HN, Pawar PP. Urea biosensors: A comprehensive review. *Biotechnology and Applied Biochemistry*. 2023 Apr;70(2):485-501.
38. Hernández-Ramírez D, Mendoza-Huizar LH, Galán-Vidal CA, Aguilar-Lira GY, Álvarez-Romero GA. Review—Trends on the Development of Non-Enzymatic Electrochemical Sensors Modified with Metal-Oxide Nanostructures for the Quantification of Uric Acid. *J Electrochem Soc*. 2021 May 1;168(5):057522.
39. Jagannathan M, Dhinasekaran D, Rajendran AR, Cho S. A review of electroactive nanomaterials in the detection of nitrogen-containing organic compounds and future applications. *Biosensors*. 2023 Nov 18;13(11):989.
40. Naz I, Tahira A, Shah AA, Bhatti MA, Mahar IA, Markhand MP, Mastoi GM, Nafady A, Medany SS, Dawi EA, Saleem LM. Green synthesis of NiO nanoflakes using bitter gourd peel, and their electrochemical urea sensing application. *Micromachines*. 2023 Mar 19;14(3):677.
41. Amin S, Tahira A, Solangi A, Beni V, Morante JR, Liu X, et al. A practical non-enzymatic urea sensor based on NiCo₂O₄ nanoneedles. *RSC Adv*. 2019;9(25):14443–51.
42. Sunil Kumar Naik TS, Saravanan S, Sri Saravana KN, Pratiush U, Ramamurthy PC. A non-enzymatic urea sensor based on the nickel sulfide / graphene oxide modified glassy carbon electrode. *Mater Chem Phys*. 2020 Apr 15;245.

Chapter **7**

CONCLUSIONS

Conclusions

The summary and conclusions of the present study on the synthesis of activated carbon from biomass waste and the study of its suitability for applications in electrochemical systems are as follows:

This thesis describes the potential of biomass-derived activated carbon (BDAC) for electrode applications in various electrochemical systems, including supercapacitors, lithium-ion batteries (LIBs), and electrochemical sensors. The study highlights a cost-effective and environmentally friendly method for preparing BDAC-based electrode materials that possess unique structural and electrochemical properties. In this research, biomass waste materials such as cashew nut shells, mahogany fruit shells, and nutmeg shells were used as precursors. The prepared BDAC samples are respectively named as CNSAC, MSAC, and ACNM. Their structural properties were evaluated using various physicochemical characterisation techniques.

All the BDAC materials exhibit remarkable surface areas with well-developed pore distributions. The formation and distribution of micropores, mesopores and macropores in the prepared materials are significantly influenced by the composition of organic polymers such as cellulose, hemicellulose, and lignin in their pristine form. The highest values of surface area for the electrode materials CNSAC, MSAC, and ACNM are obtained as $835 \text{ m}^2\text{g}^{-1}$, $1072 \text{ m}^2\text{g}^{-1}$, and $1011 \text{ m}^2\text{g}^{-1}$, respectively. The microporous nature of these materials is attributed to the lignocellulosic nature of their precursors, along with the effects of KOH activation during the preparation process. Additionally, the presence of mesopores in MSAC and ACNM contributes significantly to enhancing their electrochemical efficiency as electrode materials.

This study systematically investigates the electrochemical performance and charge storage capabilities of prepared electrode materials. Among these, ACNM displayed a superior specific capacitance of 314 F g^{-1} at 1 A g^{-1} . This remarkable capacitive behaviour is attributed to its hierarchical pore structure, which include significant micro- and mesopores. This porous structure facilitates rapid ion transport and provides abundant active sites for charge accumulation. The other electrode materials, MSAC and CNSAC, also demonstrated competitive specific capacitances of 267 F g^{-1} and 214 F g^{-1} at the same current density of 1 A g^{-1} , respectively. The variation

in their performance may be attributed to differences in surface area and pore size distribution. Ragone plots of different BDAC materials illustrate the exceptional balance between energy and power density values of ACNM. Furthermore, all prepared BDAC materials demonstrate outstanding cycling stability and capacitive retention of over 95% after 10,000 charge-discharge cycles at a current density of 20 A g^{-1} , confirming their structural stability and electrochemical reliability.

The successful fabrication of symmetric supercapacitors (SSCs) and flexible supercapacitors (FSCs) further validates the practical viability of these materials. The SSC with CNSAC electrodes and water-in-salt electrolyte demonstrates superior specific capacitance of 110 F g^{-1} over a wider potential window (0-2V). It also exhibited excellent cycle stability, with 83% capacitance retention. Moreover, it demonstrated a lower equivalent series resistance compared to conventional aqueous electrolyte-based SSC systems. The FSC fabricated with gel polymer electrolyte and MSAC electrodes achieved a high specific capacitance of 121 F g^{-1} at a current density of 1 A g^{-1} , maintaining a capacitance retention of 78% over 2,000 cycles of charging and discharging. The wider potential window of 2V with a high specific capacitance of FSC suggests excellent energy and power densities. Furthermore, the scalability of these FSC systems in wearable devices are validated by studying their capacitive properties at different bending angles. These findings provide valuable insight into pore structure engineering and surface chemistry in optimising supercapacitor performance while highlighting the potential of sustainable biomass precursors as low-cost alternatives to conventional carbon materials.

The suitability of BDAC materials for LIB applications was studied using ACNM. The fabricated anode half-cell exhibited a remarkable specific capacity of 610 mAh g^{-1} at a current rate of 0.1 C and excellent stability over 200 cycles at a current rate of 2 C. The rate capability test further validated its efficiency as an anode material in LIBs. The large surface area of the anode material benefits lithium intercalation and deintercalation, enhancing the capacity of the LIBs. However, this may facilitate the formation of the solid electrolyte interface (SEI) and lead to irreversible capacity loss. This issue can be effectively addressed by optimising the structural properties of the anode material. This study highlights the impact of the structural and electrochemical properties of the anode on the formation of a stable and well-developed SEI.

Additionally, it includes insights from scanning electrochemical microscopy analysis, validating the effective formation of SEI in the fabricated half-cells.

The efficiency of ACNM is further examined in detecting the urea from real-world samples. The electrode material used in this work is composite materials containing ACNM and NiO prepared through the cost-effective coprecipitation method. The efficiency of these materials for urea sensing applications is evaluated using different electrochemical analysis techniques. It exhibited a sensitivity of $1620 \mu\text{A mM}^{-1} \text{cm}^{-2}$, with superior values of the limit of detection and limit of quantification of $1.69 \mu\text{M}$ and $9.6 \mu\text{M}$, respectively. The efficiency of the prepared electrode material was confirmed by the significant recovery percentage of urea in tap water samples. The materials also demonstrated excellent selectivity against other interfering species, a wide linear range for urea detection, and good reproducibility. Overall, the AC/NiO composite is a promising, cost-effective material for urea sensing applications in various fields, including dairy industries, clinical diagnostics, and environmental monitoring.

In summary, this research confirms that BDACs can compete with or even surpass conventional carbon materials in terms of performance, offering a green alternative for energy storage and sensing technologies. Additionally, the study emphasises the potential of BDACs for a wide range of applications beyond those currently explored. By connecting fundamental understanding with scalable fabrication strategies, this research provides practical insights for the industrial adoption of sustainable carbon materials in next-generation electrochemical devices.

Chapter **8**

RECOMMENDATIONS

8.1 Future works

This work emphasises the promising electrochemical properties of activated carbon derived from biomass waste (BDAC) in various electrochemical systems. This extensive study holds significant potential for future research and plays a critical role in sustainable development. The application of BDAC is not confined to the areas discussed but extends to other fields that support sustainable development and the circular economy.

This thesis successfully demonstrated the application of BDAC electrodes in supercapacitors, lithium-ion battery (LIB) systems, and electrochemical sensors. However, there is still considerable potential for further exploration and optimisation of BDAC in these fields. Based on the material and electrochemical performance of BDAC, several key recommendations can be made to guide future research efforts, ensuring ongoing advancements in material design and application.

The structural and electrochemical characteristics of the prepared materials, such as their high surface area, well-defined pore distributions, enhanced capacitance, and improved capacity, contribute to their effectiveness in various electrochemical applications. However, further enhancements can be achieved by refining the synthesis techniques and material composition. For instance, implementing advanced doping strategies that involve incorporating heteroatoms and exploring alternative synthesis methods could provide better control over the morphology and crystallinity of BDAC, improve ion transport kinetics, and result in superior electrochemical performance.

The BDAC-based materials are highly versatile, allowing for applications beyond supercapacitors, LIBs and urea sensors. One promising direction is their integration into sodium-ion batteries, which can serve as a more cost-effective and sustainable energy storage solution compared to LIBs. Additionally, their sensing capabilities can be expanded to detect other biomolecules and environmental pollutants. This would extend their applications to medical diagnostics and environmental monitoring.

The efficiency of various BDAC-based electrochemical systems is validated on a laboratory scale through this work. However, the large-scale fabrication of these

systems is essential for their practical implementation. To ensure this transition, future studies focusing on cost-effective and environmentally friendly synthesis and fabrication techniques are mandatory. Additionally, the integration of these materials into portable and wearable electronics should be explored to meet the increasing demand for lightweight energy storage and sensing devices.

The materials based on BDAC developed in this study show significant potential for various electrochemical applications, including energy storage and sensors. Their advantages, such as cost-effectiveness, environmental friendliness, and ease of handling, support the widespread use of BDAC materials. The application of BDAC can be further enhanced by employing optimised synthesis methods, expanding its applications, and ensuring scalability.

